

Understanding and controlling properties of bulk Ni-Mo-W sulfides for hydrodefunctionalization

Sylvia Albersberger

Vollständiger Abdruck der von der Fakultät für Chemie der Technischen Universität München zur Erlangung des akademischen Grades eines

Doktors der Naturwissenschaften (Dr. rer. nat.)

genehmigten Dissertation.

Vorsitzender: Hon.-Prof. Dr. Richard W. Fischer

Prüfer der Dissertation: 1. Prof. Dr. Johannes A. Lercher

2. Prof. Dr. Fritz E. Kühn

Die Dissertation wurde am 11.06.2019 bei der Technischen Universität München eingereicht und durch die Fakultät für Chemie am 19.11.2019 angenommen.

*Nothing in life is to be feared, it is only to be understood.
Now is the time to understand more, so that we may fear less.
(Marie Curie)*

Statutory Declaration

I declare that I have authored this thesis independently and that I have solely used the declared (re)sources and that I have marked all material, which has been quoted either literally or by content from the used sources. All collaborators are named and their specific contribution is addressed. Published content of this thesis is clearly marked.

Acknowledgements

Many people accompanied me during my PhD study and contributed to the success of this work. I take this opportunity to thank all of them.

First, I want to thank Prof. Johannes A. Lercher for the possibility to work on a very interesting and challenging research topic in his group, his guidance, and the inspiring discussions. I highly appreciated all the chances you gave me to evolve myself - scientifically and personally.

I also thank my project partner Chevron Energy Technology for the financial support of my thesis. I especially want to thank Alexander Kuperman, Axel Brait, and Jinyi Han. Besides your helpful and motivating input and support, it has always been a pleasure to share ideas and experiences with you. I enjoyed the meetings with all of you, particularly the once in person.

I owe my supervisors Oliver Y. Gutiérrez and Hui Shi a special thank. I really liked to work and discuss with you. I thank you for your guidance, for the patience you had, and your assistance in solving any problems. You helped me to further improve my knowledge and skills as a scientist and personally.

I am also very grateful for the assistance and advices of Prof. Andreas Jentys regarding XAS measurements and other technical issues.

Very special thanks go to the staff of TC II, who keep TC II running. I gratefully thank Xaver Hecht for all his support in the lab and the BET measurements. Bettina, Steffi, and Uli, all of you always had an open ear for me and helped me with all organizational work – thank you! Moreover, I want to thank Kateryna, Andreas, and Martin for their help.

Many SEM and TEM pictures needed to be recorded during my PhD study. Thus, I want to thank both teams, especially Daniel, Martin and Takaaki for the SEM measurements as well as Ehrmi and Lara for the TEM measurements.

I also want to thank Matthias and Rachit for organization of the XAS trips and all other support regarding this. In this line, I thank all other colleagues who took part at the XAS trip and shared the time with me at the beamline, in particular Daniel, Ehrmi, Insu, Kai, Manuel, and Matthias.

A lot of students contributed with their great work to the final success of my thesis. I want to acknowledge Anna, Stephanie, Maximilian, Matthias, Santiago, Yap Wei, Carolin, Laura, Andreas, Bruno, Maximilian, Moritz, Niklas, and Richa.

Of course, I thank my colleagues at TC II for their input and support but also for the fun we had. It was a pleasure to be part of this great international team! I owe my project predecessors, Eva and Jennifer, a special thank. Especially, Eva helped me a lot at the beginning of my thesis

with her council and support. Martina, Daniel, Guoju, Ricardo, Manuel (the real one), and Manuel, thank you for the great working atmosphere and the fun we had in our “old” office. Edith, Martina, Tessi, Verena, Daniel, Ecki, Ehrmi, Felix, Kai, Manuel, Matthias, Niklas, and Peter thank you for the enjoyable lunch time and after work sit-ins. I also want to thank Wanqiu for the nice time we had at several conferences and at the trip to Chevron and for the good collaboration. Finally, I want to point out some of my companions who really became friends and supported me every time: Eva, Daniel, Ehrmi, Felix, and Niklas. I hope we will stay in contact even though some miles will be between us.

As work is not everything, I also want to thank all my friends who enabled a perfect work-life balance, shared my ups and downs, and have been there when I needed them. Special thanks go to Renate! You provided me a wonderful home during the last 3.5 years but more important you became my best friend and we shared a lot of good times but also bad times together.

Last but not least, I thank my parents, my brother Markus, my sister-in-law Julia, and my niece and godchild Miriam. Thank you all for your support and for being there all the time!

Sylvia

Abstract

The concentration of active sites on bulk Ni-Mo(W)S₂ is governed by the sulfide phase composition, the synthesis procedure of the precursor, and the sulfidation protocol. In contrast, the nature of the active sites is independent of these parameters. For hydrogenation reactions, the rate determining step is shifted by the concentration of active sites. Ring opening and hydrogenation reactions are catalyzed different active sites inducing different adsorption modes of the reactant.

Kurzzusammenfassung

Die Konzentration der aktiven Stellen in Ni-Mo(W)S₂ wird durch die Zusammensetzung der Sulfidphasen, das Syntheseverfahren der Katalysatorvorstufen und das Sulfidierungsprotokoll bestimmt. Im Gegensatz dazu ist die Art der aktiven Zentren unabhängig von diesen Parametern. Bei der Hydrierung aromatischer Moleküle wird der geschwindigkeitsbestimmende Schritt der Umsetzung durch die Konzentration der aktiven Stellen verschoben. Ringöffnungs- und Hydrierreaktionen werden durch verschiedene aktive Zentren katalysiert. Dies ist durch unterschiedlichen Adsorptionsmodi des Reaktanten bedingt.

Abbreviations

Symbol	Description
API	American Petroleum Institute
as	Asymmetric
BCH	Bicyclohexane
BET	Brunauer-Emmett-Teller
BJH	Barrett-Joyner-Halenda
BP	Biphenyl
BT	Butanethiol
Γ	Lattice vibration
c_i	Concentration of a component i
cat	Catalyst
CCD	Charge coupled device
COD	Crystallography open database
CUS	Coordinatively unsaturated sites
δ	Bending vibration
DBT	Dibenzothiophene
DDN	Direct denitrogenation
DDS	Direct desulfurization
Decalin	<i>cis, trans</i> -Decahydronaphthalene
DFT	Density functional theory
DHQ	<i>cis, trans</i> -Decahydroquinoline
DM-BCH	3,3'-Dimethylbicyclohexane
DM-BP	3,3'-Dimethylbiphenyl
DM-PC	3,3'-Dimethylphenylcyclohexane
DMDBT	4,6-Dimethyldibenzothiophene
DMDS	Dimethyl disulfide
E_a	Activation energy
E_{app}	Apparent activation energy
E_{kin}	Binding energy
ECH	Ethylcyclohexane
EU	European Union
EXAFS	Extended X-ray absorption fine structure
f_i	Fraction of component i
FCC	Fluid catalytic cracking

FID	Flame ionization detector
GC	Gas chromatography
4H-DBT	Tetrahydrodibenzothiophene
4H-DMDBT	Tetrahydro-4,6-dimethyldibenzothiophene
6H-DMDBT	Hexahydro-4,6-dimethyldibenzothiophene
HD	<i>n</i> -Hexadecane
HDN	Hydrodenitrogenation
HDO	Hydrodeoxygenation
HDS	Hydrodesulfurization
HOMO	Highest occupied molecular orbital
HPLC	High performance liquid chromatography
HT	Hydrothermal
HYD	Hydrogenation
HYDN	Hydrogenation pathway within hydrodenitrogenation
HYDS	Hydrogenation pathway within hydrodesulfurization
ICSD	Inorganic crystal structure database
IR	Infrared
k_i	Reaction rate constant of a reaction <i>i</i>
K_i	Adsorption or equilibrium constant of a component <i>i</i>
K_{sp}	Solubility product constant
L	Length of sulfide slab
LCF	Linear combination fit
LHSV	Liquid hourly space velocity
LPG	Liquified petroleum gas
m	Mass
MS	Mass spectrometry
OPA	<i>o</i> -Propylaniline
Ox	Oxide
Q	Quinoline
p	Pressure
PB	Propylbenzene
PC	Phenylcyclohexane
PCH	Propylcyclohexane
PCHA	<i>o</i> -Propylcyclohexylamine
PCHE	1-Propylcyclohexene, 3-propylcyclohexene, and propylidene cyclohexane
r_i	Reaction rate of a reaction <i>i</i>
R	Radical intermediate

RDS	Rate determining step
RO	Ring opening
θ_i	Fractional coverage of a molecule <i>i</i>
s	Symmetric
S _{BET}	Specific surface area
SAED	Selected area electron diffraction
SEM	Scanning electron microscopy
SH group	Sulfhydryl group
Stk	Stacking degree
T	Temperature
TD	<i>n</i> -Tetradecane
TEM	Transmission electron microscopy
1-4 THQ	1,2,3,4-Tetrahydroquinoline
5-8 THQ	5,6,7,8-Tetrahydroquinoline
TPS	Temperature programmed sulfidation
ULSD	Ultra-low sulfur diesel
ν	Stretching vibration
V	Volume
V _{ads}	Adsorbed volume
VGO	Vacuum gas oil
x_i	Metal molar fraction of component <i>i</i>
XANES	X-ray absorption near edge structure
XAS	X-ray absorption spectroscopy
XPS	X-ray photoelectron spectroscopy
XRD	X-ray diffraction

Table of Contents

Chapter 1- Introduction

1. Crude oil - Feedstock Quality vs. Environmental Restrictions	
1.1. Classification of Crude Oil.....	3
1.2. Consequences of the Crude Oil Quality for Refining	5
2. Hydrotreating-The Industrial Process	
2.1. Role of Hydrotreating within a Refinery.....	6
2.2. Hydrotreating Process	7
2.3. Commercially used Hydrotreating Catalysts.....	9
2.4. Hydrotreating Reactions	11
2.4.1. Hydrodesulfurization.....	11
2.4.2. Hydrodenitrogenation	14
2.4.3. Hydrodeoxygenation	18
2.4.4. Hydrogenation of (poly)aromatic compounds	18
3. Hydrotreating Catalysts-Molybdenum and Tungsten Sulfides	
3.1. Synthesis of Supported Catalyst Precursors	20
3.2. Synthesis of Unsupported Catalyst Precursors	20
3.2.1. Co-precipitation of oxide catalyst precursors	20
3.2.2. Hydrothermal synthesis methods	21
3.3. Structure of Unsupported Oxide Precursor	21
3.4. Sulfidation of Oxide Precursors.....	22
3.4.1. Sulfidation of molybdenum oxide.....	22
3.4.2. Sulfidation of tungsten oxide	22
3.4.3. Impact of nickel on the sulfidation of molybdenum and tungsten oxide phases	25
3.5. Structure of the Sulfide Catalysts.....	26
3.5.1. Structure of molybdenum and tungsten disulfide.....	26
3.5.2. Structural models for the incorporation of nickel into the sulfide phase.....	27
3.5.3. Consequences of the incorporation of nickel into the sulfide phase.....	28
3.5.4. Characteristics of trimetallic sulfides	29
3.6. Activation of Hydrogen on the Sulfide Surface	30
3.7. Scope of this Thesis.....	30

Chapter 2 - Bulk Ni-Mo-W Sulfides – Simultaneous hydrodenitrogenation and hydrodesulfurization

Abstract	32
1. Introduction	33
2. Experimental.....	35
2.1. Synthesis of oxide precursors	35
2.1.1. Salt precursor route (WMoNi-a _{ox} and WMoNi-aHT _{ox}).....	35
2.1.2. Oxide precursor route (WMoNi-b _{ox} and WMoNi-bHT _{ox}).....	35
2.1.3. H ₂ S precipitation route (WMoNi-s _{ox}).....	36
2.1.4. Hydrothermal decomposition (WMoNi-sHT _{ox})	36
2.2. Synthesis of sulfide catalysts	36
2.3. Characterization.....	37
2.4. Catalysis	38
3. Results and Discussion.....	40
3.1. Characterization of the oxide catalyst precursors.....	40
3.2. Chemical and physicochemical properties of the sulfide catalysts.....	45
3.3. Catalysis	51
3.3.1. Hydrodenitrogenation of <i>o</i> -propylaniline	51
3.3.2. Hydrodenitrogenation of quinoline	54
3.3.3. Hydrodesulfurization of dibenzothiophene.....	59
3.3.4. Apparent activation energies	62
3.4. Empirical correlation of physicochemical properties and catalytic performance.....	63
3.5. Structure activity correlations	65
3.5.1. Implications of the empirical modeling.....	66
3.5.2. Hydrotreating activity in the presence of <i>o</i> -propylaniline.....	67
3.5.3. Hydrotreating activity in the presence of quinoline.....	68
3.5.4. Hydrodesulfurization activity in the presence of <i>o</i> -propylaniline and quinoline.....	69
3.5.5. Comparison of supported and unsupported bimetallic and trimetallic sulfides	69
4. Conclusion.....	71

Chapter 3 – Uncovering Active Sites–Enhancing the Activity of trimetallic Ni-Mo-W Sulfides for Quinoline Hydrodenitrogenation

Abstract	74
1. Introduction.....	75

2. Experimental.....	77
2.1. Synthesis of the oxide precursor.....	77
2.2. Synthesis of the sulfide catalyst.....	77
2.3. Selective removal of nickel sulfides.....	78
2.4. Characterization.....	79
2.5. Kinetic measurements.....	81
3. Results and Discussion.....	82
3.1. Physicochemical properties of parent and HCl-treated sulfide catalysts.....	82
3.2. Reaction network of the hydrodenitrogenation of quinoline.....	88
3.3. Hydrodenitrogenation of <i>cis</i> , <i>trans</i> -decahydroquinoline.....	92
3.4. Comparison of the catalytic activity of parent and HCl-treated sulfides.....	94
3.5. Detailed evaluation of ring opening and hydrogenation pathway.....	97
3.5.1. Ring opening pathway.....	97
3.5.2. Hydrogenation pathway.....	101
3.5.3. Site requirement for ring opening and hydrogenation.....	104
3.5.4. Towards the understanding of hydrodenitrogenation activity across different elemental compositions of bulk sulfide catalysts.....	106
4. Conclusion.....	109

Chapter 4 – Hydrotreating Catalysts- Liquid-phase Sulfidation

1. Introduction.....	112
2. Experimental.....	115
2.1. Synthesis of the Trimetallic Oxide Precursor.....	115
2.2. Liquid-phase Sulfidation.....	115
2.3. Kinetic measurements.....	118
2.4. Characterization.....	120
3. In-situ XAS Investigation of the Liquid-phase Sulfidation.....	123
4. Temperature-programmed Sulfidation.....	128
5. Reaction Networks for the Conversion of the Reactants.....	130
5.1. Hydrodenitrogenation of <i>o</i> -propylaniline.....	130
5.2. Hydrodesulfurization of dibenzothiophene.....	132

5.3. Hydrodesulfurization of 4,6-dimethyldibenzothiophene	134
6. Mutual Impact of the Hydrotreating Reactions.....	137
7. Impact of Sulfidation Parameters on the Catalytic Performance.....	139
7.1. Influence of an increased sulfidation pressure	139
7.2. Effect of the sulfur content	142
7.3. Influence of the hydrogen to sulfur ratio	147
7.4. Effect of the sulfiding agent.....	152
7.5. Combined effects of nature and concentration of the sulfiding agent	156
8. Conclusion.....	160
 <i>Chapter 5</i>	
Summary	164
Zusammenfassung	166
References	169
Appendix.....	183
Curriculum Vitae	199
Conference Contributions & Publications	200

Chapter 1- Introduction

1. CRUDE OIL-

Feedstock Quality vs. Environmental Restrictions

1.1. Classification of Crude Oil

Crude oil primary consists of various alkanes, alkenes, and (poly)aromatic molecules which range from methane (CH₄) to heavy molecules with more than one hundred carbon atoms. A minority of the hydrocarbons contain heteroatoms, i.e., sulfur, nitrogen, or oxygen. Moreover, metals, mainly nickel and vanadium, are present in crude oils. The exact composition of crude oil, however, widely differs and depends strongly on the location of the crude oil exploitation.¹

Key properties of crude oil for further processing are its density, its sulfur content, and its distillation curve. A classification can be, for instance, made according to the density of the crude oil. A measure for this is the *American Petroleum Institute* gravity (API gravity). Commonly, the API gravity ranges from 45 to 10. A high API gravity is, thereby, related to heavy crude oil types, which are in most cases accompanied with a high content of heteroatoms and metals as well as a low content of middle distillates. A low API gravity, in contrast, indicates light types of crude oil containing little amounts of impurities. Processing of such a type leads to a relatively high fraction of transportation fuels and only small residue fractions. Despite a similar density and API gravity the exact product distribution can vary in a relatively wide range.¹⁻² This is exemplarily shown in Table 1 for different types of crude oil from various geographical origins.

Crude oil can also be classified by its hydrogen-to-carbon (H/C) ratio. High quality crude oil is characterized by a H/C ratio larger than 1.5 whereas the H/C ratio of crude oil with poor quality is below 0.8.²

Both API gravity and H/C ratio indicate the quality of the respective crude oil. Usually crude oils of the same geographical origin have similar compositions and characteristic properties. Crude oils from the Arabian region, for instance, are medium or heavy accompanied with a high content of S-containing molecules. Light crude oils with a rather low sulfur content can be extracted in the North Sea and in North and West Africa. The crude oils from North and South America are rather heavy and of low quality.

Table 1. Composition of different crude oils together with their density [g/mL], their API gravity, and their content of sulfur [wt. %].

Crude Oil	Content [wt. %]				Density [g/mL]	API	Sulfur content [wt. %]
	Gas	Gasolines	Middle Distillates	Heavy Products			
Sahara Crude Oil	6.7	31.1	35.6	24.4	0.806	44	0.2
Brent (North Sea)	4.4	28.9	35.6	26.7	0.837	38	0.3
Arabian Light (Saudi Arabia)	2.2	20	35.6	35.6	0.855	34	1.7
Arabian Heavy (Saudi Arabia)	4.4	8.9	28.9	51.1	0.893	27	2.8
Boscan Heavy Crude (Venezuela)	2.2	0	24.4	68.9	0.995	11	5.3

1.2. Consequences of the Crude Oil Quality for Refining

Commonly, light crude oil with a high content of light and middle distillates is desired for processing, as low-quality crude oil requires higher production efforts to convert the large amounts of heavy products into more valuable products and to remove the impurities. But due to the decline of light crude oil, the conversion of heavy feedstocks into middle distillates is gaining increasing importance.^{1,2} There are two possible ways to upgrade heavy crude oil fractions, i.e., addition of hydrogen and removal of carbon. Processes like hydrocracking and hydrotreating increase the hydrogen to carbon ratio. Since these processes are catalytic and require large amounts of hydrogen, they are very cost-intensive. In contrast, the processes which reject carbon, e.g., coking and visbreaking, are usually non-catalytic and thermal. The formation of large amounts of coke and low liquid yields make these kinds of processes disadvantageous.²

In addition to the increasing demand of converting heavy feedstocks due to decreasing resources of high-quality crude oil, the stricter environmental restrictions regarding the sulfur content in transportation fuels challenge refineries. Currently, the sulfur level in transportation fuels, i.e., gasoline, diesel, and kerosene, is restricted below 15 ppm in Europe and North America.^{1,3}

China also wants to reach this level within the next years.³ Furthermore, restriction of the relatively high sulfur content of marine fuels is of topical interest. The European Union (EU), for instance, limited the sulfur level of marine fuels to 100 ppm in all EU ports and to 500 ppm on all EU waters from 2020 onwards.⁴

These regulations combined with the increasing need of processing heavy crude oils make a very efficient removal of heteroatoms, especially sulfur, indispensable. In respect thereof, hydrotreating processes, aiming at the removal of heteroatoms, increase in importance. Their efficiency can be increased by changing the reactor design and the reactions conditions as well as by improving the performance of the catalysts used.

2. HYDROTREATING -

The Industrial Process

2.1. Role of Hydrotreating within a Refinery

Hydrotreating in an oil refinery comprises several catalytic reactions in which hydrocarbons react with hydrogen. These processes aim to remove impurities from the feed to avoid catalyst poisoning of other catalytic refining processes, e.g., catalytic reforming or fluid catalytic cracking (FCC), and/or to achieve final product specifications. More than half of all refinery streams therefore pass through hydrotreating units making hydrotreating catalysts the most used catalysts on weight basis per year.⁵⁻⁶

Hydrotreating processes are, for instance, applied to improve the product stability by hydrogenation of olefins or to increase the cetane number by hydrogenation of aromatic compounds. It further aims to reduce the sulfur content to avoid corrosion of process units and to ensure compliance of environmental restrictions regarding the emission of sulfur dioxide (SO₂).⁶

Especially the new environmental regulations regarding the sulfur content in the last decades have increased the importance of hydrotreating processes in refineries. In the United States of America, ultra-low sulfur diesel (ULSD) was established in which the sulfur content was limited to maximum 15 wt. ppm. In Europe, an even higher gas oil quality is required as the sulfur content is restricted to 10 wt. ppm since 2010.^{1, 3}

These new specifications cause remarkable changes of the hydrotreating processes, e.g., increase of the reactor volume and implementation of amine washers in the recycling process. Moreover, steam reforming and partial oxidation units have been built to meet the increased hydrogen consumption arising from the conversion of heavy feedstocks. Further, research on hydrotreating catalysts has been pushed forward to improve the performance of the existing material and to develop new materials with a higher activity.¹

Consequently, the tasks of the individual hydrotreating process are related to the desired technical and environmental specifications of each product stream. This together with fluctuations in feed compositions require a high flexibility of hydrotreating processes in terms of reaction conditions and the catalysts used.

2.2. Hydrotreating Process

Product specifications as well as process conditions demand that most product streams in a refinery pass through hydrotreating units at several production steps. Figure 1 shows a simplified scheme of a typical refinery.

After desalting, the crude oil is separated into the so-called straight-run fractions by atmospheric distillation according to their boiling point ranges. The light fractions are chemically converted to render product and environmental specifications. Examples of these treatments are catalytic reforming, isomerization, and alkylation. The atmospheric residue can be either directly used as heavy oil after adjustment of its physicochemical properties or is vacuum distilled. Bitumen, waxes, and lubricants can be, for example, gained from the lighter fractions of the heavy oil. The heavy fractions are processed further by different cracking procedures and alkylation.^{1, 6}

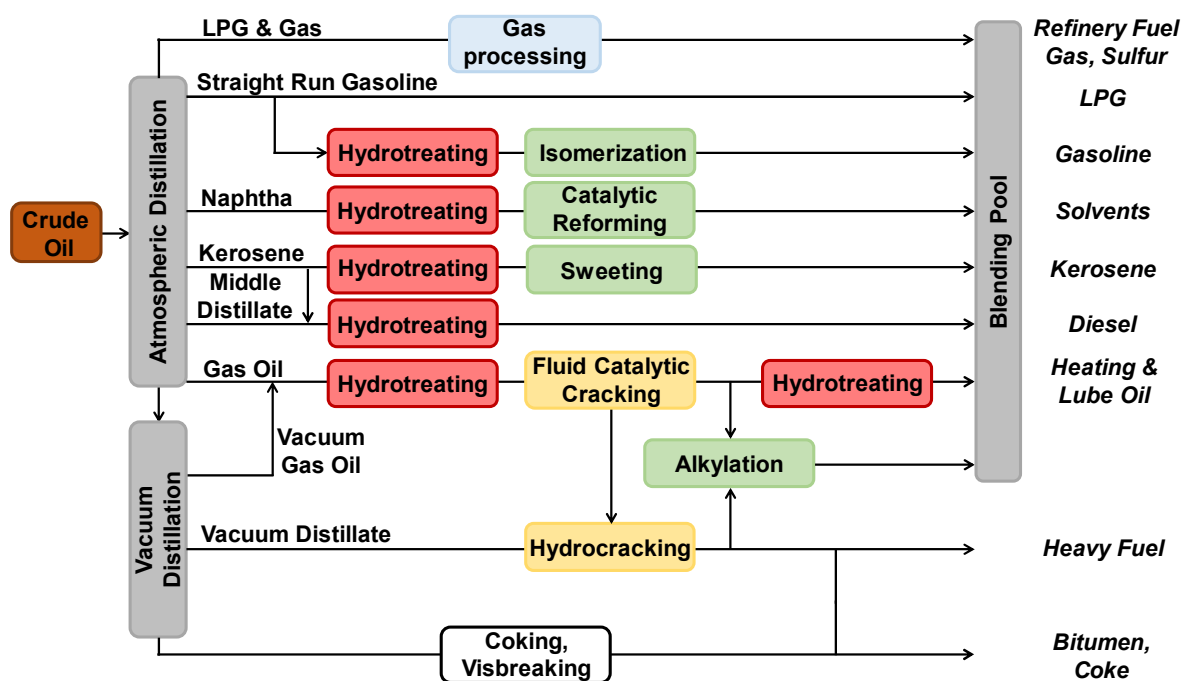


Figure 1. Simplified flow diagram of typical process steps within a refinery.

Hydrotreating processes are commonly carried out in a trickle-bed downflow reactor combined with a gas recycle system as hydrogen is added in excess. The compressed recycle gas and a make-up hydrogen stream are mixed before introduced to the reactor. The feedstock, which is liquid or a liquid-gas mixture, is pumped with a centrifugal pump, mixed with a H₂-enriched gas stream, and pressurized. The applied pressure ranges from 10 to 150 bar.

The reaction mixture is heated to 270–300 °C using a feedstock/product heat exchanger. The final reaction temperature of 320–400 °C is reached in a furnace before the feed is introduced

to the trickle-bed downflow reactor. The applied reaction conditions depend on the composition of the feedstock and the desired product quality.^{1, 6}

The fixed bed in the reactor contains the catalyst bed consisting in most of the cases of different sections and kinds of catalysts. Depending on the process requirements the reaction stream can be quenched between each catalyst bed to counteract the heat production arising from the exothermicity of hydrotreating reactions. The use of different types of catalysts along the fixed bed also diminishes catalyst deactivation which is mainly caused by coking, deposition of metals, and sintering. The outlet stream is heat exchanged with the reactor feed and cooled. After fractionating at high pressure, dihydrogen sulfide (H_2S), ammonia (NH_3), and other gases are removed from the recycle gas stream in an absorber unit.^{1, 6}

The trickle-bed downflow reactor is still the most abundantly used hydrotreating reactor, but ebullating-bed and slurry reactors are gaining more interest because of the increasing demand in hydrotreating of heavy feedstocks and simultaneously stricter environmental regulations. These other reactor types can be advantageous in the conversion of heavy feedstocks as coke and metal deposits as well as diffusion limitations are more severe in the case of converting heavy feedstocks than lighter feedstocks.^{1, 6-7}

2.3. Commercially used Hydrotreating Catalysts

Activity, lifetime, and regeneration play an important role in the selection of the catalysts. Furthermore, product selectivity of the catalyst as well as engineering and economic issues are decisive criteria.⁶ Hydrotreating catalysts must be able to activate hydrogen, to remove heteroatoms from polyaromatic compounds, and to saturate hydrocarbons.⁸

The best compromise between catalytic performance and economic efficiency is represented in CoMo-, NiMo-, and NiW-type sulfides supported on alumina, silica-alumina, or silica. Therefore, these materials are used to catalyze hydrotreating reactions in refineries. These catalysts usually contain around 8-16 wt. % of molybdenum and 12-25 wt. % of tungsten. The amount of cobalt and nickel ranges from 1-4 wt. %. Silicon, phosphorus, boron, or fluorine can be added as second dopants to modify the catalytic and mechanical properties of the material. The exact composition of the catalyst used depends on the feed and the desired quality of the product stream.⁶

CoMo sulfide catalysts show a high activity for hydrodesulfurization reactions but are less active in hydrogenation reactions needed in hydrodenitrogenation reactions and the saturation of aromatic compounds. NiMo sulfide catalysts, in contrast, exhibit a higher hydrogenation activity but consume more hydrogen compared to CoMo sulfides. Thus, NiMo sulfides are used if a high hydrogenation functionality is required.⁹ NiW sulfide catalysts are even more active in hydrogenation reactions than NiMo sulfides. Their industrial use, however, is limited due to economic reasons.^{1, 6}

In the last decades unsupported sulfide catalyst have gained more attention since the trimetallic NEBULA[®] catalyst was developed showing an extraordinary catalytic performance in hydrotreating reactions. Consequently, this catalyst can be used in the production of ultra-low sulfur diesel. The NEBULA[®] catalyst is a trimetallic bulk sulfide containing nickel, molybdenum, and tungsten. The higher metal content compared to the supported catalysts accompanied with the higher costs per catalyst fill must be compensated by the higher intrinsic activity of the trimetallic sulfides to make these materials profitable for industrial use. Moreover, the higher intrinsic activity of the trimetallic bulk sulfides, especially in hydrogenation reactions, leads to an increased hydrogen consumption and requires an improved heat removal due to the temperature increase in the reactor caused by the exothermicity of the chemical reactions. Therefore, changes in the reactor design are prerequisite to meet the requirements arising from the new, more active catalyst generation.¹⁰⁻¹²

In the case of supported and unsupported sulfide catalysts the synthesis routes often proceed via oxide precursors that are easier to store and to handle than the pyrophoric sulfides.

The oxide precursors are converted into their active form via sulfidation in the start-up phase of the hydrotreating process by exposing the catalyst precursor to a S-containing feed and/or the extra addition of H₂S, dimethyl disulfide (C₂H₆S₂), or carbon disulfide (CS₂) to the recycled hydrogen stream.^{1, 6}

Sulfidation is typically carried out between 300–400 °C and in a pressure range from 2-50 bar depending on the sulfiding agent and the type of catalyst.^{1, 13} Considering the exothermicity of the sulfidation reaction, the temperature can be increased stepwise.^{1, 14} The applied sulfidation procedure is a decisive factor in the synthesis of the catalyst as it highly influences the catalyst activity and stability (section 3.4.).⁶ Nowadays also pre-sulfided materials are filled into the reactor. Thus, less harsh sulfidation conditions are required diminishing catalyst deactivation due to sintering during sulfidation.^{13, 15-16}

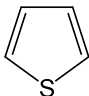
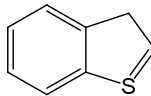
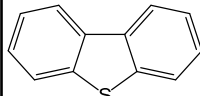
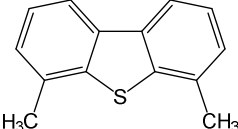
2.4. Hydrotreating Reactions

Several, different reactions take place during the hydrotreating processes, i.e., various bond cleavages as well as hydrogenation and dehydrogenation reactions. Which reaction dominates the conversion of the molecules is mainly governed by the molecular structure of the reactant, the reaction conditions, and the feed composition.^{1, 6} Another aspect is inhibition or acceleration of an overall reaction or a conversion pathway by the presence and the reaction of other components. The effect of molecules on the conversion of another component primarily depends on the adsorption strength of the reactants on the catalyst surface.^{1, 6} The following section outlines the most important hydrotreating reactions, i.e., hydrodesulfurization, hydrodenitrogenation, hydrodeoxygenation, and hydrogenation.

2.4.1. Hydrodesulfurization

The origin of the crude oil governs the content of sulfur as well as the nature of the S-containing compounds. Crude oil typically contains 1-5 wt. % sulfur. The S-containing components range from thiols over disulfides to thiophenes, benzothiophenes, and other polyaromatic hydrocarbons.^{1, 6} Examples of typical S-containing compounds in crude oil are shown in Table 2.

Table 2. Structural formula of representative S-containing hydrocarbons in crude oil.^{1, 6, 17}

Compound	Thiole	Thiophene	Benzothiophene	Dibenzothiophene	4,6-Dimethyldibenzothiophene
Structure	R—SH				

Sulfur removal from thiols and disulfides is relatively easy. They are converted through the elimination of H₂S and subsequent hydrogenation or hydrogenolysis. Thiols containing a β-H atom react preferably through elimination. The reactivity of the S-containing molecule decreases significantly with increasing structural complexity and molecular size. Thus, the hydrodesulfurization reactivity gets more demanding for the catalysts and reaction conditions in the order



Sulfur removal of polyaromatic compounds, which particularly occur in heavy boiling fractions, is often called deep hydrodesulfurization.^{6, 15, 17}

One of the most studied model S-containing compounds is dibenzothiophene as it has a relatively low reactivity. Moreover, dibenzothiophene and its alkyl-substituted derivatives are present in high amounts in crude oil. In general, all S-containing molecules can be converted via two reaction pathways, i.e., the direct desulfurization and the hydrogenation pathway. In the hydrogenation pathway the heteroaromatic ring is saturated prior to the sulfur removal. The reaction network of the hydrodesulfurization of dibenzothiophene is shown as an example in Figure 2.

In the case of dibenzothiophene, the hydrogenation pathway leads to the formation of tetrahydrodibenzothiophene and after the removal of sulfur to phenylcyclohexane. In the direct desulfurization route, the C-S bonds are directly split to form biphenyl. Subsequent hydrogenation of the resulting aromatic molecule to phenylcyclohexane and bicyclohexane can occur under hydrodesulfurization conditions. In the case of dibenzothiophene, the direct desulfurization pathway is favored compared to the hydrogenation pathway. It is assumed that dibenzothiophene preferentially adsorbs via the sulfur atom on Lewis-acid sites of the catalyst surface. This adsorption mode is, in turn, prerequisite for the direct desulfurization route.^{6, 15, 17}

Alkyl substituents adjacent to the sulfur atom generally retard hydrodesulfurization due to steric hindrance. Another consequence of alkyl substituents in this position is a change in pathway selectivity as adsorption through the sulfur atom and in turn, conversion via the direct desulfurization pathway is impeded. Thus, alkyl-substituted dibenzothiophenes are preferably converted via the hydrogenation pathway which is more pressure- and temperature-sensitive than the direct desulfurization route.^{8, 18-20}

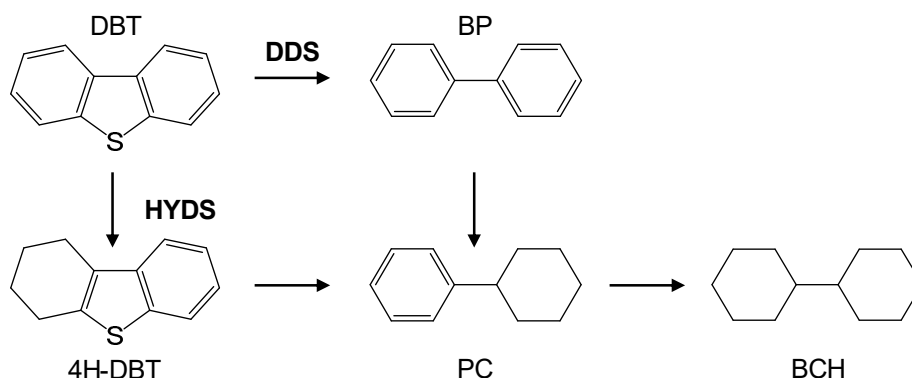


Figure 2. Reaction network for the hydrodesulfurization of dibenzothiophene (DBT) showing the two possible conversion pathways, i.e. direct desulfurization (DDS) and the hydrogenation (HYDS) route. The major product of the DDS is biphenyl (BP) whereas the HYDS route proceeds via tetrahydrodibenzothiophene (4H-DBT). Phenylcyclohexane (PC) and bicyclohexane (BCH) can be formed via both pathways.

The hydrodesulfurization of alkyl-substituted dibenzothiophenes thus consumes more hydrogen and requires a more active hydrogenation catalyst than the hydrodesulfurization of non-substituted polyaromatic compounds. This is of particular interest to meet the stricter legislative specifications for the emission of sulfur dioxide (SO₂) and the sulfur content in transportation fuels.²¹⁻²⁴ It is assumed that adsorption occurs through the aromatic π -electron system of the S-containing molecule in the hydrogenation pathway. Consequently, different adsorption modes are prerequisite in the two pathways, i.e., π -adsorption mode for hydrogenation and σ -adsorption mode for direct desulfurization.^{8, 17-19}

Alkyl substituents further away from the sulfur atom, in contrast, enhance the hydrodesulfurization reactivity due to their inductive effect and are mainly converted via the less demanding direct desulfurization pathway.⁶

Another limiting factor in the conversion of S-containing molecules is inhibition by the adsorption of other reactants on the active sites. A general order in the adsorption strength of molecules on the catalyst surface corresponding to a larger inhibition effect on others hydrotreating reactions is

N-containing compounds > S-containing compounds > polyaromatics \approx O-containing compounds \approx H₂S > monoaromatics.²¹

Thus, hydrodesulfurization reactions can be inhibited by N-containing compounds due to their stronger adsorption on the catalyst surface. The inhibition effect of N-containing compounds increases with their basicity in the order

quinoline < tetrahydroquinoline < indole < dihydroindole < ammonia.^{6, 25-27}

The rate of the hydrogenation pathway of S-containing compounds is, thereby, diminished to a higher extent by the N-containing compounds than the direct desulfurization pathway since the hydrodenitrogenation preferentially proceeds via hydrogenation. Complete poisoning by N-containing compounds, however, does not occur.^{6, 25-27}

2.4.2. Hydrodenitrogenation

Regarding its nitrogen content, crude oil can be classified into N-poor oils containing less than 0.25 wt. % of nitrogen and N-high oils which contain up to 1 wt. % of nitrogen. N-containing compounds, however, hardly contribute to the emission of NO_x in exhaust gases, hence the amount of nitrogen in refinery products is not specified. Nevertheless, the removal of nitrogen is important as N-containing compounds poison catalysts used in other refinery processes and strongly impede hydrodesulfurization reactions during hydrotreating due to their strong adsorption on catalyst surfaces.^{1, 28-30} Moreover, product specifications like gum content, storage, and thermal stability require the removal of nitrogen from product streams.²⁹ Since the content of N-containing compounds increases with increasing boiling point of the oil fraction, hydrodenitrogenation reactions gain increasing importance in the treatment of these heavy fractions.²⁹

N-containing compounds can be divided into heterocyclic and non-cyclic compounds, which include anilines and amines. The hydrodenitrogenation of aliphatic amines proceeds relatively rapidly compared to heterocyclic N-containing compounds. These heterocyclic compounds comprise pyridinic and pyrrolic compounds. In pyrrolic systems the electron lone pair of the nitrogen interacts with the π -electron system of the ring and is, thus, not available to interact with other species. In contrast to this non-basic pyrrolic compounds, pyridinic compounds are basic since the electron lone pair of the nitrogen is not involved in the π -electron system of the ring. Basic pyridinic compounds can act as Brønsted or Lewis base. Consequently, the basicity of the N-containing compound is important for the kind and the nature of interaction with sites on the catalyst surface.³⁰ The higher the basicity of the molecule is, the stronger the adsorption on the catalyst surface becomes leading to a stronger inhibition effect on other reactions.²⁶ Representative N-containing compounds together with their pK_a values and adsorption constants are shown in Table 3.

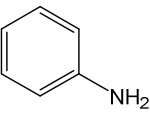
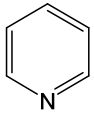
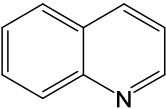
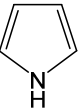
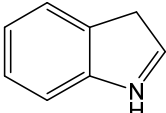
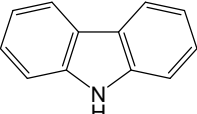
In accordance with the structure of the N-containing compounds in crude oil, three different types of reactions are involved in the hydrodenitrogenation, i.e., hydrogenation of N-containing heterocycles, hydrogenation of benzene rings, and C-N bond cleavages.³¹

Complete saturation of the aromatic heterocycle prior to the C-N bond cleavage is required because of the stronger C(sp²)-N bond compared to the aliphatic C(sp³)-N bond. The direct denitrogenation of N-containing heterocycles is hardly observable. The prerequisite hydrogenation of the aromatic ring prior to the removal of nitrogen makes hydrodenitrogenation reactions highly hydrogen-consuming and demands catalysts with a high hydrogenation activity.^{1, 29-30, 32}

Contrary to the C-N bond cleavage, hydrogenation reactions are in general reversible. Under hydrodenitrogenation condition, hydrogenation of benzene rings is thermodynamically favored

whereas saturation of N-containing heterocycle is kinetically favored. Moreover, the hydrogenation of a benzene ring is remarkably slower than hydrogenation of the N-containing heterocycle. The overall hydrodenitrogenation process is exothermic and kinetically driven at high temperature and pressure occurring under industrial hydrotreating conditions.^{1, 6, 29-30, 32}

Table 3. List of typical N-containing compounds present in crude oil including their structural formula, their corresponding pK_a^{30} values, and adsorption constants K^{22} .

Compound	Structure	Adsorption constant K^{22} [kPa ⁻¹]	pK_a^{26}
Phenylamine (Aniline)		0.094	5.0
Pyridine		0.43	5.2
Quinoline		0.98	4.9
Pyrrole		-	0.4
2,3-Benzopyrrole (Indole)		-	-3.6
Dibenzopyrrole (Carbazole)		0.51	-6.0

Pre-hydrogenation of the N-containing heterocycle is an exothermic process and hence favored at low temperature. The consumption of hydrogen shifts the equilibrium towards the saturated compounds with increasing hydrogen partial pressure. Thus, the content of saturated and unsaturated products can be influenced by the reaction temperature and the hydrogen partial pressure.³³

A typical model compound for studying hydrodenitrogenation reactions is quinoline as it is representative of the heterocyclic, basic nitrogen compounds found in significant amounts in the middle distillate fraction of fuels derived from oil shale, coal, and low-grade petroleum. Moreover, quinoline contains both a benzene ring and a heterocyclic ring, so its reaction network is representative for a great number of N-containing compounds.³²⁻³³ A general reaction network for the hydrodenitrogenation of quinoline is shown in Figure 3.

In the hydrodenitrogenation of quinoline, saturation of the benzene ring to 5,6,7,8-tetrahydroquinoline is thermodynamically slightly more favored than hydrogenation of the heterocycle to 1,2,3,4-tetrahydroquinoline which is, in contrast, kinetically favored.³³

Nevertheless, 1,2,3,4-tetrahydroquinoline is readily formed under hydrotreating conditions. This is related to the high π -electron density of the quinoline heterocycle. Usually a quasi-equilibrium between quinoline and 1,2,3,4-tetrahydroquinoline is reached under typical hydrotreating conditions.³⁴⁻³⁵

Along the kinetically preferred conversion route, 1,2,3,4-tetrahydroquinoline is subsequently hydrogenated to *cis*, *trans*-decahydroquinoline.³⁶

The C(sp³)-N cleavage in both, 1,2,3,4-tetrahydroquinoline and *cis*, *trans*-decahydroquinoline, occurs preferentially in *ortho*-position leading to *ortho*-substituted intermediates. The bond breaking proceeds either via Hofmann-type elimination or nucleophilic substitution. Ring opening of the heterocycle of 1,2,3,4-tetrahydroquinoline forms *o*-propylaniline, which is by itself more reactive than any of the heterocyclic compounds, but its conversion is suppressed in the presence of bicyclic quinoline-type compounds due to their stronger adsorption on the catalyst surface.^{30-31, 35, 37-38}

o-Propylcyclohexylamine can either be formed from *cis*, *trans*-decahydroquinoline by ring opening of the heterocycle or from *o*-propylaniline by hydrogenation of the benzene ring. The nitrogen removal from *o*-propylcyclohexylamine takes place via Hofmann-type elimination, and the three isomers of propylcyclohexene, i.e., 1-propylcyclohexene, 3-propylcyclohexene, and propylidene cyclohexane, are formed. Hydrogenation of the double bond of propylcyclohexene leads to propylcyclohexane.^{30, 32, 34, 38-39}

Propylbenzene can be formed through dehydrogenation of propylcyclohexene^{30, 40-41} or through direct denitrogenation of *o*-propylaniline.⁴²⁻⁴³

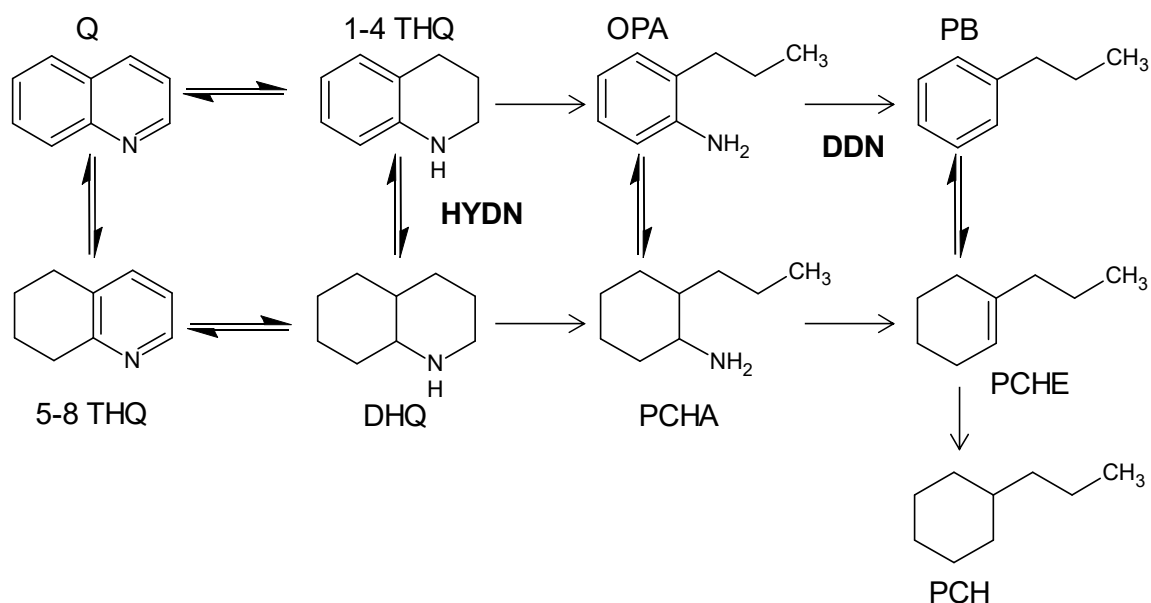


Figure 3. Reaction network for the hydrodenitrogenation of quinoline (Q) showing the two possible conversion pathways, i.e. direct denitrogenation (DDN) and the hydrogenation (HYDN) route. Equilibria among the bicyclic compounds quinoline (Q), 1,2,3,4-tetrahydroquinoline (1-4 THQ), 5,6,7,8-tetrahydroquinoline (5-8 THQ), and *cis, trans*-decahydroquinoline (DHQ) are possible. Further intermediates and products are *o*-propylaniline (OPA), *o*-propylcyclohexylamine (PCHA), propylcyclohexene (PCHE), propylcyclohexane (PCH), and propylbenzene (PB). Hydrogenation-dehydrogenation equilibria between *o*-propylaniline and *o*-propylcyclohexylamine as well as propylbenzene and propylcyclohexene can also occur.

2.4.3. Hydrodeoxygenation

The overall content of oxygen in crude oil is usually less than 0.1 wt. %. The most frequently occurring O-containing compounds are carboxylic acids and phenols in low and medium boiling point fractions. Shale oil, tar sand, and coal-derived liquids, in contrast, show a larger fraction and a broader variety of O-containing compounds since esters and furans are additionally present.⁶

If biomass is used as feedstock, the concentration of oxygen gets even more abundant and thus, hydrodeoxygenation gains importance. In Europe, the fraction of biofuels used in transportation fuels has, for instance, been set to at least 5.75 % in 2010. Hydrotreating of biomass and crude oil is conducted under similar reaction conditions, i.e., 300-450 °C and ~135 bar. Moreover, the typical hydrotreating catalysts, such as NiMo and CoMo sulfides, can be used.⁴⁴⁻⁴⁷

Hydrogenation, decarbonylation, and decarboxylation are part of hydrodeoxygenation reactions.⁴⁴

2.4.4. Hydrogenation of (poly)aromatic compounds

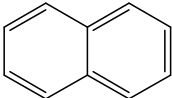
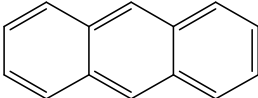
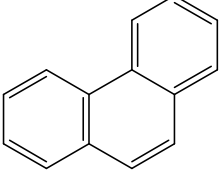
Hydrogenation reactions of olefins and (poly)aromatic compounds also belong to hydrotreating reactions. Typical (poly)aromatic hydrocarbons are present in crude oil are shown in Table 4. Saturation of (poly)aromatic molecules is needed to improve the fuel quality by preventing the formation of gums and increasing the cetane number. Olefins are highly reactive and hence already saturated in the first sections of the hydrotreating reactor. Hydrogenation of (poly)aromatic compounds is reversible but thermodynamically favored at high pressure and low temperature. The reaction temperature must, therefore, be chosen in the way that the exothermic hydrogenation is hardly limited kinetically and not thermodynamically.¹

Hydrogenation of olefins already takes place under atmospheric hydrogen pressure. The reactivity, in general, decreases with increasing chain length and substituents adjacent to the double bond. Hydrogenation of (poly)aromatic compounds, in contrast, requires high hydrogen partial pressure because of the resonance stabilization of the conjugated systems.⁶

Polyaromatic compounds become more reactive with an increasing number of benzene rings present, e.g., the reactivity increases from benzene over naphthalene to anthracene. Alkyl substituents on the benzene ring additionally increase the hydrogenation reactivity. Phenanthrene, however, has a much lower reactivity than anthracene due to its lower electron density leading to weaker adsorption, which occurs through π -bonding with the catalyst

surface. Through this adsorption mode the double bonds of the adsorbed molecule is weakened, hence the aromatic ring is more susceptible to the attack of a hydrogen atom.^{6, 48}

Table 4. Structural formula of olefins and polyaromatic compounds present in crude oil.

Compound	Naphthalene	Anthracene	Phenanthrene
Structure			

3. HYDROTREATING CATALYST

Molybdenum and Tungsten Sulfides

3.1. Synthesis of Unsupported Catalyst Precursors

Supported hydrotreating catalysts are commonly synthesized via impregnation methods. The chemical properties and the geometry of the support strongly influences the preparation of the catalyst, the catalytic activity, and the deactivation of the catalyst by metal and coke depositions.^{6, 49} γ -Alumina (γ -Al₂O₃) is mostly chosen as support material as it has a high specific surface area as well as good chemical and mechanical stability. Impregnation of the support with the metal solution can be performed via incipient wetness impregnation or wetness impregnation. In the case of multimetallic catalysts the impregnation can be performed simultaneously or sequentially.^{6, 50} Key parameters during the synthesis are, for instance, the pH value and the calcination temperature.⁴⁹

3.2. Synthesis of Unsupported Catalyst Precursors

A variety of synthesis methods are known for unsupported sulfide hydrotreating catalysts. In the most practiced preparation, an oxide precursor is synthesized prior to *in-situ* or *ex-situ* sulfidation of the material.⁵¹⁻⁵² In the following the most relevant preparation routes of catalyst precursors are presented. The examples shown are based on Ni-containing materials, but the synthesis of Co-containing materials can be performed in a similar manner using cobalt salts.

3.2.1. Co-precipitation of oxide catalyst precursors

In the co-precipitation route a nickel salt solution, e.g., nickel(II) nitrate (Ni(NO₃)₂), is added to a solution of a molybdenum salt and/or a tungsten salt. For example, ammonium molybdate ((NH₄)₂MoO₄) or ammonium tungstate ((NH₄)₁₀H₂(W₂O₇)₆) can be used. The ratio of molybdenum to tungsten can be easily adjusted without any impact on the following procedure. During synthesis, the pH value of both solutions and during the co-precipitation is of high importance to gain a precursor with the desired morphology and texture. The addition of

chelating agents, e.g., citric or maleic acid, improves the interactions among the metal cations and influences the morphology of the precursor.^{12, 51, 53-54}

3.2.2. Hydrothermal synthesis methods

Hydrothermal conditions can also be applied during synthesis of an oxide precursor. This can be performed as one pot synthesis with all the metals added at once or the addition of nickel proceeds via impregnation of the hydrothermally synthesized molybdenum and/or tungsten oxide. As molybdenum and tungsten sources the corresponding oxides or ammonium salts can be used.⁵⁵⁻⁵⁶

Another approach is the hydrothermal synthesis of a sulfide precursor. In this case, thiosalts of molybdenum and tungsten are prepared first by introducing H₂S into a solution of molybdenum and/or tungsten salts. This synthesis step can be performed under hydrothermal and atmospheric conditions.⁵⁷⁻⁵⁸ Quaternary alkylammonium halides can subsequently be added to tune the morphology of the sulfide.⁵⁹⁻⁶¹ Addition of nickel can either be performed via impregnation of the obtained powder^{59-60, 62-64} or the sulfide powder is solved and mixed with a nickel salt solution out of which the Ni-containing sulfide precipitates⁵⁷⁻⁵⁸. As the precursor in this case is already a sulfide material, sulfidation prior to catalysis can be performed under milder reaction conditions compared to the sulfidation of oxide precursor.⁵⁸

3.3. Structure of Unsupported Oxide Precursor

The structure of unsupported oxide precursors consists of different phases. Besides monometallic oxide phases, bimetallic or trimetallic phases are present. Nickel atoms are mostly octahedrally coordinated as is in nickel(II) oxide (NiO) or nickel(II) hydroxide (Ni(OH)₂).^{15, 65} Molybdenum atoms are tetrahedrally coordinated in a molybdenum trioxide (MoO₃)-type or in a polymolybdate environment.^{15, 65} Tungsten atoms are located in polytungstate phase like hydrated tungsten trioxide (WO₃).⁶⁵⁻⁶⁷ In the case of NiMo oxide precursors a bimetallic phase closely related to the structure of ammonium nickel molybdate (H(NH₄)Ni(OH)₂(MoO₄)₂) is formed. Herein, layers of [NiO₆]-octahedra alternate with layers of [MoO₄]-tetrahedra. Ammonium ions (NH₄⁺) and hydroxide anions (OH⁻) are located in the cavity of the layers.⁶⁵ In the case of NiW oxide precursors a nickel wolframite (NiWO₄) structure can be identified as the bimetallic phase. This structure consists of layers of edge connected [NiO₆]-octahedra, which are corner-connected to [WO₆]-octahedra also arranging in a layer-by-layer fashion.⁶⁵ In the case of trimetallic oxide precursors [MoO₄]-tetrahedra and [WO₆]-octahedra can be mixed within one layer. The other layer again consists of [NiO₆]-octahedra. The

polyhedra in the trimetallic oxide, however, are more distorted compared to the bimetallic oxide due to the interaction among them.⁵⁰ The interaction among the metals already in the oxide precursor shows the importance of the synthesis of the oxide since the interaction determines the sulfidability of molybdenum and tungsten and hence governs the performance of the sulfide catalyst.⁶⁵

3.4. Sulfidation of Oxide Precursors

The key to a high hydrotreating activity is the dispersion of molybdenum and/or tungsten sulfide (Mo(W)S₂) phase, its sulfidation degree, and the interaction of cobalt or nickel cations with the Mo(W)S₂ phase. All these factors are profoundly affected by the sulfidation protocol.⁶⁸ The conversion of the precursor, being an oxide or a sulfide, into the active sulfide form is thus a critical step in the catalyst synthesis. This gets even more important in the case of multimetallic catalysts but time this becomes also more difficult to synchronize the different sulfidation of the different metal cations such that different metals are optimally incorporated and dispersed within the final active phase.^{1, 6, 15}

The transformation into the sulfide phase of each metal consists of a complex combination of various O-S exchanges and reduction steps. The complete sulfidation of one metal prior to the other one should be avoided to ensure a close interaction among them leading to high hydrotreating activity.^{1, 6, 15} Hence, additives, e.g., chelating agents like citric acid and urea, are often added to increase the sulfidation temperature of cobalt and nickel oxide phases leading to a better dispersion.¹⁵

The sulfidation can be performed in either gas or liquid phase. In gas-phase sulfidation dihydrogen sulfide (H₂S) is the most common sulfiding agent. Dimethyl disulfide (C₂H₆S₂), carbon disulfide (CS₂), or other S-containing compounds are potential sulfiding agents in liquid phase.^{13, 69-70} The nature of the sulfiding agent and its decomposition under sulfidation condition influences the transformation of the precursor.^{13, 70-71}

The decomposition of dimethyl disulfide, for instance, involves several decomposition intermediates, including radicals, before H₂S is formed. All S-containing decomposition products can interact with the precursor and are possible sulfiding agents. The thermal decomposition of disulfides can either proceed via radicals, i.e., homolytic cleavage of the sulfur-sulfur bond, or via an intramolecular rearrangement. The impact of the different intermediates of the decomposition route on the structure and morphology of the sulfide is not yet clarified.⁷² Under common sulfidation conditions, the decomposition of a disulfide mostly occurs via radicals leading to a complex decomposition network.^{71, 73-74} As an example the primary radical decomposition network of dimethyl disulfide is depicted in Figure 4. Indeed, the formed radicals can react further and/or interact with the catalyst precursor.

3.4.1. Sulfidation of molybdenum oxide

The conversion of pure molybdenum trioxide (MoO_3) into molybdenum disulfide (MoS_2) proceeds via the formation of molybdenum oxysulfide species. First, terminal $\text{Mo}=\text{O}$ groups, which are rather unstable, are replaced by sulfur atoms and water (H_2O) is released being the thermodynamic driving force for this reaction. Subsequently, molybdenum(VI) ions (Mo^{6+}) are reduced to molybdenum(V) ions (Mo^{5+}) by a metal-ligand redox reaction. Two sulfur(-II) anions (S^{2-}) adjacent to Mo^{6+} cations are, in turn, oxidized to disulfide(I) anions (S_2^{2-}). This stepwise formation of oxysulfide species occurs up to 200 °C. Above 200 °C, further reduction of the molybdenum to its final oxidation state molybdenum(IV) (Mo^{4+}) takes place. Along with this, the O-S exchange gets completed resulting in MoS_2 .^{15, 83-84} The exact temperature ranges of the different transformation steps are strongly influenced by the applied pressure. Moreover, it is still in discussion whether molybdenum trisulfide (MoS_3) is formed prior to stable molybdenum disulfide (MoS_2) or not.¹

3.4.2. Sulfidation of tungsten oxide

The sulfidation of tungsten oxide phases is more difficult than in the case of molybdenum oxide phases. This is caused by the stronger W-O bond compared to the Mo-O bond.⁶⁸ As a consequence, a higher temperature is needed to cleave the W-O bond and to transform the oxide into the sulfide. Similar to the conversion of the molybdenum oxide phase, the sulfidation of tungsten oxide phases also proceeds via the formation of tungsten oxysulfide species.⁶⁸ The stronger W-O bond, however, requires a reduction of tungsten(VI) ions (W^{6+}) to tungsten(IV) ions (W^{4+}) prior to the O-S exchange.^{80, 85} The formation of the stable tungsten disulfide (WS_2) proceeds via formation of the intermediate tungsten trisulfide (WS_3).^{82, 86}

3.4.3. The impact of nickel on the sulfidation of molybdenum and tungsten oxide phases

In contrast to the transformation of the molybdenum and tungsten oxide phases, sulfidation of nickel oxide phases already starts at ambient temperature. The shift in sulfidation temperature may contribute to the formation of crystalline nickel sulfide phases in addition to the active Ni-containing Mo(W)-S phase.^{1, 87-88}

A delay in the formation of nickel sulfide phases may therefore retard the crystal growth and thus, a higher concentration of nickel can be substituted into the Mo(W)S₂ phase. This delay can be, for example, achieved by the use of another sulfiding agent or the addition of a chelating agent to the sulfidation feed (section 1.7.).^{13, 69, 78}

In the presence of tungsten, structural changes of the previously formed nickel sulfide phases hint to a re-dispersion of these nickel sulfide phases over the tungsten oxysulfide edge during its the final transformation to WS₂ resulting in the formation of the active Ni-W-S phase.⁶⁸ Furthermore, the presence of nickel facilitates the sulfidation of molybdenum and tungsten oxide phases and lowers the sulfidation temperature significantly.^{65, 82, 85, 89}

3.5. Structure of the Sulfide Catalysts

The structure of the active sulfide phase continuously changes under reaction conditions. Indeed, catalyst characterization under operating conditions is challenging and therefore, several models regarding the active sulfide phase have been proposed in the last decades.⁶ The following section describes the structure of molybdenum and tungsten sulfides and shows possible models for the interaction of these sulfides with nickel(II) cations together with the consequences for catalysis. Moreover, the specific features of a trimetallic sulfide phase are outlined.

3.5.1. Structure of molybdenum and tungsten disulfide

Molybdenum disulfide (MoS_2) and tungsten disulfide (WS_2) occur in nature as the minerals molybdenite and tungstenite, respectively.

MoS_2 forms black or lead-silvery grey crystallites or aggregates.¹⁵ Its structure consists of highly anisotropic layers with two different planes, i.e., edge and basal planes. Each hexagonal MoS_2 slab has a 2:1 ratio of sulfur to metal atoms.^{6, 90-91} The predominant crystallographic form of MoS_2 is hexagonal and assigned to the space group D_{6h} ($P6_3/mmc$).⁹² In this 2H- MoS_2 structure (H = hexagonal; 2 = two MoS_2 slabs in a unit cell) van-der-Waals forces connect the consecutive S-Mo-S layers together. In these layers the sulfur atoms and the metal atoms are covalently bound to each other. The molybdenum atoms are surrounded by a trigonal prismatic environment of six sulfur atoms. These MoS_6 polyhedra are edge-connected within one sulfide slab. Consecutive layers of these polyhedra are stacked in an ABAB order preferentially in the (002) direction. This implies that the (100) and the (010) edge planes, i.e., metal- and sulfur-terminated, are exposed to the gas and liquid phase.^{1, 15, 90, 93-98} The exposed edge of can either be terminated by a metal atom (1010) or by a sulfur atom (1010).⁹⁹ However, the most stable edge structure is achieved if the metal edges are at least partially covered with sulfur atoms.¹⁰⁰ WS_2 is isomorphous to MoS_2 .¹⁰¹

However, in comparison to MoS_2 the tungsten-sulfur bonds are weaker leading to a less stable material in oxidizing atmosphere. This weaker tungsten-sulfur bond strength favors the formation of coordinatively unsaturated sites (CUS). Hence, WS_2 is a more Lewis acidic material than MoS_2 .

The higher Lewis acidity of WS_2 promotes the activation of hydrogen leading to a higher activity on hydrogenation reactions of WS_2 compared to MoS_2 .¹⁰²⁻¹⁰⁴

3.5.2. Structural models for the incorporation of nickel into the sulfide phase

Adding cobalt or nickel to MoS_2 , WS_2 , or a mixed Mo(W)S_2 phase increases the hydrotreating activity significantly. Chianelli et al. found that the addition of cobalt or nickel cations causes a synergetic effect which modifies the electronic and geometric structure of the base metal sulfides.¹⁰⁵⁻¹⁰⁶ During the last decades several models for Co- or Ni-containing Mo(W)S_2 have been proposed to reveal the atomic structure of these materials and the interaction among the metal cations. One model was the 'intercalation model' first proposed by Voorhoeve and Stuver.¹⁰⁷ Herein, the cobalt(II) (Co^{2+}) or nickel(II) cation (Ni^{2+}) occupies an octahedral or tetrahedral position in the van-der-Waals gap between two Mo(W)S_2 layers. DFT calculations, however, revealed that intercalation of Co^{2+} or Ni^{2+} cations in an ideal Mo(W)S_2 crystal is energetically unlikely. Hence, the intercalation of promoter cations was confined to the edges of the sulfide slabs, according to Cossee and Farragher.¹⁰⁸ This is known as 'surface intercalation' or 'pseudo-intercalation'. In these models, the activity increase is related to electron transfer from Co^{2+} or Ni^{2+} cations to Mo(W)S_2 . This enhances the concentration of active Mo^{3+} and W^{3+} sites without changing their nature.¹⁰⁹

The presence of crystalline cobalt sulfide phases, e.g., Co_9S_8 , in unsupported CoMo-sulfide catalysts prompted Delmon et al. to put forward another model, the 'contact synergy' or 'remote-control' model. Herein, spill-over of hydrogen atoms from cobalt and nickel sulfide particles, the so-called donor-phases, to the acceptor phase Mo(W)S_2 is proposed. According to this model, the donor and the acceptor phases are thereby in contact and the hydrogen atoms which have spilt over create additional active sites on Mo(W)S_2 . Consequently, this higher concentration of active sites results in an increased catalytic activity. Thus, hydrogen activation takes place on cobalt or nickel sulfide phases while the hydrotreating reactions proceed on Mo(W)S_2 .¹¹⁰⁻¹¹¹

This model, however, was refuted by multiple experimental evidence from Mössbauer spectroscopy, nitric oxide (NO) adsorption, IR, and EXAFS studies, as well as DFT calculations, which together showed that cobalt(II) and nickel(II) cations are directly incorporated in the Mo(W)S_2 structure causing an enhanced catalytic activity and not due to the interaction between the two phases.¹¹²⁻¹¹³

This findings led to the currently widely accepted 'Co-Mo-S' model developed by Topsøe et al.¹¹⁴ This model assumes that the cobalt(II) cations are located at the edges of a (1010) Mo(W)S_2 plane. The structure of the 'Co-Mo-S' structure is not homogeneous with a fixed stoichiometry. The decoration degree of the cation ranges from a non-decorated to a fully covered sulfide edge.¹¹⁴

The 'Co-Mo-S' model can be borrowed to describe Ni-containing and W-containing sulfide catalysts.¹¹⁵ In contrast to cobalt(II) cations, which are exclusively located at the sulfur edge,

nickel(II) cations are preferentially located at the metal edge. This contributes to the higher hydrogenation activity of Ni-containing systems compared to Co-containing systems since the metal edges play a crucial role in hydrogenation reactions.¹

3.5.3. Consequences of the incorporation of nickel into the sulfide phase

The incorporation of nickel(II) cations at the sulfide edge induces significant changes in morphology since nickel(II) cations are preferably incorporated at high-indexed edges.¹¹⁶⁻¹¹⁷ Thus, larger Ni-Mo-S particles occur in a truncated triangular shape while smaller particles have a dodecagonal shape.¹¹⁸ In principle, nickel(II) cations are coordinated square planar at the sulfide edges and can fully cover them. However, the incorporation of nickel is thermodynamically more stable on the metal edge compared to the sulfur edge.

The fact that the Ni-S bond is significantly weaker than the Mo(W)-S bond implies that a pairing configuration (-Ni-Ni-Mo(W)-Mo(W)-) is stabilized compared to an alternating configuration (-Ni-Mo(W)-Ni-Mo(W)-).^{1, 119} Whether the incorporation of nickel(II) cations in the metal edge or on the sulfur edge prevails, depends strongly on sulfidation and reaction conditions. Nickel(II) cations, for instance, substitute molybdenum(IV) or tungsten(IV) cations completely at both edges in highly sulfiding atmosphere whereas nickel segregation occurs at a high a $p(\text{H}_2)/p(\text{H}_2\text{S})$ ratio. In hydrotreating atmosphere, 100 % and 50 % decoration of nickel(II) cations on both edges are equally feasible. Thus, a large range of different edge structures occurs which causes the truncated morphology of Ni-containing sulfides. Moreover, the active edge sites rearrange dynamically during reaction depending on the reaction conditions and the reactants present as the edge structure counteracts to the exposed reaction conditions according to the Principle of Le Chatelier.^{1, 120-122}

The incorporation of nickel(II) cations into the Mo(W)S₂ edge leads to a weaker Mo(W)-S bond strength. Thus, the Mo(W)-S bond strength is in the optimum medium range needed for high hydrotreating activity as proposed by Chianelli et al. using the Sabatier Principle.¹²³⁻¹²⁴ The metal-sulfur bond strength energy at the sulfide edge decreases in the order



More precisely, they related the catalytic activity to the nature and occupancy of the highest occupied molecular orbital (HOMO) and the metal-sulfur bond strength. In the case of the incorporation of the nickel(II) cation at the sulfide slab edge the number of electrons in the highest occupied molecular orbital (HOMO) of Mo(W) increases as empty *d*-type orbitals of the Mo(W) are filled with 3*d* electrons of nickel. Nickel has nine electrons in its valence shell in its ground state compared to six electrons of molybdenum and tungsten. Thus, molybdenum and tungsten cations are formally reduced and the Mo(W)-S bond is weakened leading to a higher

Lewis acidity of Mo(W) compared to unpromoted MoS₂ and WS₂.^{120, 123, 125-126} Consequently, the sulfur atom located between Ni(Co) and Mo(W) has the desired medium bond strength for optimal catalytic activity and is, therefore, a stronger base than in the unpromoted sulfide. This results in a higher concentration of Lewis acid sites, which can be the coordinatively unsaturated sites, and Brønsted acid sites (sulfhydryl (SH) groups) which are the active hydrogenation sites.^{1, 127-128}

Besides the electronic effect accompanied with its consequences, the incorporation of nickel(II) cations also increases the flexibility of the sulfide to compensate charge differences by dynamic reconstructions depending on the changing reaction environment.^{98, 115}

3.5.4. Characteristics of trimetallic sulfides

Ternary Ni-containing Mo(W)S₂ crystallizes in a layered structure with hexagonal shape. Dumcenco et al. showed that molybdenum and tungsten atoms share metal sites and they alloy randomly without phase segregation.¹²⁹ Molybdenum and tungsten atoms form an intralayer-mixed sulfide slab. This mixed sulfide phase leads to the highest concentration of nickel cations incorporated at the sulfide edge compared to the bimetallic Ni-MoS₂ and Ni-WS₂. This contributes to the higher hydrotreating activity of ternary sulfides.^{21, 43}

The textural synergism in the trimetallic sulfide leads to an increased number of active sites upon mixing the individual sulfides. Furthermore, the configuration of the nickel(II) cation at the mixed Mo(W)S₂ edge is more stable than at the pure MoS₂ or WS₂ edge as well as segregation of nickel sulfide phases.¹³⁰

The surface energy of a ternary sulfide is lower than that of the bimetallic sulfides. Thus, the trimetallic surface can be formed more easily. This, in turn, influences the type of exposed facets. The easier formation of a ternary surface suggests also a higher concentration of incorporated nickel(II) cations at the mixed Mo(W)S₂ edges resulting in a higher concentration of active sites and finally in higher hydrotreating activity.¹²⁶

The incorporation of nickel(II) cations in the Mo(W)S₂ edge causes an elongation and weakening of Mo(W)-S bond leading to an easier formation of coordinatively unsaturated sites, which are possible adsorption sites for reactants and are active in the dissociation of hydrogen.¹³¹ Moreover, the ternary metal sulfide edge has a higher population of the *d*-type states over the Fermi level. This leads to an enhanced reactivity of the sulfide surface towards electron donating species. Thus, substituting molybdenum(IV) cations by tungsten(IV) cations together with the incorporation of nickel(II) cations at the sulfide edge leads to an electronic modification of the active edge. These findings contribute to the enhanced catalytic activity of trimetallic sulfides compared to the bimetallic ones.^{64, 126, 132}

3.6. Activation of Hydrogen on the Sulfide Surface

Activation of hydrogen on Ni-Mo(W)S₂ implies that one H₂ molecule is adsorbed from the gas phase on an active site on the catalyst surface, before it is split. Whether the H-H bond cleavage takes place heterolytically or homolytically is still a matter of debate. Both ways, however, lead to the formation of two sulfhydryl (SH) groups on the catalyst surface.¹³³⁻¹³⁴

Anderson et al. suggested that both kinds of hydrogen activation, heterolytic and homolytic, might occur in parallel but on different locations of the catalyst surface. Heterolytic adsorption is the most stable form at the edges of the MoS₂ layer. Homolytic adsorption of hydrogen, in contrast, is stabilized on sulfur basal planes of MoS₂.¹³⁴

Hence, the ability to dissociate hydrogen depends on the nature of the metal cation and its coordination sphere. Both features govern the Lewis acidity of the metal cation. The Brønsted basicity of the sulfur anion is an additional key factor in the activation of hydrogen.¹³⁵ Indeed, the nature of the catalyst surface and the thermodynamic stability of the chemisorbed hydrogen atom depend strongly on the reaction conditions as well as the partial pressure of H₂, H₂S, and the present hydrocarbons.¹³⁶

3.7. Scope of this Thesis

The need of more active catalysts requires deeper understanding of the local structure of the active sites as well as the differences between the transition metal sulfide phases. This work aims to elucidate the impact of the transition metal sulfide phase on the performance of the catalyst in hydrotreating reactions, specifically hydrodenitrogenation and hydrodesulfurization reactions of model heterocyclic compounds. Investigation of the influence of various synthesis procedures, including sulfidation conditions, (Chapter 2 and 4) should also help to meet the required catalyst properties for high activity and thereupon to maximize the performance of the catalyst.

Another focus of this thesis is put on the investigation of bulk Ni-containing MoS₂ and WS₂ as well as the trimetallic counterparts to elucidate the properties leading to different catalytic activities (Chapter 2 and 3). Hydrodenitrogenation reactions are mainly used, sometimes together with hydrodesulfurization reactions, to evaluate the catalytic performance of the sulfide materials. An emphasis is placed on the conversion of quinoline to establish the mechanism and reaction pathway as well as to identify the structural and physicochemical requirements of a highly active catalyst (Chapter 3).

Chapter 2

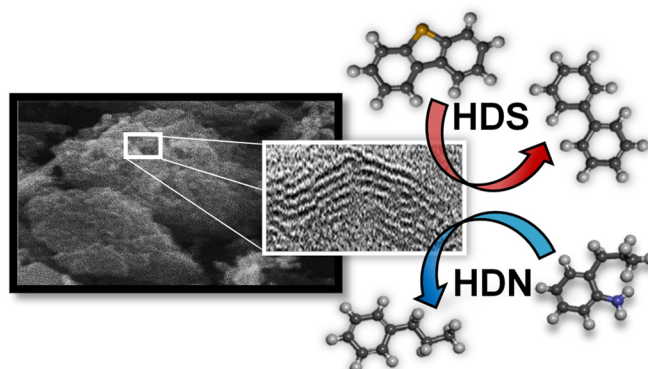
BULK Ni-Mo-W SULFIDES –

Simultaneous hydrodenitrogenation and hydrodesulfurization

This chapter is based on

Albersberger, S.; Hein, J.; Schreiber, M. W.; Guerra, S.; Han, J.; Gutiérrez, O. Y.; Lercher, J. A., *Catalysis Today*, **2017**, 297, 344-355.
DOI: 10.1016/j.cattod.2017.05.083.

Reprinted or adapted from Catalysis Today, with permission from Elsevier



Abstract

The catalytic properties of unsupported Ni-Mo-W sulfides (composites of Ni-Mo(W)S₂ mixed sulfides and Ni₃S₂) obtained from precursors synthesized via co-precipitation, hydrothermal, and thiosalt decomposition were explored for hydrodenitrogenation of *o*-propylaniline or quinoline in presence and absence of dibenzothiophene undergoing hydrodesulfurization. The conversion rates varied with the reacting substrate and were related to specific catalyst properties such as morphology, texture, surface and composition. For hydrodenitrogenation of *o*-propylaniline and hydrodesulfurization of dibenzothiophene in presence of *o*-propylaniline, high concentrations of coordinatively unsaturated cationic sites, as characterized by NO adsorption and the specific surface areas determined the rates of reaction. For the hydrodenitrogenation of quinoline and the hydrodesulfurization of dibenzothiophene in the presence of quinoline, the high hydrogenation activity of tungsten sulfide and length of the slabs was found to be more important. Overall, the activity of unsupported catalysts relates to the provided size of sulfide slabs that nickel(II) cations are present at the perimeter of the slabs.

1. Introduction

Hydrotreating of sulfur and nitrogen rich feeds requires highly active MoS₂ and WS₂ catalysts that retain higher rates in hydrogenation and hydrodefunctionalization reactions in presence of significant concentrations of heterocompounds.¹⁷ Most catalyst formulations include cobalt or nickel as promoters and Al₂O₃ as support.^{15, 32, 137} However, the exceptional activity of unsupported trimetallic Ni-Mo-W sulfides¹⁰ has triggered substantial activity to improve catalytic activity beyond present levels and to understand the role of the catalyst components.^{64, 138-141}

Unsupported multimetallic sulfide catalysts consist of complex mixtures of mono-, bi-, and trimetallic phases. To understand these local structures, it is important to note that MoS₂ and WS₂ are anisotropic materials and their activity strongly depends on morphology and crystallinity.¹⁰ Thus, several parameters might influence the intrinsic activity and availability of active sites. As the catalytic pathway strongly depends on the nature of the reacting substrates, catalyst formulation have to be adjusted to the characteristics of the feed.⁶

In the context of drawing activity-structure correlations for complex unsupported multimetallic sulfides, this work aims to study series of materials with diverse physicochemical properties. It was hypothesized that such properties are indicators of the parameters that directly determine activity, i.e., concentration and intrinsic activity of active sites. In order to verify the hypothesis, the diverse materials were tested in the conversion of model molecules that requires well-defined hydrogenation and hydrodefunctionalization steps. In the final step, the activity trends were compared with the accessed physicochemical properties and structure–activity correlations were discussed.

Common routes towards synthesis of unsupported sulfide catalysts comprise sulfidation of oxide precursors, which are obtained by co-precipitation.¹⁴² This synthesis approach is usually practiced in industry because it produces materials with Ni/Mo/W ratios optimized for hydrodesulfurization and hydrodenitrogenation.^{55, 143} Co-precipitation also allows varying the Mo/W ratio in the resulting solids leading to different oxide precursor structures. The structure and composition of the precursor influence the sulfidation kinetics and the cation distribution in the final mixture of sulfide phases.⁶⁵

As an alternative to the “oxide routes”, direct precipitation of sulfides from the synthesis solution has been reported as advantageous for the activity of the materials, which is often attributed to improved Ni-Mo(W) interactions.^{64, 138, 144-145}

Thus, in this work, several Ni-Mo-W catalyst precursors were synthesized following co-precipitation and decomposition of thiosalts. Some procedures have been adapted to hydrothermal conditions in order to obtain precursor phases different to those resulting of low

temperature precipitation from identical precursor solutions.^{43, 65} Precursors and the corresponding sulfides were characterized by means of N₂ physisorption, X-ray diffraction, Raman spectroscopy, pulse NO titration, as well as scanning and transmission electron microscopy. The sulfide catalysts were studied with respect to activity and selectivity for hydrodenitrogenation of *o*-propylaniline, and quinoline, in presence and absence of dibenzothiophene undergoing hydrodesulfurization. Structure-activity correlations were rationalized in terms of properties and availability of active sites.

2. Experimental

2.1. Synthesis of oxide precursors

2.1.1. Salt precursor route (*WMoNi-a_{ox}* and *WMoNi-aHT_{ox}*)

The synthesis of *WMoNi-a_{ox}* was performed according to Maesen et al.¹⁴⁶ Solution A was prepared by consecutively dissolving ammonium heptamolybdate (25 mmol Mo, $(\text{NH}_4)_6\text{Mo}_7\text{O}_{24}$, Sigma-Aldrich, $\geq 99\%$) and ammonium metatungstate hydrate (25 mmol W, $(\text{NH}_4)_6\text{H}_2\text{W}_{12}\text{O}_{40}\cdot x\text{H}_2\text{O}$, Sigma-Aldrich, $\geq 99\%$) in 200 mL bidistilled water. Under continuous stirring, 7.5 mL of aqueous ammonia (28-30 wt. %, NH_4OH , Sigma-Aldrich) were added before heating up to 90 °C. For solution B, nickel(II) nitrate hexahydrate (50 mmol Ni, $\text{Ni}(\text{NO}_3)_2\cdot 6\text{H}_2\text{O}$, Sigma-Aldrich, $\geq 98.5\%$) was dissolved in 12.5 mL bidistilled water and heated to 70 °C. The warm solution B was added dropwise to solution A, which forced the precipitation of the catalyst precursor. After 30 minutes at 90 °C and hot filtration, the obtained solid was suspended in an aqueous solution of maleic acid (0.05 M, $\text{C}_4\text{H}_4\text{O}_4$, Fluka, $\geq 98.0\%$) and kept at 70 °C (solution C). The precipitate was filtrated and dried in vacuum overnight as well as in synthetic air at 120 °C for 12 hours.

The synthesis of the *WMoNi-aHT_{ox}* precursor was performed under hydrothermal conditions using a 300 mL Parr autoclave (Series 4843). Solution A was heated in the autoclave to 250 °C for 30 minutes reaching a H_2 pressure of 40 bar. Solution B was heated to 90 °C before injecting it via an injection pipette to the autoclave. After 90 minutes at 250 °C, the reaction mixture was cooled to 80 °C and filtrated. The resulting yellow precipitate was slurred in solution C at 70 °C for 30 minutes. The obtained solid was dried as described for *WMoNi-a_{ox}*.

2.1.2. Oxide precursor route (*WMoNi-b_{ox}* and *WMoNi-bHT_{ox}*)

The synthesis of *WMoNi-b_{ox}*, derived from that reported by Soled et al.,¹⁴⁷ was performed as follows. Suspension A was prepared by slurring molybdenum(VI) trioxide (10 mmol Mo, MoO_3 , Sigma-Aldrich, 99.98 %) and tungstic acid (10 mmol W, H_2WO_4 , Sigma-Aldrich, $\geq 99.0\%$) in 160 mL of bidistilled water. Subsequently, this mixture was heated to 90 °C. Suspension B, consisting of nickel(II) carbonate hydroxide tetrahydrate (20 mmol Ni, $2\text{NiCO}_3\cdot 3\text{Ni}(\text{OH})_2\cdot 4\text{H}_2\text{O}$, Sigma-Aldrich) and 40 mL bidistilled water, was also heated to 90 °C before adding dropwise to solution A. The resulting green precipitate was separated and dried under vacuum overnight and in synthetic air at 120 °C for 12 hours.

Hydrothermal conditions were applied for the synthesis of *WMoNi-bHT_{ox}*. Suspensions A and B were mixed in an autoclave (Series 4843) and heated to 250 °C under a H_2 pressure of 40 bar for 6 hours. The drying procedure of *WMoNi-b_{ox}* was also applied for this material.

2.1.3. H_2S precipitation route (WMoNi-s_{Ox})

This synthesis was adapted from Yi et al. and Nava et al.^{145, 148} Ammonium heptamolybdate (10 mmol Mo, $(NH_4)_6Mo_7O_{24}$, Sigma-Aldrich, $\geq 99\%$), and ammonium metatungstate hydrate (10 mmol W, $(NH_4)_6H_2W_{12}O_{40}\cdot xH_2O$, Sigma-Aldrich, $\geq 99\%$) were dissolved in 30 mL of aqueous ammonia (28-30 wt. %, NH_4OH , Sigma-Aldrich). A gaseous mixture of H_2S in H_2 (10 vol. % H_2S , 40 mL/min) was bubbled through this solution for 6 hours under vigorous stirring. At 70 °C a deep red solution was obtained (solution A). After cooling to room temperature, a solution B, consisting of tetramethyl ammonium chloride (2.7 M, $(CH_3)_4NCl$, Sigma-Aldrich, $\geq 99.0\%$) and sodium hydroxide (2.7 M, $NaOH$, Sigma-Aldrich, $\geq 99.0\%$) in 15 mL bidistilled water, was dropped to solution A and stirred for 20 minutes. Solution C, containing nickel(II) nitrate hexahydrate (20 mmol Ni, $Ni(NO_3)_2\cdot 6H_2O$, Sigma-Aldrich, $\geq 98.5\%$) in 30 mL bidistilled water, was added to the reaction mixture. The red precipitate was filtrated and dried at 120 °C for 12 hours in synthetic air.

2.1.4. Hydrothermal decomposition (WMoNi-sHT_{Ox})

The WMoNi-sHT_{Ox} precursor was prepared by a novel hydrothermal method using a Parr autoclave (Series 4843). The salt precursors, i.e., ammonium tetrathiomolybdate (7.2 mmol Mo, $(NH_4)_2MoS_4$, Aldrich, 99.97%), ammonium tetrathiotungstate (7.2 mmol W, $(NH_4)_2WS_4$, Aldrich, $\geq 99.9\%$), and nickel(II) hydroxide (14.4 mmol Ni, $Ni(OH)_2$, Aldrich), were suspended in 75 mL bidistilled water in the autoclave. The mixture was heated to 250 °C reaching a H_2 pressure of 40 bar. This solution was isothermally kept at 250 °C and 40 bar for 16 hours. A dark blue precipitate was recovered by hot filtration, dried under vacuum overnight, and at 120 °C for 12 hours in synthetic air (200 mL/min).

2.2. Synthesis of sulfide catalysts

The precursors, denoted as WMoNi-a_{Ox}, WMoNi-aHT_{Ox}, WMoNi-b_{Ox}, WMoNi-bHT_{Ox}, WMoNi-s_{Ox}, and WMoNi-sHT_{Ox} (according to the experimental descriptions above), were sulfided to obtain the active catalysts. The sulfidation was carried out in a trickle bed flow-reactor using a mixture of H_2S in H_2 (10 vol. % H_2S , 40 mL/min) at 20 bar and 400 °C for 12 hours. The resulting sulfide materials are denoted according to the name of the corresponding precursor, i.e., WMoNi-a, WMoNi-aHT, WMoNi-b, WMoNi-bHT, WMoNi-s, and WMoNi-sHT.

2.3. Characterization

The elemental analysis of the oxidic precursors and sulfide catalysts were conducted by the micro analytic laboratory of the Technische Universität München. The concentrations of nickel, molybdenum, and tungsten were determined photometrically whereas the contents of hydrogen, carbon, nitrogen, and sulfur were analyzed using an automated element analyzer instrument (vario EL CHN analyser, ELEMENTAR). The analysis of several batches of selected samples showed identical elemental contents. The concentration of oxygen was determined as the difference between the total mass and the masses of the elements quantified.

Isotherms of adsorption and desorption of N₂ at -196 °C were performed with an automated nitrogen adsorption analyzer Sorptomatic 1990 Series (Thermo Finnigan). Prior to the measurements, the samples were evacuated at 120 °C for 4 hours. BET analysis was used to determine the surface area of the oxide and sulfide materials. The error determined for the N₂ physisorption was up to ± 20 % of the reported value.

The crystal structures of the materials were analyzed by powder X-ray diffraction (XRD). The measurements were carried out in a X'Pert Pro PW 3040/60 instrument by PANalytical equipped with a copper X-ray tube (Cu-K α radiation, 0.1542 nm), a nickel K β -filter, and solid-state detector (X'Celerator) operated at 45 kV/40 mA with step size of 0.017 ° and scan time of 115 seconds per step.

SEM images of the materials were recorded using a REM JEOL 5900 LV microscope. A secondary electron detector and an Everhart-Thornley detector for backscattered electrons were employed. The SEM images of the secondary electron detector were taken with an acceleration voltage of 25 kV. Before the measurements, the samples were outgassed for two days, transferred on a graphite foil and coated with gold by sputtering.

Transmission electron microscopy (TEM) was performed in an instrument (JEOL JEM-2011) with an accelerating voltage of 120 keV. SAED measurements were taken with the same instrument. The samples were prepared grinding a small amount of material and dispersing it ultrasonically in ethanol. Subsequently, drops of this dispersion were applied on a copper carbon grid and the ethanol was evaporated at room temperature. Statistical analysis of the length and stacking height was achieved by counting at least 300 slabs distributed in different regions of the sample.

Raman measurements of the catalyst precursors and their corresponding sulfides were carried out in a Renishaw Raman Spectrometer (Type 1000). The instrument was equipped with a CCD (charge-coupled device) detector and a microscope (Leica microscope DM LM). As excitation source an argon laser (514 nm) was used. The spectra were conducted with a

50-fold magnification in the range of 100–4000 cm^{-1} . The measurement time was set 10 seconds. With these settings, at least five different positions on each sample were measured. Before the measurements, the system was calibrated to the wavelength 520 cm^{-1} using a Si (111) crystal.

The adsorption of nitric oxide (NO) on sulfided samples was carried out at ambient conditions using a pulse technique. Prior to the experiment, the precursors were treated under a mixture of 2 mL/min of H_2S in H_2 (10 vol. % H_2S) and 8 mL/min of helium at 400 °C (5 °C/min) for 2 hours. Once the reactor reached room temperature and was flushed with helium (10 mL/min), pulses of NO were introduced periodically until the NO adsorption-desorption equilibrium was established. The adsorption of NO was monitored by a mass spectrometer (Blazers QME 200). The concentration of adsorbed NO was calculated as the sum of the individual NO uptakes per pulse. The error in the determination of adsorbed NO was around 10 %.

X-ray photoelectron spectroscopy (XPS) measurements were performed using a Phi Quantera Scanning X-ray Microprobe instrument at the Chevron Technology Center. This instrument was equipped with a hemispherical energy analyzer with multichannel detection at an energy resolution of 1.1 eV. As energy source monochromatic Al $K\alpha$ X-rays ($h\nu = 1486.7$ eV) were used. The powdered catalyst was mounted in an area of approximately 0.8 cm x 0.8 cm of double-sticky tape. The surface of the tape was completely covered by the catalyst powder. Five analysis areas (1.2 mm x 100 μm) were selected for detailed spectral characterization for each catalyst. At each area, detailed spectra were collected for W 4*f*, S 2*p*, Mo 3*d*, C 1*s*, O 1*s*, and Ni 2*p*³ photoelectron peaks. Total spectral accumulation times were 100 minutes per analysis area while irradiating with 100 W of X-radiation. The binding energies were referenced to the C 1*s* peak (284.8 eV) to account for charging effects. Spectral envelopes were deconvoluted using an iterative least square algorithm provided in Phi Multipak software.

2.4. Catalysis

The hydrotreating activity of the catalysts was evaluated with respect to hydrodenitrogenation using *o*-propylaniline ($\text{C}_9\text{H}_{11}\text{NH}_2$, Sigma-Aldrich, 97 %) and quinoline ($\text{C}_9\text{H}_7\text{N}$, Sigma-Aldrich, 98 %) as model compounds. In addition, dimethyl disulfide ($\text{C}_2\text{H}_6\text{S}_2$, Sigma-Aldrich, ≥ 99 %) was added to the liquid feed. In a separate series of experiments, hydrodesulfurization of dibenzothiophene ($\text{C}_{12}\text{H}_8\text{S}$, Sigma-Aldrich, ≥ 99 %) was simultaneously performed with the hydrodenitrogenation of *o*-propylaniline and quinoline. The experiments were performed in a trickle fixed bed flow-reactor, where liquid and gas feeds were introduced using a HPLC pump (Shimadzu LC-20AD) and high-pressure mass flow controllers (Bronkhorst). Gas and liquid streams were introduced in concurrent downflow mode in a glass-coated tubular reactor (\varnothing ¼ inches) loaded with the catalytic material as described below. The reactor is surrounded

by a brass heating jacket equipped with a thermocouple that measures the temperature in the isothermal zone of the reactor. The pressure is fixed by a homemade back-pressure controller connected to a high-pressure N₂ line.¹⁴⁹ Prior to the activity test, pellets of the precursors (typically 50 mg, 250-355 μm) were mixed with $\gamma\text{-Al}_2\text{O}_3$ (1 part of precursor and 1 part of $\gamma\text{-Al}_2\text{O}_3$ in weight) and with SiC (355-500 μm , 1 part catalyst 20 parts silicon carbide (SiC) in weight).

The precursor packed in the reactor was sulfided with a mixture of H₂S in H₂ (10 vol. % H₂S, 40 mL/min) at 20 bar and 400 °C for 12 hours. Tetradecane (C₁₄H₃₀, Alfa Aesar, $\geq 99\%$) was used as solvent and hexadecane (C₁₆H₃₄, Sigma-Aldrich) as internal standard. The mixtures of the liquid feed applied for the activity tests are listed in Table 5.

Table 5. Composition [wt. %] of the liquid feed applied in the conducted catalytic experiments (*o*-propylaniline (OPA), quinoline (Q), dibenzothiophene (DBT), dimethyl disulfide (DMDS), *n*-hexadecane (HD), and *n*-tetradecane (TD)).

Experiment	Feed composition [wt. %]					
	OPA	Q	DBT	DMDS	HD	TD
HDN OPA	0.97	-	-	0.15	4.94	93.94
HDN Q	-	0.92	-	0.15	4.95	93.98
HDN OPA/HDS DBT	0.97	-	0.29	0.15	4.93	93.66
HDN Q/HDS DBT	-	0.92	0.29	0.15	4.94	93.70

The ratio of liquid to hydrogen (H₂) was 1:330 Ndm³/dm³. Typical liquid flows of around 0.1 mL/min were applied, which is equivalent to a liquid hourly space velocity (LHSV) of 109 h⁻¹ based on the volume of catalyst. Alternatively, the space time was typically 153 mol/(g_{cat}·min) for *o*-propylaniline, 154 mol/(g_{cat}·min) for quinoline, and 705 mol/(g_{cat}·min) for dibenzothiophene. Here, space time is defined as m_{cat}/F , where m_{cat} is the mass of the catalyst and F is the molar flow of the reactant. The temperatures applied were 310 °C, 330 °C, 350 °C, and 370 °C at constant pressure of 50 bar H₂. These conditions allowed to control the reaction rates in a wide range below complete reactant conversion in order to obtain reliable kinetic data. Prior to sampling, the reaction conditions applied were kept for at least 12 hours to ensure steady state.

The product stream was analyzed off-line using a gas chromatograph (HP 6890) equipped with a flame ionization detector (FID) and an Agilent DB-17 capillary column. Liquid samples were collected by a 16-port sampling valve after liquid-gas separation. The presented data were acquired after 24 hours on stream to obtain results representative of stable catalysts. The reproducibility of the measurements was $\pm 5\%$.

3. Results and Discussion

Six precursors and the corresponding sulfide catalysts were synthesized as described in the experimental section and schematically shown in Figure 5. This figure also shows the names of the precursors. The characterization of the precursors is shown in the supporting information. In the following, the physicochemical and kinetic characterization of the oxide precursors and the materials after sulfidation are described.

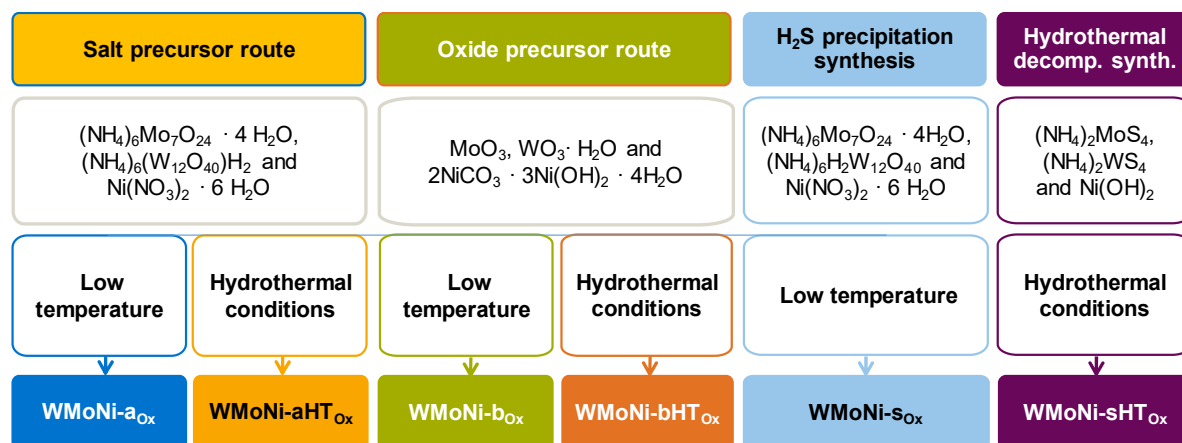


Figure 5. Schematic representation of the synthesis routes applied in this work to prepare precursors of Ni-Mo-W sulfide catalysts.

3.1. Characterization of the oxide catalyst precursors

Table 6 summarizes the elemental content, metal molar fraction, and BET surface area of the precursor materials. All of them contained nickel in a molar fraction between 0.47 and 0.53 with exception of WMoNi-sHT_{Ox} (0.59).

The precursors prepared using oxides (WMoNi-b_{Ox} and WMoNi-bHT_{Ox}) exhibited equimolar concentrations of molybdenum and tungsten, whereby the molar concentration of molybdenum was higher than of tungsten in WMoNi-aHT_{Ox}, WMoNi-s_{Ox}, and WMoNi-sHT_{Ox}. The precursor WMoNi-a_{Ox} was the only material with higher tungsten than molybdenum concentration. Traces of carbon, hydrogen, and nitrogen were detected in some precursors as remainder of the educts used in the synthesis. The BET surface areas of the materials prepared from ammonium salts and oxides, respectively, were higher compared to the precursors obtained from thiosalts decomposition (WMoNi-s_{Ox} and WMoNi-sHT_{Ox}). The surface area of WMoNi-b_{Ox} was the highest. Although the elemental contents and surface area of the materials strongly varied with the preparation procedure, it was not possible to draw correlations between a given group of methods, e.g., hydrothermal synthesis and the properties of the resulting precursor.

Table 6. Elemental content [mmol/g], metal molar fractions (x_W , x_{Mo} , x_{Ni}), and BET surface area (S_{BET} , m^2/g) of the oxide catalyst precursors WMoNi-a_{Ox}, WMoNi-aHT_{Ox}, WMoNi-b_{Ox}, WMoNi-bHT_{Ox}, WMoNi-s_{Ox}, and WMoNi-sHT_{Ox}.

Catalyst precursor	Elemental content [mmol/g]								x_W	x_{Mo}	x_{Ni}	S_{BET} [m ² /g]
	W	Mo	Ni	S	O	N	C	H				
WMoNi-a _{Ox}	0.7	0.3	1.2	-	6.6	0.13	0.12	3.60	0.31	0.16	0.53	32
WMoNi-aHT _{Ox}	0.3	0.7	1.1	-	5.1	0.02	0.05	1.85	0.14	0.33	0.53	24
WMoNi-b _{Ox}	1.6	1.5	2.9	-	18.2	-	-	-	0.27	0.25	0.48	84
WMoNi-bHT _{Ox}	1.7	1.7	3.0	-	15.8	-	-	-	0.27	0.27	0.47	17
WMoNi-s _{Ox}	1.0	1.3	2.2	3.5	16.0	2.60	4.50	21.3	0.22	0.29	0.49	3
WMoNi-sHT _{Ox}	0.6	1.7	3.4	7.9	10.9	0.50	0.10	3.90	0.11	0.30	0.59	5

The X-ray diffraction patterns of all precursors are presented in Figure 6. All materials were reactant-free as no reflections could be assigned to the educts applied using a reference database (ICSD) or comparing with reference materials. The diffractograms of WMoNi-a_{Ox} and WMoNi-s_{Ox} exhibited broad reflections interpreted as anomalous scattering of amorphous phases. The pattern of WMoNi-b_{Ox} had sharp and broad signals pointing to a mixture of crystalline and amorphous phases. The crystalline phases were identified as NiMoO₄·H₂O (comparison with the commercially available compound from Alfa Aesar) and WO₃ (ICSD # 50731).

The materials obtained under hydrothermal conditions showed higher crystallinity than their corresponding counterparts (Figure 6, right). The reflections present in the pattern of WMoNi-aHT_{Ox} corresponded to NiMoO₄·H₂O (comparison with the commercially available compound from Alfa Aesar), NiMoO₄ (ICSD # 81060), and NiWO₄ (ICSD # 15852). NiMoO₄ was also found in WMoNi-bHT_{Ox} with higher crystallinity than in WMoNi-aHT_{Ox}. The remaining reflections in the pattern of WMoNi-bHT_{Ox} were assigned to Ni(OH)₂ (comparison with the commercially available compound from Sigma-Aldrich). The crystalline phases in WMoNi-sHT_{Ox} were orthorhombic Ni₉S₈, cubic NiS₂ (ICSD # 164879 and 36338, respectively), Ni₃S₂ (comparison with the commercially available compound from Sigma-Aldrich) and hexagonal MoS₂ and/or WS₂ (ICSD # 644245 and 202366, respectively). These two phases could not be differentiated because both have the same hexagonal crystalline structure.

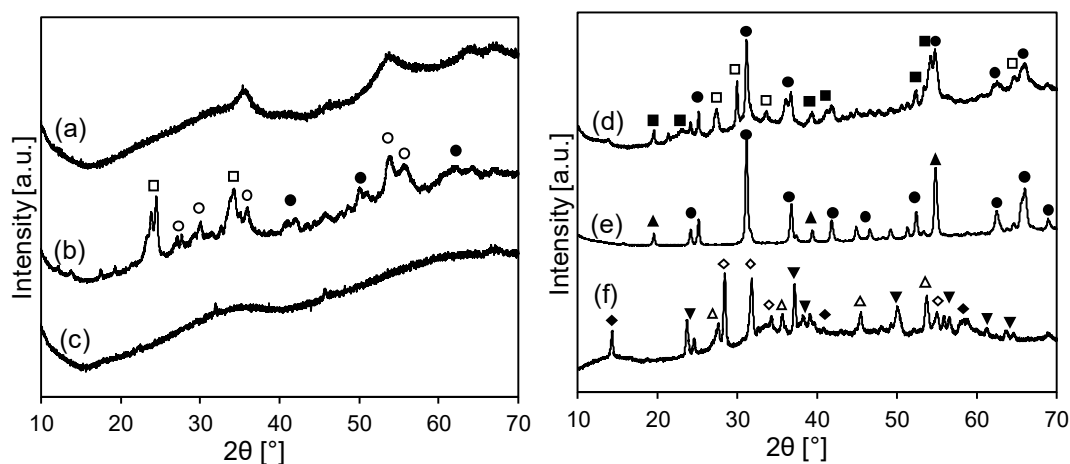


Figure 6. X-ray diffraction patterns of the precursors of the catalysts WMoNi-a_{ox} (a), WMoNi-b_{ox} (b), WMoNi-s_{ox} (c), WMoNi-aHT_{ox} (d), WMoNi-bHT_{ox} (e), and WMoNi-sHT_{ox} (f). The reflections marked correspond to NiMoO₄·H₂O (□), NiMoO₄ (●, ICSD # 81060), WO₃ (○, ICSD # 50731), NiWO₄ (■, ICSD # 15852), Ni(OH)₂ (▲) MoS₂ or WS₂ (◆, ICSD # 644245, 202366), NiS₂ (△, ICSD # 36338), Ni₃S₂ (▼, ICSD # 27521), and Ni₉S₈ (◇, ICSD # 164879).

SEM measurements of all precursors were taken in order to examine their morphologies. Representative images are shown in Figure 7. According to the observations, the precursors could be divided in structurally homogeneous and inhomogeneous materials.

The precursors WMoNi-a_{ox} and WMoNi-s_{ox} showed a homogeneous structure of ragged, round plates (0.2-0.45 μm for WMoNi-a_{ox} and 0.1-0.25 μm for WMoNi-s_{ox}), which agglomerated to form larger ones. WMoNi-bHT_{ox} had also a homogeneous, ragged structure but consisted of very small particles (~0.08 μm) which agglomerated into compact and large particles. The precursors with heterogeneous morphology, i.e., WMoNi-aHT_{ox}, WMoNi-b_{ox}, and WMoNi-sHT_{ox}, contained particles with sizes in the range of 0.1-0.5 μm, 0.2-0.5 μm, and 0.2-1.2 μm, respectively, which looked like the ones found in WMoNi-a_{ox} and WMoNi-s_{ox}. Additionally, needles (particles with a length to width ratio higher than 6) were observed next to those agglomerated plates.

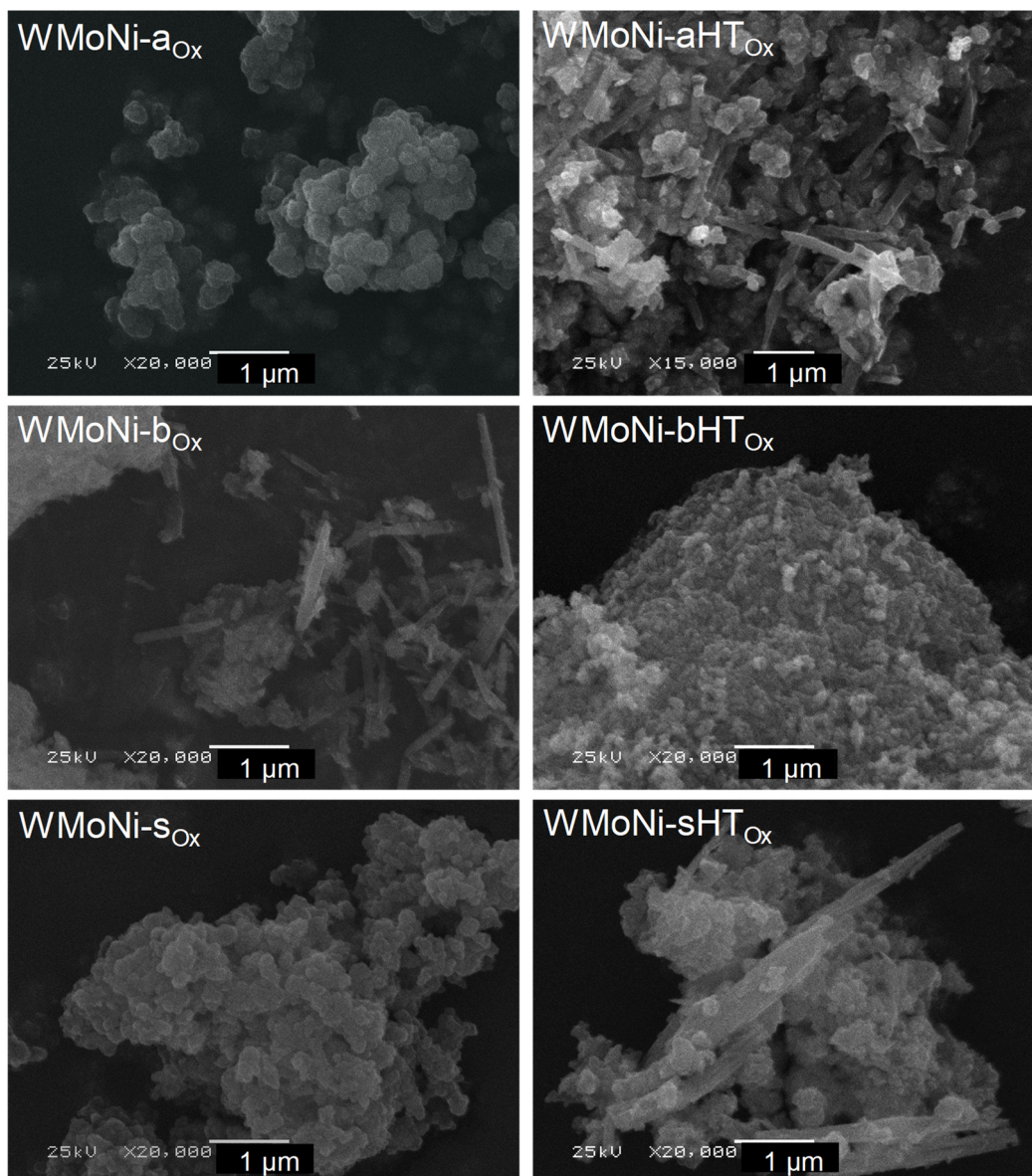


Figure 7. SEM images of the catalyst precursors WMoNi-a_{Ox}, WMoNi-aHT_{Ox}, WMoNi-b_{Ox}, WMoNi-bHT_{Ox}, WMoNi-s_{Ox}, and WMoNi-sHT_{Ox}.

Electron backscattering experiments were conducted in order to study the composition of the structures observed by TEM. Homogenous elemental distributions were present for the materials with homogenous structure, i.e., WMoNi-a_{Ox}, WMoNi-bHT_{Ox}, and WMoNi-s_{Ox}. The two different kinds of particles observed in WMoNi-aHT_{Ox} and WMoNi-b_{Ox} (“plates” and “needles”) exhibited the same elemental composition. In WMoNi-sHT_{Ox}, the needles were caused by nickel sulfide species as concluded from the reflections in its XRD pattern.

Raman spectra of the precursors are presented in Figure 8. For the materials synthesized via the salt and the oxide precursor route (WMoNi-a_{Ox}, WMoNi-aHT_{Ox}, WMoNi-b_{Ox}, and WMoNi-bHT_{Ox}) typical bands of NiMo(W)O₄ and NiMo(W)O₆ were observed. The bands over 900 cm⁻¹ were assigned to the symmetric Mo(W)=O stretching vibrations associated with a MoO₄ or WO₄ unit. The corresponding asymmetric stretching vibrations appeared below

900 cm^{-1} .¹⁵⁰⁻¹⁵¹ The band around 850 cm^{-1} was assigned to bridging Mo(W)-O-Mo(W) bonds connecting Mo(W)O₄ species.¹⁵² The bending vibrations of the tetrahedral structure occurred between 340 and 410 cm^{-1} . Moreover, bands representing the octahedrally coordinated MoO₆, and WO₆ were observed, namely, the symmetric stretching vibrations (675 - 700 cm^{-1}), and the bending vibrations (320 cm^{-1}) of the Mo(W)O₆ species as well as the typical band for the bridging species (260 cm^{-1}).¹⁵⁰⁻¹⁵¹ The Raman spectrum of WMoNi-sO_x showed in addition bands of the tetrahedral and octahedral molybdenum and tungsten oxide species.¹⁵⁰⁻¹⁵¹ In contrast, the vibration bands in the spectrum of WMoNi-sHTO_x were ascribed to various molybdenum oxysulfides, i.e., MoO₂S₂ and MoO₃S.¹⁵³ Summaries of the bands and assignments are presented in the Appendix (Tables A32-A37).

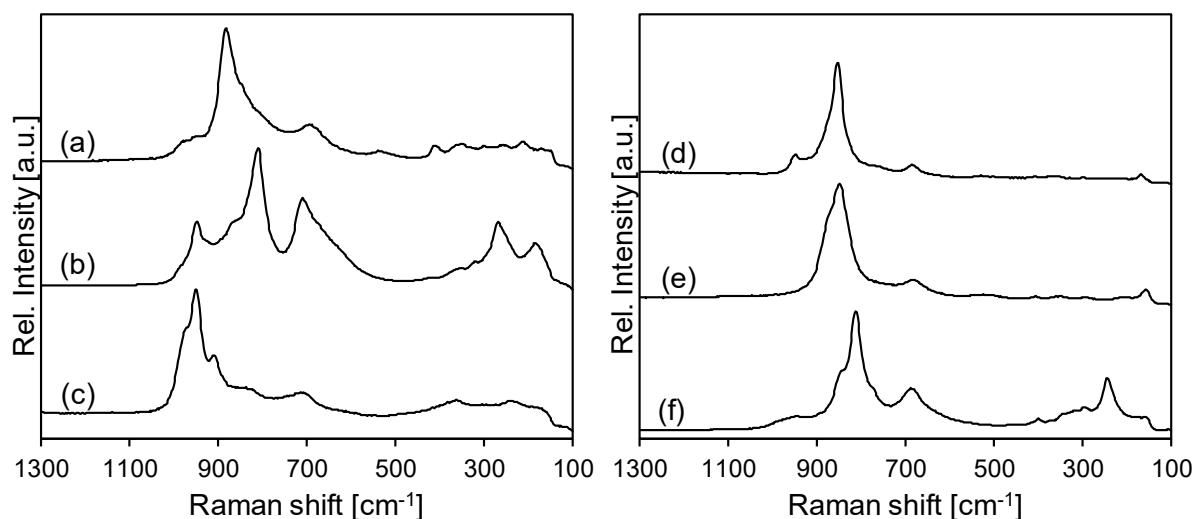


Figure 8. Raman spectra of the precursors of the catalysts WMoNi-aO_x (a), WMoNi-bO_x (b), WMoNi-sO_x (c), WMoNi-aHTO_x (d), WMoNi-bHTO_x (e), and WMoNi-sHTO_x (f).

3.2. Chemical and physicochemical properties of the sulfide catalysts

The sulfide catalysts are denoted according to the name of the corresponding precursor, i.e., WMoNi-a, WMoNi-aHT, WMoNi-b, WMoNi-bHT, WMoNi-s, and WMoNi-sHT. The metal contents in all materials led to nickel metal molar fractions from 0.47 to 0.59 and varying molybdenum to tungsten molar ratios (Table 7). The complete elemental compositions of the catalysts differed from those of the corresponding precursors (Tables 6 and 7) due to elimination of carbon and nitrogen, and the substitution of oxygen by sulfur during sulfidation.

Table 7. Elemental content [mmol/g], metal molar fractions (x_W , x_{Mo} , and x_{Ni}), and BET surface area (S_{BET} , m^2/g) of the sulfide catalysts WMoNi-a, WMoNi-aHT, WMoNi-b, WMoNi-bHT, WMoNi-s, and WMoNi-sHT.

Catalyst	Elemental content [mmol/g]								x_W	x_{Mo}	x_{Ni}	S_{BET} [m^2/g]
	W	Mo	Ni	S	O	N	C	H				
WMoNi-a	1.8	1.0	3.0	8.8	4.0	0.0	0.4	1.5	0.31	0.16	0.53	5.3
WMoNi-aHT	0.9	2.2	3.4	9.7	4.2	0.1	0.3	1.2	0.14	0.33	0.53	9.8
WMoNi-b	1.6	1.5	3.0	9.0	3.3	0.0	0.1	1.0	0.27	0.25	0.48	7.9
WMoNi-bHT	1.6	1.5	2.9	9.3	3.3	0.0	0.1	1.0	0.27	0.27	0.47	15.2
WMoNi-s	1.2	1.6	2.8	8.8	3.9	0.1	0.1	1.9	0.22	0.29	0.49	8.0
WMoNi-sHT	0.7	2.0	4.0	9.3	5.9	0.1	0.2	1.8	0.11	0.30	0.59	19.8

The concentration of nickel determined by XPS was higher than the bulk values for many catalysts, whereas the bulk content of tungsten was higher than its content determined by XPS (Table 8). This indicates that the distribution of the metals is not heterogeneous along the volume of the materials. This suggests, in accordance with literature,⁶⁵ that the heterogeneous elemental composition of the sulfides reflects the presence of several phases in the catalysts. Thus, the high segregation of nickel towards the surface (XPS Ni content higher than the bulk Ni content) was related with the NiS_x species formed on the surface of the catalysts.⁶⁵

The concentration of adsorbed nitric oxide (NO) did not correlate with the specific surface area (Tables 7 and 8), which is attributed to the anisotropy of MoS_2 and WS_2 (where adsorption sites for NO are available only at the edges) and to the varying stoichiometry of NO adsorbed on $Mo(W)S_2$ and nickel sulfides.¹⁵⁴

The BET surface areas of the sulfides did not resemble the trends of the precursors because each material followed a particular sulfidation and reconstruction mechanism as the precursors were prepared by different methods and contained different phases.

The X-ray diffractograms of all materials (Figure 9) exhibited diffraction peaks characteristic of MoS_2 , WS_2 , Ni_9S_8 , and Ni_3S_2 (ICSD # 644245, 202366, 164879, and 27521, respectively). WMoNi-s and WMoNi-sHT showed additional reflections assigned to α -NiS (ICSD # 29313).

Table 8. Metal molar fractions (x_W , x_{Mo} , x_{Ni}) derived from the XPS characterization, and concentration of NO adsorbed on the sulfide catalysts (NO) (L) for the sulfide catalysts WMoNi-a, WMoNi-aHT, WMoNi-b, WMoNi-bHT, WMoNi-s, and WMoNi-sHT.

Catalyst	XPS analysis			NO [$\mu\text{mol/g}$]
	x_W	x_{Mo}	x_{Ni}	
WMoNi-a	0.04	0.15	0.81	72
WMoNi-aHT	0.06	0.42	0.51	57
WMoNi-b	0.19	0.23	0.57	91
WMoNi-bHT	0.28	0.31	0.40	38
WMoNi-s	0.08	0.19	0.73	109
WMoNi-sHT	0.08	0.15	0.77	111

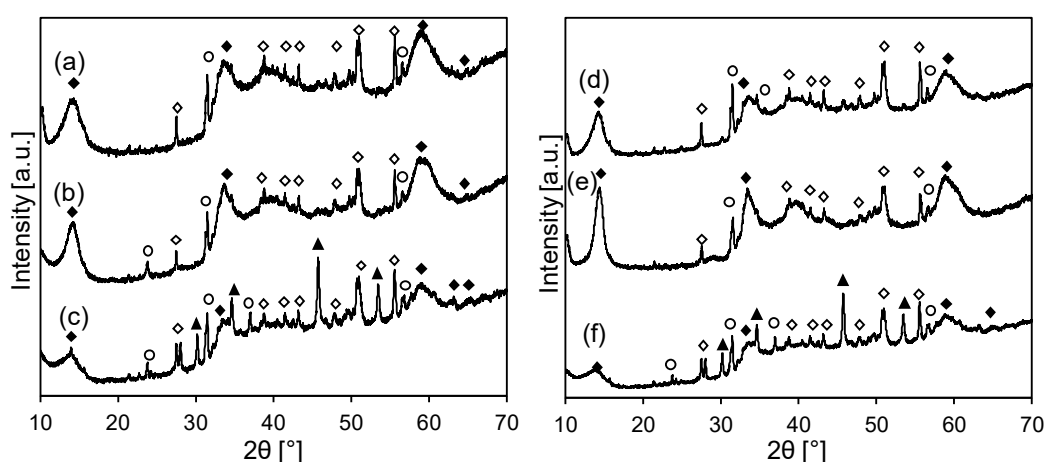


Figure 9. X-ray diffraction patterns of the sulfided catalysts WMoNi-a (a), WMoNi-b (b), WMoNi-s (c), WMoNi-aHT (d), WMoNi-bHT (e), WMoNi-sHT (f). The marked reflections correspond to MoS_2 or WS_2 (◆, ICSD # 644245, 202366), Ni_9S_8 (◇, ICSD # 164879), Ni_3S_2 (○, ICSD # 27521), and $\alpha\text{-NiS}$ (▲, ICSD # 29313).

However, after catalysis, the spent catalysts (Figure 10) exhibited reflections of MoS_2 , WS_2 , and Ni_9S_8 (ICSD # 644245, 202366, 164879, respectively) as the only nickel sulfide phase. Sharper reflections and flatter baselines indicated higher crystallinity of the spent catalysts than the freshly sulfided ones. The Scherrer equation, applied on the reflection at $14^\circ 2\theta$ corresponding to the (002) lattice plane of Mo(W)S_2 , showed that the crystal sizes of WMoNi-a, WMoNi-b, and WMoNi-s increased during the reaction, whereas those of the hydrothermal treated materials hardly changed (Table 9). However, the trend of crystal sizes was the same for spent and freshly sulfided catalysts.

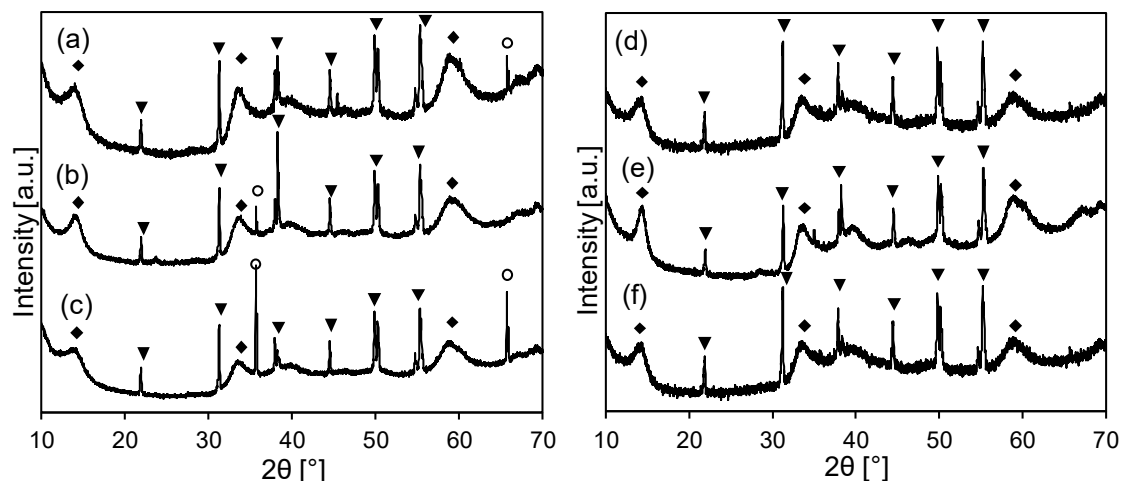


Figure 10. X-ray diffraction patterns of the spent sulfided catalysts WMoNi-a (a), WMoNi-b (b), WMoNi-s (c), WMoNi-aHT (d), WMoNi-bHT (e), WMoNi-sHT (f). The reflections marked correspond to MoS₂ or WS₂ (♦, ICSD # 644245, 202366), Ni₉S₈ (▼, ICSD # 164879), and SiC (○).

In TEM images of all materials (Figure 11), typical lattice fringes with an interplanar distance of 0.62 nm, corresponding to the layered structure of MoS₂ and WS₂, were observed. The trends in average stacking degrees of the Mo(W)S₂ slabs, obtained by inspection of TEM images, were in qualitative agreement with those determined from the Scherrer equation (Table 9). The average slabs lengths varied in a relatively wide range (6-48 nm) and exhibited broad distributions (Appendix Figure A84).

Table 9. Crystallite size (z-direction) [Å] and stacking degree of MoS₂/WS₂ crystals in fresh-sulfided and spent catalysts derived from XRD as well as length [nm] and stacking degree of the fresh sulfide catalysts estimated from TEM (The numbers in brackets shows the corresponding standard deviation)

Catalyst	Crystallite size [Å]		Stacking degree		TEM measurements	
	Fresh	Spent	Fresh	Spent	Length [nm]	Stacking degree
WMoNi-a	33	40	5	6	6.0 (±2.0)	3.6 (±1.7)
WMoNi-aHT	55	54	9	9	6.0 (±2.1)	5.0 (±1.4)
WMoNi-b	41	55	7	9	10.1 (±4.9)	4.7 (±1.9)
WMoNi-bHT	71	72	12	12	48.0 (±15.3)	8.6 (±3.7)
WMoNi-s	33	42	5	7	9.3 (±2.6)	3.9 (±1.3)
WMoNi-sHT	32	32	5	5	11.6 (±3.4)	5.0 (±1.6)

A second phase was identified by means of selected area diffraction (SAED) as Ni₉S₈. For instance, Figure 11 shows for WMoNi-b that the SAED contained reflections of Ni₉S₈ (bright dots) besides those of Mo(W)S₂ (rings). It was hypothesized that these nickel sulfide crystals indicated by SAED are not those that produced X-ray diffraction peaks, which correspond to crystals sizes in the range of microns. The large crystals of nickel sulfide are directly observed

by SEM (Figure 12). Thus, nickel sulfide particles are present in sizes ranging from nanometers (TEM) to micrometers (SEM) and are surrounded by Mo(W)S₂ slabs.

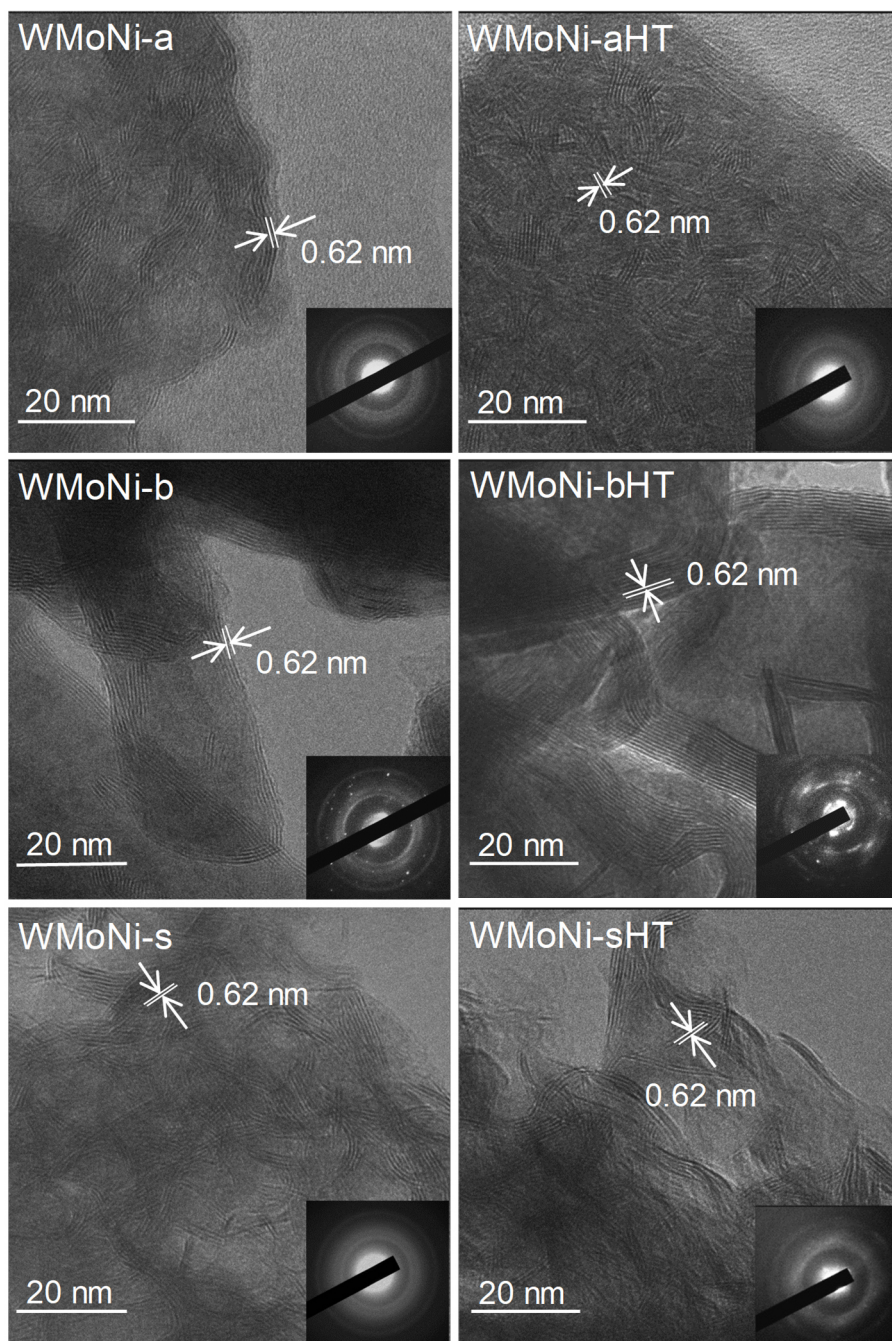


Figure 11. Representative TEM micrographs of the sulfided catalysts WMoNi-a, WMoNi-b, WMoNi-s, WMoNi-aHT, WMoNi-bHT, and WMoNi-sHT.

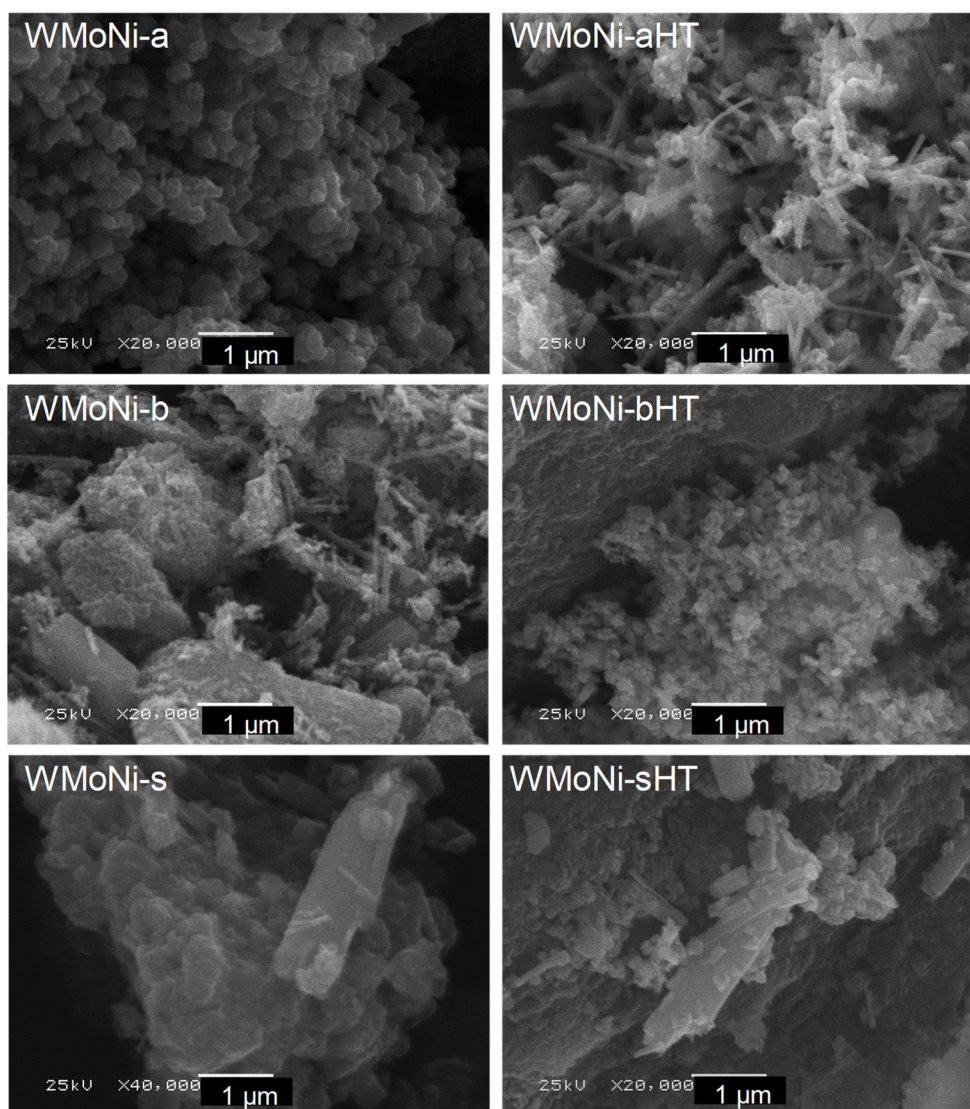


Figure 12. SEM images of the sulfide catalysts WMoNi-a, WMoNi-aHT, WMoNi-b, WMoNi-bHT, WMoNi-s, and WMoNi-sHT.

WMoNi-aHT, WMoNi-b, and WMoNi-sHT contained mixtures of ragged plates and needles, which were abundant in WMoNi-aHT. In contrast, WMoNi-a, and WMoNi-bHT were dominated by round, ragged particles. Only the morphology of WMoNi-s seemed to change as needles develop. The round particles had been associated to Mo(W)S_2 agglomerates and the better-defined needles had been identified as nickel sulfides.⁴³

The Mo(W)S_2 phases in similar sulfide Ni-Mo-W catalysts consisted of intralayer mixed $\text{Mo}_x\text{W}_{x-1}\text{S}_2$ slabs as deduced from XAS and Raman spectroscopy.^{43, 141, 155} These studies also showed that atomically dispersed nickel is present at the edges of the Mo(W)S_2 crystals.⁴³ In agreement with these reports, the Raman spectra of the catalysts in this work (Figure 13) showed bands in the range of $372\text{-}378\text{ cm}^{-1}$, attributed to the E^{1}_{2g} mode of Mo-S, and bands around 346 cm^{-1} ascribed to the E^{1}_{2g} mode of W-S (specific position of the bands is described in Table 10).

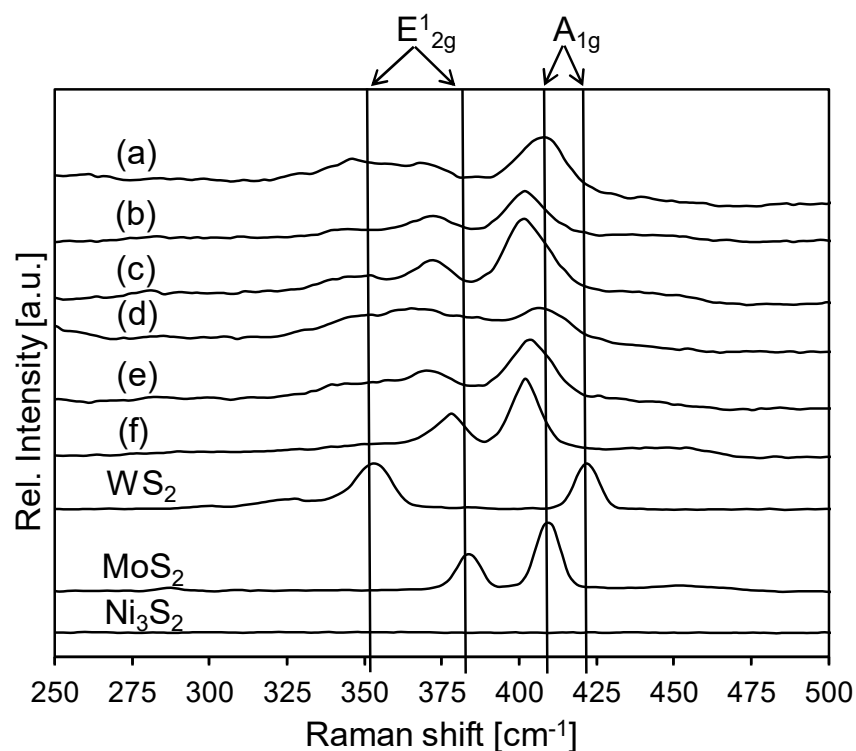


Figure 13. Raman spectra of the spent catalysts WMoNi-a (a), WMoNi-b (b), WMoNi-s (c), WMoNi-aHT (d), WMoNi-bHT (e), and WMoNi-sHT (f) as well as Raman spectra of the references WS_2 , MoS_2 , and Ni_3S_2 .

The A_{1g} modes of Mo-S and W-S in the reference materials were observed at 410 and 424 cm^{-1} , respectively. The bands shifting to around 408 cm^{-1} for WMoNi-a, and WMoNi-bHT and around 402 cm^{-1} for the other four materials were assigned to the A_{1g} mode of Mo-W composite species ($Mo_{1-x}W_xS_2$).¹⁵⁶⁻¹⁵⁷ Thus, the catalytic activity is likely dominated by Ni-containing $Mo_xW_{x-1}S_2$, as nickel sulfides do not have a relevant hydrotreating activity.¹⁵⁸

Table 10. Assignments and vibration modes of the Raman bands observed in the spectra of the spent catalysts WMoNi-a, WMoNi-aHT, WMoNi-b, WMoNi-bHT, WMoNi-s, and WMoNi-sHT.

Catalyst	A_1 mode Raman shift [cm^{-1}]	E^1_{2g} mode Raman shift [cm^{-1}]	
		Mo-S	W-S
WMoNi-a	409	368	345
WMoNi-aHT	402	373	352
WMoNi-b	404	370	352
WMoNi-bHT	402	373	344
WMoNi-s	407	365	347
WMoNi-sHT	402	384	-

3.3. Catalysis

3.3.1. Hydrodenitrogenation of *o*-propylaniline

The apparent rate constants of the sulfide catalysts in the hydrodenitrogenation of *o*-propylaniline as a function of the inverse temperature are shown in Figure 14 (further graphical representations of the catalytic results are presented in the Appendix Figures A85 and A86).

The rate constants increased in the sequence

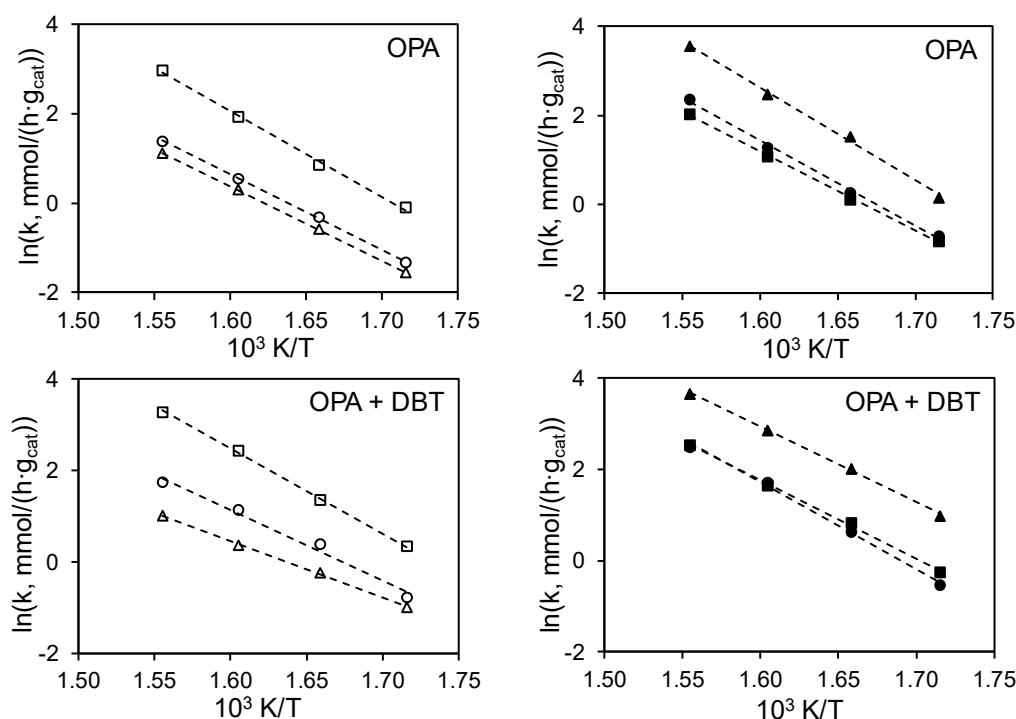


Figure 14. Reaction rate constants for the hydrodenitrogenation of *o*-propylaniline without (top) and in the presence of dibenzothiophene (below) at varying temperatures on the sulfided catalysts WMoNi-a (circle, unfilled), WMoNi-b (square, unfilled), WMoNi-s (triangle, unfilled), WMoNi-aHT (circle, filled), WMoNi-bHT (square, filled), and WMoNi-sHT (triangle, filled) assuming first order reaction.

The conversion rates of *o*-propylaniline (Figure 14) increased in presence of dibenzothiophene without changing the order of activity. The rates of hydrodenitrogenation of *o*-propylaniline have been concluded to increase in presence of dibenzothiophene only on Ni-containing $\text{MoS}_2/\text{Al}_2\text{O}_3$ but not on $\text{MoS}_2/\text{Al}_2\text{O}_3$.^{39, 159} Hence, the positive influence of dibenzothiophene on the catalytic activity suggests that NiMo(W)S₂ dominates the catalytic performance.

The products observed during the hydrodenitrogenation of *o*-propylaniline were *o*-propylcyclohexylamine, three isomers of propylcyclohexene, i.e., 1-propylcyclohexene, 3-propylcyclohexene, and propylidene cyclohexane), and propylcyclohexane.

Thus, hydrogenation of *o*-propylaniline to *o*-propylcyclohexylamine is followed by removal of the nitrogen atom towards propylcyclohexene and consecutive saturation to propylcyclohexane. Propylbenzene was the product of the direct denitrogenation of *o*-propylaniline.^{39, 160} The corresponding reaction network is presented in Figure 19.

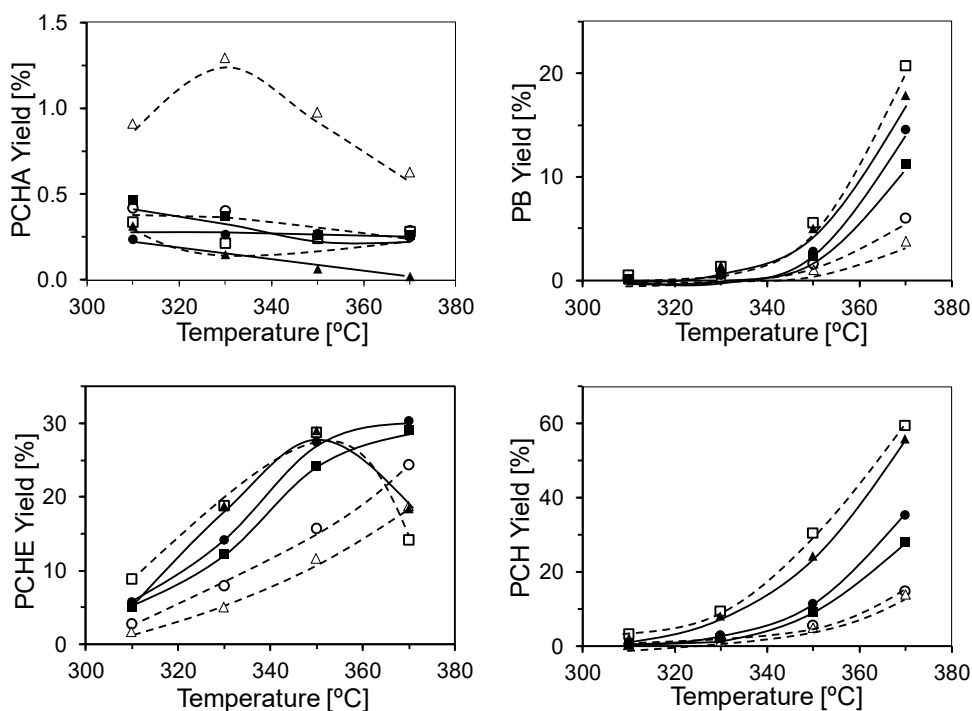


Figure 15. Product yields of the hydrodenitrogenation of *o*-propylaniline over temperature on the sulfided catalysts WMoNi-a (circle, unfilled), WMoNi-b (square, unfilled), WMoNi-s (triangle, unfilled), WMoNi-aHT (circle, filled), WMoNi-bHT (square, filled), and WMoNi-sHT (triangle, filled). The products depicted in the figure are *o*-propylcyclohexylamine (PCHA), propylbenzene (PB), propylcyclohexene (PCHE), and propylcyclohexane (PCH).

Figure 15 shows the product yields as a function of temperature at similar reactant conversions. *o*-propylcyclohexylamine had very low yields, which indicates that the hydrogenation of *o*-propylaniline is slower than the denitrogenation of *o*-propylcyclohexylamine. Declining yields of *o*-propylcyclohexylamine with increasing temperature point to increasing differences in the rates of *o*-propylaniline hydrogenation and *o*-propylcyclohexylamine denitrogenation as the temperature increased. The yields of propylbenzene were higher than those of *o*-propylcyclohexylamine but much lower than those of propylcyclohexene and propylcyclohexane.

This indicates that direct denitrogenation of *o*-propylaniline ($C(sp^2)$ -N cleavage) is less favored than its hydrogenation and further $C(sp^3)$ -N bond hydrogenolysis. The marked increase of the yield of propylbenzene above 350 °C is speculated to be caused by dehydrogenation of propylcyclohexene. The latter product increased with temperature but passed through a maximum on the most active catalysts as a function of temperature. The yield of the final

product propylcyclohexane increased steadily with temperature and followed the same trend than the *o*-propylaniline conversion. In all cases, the propylcyclohexane yield was higher than the yield of propylcyclohexene, which indicates faster hydrogenation of propylcyclohexene than hydrogenation of *o*-propylaniline followed by denitrogenation of *o*-propylcyclohexylamine.

The differences among the yield profiles observed for the hydrodenitrogenation of *o*-propylaniline were caused by varying conversion degrees on the different catalysts. Thus, the chemical composition of the catalysts marginally influences the selectivity of hydrodenitrogenation of *o*-propylaniline. The product yields in the presence of dibenzothiophene (Figure 16) were very similar to those observed in the absence of dibenzothiophene.

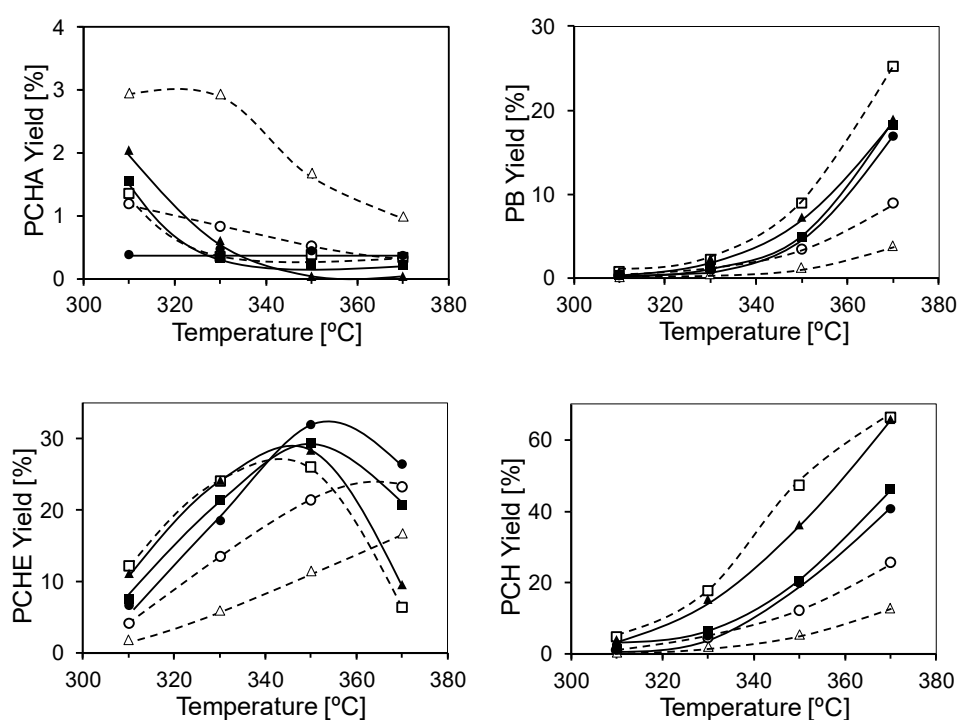


Figure 16. Evolution of the yields of the products of the hydrodenitrogenation of *o*-propylaniline over temperature in the presence of dibenzothiophene on the sulfided catalysts WMoNi-a (circle, unfilled), WMoNi-b (square, unfilled), WMoNi-s (triangle, unfilled), WMoNi-aHT (circle, filled), WMoNi-bHT (square, filled), and WMoNi-sHT (triangle, filled). The products depicted in the figure are *o*-propylcyclohexylamine (PCHA), propylbenzene (PB), propylcyclohexene (PCHE), and propylcyclohexane (PCH).

3.3.2. Hydrodenitrogenation of quinoline

The rate constants of the sulfide catalysts in the hydrodenitrogenation of quinoline at different temperatures are compiled in Figure 18 (see also Figures A87 and A88 in the Appendix). The conversion of quinoline to 1,2,3,4-tetrahydroquinoline was equilibrated (Figure 17), while all other steps were kinetically controlled. Hence, the sum of the concentrations of quinoline and 1,2,3,4-tetrahydroquinoline was used to describe the rates. The conversions rates were lower than those observed for *o*-propylaniline and the activity rankings for quinoline and *o*-propylaniline conversions differed. For the conversion of quinoline, the activity increased as follows

$$\text{WMoNi-s} < \text{WMoNi-bHT} < \text{WMoNi-a} < \text{WMoNi-sHT} < \text{WMoNi-aHT} < \text{WMoNi-b.}$$

The presence of dibenzothiophene increased the conversion rates of quinoline as shown in Figure 18 and modified the activity ranking making WMoNi-a more active than WMoNi-bHT. This increase of conversion rates of quinoline and 1,2,3,4-tetrahydroquinoline in the presence of dibenzothiophene is attributed to enhanced concentration of active sites for the hydrogenation reactions and the ring opening of 1,2,3,4-tetrahydroquinoline and *cis*, *trans*-decahydroquinoline. The rationale is that direct desulfurization of dibenzothiophene creates basic S²⁻ groups, which in turn lead to a higher concentration of activated hydrogen (presumably in the form of SH groups) at the surface.¹⁵⁹

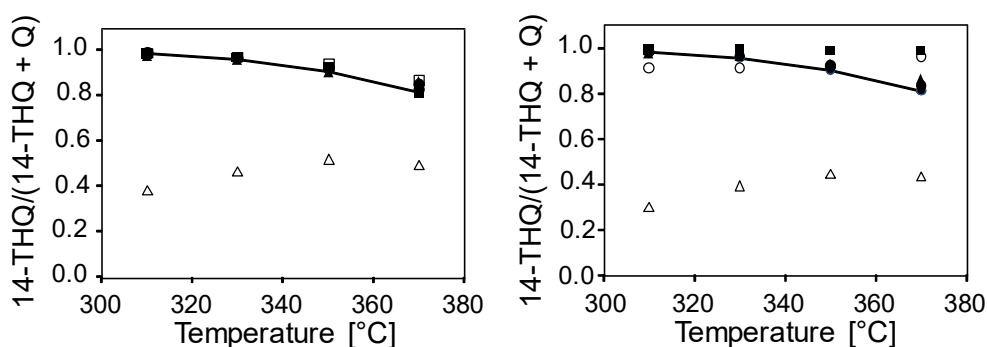


Figure 17. Equilibrium between quinoline (Q) and 1,2,3,4-tetrahydroquinoline (14-THQ) at varying temperatures (line) on the sulfided catalysts WMoNi-a (circle, unfilled), WMoNi-b (square, unfilled), WMoNi-s (triangle, unfilled), WMoNi-aHT (circle, filled), WMoNi-bHT (square, filled), and WMoNi-sHT (triangle, filled) in the presence of DBT (left) and in its absence (right).

The products observed during the hydrodenitrogenation of quinoline were 1,2,3,4-tetrahydroquinoline, 5,6,7,8-tetrahydroquinoline, both isomers of decahydroquinoline i.e., (*cis*, *trans*-decahydroquinoline, as well as *o*-propylaniline and the products observed during the hydrodenitrogenation of *o*-propylaniline (PCHA, PCHE, PCH, and PB). The overall reaction network of the hydrodenitrogenation of quinoline, which comprises the conversion of *o*-propylaniline, is presented in Figure 19.¹⁵⁹

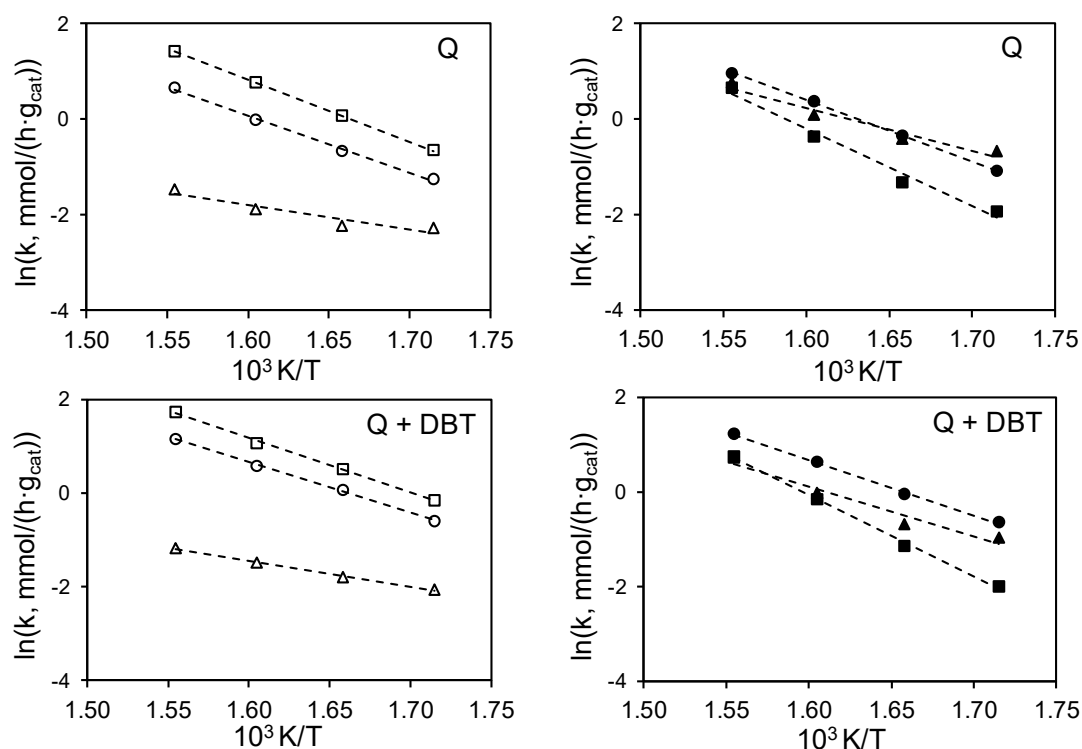


Figure 18. Reaction rates of the merged conversion of quinoline and 1,2,3,4-tetrahydroquinoline without (top) and in the presence of dibenzothiophene (below) at varying temperatures on the sulfided catalysts WMoNi-a (circle, unfilled), WMoNi-b (square, unfilled), WMoNi-s (triangle, unfilled), WMoNi-aHT (circle, filled), WMoNi-bHT (square, filled), and WMoNi-sHT (triangle, filled).

Quinoline was fully hydrogenated to decahydroquinoline via 1,2,3,4-tetrahydroquinoline or 5,6,7,8-tetrahydroquinoline. Under our reaction conditions only the (de)hydrogenation equilibrium between quinoline and 1,2,3,4-tetrahydroquinoline was reached. Ring opening reactions are key steps in the hydrodenitrogenation network producing monocyclic compounds that react more readily than bicyclic compounds, i.e., ring opening from 1,2,3,4-tetrahydroquinoline to *o*-propylaniline, and ring opening from decahydroquinoline to *o*-propylcyclohexylamine. Decahydroquinoline reacts faster than 1,2,3,4-tetrahydroquinoline while a dehydrogenation step from *o*-propylcyclohexylamine to *o*-propylaniline is possible, especially at high temperatures.

Figure 20 shows the product yields for the hydrodenitrogenation of quinoline over temperature. The yields of 5,6,7,8-tetrahydroquinoline are not shown, because they were negligible. The yields of decahydroquinoline increased with temperature up to maximum values at approximately 350 °C on most catalysts. The increase of the yields of propylbenzene paralleled the increase of *o*-propylaniline, although yields of propylbenzene remained in very low concentrations. The yields of *o*-propylcyclohexylamine increased with temperature passing through a maximum at 350 °C.

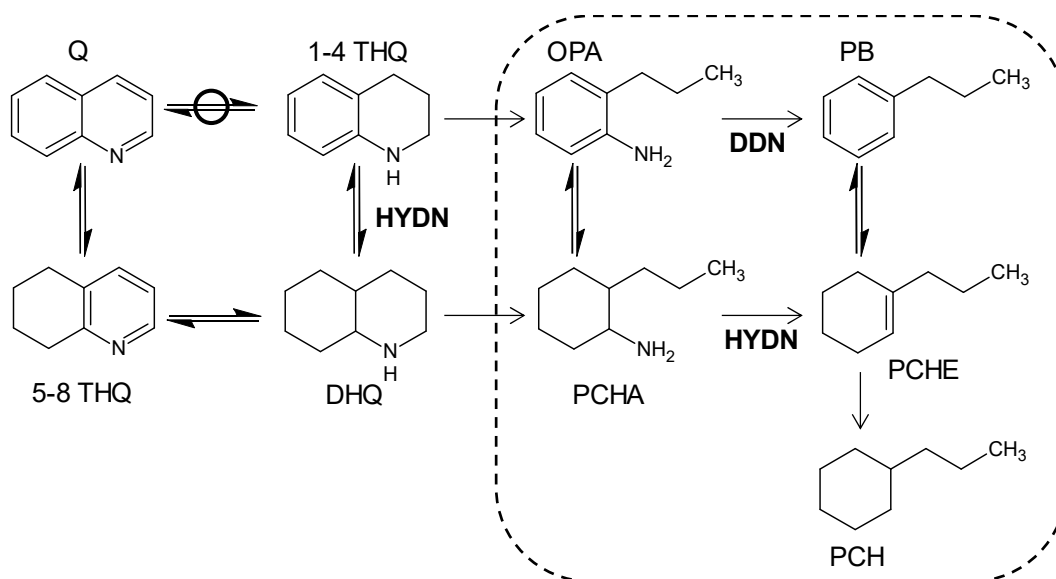


Figure 19. Reaction network for the hydrodenitrogenation of quinoline and the intermediate *o*-propylaniline (OPA) (within the dotted square); the compounds depicted in the figure are quinoline (Q), 1,2,3,4-tetrahydroquinoline (14-THQ), 5,6,7,8-tetrahydroquinoline (58-THQ), decahydroquinoline (DHQ), *o*-propylaniline (OPA), *o*-propylcyclohexylamine (PCHA), propylcyclohexene (PCHE), propylcyclohexane (PCH), and propylbenzene (PB). DDN and HYDN stand for the routes direct denitrogenation and hydrogenation, respectively.

The yields of the denitrogenated products, propylcyclohexene and propylcyclohexane, increased above 350 °C. Hence, 350 °C seems to be a turning point, at which the rates of ring opening, and subsequent denitrogenation become comparable to those of the (de)hydrogenation steps of bicyclic compounds. Note that, the yields of propylcyclohexane were lower than those of propylcyclohexene. This indicates, in contrast to the observations with the hydrodenitrogenation of *o*-propylaniline, that in the presence of quinoline and its bicyclic hydrogenated intermediates the hydrogenation of propylcyclohexene is suppressed to some extent probably due to competitive adsorption of bicyclic compounds on hydrogenation sites.

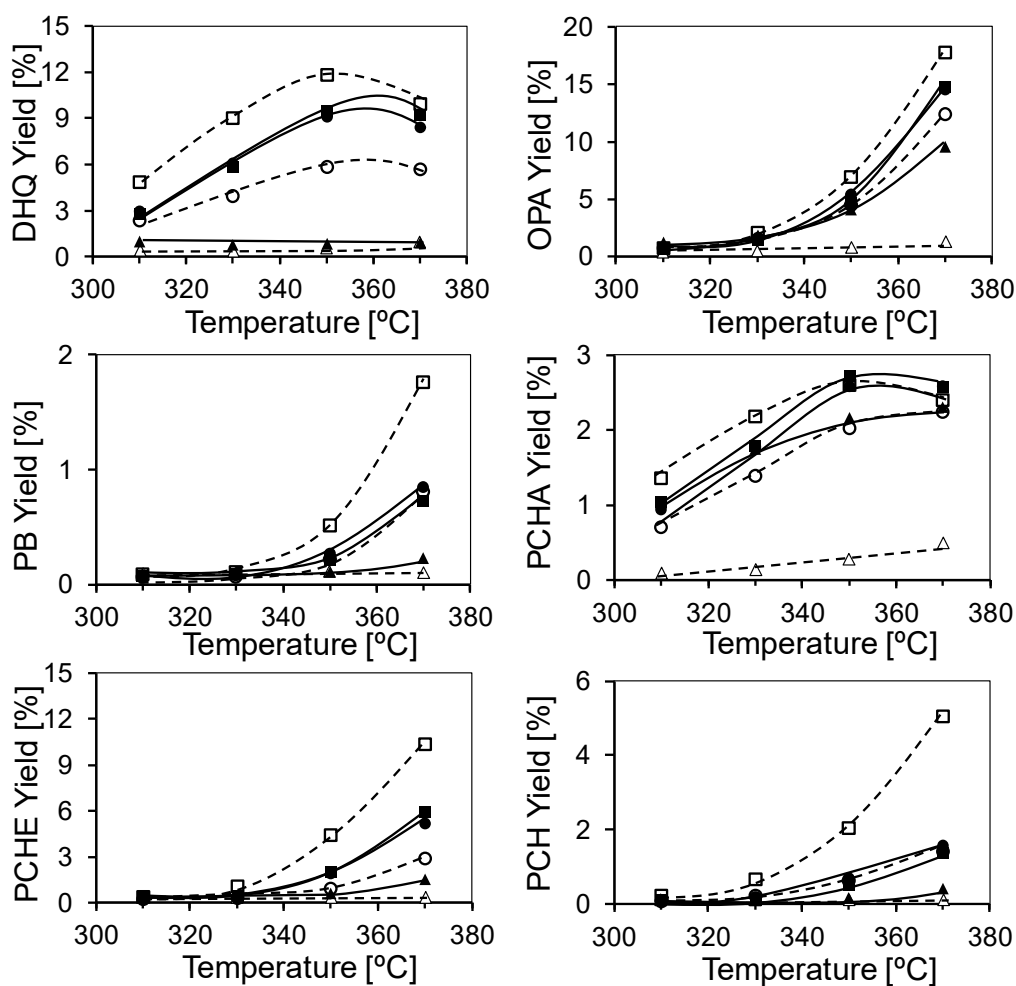


Figure 20. Evolution of the yields of selected products of the hydrodenitrogenation of quinoline over temperature on the sulfide catalysts WMoNi-a (circle, unfilled), WMoNi-b (square, unfilled), WMoNi-s (triangle, unfilled), WMoNi-aHT (circle, filled), WMoNi-bHT (square, filled) and, WMoNi-sHT (triangle, filled) assuming first order reaction. The compounds depicted in the figure are decahydroquinoline (DHQ), *o*-propylaniline (OPA), propylbenzene (PB), *o*-propylcyclohexylamine (PCHA), propylcyclohexene (PCHE), and propylcyclohexane (PCH).

The product yields in the presence of dibenzothiophene (Figure 21) changed only slightly compared to that observed in the absence of dibenzothiophene.

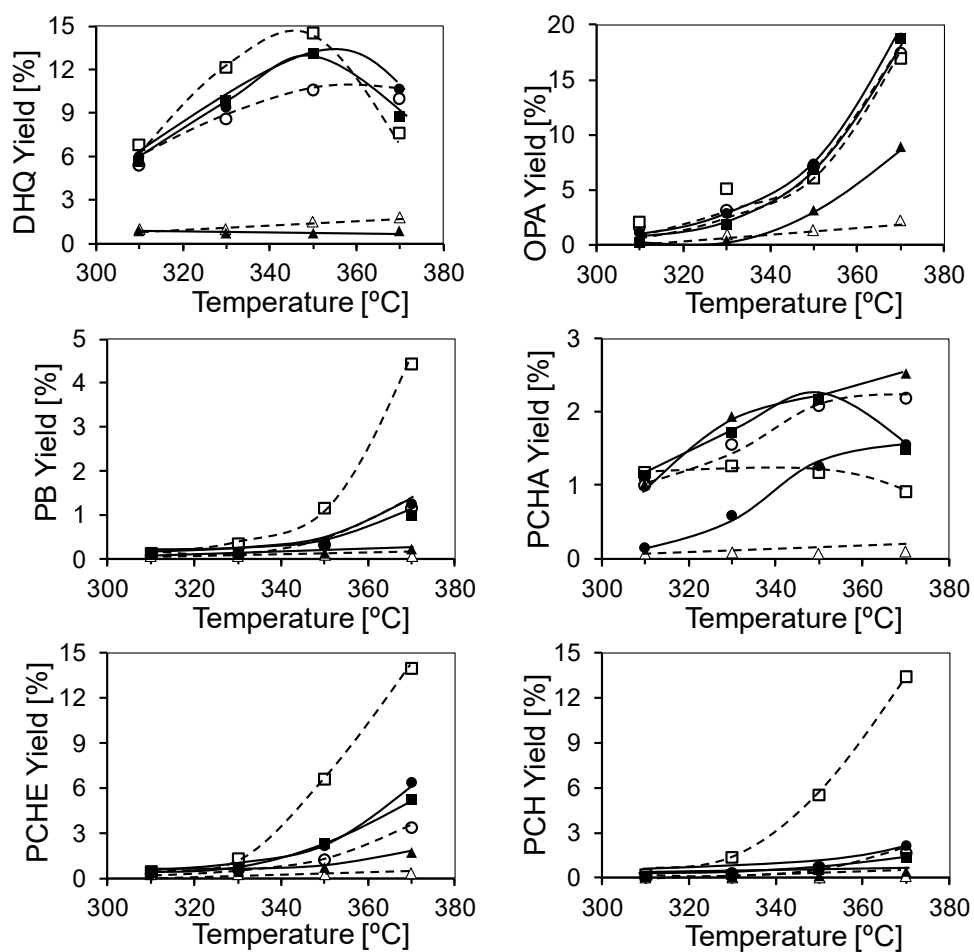


Figure 21. Evolution of the yields of selected products of the hydrodenitrogenation of quinoline in the presence of dibenzothiophene over temperature on the sulfide catalysts WMoNi-a (circle, unfilled), WMoNi-b (square, unfilled), WMoNi-s (triangle, unfilled), WMoNi-aHT (circle, filled), WMoNi-bHT (square, filled), and WMoNi-sHT (triangle, filled) assuming first order reaction. The compounds depicted are decahydroquinoline (DHQ), *o*-propylaniline (OPA), propylbenzene (PB), *o*-propylcyclohexylamine (PCHA), propylcyclohexene (PCHE), and propylcyclohexane (PCH).

3.3.3. Hydrodesulfurization of dibenzothiophene

The hydrodesulfurization of dibenzothiophene proceeded at lower rates than the hydrodenitrogenation of *o*-propylaniline and quinoline. Figure 22 shows Arrhenius-type plots for the hydrodesulfurization of dibenzothiophene during the hydrodenitrogenation of *o*-propylaniline at varying temperature (see also Figures A89 and A90 in the Appendix). The apparent rate constants increased in the sequence

$$\text{WMoNi-bHT} \cong \text{WMoNi-a} < \text{WMoNi-s} \cong \text{WMoNi-aHT} < \text{WMoNi-b} < \text{WMoNi-sHT}.$$

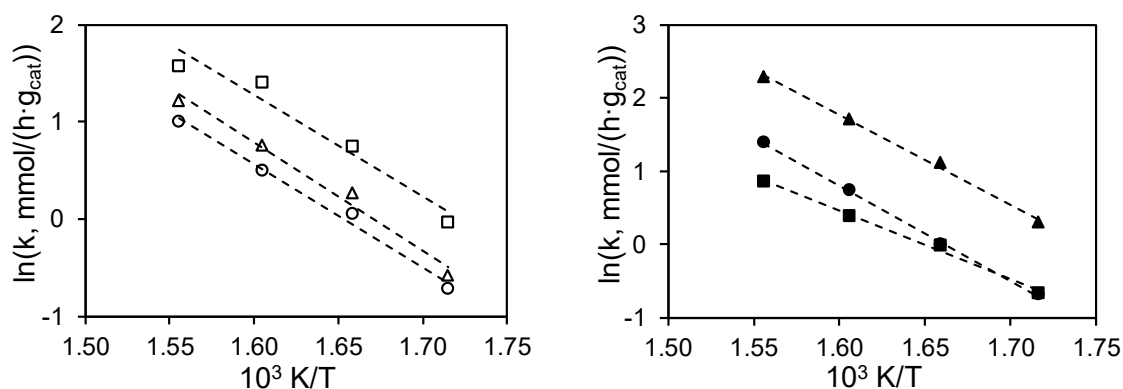


Figure 22. Reaction rate constants for the hydrodesulfurization of dibenzothiophene at varying temperatures during hydrodenitrogenation of *o*-propylaniline on the sulfide catalysts WMoNi-a (circle, unfilled), WMoNi-b (square, unfilled), WMoNi-s (triangle, unfilled), WMoNi-aHT (circle, filled), WMoNi-bHT (square, filled), and WMoNi-sHT (triangle, filled).

In the presence of quinoline, the hydrodesulfurization rates (Figure 23) were lower than in the presence of *o*-propylaniline. However, the differences varied randomly. As consequence, the hydrodesulfurization activity ranking in the presence of quinoline, being

$$\text{WMoNi-s} < \text{WMoNi-a} \cong \text{WMoNi-sHT} < \text{WMoNi-aHT} < \text{WMoNi-bHT} < \text{WMoNi-b},$$

differed from the rates observed for hydrodesulfurization in the presence of *o*-propylaniline. Hence, *o*-propylaniline, quinoline, and the corresponding products of the hydrodenitrogenation reactions differently affect the hydrodesulfurization of dibenzothiophene. In the hydrodenitrogenation of quinoline the strong adsorption of this reactant and the hydrogenated products, i.e., 1,2,3,3-tetrahydroquinoline, 5,6,7,8-tetrahydroquinoline, and *cis*, *trans*-decahydroquinoline, hinders hydrodesulfurization to a larger extent than in the hydrodenitrogenation of *o*-propylaniline.²⁶

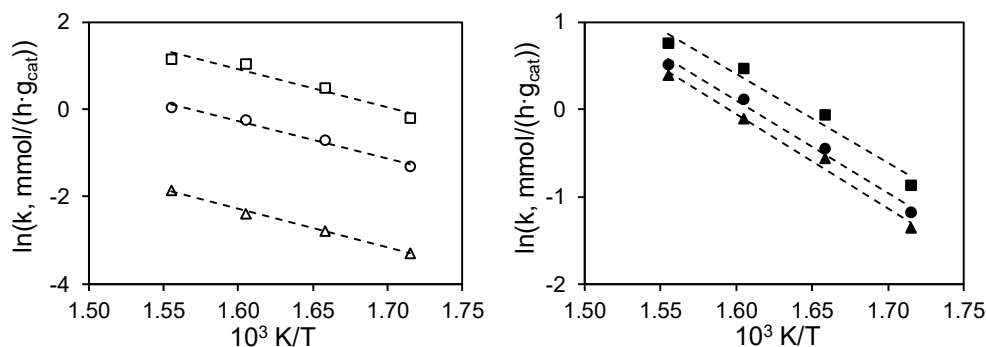


Figure 23. Reaction rate constants for the hydrodesulfurization of dibenzothiophene at varying temperatures on the sulfided catalysts in the presence of quinoline: WMoNi-a (sphere, unfilled), WMoNi-b (square, unfilled), WMoNi-s (triangle, unfilled), WMoNi-aHT (sphere, filled), WMoNi-bHT (square, filled), and WMoNi-sHT (triangle, filled) assuming first order reaction.

In the reaction network of the hydrodesulfurization of dibenzothiophene (Figure 24), biphenyl, tetrahydrodibenzothiophene, and phenylcyclohexane were formed. Biphenyl was the only product of the direct desulfurization route, whereas the hydrogenation route of dibenzothiophene produced phenylcyclohexane via tetrahydrodibenzothiophene.¹⁶⁰

The yields of the hydrodesulfurization products, observed during the hydrodenitrogenation of *o*-propylaniline, are presented in Figure 25. The yields of tetrahydrodibenzothiophene are not presented because they were below 1 %. Biphenyl was the main product of the reaction and increased along temperature reaching a maximum between 350 °C and 370 °C. Phenylcyclohexane was formed in negligible concentrations below 340 °C but its concentration increased exponentially at higher temperatures. Thus, biphenyl was hydrogenated to phenylcyclohexane at higher temperature. The hydrodesulfurization of dibenzothiophene was concluded, therefore, to occur predominantly via direct desulfurization followed by hydrogenation.

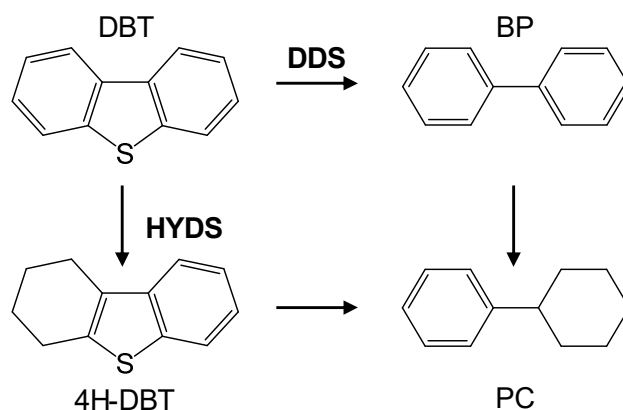


Figure 24. Reaction network for the hydrodesulfurization of dibenzothiophene (DBT) with the products biphenyl (BP), tetrahydrodibenzothiophene (4H-DBT), and phenylcyclohexane (PC). DDS and HYDS stand for the routes direct desulfurization and hydrogenation, respectively.

The product distribution of the hydrodesulfurization of dibenzothiophene was identical in the presence of quinoline to that observed in the presence of *o*-propylaniline (Figure 26).

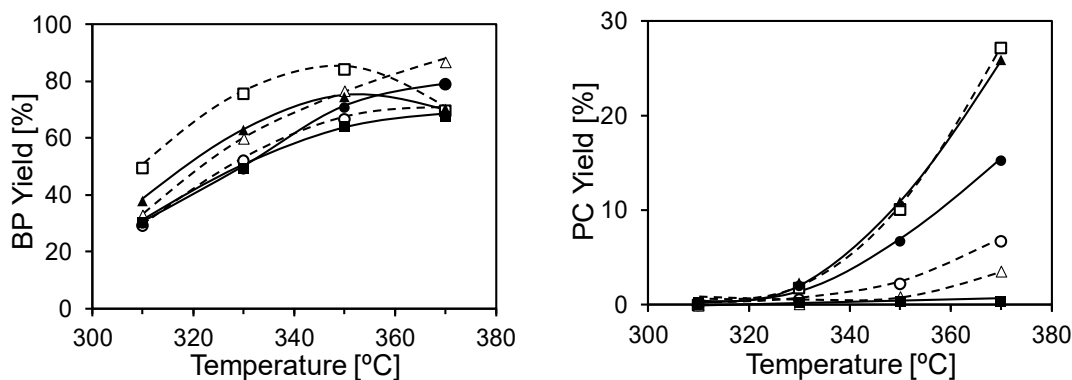


Figure 25. Yield of the products biphenyl (BP) and phenylcyclohexane (PC) of the hydrodesulfurization of dibenzothiophene on the sulfided catalysts in the presence of *o*-propylaniline: WMoNi-a (circle, unfilled), WMoNi-b (square, unfilled), WMoNi-s (triangle, unfilled), WMoNi-aHT (circle, filled), WMoNi-bHT (square, filled), and WMoNi-sHT (triangle, filled).

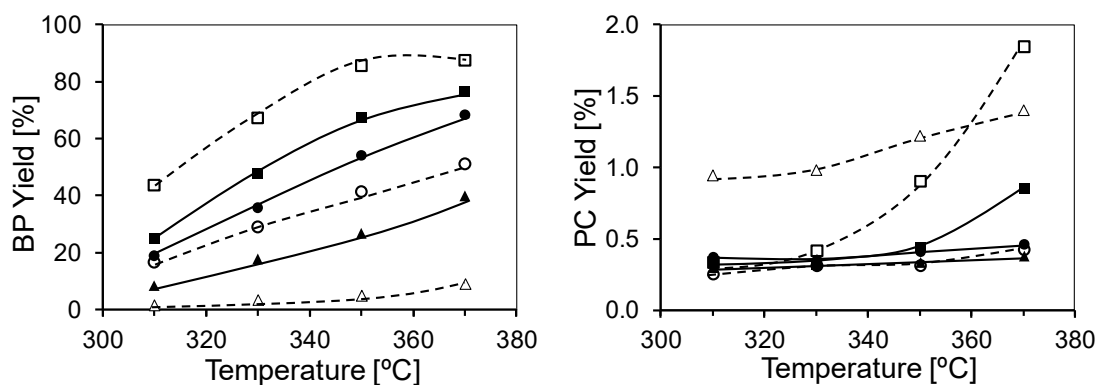


Figure 26. Yield of the products biphenyl (BP) and phenylcyclohexane (PC) of the hydrodesulfurization of dibenzothiophene on the sulfided catalysts in the presence of quinoline: WMoNi-a (circle, unfilled), WMoNi-b (square, unfilled), WMoNi-s (triangle, unfilled), WMoNi-aHT (circle, filled), WMoNi-bHT (square, filled), and WMoNi-sHT (triangle, filled).

3.3.4. Apparent activation energies

The apparent activation energies for the conversion of *o*-propylaniline (138 kJ/mol in average) were higher than the apparent activation energies of quinoline (94 kJ/mol in average) regardless of the presence of dibenzothiophene (Table 11). As the hydrodenitrogenation of *o*-propylaniline proceeded faster than the hydrodenitrogenation of quinoline, the higher activation energy of the former must be overcompensated by the pre-exponential factors, which merge concentration of active sites and entropic factors. Probably the concentration of active sites accessible for *o*-propylaniline is higher than for quinoline.

In the presence of dibenzothiophene, all apparent activation energies for hydrodenitrogenation of *o*-propylaniline increased to 154 kJ/mol in average, but the reaction rates for hydrodenitrogenation also increased. Increasing rates paralleling increasing activation energies suggest that the presence of dibenzothiophene enhances the concentration of sites for the conversion of *o*-propylaniline at the sulfide edges. The average apparent activation energies of the conversion of dibenzothiophene (79 kJ/mol) was lower in the presence of quinoline than in the presence of *o*-propylaniline (92 kJ/mol). Given that faster hydrodesulfurization is observed in the presence of *o*-propylaniline, it is concluded as in previous cases, that quinoline decreased the hydrodesulfurization rates of dibenzothiophene mainly due to blocking of active hydrodesulfurization sites.

Table 11. Apparent activation energies (E_{app}) [kJ/mol] determined from the hydrodenitrogenation (HDN) of *o*-propylaniline (OPA) and quinoline (Q) and the hydrodesulfurization (HDS) of dibenzothiophene (DBT).

Catalyst	E_{app} HDN [kJ/mol]				E_{app} HDS [kJ/mol]	
	OPA ^a	Q ^b	OPA-DBT ^c	Q-DBT ^d	DBT-OPA ^e	DBT-Q ^f
WMoNi-a	130 ± 6	90 ± 4	141 ± 7	100 ± 5	88 ± 4	71 ± 3
WMoNi-aHT	159 ± 7	98 ± 4	160 ± 8	107 ± 5	108 ± 5	88 ± 4
WMoNi-b	155 ± 7	96 ± 4	160 ± 8	108 ± 5	86 ± 4	72 ± 3
WMoNi-bHT	143 ± 7	146 ± 7	148 ± 7	134 ± 6	78 ± 3	85 ± 4
WMoNi-s	103 ± 5	45 ± 2	139 ± 6	43 ± 2	92 ± 4	71 ± 3
WMoNi-sHT	138 ± 6	89 ± 8	175 ± 8	74 ± 3	102 ± 5	89 ± 4

^a HDN of *o*-propylaniline in the absence of dibenzothiophene.

^b HDN of quinoline in the absence of dibenzothiophene.

^c HDN of *o*-propylaniline in the presence of dibenzothiophene.

^d HDN of quinoline in the presence of dibenzothiophene.

^e HDS of dibenzothiophene in the presence of *o*-propylaniline.

^f HDS of dibenzothiophene in the presence of quinoline.

3.4. Empirical correlation of physicochemical properties and catalytic performance

The parameters taken into account as independent variables were bulk and near surface metal composition determined by elemental analysis and XPS, respectively, surface area (BET analysis), concentration of adsorbed nitric oxide (NO) as well as slab length and stacking degree of Mo(W)S₂ (TEM analysis). The responses or dependent variables were the reaction rate constants of *o*-propylaniline, quinoline, and dibenzothiophene conversion.

Table 12. Scaled values of the physicochemical properties of the sulfide catalysts.

Catalyst	X _W	X _{Mo}	X _{Ni}	X _{W,XPS}	X _{Mo,XPS}	X _{Ni,XPS}	Adsorbed NO	Slab length	Stacking degree	Surface area
WMoNi-a	1.00	0.00	0.50	0.00	0.00	0.81	0.47	0.00	0.00	0.00
WMoNi-aHT	0.15	1.00	0.50	0.08	1.00	0.51	0.26	0.00	0.28	0.31
WMoNi-b	0.80	0.53	0.08	0.63	0.30	0.57	0.73	0.10	0.22	0.18
WMoNi-bHT	0.80	0.65	0.00	1.00	0.59	0.40	0.00	1.00	1.00	0.68
WMoNi-s	0.55	0.76	0.17	0.17	0.15	0.73	0.97	0.08	0.06	0.18
WMoNi-sHT	0.00	0.82	1.00	0.17	0.00	0.77	1.00	0.13	0.28	1.00

The empirical Equation 1 was proposed to correlate dependent and independent variables, where $f_j(i)$ is the predicted rate constant of the reaction j , i.e., hydrodenitrogenation of *o*-propylaniline in the absence and the presence of dibenzothiophene, hydrodenitrogenation of quinoline in the absence and the presence of dibenzothiophene, and hydrodesulfurization of dibenzothiophene in the presence of *o*-propylaniline or quinoline; n_i is the weighting factor of the parameter i ; and x_i is the scaled value of the parameter i . The scaled values were obtained according to Equation 2. Therefore, the values of x_i were comprised between 0 and 1. The scaled values of the properties are shown in Table 12.

Equation 1. Correlation of dependent and independent variables where $f_j(i)$ is the predicted rate constant of the reaction j , n_i is the weighting factor of the parameter i ; and x_i is the scaled value of the parameter i .

$$f_j(i) = \sum n_i x_i$$

Equation 2. Scaling of the values x_i where V_{max} , V_{min} , and V_i are the maximum value of the parameter i , the minimum value of the parameter i , and the value of the parameter for a specific catalyst, respectively.

$$x_i = \frac{V_i - V_{min}}{V_{max} - V_{min}}$$

Following this approach, Equation 3 predicts the rate constant of a reaction on a given catalyst. One can consider each catalyst as a set of parameters, which, multiplied by the corresponding

set of weighting factors, determine the magnitude of the responses (reaction rate constant). Hence, a system of six linear equations of the form shown in (III) can be created for each reaction (one equation per catalyst).

Equation 3. Predicted reaction rate $f_j(i)$ with the subscriptions of the weighting factors n_i and scaled parameters x_i bulk metal content (Mo , W , Ni), metal content according to XPS (Mo , XPS , W , XPS , Ni , XPS), concentration of adsorbed NO (NO), length and stacking degree of Mo(W)S₂ slabs (L and Stk , respectively), and surface area (S , BET).

$$f_j(i) = n_{Mo}x_{Mo} + n_Wx_W + n_{Ni}x_{Ni} + n_{Mo,XPS}x_{Mo,XPS} + n_{W,XPS}x_{W,XPS} \\ + n_{Ni,XPS}x_{Ni,XPS} + n_{NO}x_{NO} + n_Lx_L + n_{Stk}x_{Stk} + n_{S,BET}x_{S,BET}$$

Preliminary fitting showed that content of nickel in the bulk (x_{Ni}), content of molybdenum ($x_{Mo, XPS}$) and tungsten ($x_{W, XPS}$) near the surface (XPS), as well as the stacking degree of the Mo(W)S₂ slabs (Stk) are parameters with negligible influence on the fitted rates, i.e., the corresponding weighting factors are rather small. Thus, the empirical equations used to correlate the physicochemical parameters of the catalysts with their activity were simplified to Equation 4.

The weighting parameters n_i that fit the empirical model with the experimental data are listed in the Appendix Tables A38-A40. The values of the fitted rates constants are compiled in the Tables A41-43 of the Appendix, while the contributions to the different rate constants of each parameter are shown in the Tables A44-46 of the Appendix. The parity plots, i.e., correlation between experimental rate constants and rate constants predicted by the model, are shown in the Appendix Figure A91. Excellent linear correlations were observed in all cases.

Equation 4. Simplified correlation of the physicochemical parameters and the activity with the subscriptions of the weighting factors n_i and scaled parameters x_i bulk metal content (Mo , W), metal content according to XPS (Ni , XPS), concentration of adsorbed NO (NO), length of Mo(W)S₂ slabs (L), and surface area (S , BET).

$$f_j(i) = n_{Mo}x_{Mo} + n_Wx_W + n_{Ni,XPS}x_{Ni,XPS} + n_{NO}x_{NO} + n_Lx_L + n_{S,BET}x_{S,BET}$$

The magnitudes of the weighting parameters reflect the impact of the parameters on the activity, whereas their sign indicates whether the impact is negative or positive. Hence, content of nickel near the surface, bulk molybdenum content, and length of the Mo(W)S₂ slabs have a negative influence, whereas tungsten bulk content, concentration of adsorbed NO, and surface area have a positive effect on the activity.

3.5. Structure activity correlations

The active sites in Mo(W)S₂ are coordinatively unsaturated sites (CUS) and acidic sulfhydryl (SH) groups located on the (10 $\bar{1}$ 0) and ($\bar{1}$ 010) surface of the crystals, i.e., at the edges of the slab terminated formally by metal cations or sulfur. coordinatively unsaturated sites and SH groups catalyze hydrogenolytic S-C bond cleavage after coordination of the hydrocarbon via sulfur atom on the coordinatively unsaturated sites.^{6, 15} SH groups are involved in hydrogenolytic and hydrogenation pathways as H-delivering sites. Coordinatively unsaturated sites, however, are not directly related with the hydrogenation of aromatic compounds, which have led to concluding that two kinds of active sites exist for hydrogenation and defunctionalization.¹⁶¹⁻¹⁶² The hydrogenation sites have been associated to the top most layer of a Mo(W)S₂ particle,^{98, 137} which leads to even stronger effects of the morphology of Mo(W)S₂ on hydrogenation than on defunctionalization.

Promoted sites are created by substitution of molybdenum or tungsten cations by nickel(II) cations at the edges of Mo(W)S₂.^{6, 15, 127, 163} This substitution leads to optimum metal-sulfur bond strength resulting in higher conversion rates of S-containing molecules due to easier C-S bond cleavage.^{112, 125} Moreover, promotion of nickel(II) cations increases the concentration SH groups at the surface active for hydrogenation.¹²⁷ Based on previous information of the relation between the presence of nickel and the degree of unsaturation and concentration of SH groups, the concentration of nickel at the edges is considered to be the most important parameter governing the activity of sulfide catalysts.^{127, 158, 164-166}

However, the agglomeration of Mo(W)S₂ crystals (associated to the absence of a support) and the presence of segregated nickel sulfides lead to cases, where the promoter effect of nickel is overcompensated by low concentrations of available Mo(W)S₂ edges.⁶⁵ As there is not a simple and direct correlation between one physicochemical property and the performances of the catalysts, it is concluded that in the series of catalysts in this study, there are complex dependencies of activity on features of the catalyst structure and molecular structure of the reactant.

At this point two levels of structure for unsupported sulfides have to be distinguished. The primary structure is defined by the morphology of the Mo(W)S₂ particles, that is, slab length, stacking degree and concentration of promoting nickel(II) cations at the edges. The secondary structure is given by the arrangement of those primary Mo(W)S₂ crystals and is reflected by surface area and NO uptake (as it does not differentiate among Mo(W)S₂ and NiS_x). The secondary structure determines the total amount of active edges exposed during reaction, whereas the primary structure (and the composition of the slabs) will determine the intrinsic properties of such edges. In the following it is discussed how the measured properties reflect

the differences of the two levels of structure of the catalysts and their activity in hydrodenitrogenation and hydrodesulfurization.

3.5.1. Implications of the empirical modeling

The results of the empirical analysis confirm that bulk molybdenum (x_{Mo}) and tungsten (x_W) content, nickel content near the surface ($x_{Ni,XPS}$), concentration of adsorbed NO (NO), length of Mo(W)S₂ slabs (L), and BET surface area (S_{BET}) are the factors that correlate the activity of all catalysts. The sign of weighting factors shown in Table 13 indicate that the content of nickel near the surface ($x_{Ni,XPS}$), bulk Mo content (x_{Mo}), and length of the Mo(W)S₂ slabs (L) have a negative influence on activity, whereas bulk content of tungsten (x_W), concentration of adsorbed NO (NO), and surface area (S_{BET}) have a positive influence.

Table 13. Weighting factors^a (n_i) [mmol/(h·g_{cat})] and respective contributions^b (in brackets, [%]) of relevant physicochemical properties of the following reactions at 330 °C: hydrodenitrogenation (HDN) of *o*-propylaniline (OPA) and quinoline (Q) in the absence of dibenzothiophene; hydrodenitrogenation (HDN-HDS) of *o*-propylaniline (OPA) and quinoline (Q) in the presence of dibenzothiophene (DBT); hydrodesulfurization (HDS) of dibenzothiophene (DBT) in the presence of *o*-propylaniline (OPA) or quinoline (Q).

Physicochemical property	HDN		HDN-HDS		HDS	
	OPA	Q	OPA-DBT	Q-DBT	DBT-OPA	DBT-Q
x_W	3.1 (8.4)	1.9 (19.3)	5.3 (9.0)	3.2 (23.6)	2.0 (12.5)	3.2 (22.6)
x_{Mo}	-1.0 (1.0)	-0.1 (0.0)	-2.2 (1.5)	-0.2 (0.1)	-0.4 (0.5)	-0.2 (0.1)
$x_{Ni, XPS}$	-2.9 (7.2)	-1.3 (9.4)	-4.7 (6.9)	-1.9 (8.8)	-1.6 (7.8)	-2.9 (19.1)
Adsorbed NO	1.1 (1.0)	0.1 (0.1)	1.7 (0.9)	0.3 (0.3)	1.4 (5.9)	0.5 (0.6)
Slab length	-5.9 (30.7)	-2.9 (43.6)	-9.4 (27.7)	-4.4 (45.3)	-2.9 (27.2)	-3.8 (31.7)
Surface area	7.7 (51.7)	2.3 (27.5)	13.1 (54.1)	3.0 (21.9)	3.8 (46.1)	3.4 (25.9)

^a The magnitudes of the weighting factors reflect the impact of the variable on the activities of the catalysts, whereas the sign indicates whether the impact was positive or negative.

^b The contributions represent the absolute effect of the parameter on the activity of the catalysts.

High concentration of nickel at the surface implies low concentration of promoted Mo(W)S₂ because slow rates of nickel incorporation into mixed phases during sulfidation lead to high proportion of segregated monometallic nickel sulfides.⁶⁵ Hence, higher concentrations of nickel at the surface correspond to lower activity. Increasing average length of the Mo(W)S₂ slabs decreases the concentration of active sites because these sites are located at the edges. Bulk molybdenum content has a small but negative influence probably because Ni-MoS₂ has lower hydrogenation functionality than Ni-WS₂.^{103, 167-168} In line with this explanation, high bulk tungsten content has a positive influence on activity.⁶⁸ The concentration of adsorbed NO has a positive effect because it reflects the density of adsorption sites in the materials, although it does not differentiate active sites from not active sites (Mo(W)S₂ and nickel sulfides,

respectively).¹⁶⁶ On the same line of thoughts, large surface areas increase the possibility of having the active surface of the crystals exposed to the reactants. Temperature has little effect on the apparent impact of the studied parameters (compare signs and magnitudes of weighting factors in Tables A38-40 in the Appendix) because all parameters taken into account are related to concentration of available active sites. Therefore, they are lumped in the pre-exponential factor of the Arrhenius equation.

3.5.2. *Hydrotreating activity in the presence of o-propylaniline*

Note that WMoNi-sHT has an outstanding activity for the hydrodenitrogenation of *o*-propylaniline (with and without dibenzothiophene present) and the hydrodesulfurization of dibenzothiophene in the presence of *o*-propylaniline. This is attributed to high concentration of accessible active edges as reflected by the fact that this material combines the highest specific surface area and concentration of adsorbed NO among the studied catalysts. Both parameters do not have a direct correlation with the concentration of the active sites because of the anisotropy of Mo(W)S₂ and of the adsorption of NO on sites active and inactive for hydrotreating (Mo(W)S₂ and nickel sulfides, respectively).¹⁶⁹ However, large surface areas and high concentration of sites adsorbing NO reflect secondary structures that increase the possibility of having the active surface of the crystals exposed to the reactants. Thus, both parameters are indicators of high hydrotreating activity in the presence of *o*-propylaniline.

Increasing the possibility of exposing active edges to the reactant is an important parameter if, as concluded above, those edges have sufficient nickel(II) cations incorporated at the edges (which is a feature of the primary structure). However, as the morphology of the catalyst varies, the promotion degree varies as well but without an apparent correlation. While the results of this work do not allow for quantifying the concentration of Ni-decorated sites, it has been previously noted that an increasing proportion of nickel in segregated nickel sulfides leads to increasing differences between the bulk nickel concentration and that estimated at the surface by XPS.^{43, 65} Thus, in accordance with the nickel molar fractions (x_{Ni}) reported in Table 7, the decoration of nickel follows the qualitative trend



In the latter three materials the concentration of nickel at the surface is outstandingly low. This suggests that segregated nickel sulfides, inactive for hydrotreating,^{1, 166} are not present at the surface to a large extent, leading to relatively large concentrations of exposed active sites. Thus, the higher hydrodenitrogenation and hydrodesulfurization activity of WMoNi-b, WMoNi-aHT, and WMoNi-bHT was caused by lower concentration of segregated nickel sulfides at the surface, which compensated the disadvantageous structural features of these

materials. In contrast, WMoNi-a and WMoNi-s showed the lowest activity for the hydrodenitrogenation of *o*-propylaniline because they had low surface area and high proportions of segregated nickel sulfides at the surface.

3.5.3. *Hydrotreating activity in the presence of quinoline*

The ranking of rate constants in the presence of quinoline differed from that in the presence of *o*-propylaniline. Thus, the hydrodenitrogenation of polyaromatic compounds, like quinoline, poses different requirements to the active phase than anilines. For instance, WMoNi-bHT, which has the largest Mo(W)S₂ slabs, is one of the less active catalysts for hydrodenitrogenation of quinoline, although it is one of the most active catalysts for hydrodenitrogenation of *o*-propylaniline. Thus, small length of Mo(W)S₂ slabs becomes very important for the conversion of quinoline. This is probably caused by short slabs having a high proportion of corners, which have been hypothesized as preferred hydrogenation sites for bulky aromatic compounds.¹⁷⁰ Thus, for hydrodenitrogenation of quinoline, the accessible edges must have a favorable primary structure, i.e., a defined slab length and edge composition.

In line with this conclusion, note that WMoNi-sHT is less active for the hydrodenitrogenation of quinoline than of *o*-propylaniline, despite its high specific surface area and NO uptake. This is attributed to its low tungsten content because Ni-WS₂ has higher hydrogenation activity than Ni-MoS₂.^{103, 167-168} The role of high tungsten content on the activity of the catalysts being evident in the presence of quinoline implies that the strong hydrogenation functionality of Ni-WS₂ becomes more important with increasing complexity of the aromatic reactant. The catalyst WMoNi-b has high content of tungsten and average nickel content at the surface and slab length. Thus, the primary structure of this catalyst combines the right features to achieve the highest activity for the conversion of quinoline.

3.5.4. Hydrodesulfurization activity in the presence of *o*-propylaniline and quinoline

WMoNi-sHT and WMoNi-b are the most active catalyst in the hydrodesulfurization of dibenzothiophene in the presence of *o*-propylaniline and are the most active for the hydrodenitrogenation of *o*-propylaniline as well. This indicates that secondary structure (surface area, density of sites for NO adsorption) and low nickel content at the surface are indicators of high accessibility of Ni-Mo(W)-S sites active for hydrodesulfurization of dibenzothiophene in the presence of *o*-propylaniline. WMoNi-bHT has the lowest hydrodesulfurization activity (which makes the difference between the hydrodenitrogenation of *o*-propylaniline and the hydrodesulfurization of dibenzothiophene due to its low concentration of active sites reflected in its low NO uptake).

In the presence of quinoline, the hydrodesulfurization of dibenzothiophene proceeds faster on WMoNi-b, WMoNi-bHT, and WMoNi-aHT, which is correlated with the low concentrations of nickel at the surface. This, in turn, implies that, in the presence of bulky aromatic N-containing compounds, the strong hydrogenolytic functionality provided by nickel sites compensates the low overall site availability.

3.5.5. Comparison of supported and unsupported bimetallic and trimetallic sulfides

Rate constants determined over the series of trimetallic sulfide catalysts studied in this work are compared in Table 14 with those previously obtained over other unsupported and Al₂O₃-supported catalysts. The rate constants for the hydrodenitrogenation of *o*-propylaniline over the trimetallic catalysts studied in this work varied between $2.7 \cdot 10^{-3}$ mol/(h·g_{cat}) and $3.9 \cdot 10^{-2}$ mol/(h·g_{cat}) (WMoNi-s and WMoNi-sHT, respectively). However, all these catalysts were more active than unsupported catalysts (Ni-Mo, Ni-W, and Ni-Mo-W) previously reported.⁴³ Interestingly, most of the unsupported catalysts of this work were also more active than Al₂O₃-supported Ni-MoS₂ catalyst ($5.1 \cdot 10^{-3}$ mol/(h·g_{cat})) previously reported.³⁹

Most of the rate constants for the hydrodenitrogenation of quinoline on the unsupported catalysts of this work (from $3.0 \cdot 10^{-4}$ mol/(h·g_{cat}) to $3.4 \cdot 10^{-3}$ mol/(h·g_{cat})) were lower than the rate on Ni-MoS₂/Al₂O₃ ($5.3 \cdot 10^{-3}$ mol/(h·g_{cat})).¹⁵⁸ The exception therein is WMoNi-b, which exhibited activity ($5.6 \cdot 10^{-3}$ mol/(h·g_{cat})) comparable to the supported catalyst. The wide range of activity observed on unsupported catalysts shows the strong impact of the precursor (varied by synthesis methods) on the activity and properties of the sulfides.

Table 14. First order rate constants k [mol/(h·g_{cat})] for the hydrodenitrogenation of *o*-propylaniline (OPA) and quinoline (Q) at 370 °C on the unsupported catalysts reported in this work and on other unsupported and supported catalysts previously reported.

Catalyst	OPA k [mol/(h·g _{cat})]	Q k [mol/(h·g _{cat})]
WMoNi-a	$5.68 \cdot 10^{-3}$	$3.17 \cdot 10^{-3}$
WMoNi-aHT	$1.21 \cdot 10^{-2}$	$3.42 \cdot 10^{-3}$
WMoNi-b	$2.65 \cdot 10^{-2}$	$5.58 \cdot 10^{-3}$
WMoNi-bHT	$1.26 \cdot 10^{-2}$	$2.13 \cdot 10^{-3}$
WMoNi-s	$2.76 \cdot 10^{-3}$	$3.04 \cdot 10^{-3}$
WMoNi-sHT	$3.91 \cdot 10^{-2}$	$2.07 \cdot 10^{-3}$
Ni-MoS ₂ ^a	$1.99 \cdot 10^{-3}$	-
Ni-Mo _x W _{1-x} S ₂ ^a	$2.15 \cdot 10^{-3}$	-
Ni-WS ₂ ^a	$1.16 \cdot 10^{-3}$	-
Ni-MoS ₂ /Al ₂ O ₃ ^{b,c}	$5.10 \cdot 10^{-3}$	$5.28 \cdot 10^{-3}$

Rate constants calculated from the data reported in literature.^{39, 43, 158}

The rate constants listed in Table 14 also show that the activity of unsupported Ni-Mo-W catalyst is higher than that of bimetallic (Ni-Mo, Ni-W) catalysts. This observation, however, is not common because the activity of the sulfides strongly depends on their structure and their cationic distribution.^{65, 171} Differences in intrinsic activity between bimetallic sulfides (NiMo, NiW) and trimetallic sulfides are still to be elucidated. Finally, the comparison shown in Table 14 indicates that the activity of the unsupported trimetallic sulfides is comparable (hydrodenitrogenation of quinoline) or much higher (hydrodenitrogenation of *o*-propylaniline) than that of the archetypical Al₂O₃-supported Ni-MoS₂. This highlights the importance of studying unsupported multimetallic sulfides more in depth in order to optimize further their preparation procedures.

4. Conclusion

Different catalyst precursors lead to sulfide catalysts with varying physicochemical properties whereby the concentration of Ni-containing sites, their primary structure and the accessibility are the main parameters determining hydrotreating activity. However, the activity of the ternary sulfides for the conversion of *o*-propylaniline, quinoline, and dibenzothiophene showed a complex dependence on these parameters. Overall, high surface area, short Mo(W)S₂ slabs, high tungsten content, and low nickel content at the surface are concluded to lead to high hydrotreating activity. Surface area and NO uptake are related to the concentration of exposed active edges, whereas the size of Mo(W)S₂ crystals and the content of tungsten and nickel reflect the intrinsic activity of those edges. That is, homogeneous distribution of nickel across the catalyst volume is associated to nickel decoration, whereas the strong hydrogenation functionality of WS₂ is required to convert polyaromatic compounds.

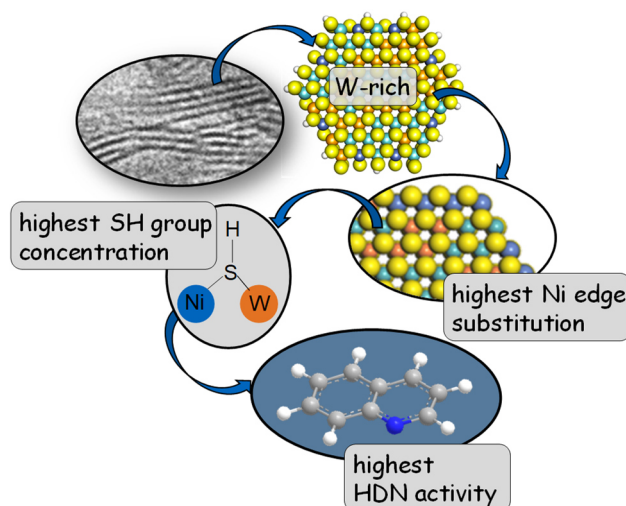
In general, if enough nickel decoration of Mo(W)S₂ edges exists, the availability of exposed edges dominates the activity for the conversion of *o*-propylaniline and dibenzothiophene in presence of *o*-propylaniline. However, for the conversion of quinoline and dibenzothiophene in the presence of quinoline, the most active edges are those, which are short and contain tungsten and high concentrations of nickel(II) cations at the edges.

In this work, WMoNi-b (mainly in the presence of quinoline) and WMoNi-sHT (mainly in the presence of *o*-propylaniline) showed the highest activities for hydrodenitrogenation and hydrodesulfurization. Whereas WMoNi-sHT is concluded to have high density of active edges exposed (large surface area and NO uptake), WMoNi-b is concluded to have the most active edges for hydrogenation (high tungsten content, and best compromise among incorporated nickel(II) cations and slab length). In contrast, WMoNi-a and WMoNi-s ranked low in most of the reactions due to the disadvantageous combination of low concentration of edges and low intrinsic activity indicated by low surface area, low content of tungsten and large content of nickel near the surface.

Chapter 3

UNCOVERING ACTIVE SITES –

*Enhancing the Activity of trimetallic Ni-Mo-W
Sulfides for Quinoline Hydrodenitrogenation*



Abstract

Tailored acid treatment allowed the selective removal of excess nickel sulfides from bi- and trimetallic Mo(W)S₂ sulfides. Reaction path analysis of quinoline hydrodenitrogenation on the acid-treated samples suggests a common nature of active sites among these catalysts, unaffected by the atomic composition of the Mo(W)S₂ phase. The hydrodenitrogenation of quinoline proceeds primarily via full hydrogenation of both rings followed by the removal of nitrogen. The rate-determining step along this dominating route, named as the hydrogenation route, appears to shift to a later addition of hydrogen as the concentration of active site increases on the sulfide surface, which is reflected by an increasing reaction order in hydrogen. While the rate of the hydrogenation route was independent of the quinoline concentration, that of ring opening (the minor route) depended on the quinoline concentration. This difference is attributed to different adsorption modes of the reactant along the two pathways, i.e., σ -adsorption for ring opening and π -adsorption for hydrogenation. The rate of ring opening was independent of the surface concentration of hydrogen, suggesting that hydrogen is not involved in the rate-determining step of the C-N bond cleavage in 1,2,3,4-tetrahydroquinoline. We infer that hydrogenation and ring opening require two types of active sites that are present at nearly identical proportions on a homologous series of samples as those prepared in this work. The correlation of hydrodenitrogenation rates with H₂-D₂ scrambling rates allows us to conclude that the Mo(W)S₂ phase composition governs the incorporation of nickel(II) cations into the slab edge leading to different nickel substitution degrees and, in consequence, to different concentrations of active sites. The SH concentration, indirectly probed by H₂-D₂ scrambling, was highest in a W-rich ternary sulfide phase leading to 5-10 times higher specific hydrodenitrogenation activity than bimetallic (Ni-Mo and Ni-W) formulations.

1. Introduction

Hydrotreating is a key process in the production of clean transportation fuels. Molybdenum disulfide (MoS_2) or tungsten disulfide (WS_2) supported on $\gamma\text{-Al}_2\text{O}_3$ and containing nickel or cobalt are mostly used as catalysts and are, thus, widely studied.^{6, 15, 17} However, heavier feedstocks require higher activity and stability of the catalysts than currently accessible.^{15, 21-22, 105} In this context, the outstanding performance of bulk trimetallic Ni-Mo-W sulfide catalysts has triggered extensive efforts in characterizing the active site structure and in further improving catalytic activity.^{10, 43, 64, 121, 130, 137, 140}

The catalytic activity of bulk sulfides depends on a combination of properties. For example, the structural anisotropy of MoS_2 and WS_2 causes the activity to depend on morphology (e.g., curvature and stacking of layers) of the sulfide material.^{10, 137, 172} Models regarding the location and the chemical impact of the catalyst components have been proposed, among which the so-called 'Ni(Co)-Mo-S' model is most widely accepted.^{113-114, 173} This model proposes that active sites are located at the edges of the hexagonal Mo(W)S_2 slab. It has been convincingly shown that nickel or cobalt cations are incorporated at the edge of the sulfide slabs substituting molybdenum or tungsten cations.^{112-115, 119} Using X-ray absorption and Raman spectroscopy, Hein et al. showed that intralayer mixing of molybdenum and tungsten cations in bulk trimetallic (NiMoW) sulfides leads to higher concentrations of edge-incorporated nickel cations compared to bimetallic (NiMo and NiW) sulfides.⁴³ In general, substitution of nickel or cobalt cations at the sulfide slab edge not only weakens the Mo(W)-S bond strength¹¹⁹ but also increases the reducibility of the Mo(W)S_2 phase.¹⁷⁴ As a result, a higher fraction of coordinatively unsaturated metal cations, which are Lewis acidic, becomes accessible on the surface of Ni-substituted Mo(W)S_2 compared to pure Mo(W)S_2 .^{8, 109, 125, 175}

As dissociative adsorption of H_2 or H_2S on a site pair consisting of the basic sulfide anion and the Lewis-acidic metal cation generates sulfhydryl (SH) groups,^{127, 176-177} significantly higher concentrations of SH groups are formed on Ni-substituted Mo(W)S_2 catalysts than pure Mo(W)S_2 , in the presence of H_2 and/or H_2S .^{127, 178} In this connection, it is worth noting that we recently identified a direct relation between the Lewis acidic and the Brønsted acidic sites for a number of transition metal sulfides supported on $\gamma\text{-Al}_2\text{O}_3$, demonstrating the interconversion of the two types of surface entities under reaction conditions.¹⁷⁸

Unsupported multimetallic sulfides usually consist of several intralayer-mixed and segregated phases.^{10, 43} The relatively high overall concentration of nickel cations, required to maximize incorporation of nickel in the sulfide slabs, leads inevitably to the presence of a variety of separate nickel sulfide phases, including materials ranging in stoichiometric composition from NiS to Ni_9S_8 .^{10, 15, 106} The presence of these nickel sulfides, which themselves are hardly active in hydrotreating reactions, in the vicinity of the Ni-containing Mo(W)S_2 phase partially limits the

accessibility of active sites.⁸⁸ Thus, the first aim of our work was to explore the selective removal of nickel sulfides from Ni-containing bi- and trimetallic sulfides with different molybdenum to tungsten (Mo/W) ratios. This reduced the structural complexity at the local active site and enabled a more reliable identification of catalytically active sites.

The hydrodenitrogenation of quinoline was chosen as the target reaction because the trimetallic sulfides are expected to be highly active especially for hydrogenation associated with hydrodenitrogenation of the heavy crude oil fractions that contain more refractory nitrogen compounds.^{29-30, 179} Although it is known that the removal of nitrogen often requires pre-saturation of the aromatic compound prior to C-N bond cleavage,²⁹⁻³⁰ the detailed kinetic aspects of the hydrogenative nitrogen removal routes remain underexplored on unsupported sulfide catalysts. In this work, we focused on studying the influence of the sulfide phase composition on the catalytic rates for the key steps in the quinoline reaction network.

2. Experimental

2.1. Synthesis of the oxide precursor

All oxide precursors were synthesized via a pH controlled co-precipitation method.⁵¹ Ammonium heptamolybdate tetrahydrate ((NH₄)₆(Mo₇O₂₄)·4H₂O, Merck, ≥ 99.0 %) and ammonium metatungstate hydrate ((NH₄)₆H₂W₁₂O₄₀·nH₂O, Sigma-Aldrich, ≥ 99.0 %) were used as the molybdenum and the tungsten source, respectively. For the synthesis of the trimetallic oxide precursors both ammonium salts were dissolved in doubly distilled water (120 mL) in the desired ratio of molybdenum to tungsten, whereas in the case of the bimetallic oxide precursors the respective ammonium salt was dissolved in doubly distilled water (120 mL). After heating the aqueous solution to 90 °C, the pH value was adjusted to 9.5 using aqueous ammonia (28-30 wt %, Sigma-Aldrich).

Under continuous stirring, 1 mL pre-heated aqueous nickel(II) nitrate (Ni(NO₃)₂·6H₂O, Sigma-Aldrich, ≥ 98.5 %) solution was added dropwise. The pH value was set to 9.5 using aqueous ammonia. Thereafter, the remaining nickel(II) nitrate solution (6.5 mL) was added dropwise and the oxide precursor precipitated. After stirring for 30 minutes at 90 °C and hot filtration, the obtained solid was suspended in an aqueous solution of maleic acid (0.05 M, Fluka, ≥ 98.0 %) and kept at 70 °C for 30 minutes. Then, the precipitate was filtered off, dried in vacuum overnight and in synthetic air at 120 °C for 12 hours.

2.2. Synthesis of the sulfide catalysts

Liquid-phase sulfidation of oxide precursors, diluted with silicon carbide (SiC), was performed in a trickle bed flow-reactor. Liquid and gas feeds were introduced using a HPLC pump (Shimadzu LC-20AD) and high-pressure mass flow controllers (Bronkhorst), respectively. First, each oxide precursor was dried in the flow reactor at 120 °C under constant N₂ flow (40 mL/min, 14 hours). Dimethyl disulfide (C₂H₆S₂, Sigma-Aldrich, ≥ 99.0 %) was used as the sulfiding agent and diluted with *n*-hexadecane (*n*-C₁₆H₃₄, Merck, ≥ 99.0 %). The liquid-phase sulfidation was carried out at 20 bar total pressure. Together with a stepwise temperature increase from 120 to 250 °C (1 °C/min, 2 hours dwell) and from 250 to 350 °C (1 °C/min, 2 hours dwell) the sulfur content of the liquid feed was increased from 4 wt. %, over 8 wt. % to 12 wt. %. The gas and liquid flows were continuously adjusted at each sulfidation step to keep a constant H₂/H₂S ratio of 5. Accordingly, the N₂ flow was adapted to ensure a constant overall gas flow. Figure 27 illustrates the sulfidation procedure.

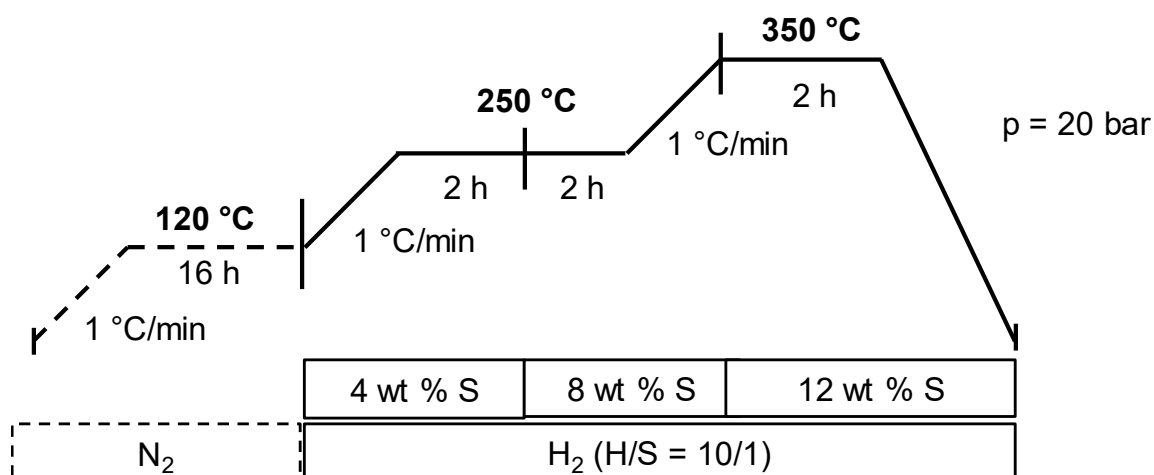


Figure 27. Liquid-phase sulfidation protocol.

The resulting sulfide materials are denoted as NiMoS, NiWS, NiMo₍₂₎W₍₁₎S, NiMo₍₁₎W₍₁₎S, and NiMo₍₁₎W₍₂₎S. The numbers in brackets in the names of the trimetallic sulfides indicate the ratio of molybdenum to tungsten.

2.3. Selective removal of nickel sulfides

Each sulfide material synthesized as described above was suspended in concentrated hydrochloric acid (HCl, Sigma-Aldrich, 37 wt. %).¹⁸⁰ The suspension was kept boiling for at least 2 minutes. After decanting the solution, the solids were washed three times with doubly distilled water. This procedure was repeated several times until the hydrochloric acid solution did not turn green while boiling. The sulfides were then washed five times with doubly distilled water and dried in a desiccator. The sulfides after the HCl treatment were denoted as NiMoS-L, NiWS-L, NiMo₍₂₎W₍₁₎S-L, NiMo₍₁₎W₍₁₎S-L, and NiMo₍₁₎W₍₂₎S-L.

The complete removal of chlorine from the sulfides was verified by a silver nitrate test. Therefore, a small amount (25 mg) of each HCl-treated sulfide was dissolved in 15 mL concentrated nitric acid (HNO₃, Sigma-Aldrich, 70 wt. %, ≥ 99.999 %). A few drops of a silver(I) nitrate solution (AgNO₃, 1 M, Sigma-Aldrich) were added to this solution and the absence of precipitation (AgCl, $K_{sp} = 1.8 \cdot 10^{-10}$ at room temperature) indicated that virtually no chlorine remained in the sulfides.¹⁸¹

2.4. Characterization

The concentrations of nickel, molybdenum, and tungsten, respectively, were determined photometrically, whereas the contents of hydrogen, carbon, nitrogen, and sulfur were analyzed using an automated element analyzer instrument (Vario EL CHN Analyzer, ELEMENTAR) at the microanalytical laboratory of the Technische Universität München.

X-ray photoelectron spectroscopy (XPS) measurements were conducted using a Phi Quantera Scanning X-ray Microprobe instrument at the Chevron Technology Center. This instrument was equipped with a hemispherical energy analyzer with multichannel (1.1 eV energy resolution). Monochromatic Al K_{α} (1486.7 eV) X-rays were used as the ionization source. Multilayers of powdered parent and HCl-treated sulfide catalysts completely covered a double-sticky tape. For each catalyst, five analysis areas were selected for detailed spectral characterization. At each area, a detailed spectrum was collected for C 1s, O 1s, S 2p, Ni 2p, Mo 3d, and W 4f. Total spectral accumulation time was 100 min per analysis area while irradiating with 100 W of X-ray radiation. Spectral envelopes were de-convoluted using an iterative least-square algorithm provided in Phi Multipak software.

Isotherms of adsorption and desorption of nitrogen at -196 °C were performed with an automated nitrogen adsorption analyzer Sorptomatic 1990 Series (Thermo Finnigan). Before the measurements, all samples were evacuated at 120 °C for 4 hours. BET and BJH analysis was used to determine specific surface area and pore volume of the parent and the HCl-treated sulfides.

The crystal structures of all sulfide materials were analyzed by powder X-ray diffraction. The measurements were performed in a PANAnalytix system equipped with a copper X-ray tube (copper (Cu) K_{α} radiation, 0.154 nm), a nickel K_{β} filter, and solid-state detector (X'Celerator) operated at 45 kV and 40 mA with step size of 0.017 ° and scan time of 115 seconds per step. The inorganic crystal structure database (ICSD) was used to assign the different reflections.¹⁸²

Scanning electron microscopy (SEM) was performed of the sulfide materials using a REM JEOL 5900 LV microscope. A secondary electron detector and an Everhart-Thornley detector for backscattered electrons were employed. The SEM images of the secondary electron detector were taken with an acceleration voltage of 25 kV. Before the measurements, the samples were outgassed for two days, transferred on a graphite foil and coated with gold by sputtering.

Transmission electron microscopy (TEM) was performed on a JEOL JEM 2010 instrument equipped with a LaB₆-cathode with an accelerating voltage of 120 kV. The samples were prepared by grinding a small amount of material and dispersing it ultrasonically in absolute ethanol (Merck Millipore). Subsequently, drops of this suspension were transferred on a copper

grid (200 mesh) with a lacey carbon film (Quantifoil Micro Tools) and the ethanol was evaporated at room temperature.

The continuous hydrogen (H_2) – deuterium (D_2) scrambling experiment was performed at ambient pressure in a quartz tube reactor which was placed in a ceramic oven. All used gas streams were controlled via mass flow controllers (Bronkhorst). The sulfide materials (100 mg, 250-355 μm) were placed in the quartz tube and dried in nitrogen atmosphere (10 mL/min) at 120 °C (5 °C/min, 1 hour dwell). Subsequently, the materials were re-sulfided using a mixture of 10 vol. % H_2S in H_2 (8 mL/min) and nitrogen (2 mL/min) at 300 °C (5 °C/min, 1 hour). After cooling down to 100 °C in nitrogen (10 mL/min), equimolar flows of hydrogen and deuterium (D_2) were introduced into the reactor and the formation of HD was monitored while varying the bed residence times of hydrogen and deuterium. The product gas stream was analyzed online with a mass spectrometer (Pfeiffer Vacuum DMQ 200). The signals for the masses (m/e) of 2 (H_2), 3 (HD) and 4 (D_2) were registered. The HD signal in the gas phase was calibrated using platinum supported on alumina (Pt/Al_2O_3 , 5 wt. % Pt, Sigma-Aldrich) enabling the equilibration between hydrogen and deuterium, i.e., a known composition of the equilibrated mixture of H_2 , HD, and D_2 in a ratio of approximately 1:2:1.

2.5. Kinetic measurements

The hydrotreating activity of the parent and the HCl-treated catalysts was evaluated in the hydrodenitrogenation of quinoline (C_9H_7N , Sigma-Aldrich, 98 %) in the same trickle bed flow-reactor as used for liquid-phase sulfidation. *n*-Hexadecane was used as the solvent. Moreover, dimethyl disulfide ($C_2H_6S_2$, Sigma-Aldrich, ≥ 99.0 %) was added to prevent losses of sulfur and thus, catalyst deactivation. Ethylcyclohexane (C_8H_{16} , Sigma-Aldrich, ≥ 99 %) was used as internal standard for GC analysis of the product stream. The glass-coated tubular reactor was loaded with 10-70 mg of a sulfide diluted with silicon carbide (SiC, 63–90 μm). Prior to kinetic measurements, the catalysts were re-sulfided with a liquid feed containing 4 wt. % sulfur as dimethyl disulfide and *n*-hexadecane as solvent. The applied ratio of H_2/S ratio was 5:1.

During re-sulfidation, the pressure was set at 20 bar and the temperature was 250 °C (2 °C/min, 2 hours). The hydrotreating experiments were performed at a total pressure of 50 bar. Total pressure and total gas volume flow were kept constant while varying the partial pressure of hydrogen by adjusting the flow of N_2 . The liquid feed contained 1000 ppm nitrogen as quinoline and the ratio of hydrocarbon to hydrogen was 1:300 N_{dm^3}/dm^3 . These conditions were also applied for experiments using *cis*, *trans*-decahydroquinoline ($C_9H_{17}N$, Sigma-Aldrich, 97 %) as the reactant. The apparent activation energies were determined in a temperature range from 290 to 350 °C. The reaction orders in quinoline and hydrogen on the HCl-treated catalysts were determined at 330 °C and a total pressure of 50 bar. The product stream was analyzed off-line using a gas chromatograph (HP 6890) equipped with a flame ionization detector (FID) and an Agilent DB-17 capillary column. Isomers of products and intermediates were lumped together and treated as one species. The presented data were acquired after 12 hours on stream after which catalytic activity became stable. Catalyst deactivation during the experiment was below 5 % on all tested catalysts. The carbon mass balance was closed within ± 2 %.

3. Results and Discussion

3.1. Physicochemical properties of parent and HCl-treated sulfide catalysts

The molar metal fractions of nickel (Ni), molybdenum (Mo), and tungsten (W) of the parent sulfides and those after the HCl treatment are listed in Table 15. Most of the parent sulfide materials contain a nickel molar metal fraction around 0.70. The HCl treatment removed about 70 % of nickel from the parent sulfides resulting in a nickel molar metal fraction around 0.2, except for NiWS. Accordingly, the relative molar metal fractions of molybdenum and tungsten increased from the parent to the HCl-treated sulfides although the ratio of molybdenum to tungsten hardly changed within the experimental error. NiWS is an exception, however, with only 30 % of nickel being leached from the parent sulfide. It should be noted that the post-synthetic treatment of NiWS had to be repeated more times than for the other parent materials to achieve essentially complete removal of large nickel sulfides from the surface of the sulfide (Figures 28, 29, and 30). As judged by AgNO₃ test, the leached samples did not contain any chlorine (Cl⁻) residues. Elemental analysis of HCl-containing decanted solutions showed that neither molybdenum nor tungsten was dissolved during the treatment.

Table 15. Metal molar fraction of nickel (Ni), molybdenum (Mo), and tungsten (W) of the parent sulfide materials NiMoS, NiMo₍₂₎W₍₁₎S, NiMo₍₁₎W₍₁₎S, NiMo₍₁₎W₍₂₎S, and NiWS and the corresponding sulfide materials after the HCl treatment, NiMoS-L, NiMo₍₂₎W₍₁₎S-L, NiMo₍₁₎W₍₁₎S-L, NiMo₍₁₎W₍₂₎S-L, and NiWS-L. The metal fraction of nickel, molybdenum, and tungsten in the bulk phase (b) was derived from elemental analysis whereas the surface metal fraction (s) was determined using XPS analysis.

Catalyst		Metal atomic fraction of parent sulfides			Metal atomic fraction of HCl-treated sulfide		
		Ni	Mo	W	Ni	Mo	W
NiMoS(-L)	b	0.77	0.23		0.24	0.76	
	s	0.56	0.44		0.14	0.86	
NiMo ₍₂₎ W ₍₁₎ S(-L)	b	0.71	0.19	0.10	0.20	0.54	0.26
	s	0.72	0.15	0.13	0.11	0.73	0.17
NiMo ₍₁₎ W ₍₁₎ S(-L)	b	0.69	0.16	0.15	0.20	0.39	0.41
	s	0.56	0.16	0.28	0.21	0.32	0.48
NiMo ₍₁₎ W ₍₂₎ S(-L)	b	0.67	0.11	0.21	0.21	0.26	0.52
	s	0.51	0.18	0.31	0.25	0.36	0.39
NiWS(-L)	b	0.51	-	0.49	0.37		0.63
	s	0.62	-	0.38	0.36		0.64

The results of the XPS analysis confirmed substantial removal of nickel sulfides from the surface, as seen from the decrease in the nickel fraction at the surface from each parent to the corresponding leached sulfides (Table 15). Comparing bulk and surface compositions of the

HCl-treated samples shows a reduced nickel fraction (and an increased molybdenum fraction) at the surface compared to the bulk for the two molybdenum-rich samples, NiMoS-L and NiMo₍₂₎W₍₁₎S-L. The other three sulfides showed a closer agreement between bulk and surface compositions (Table 15).

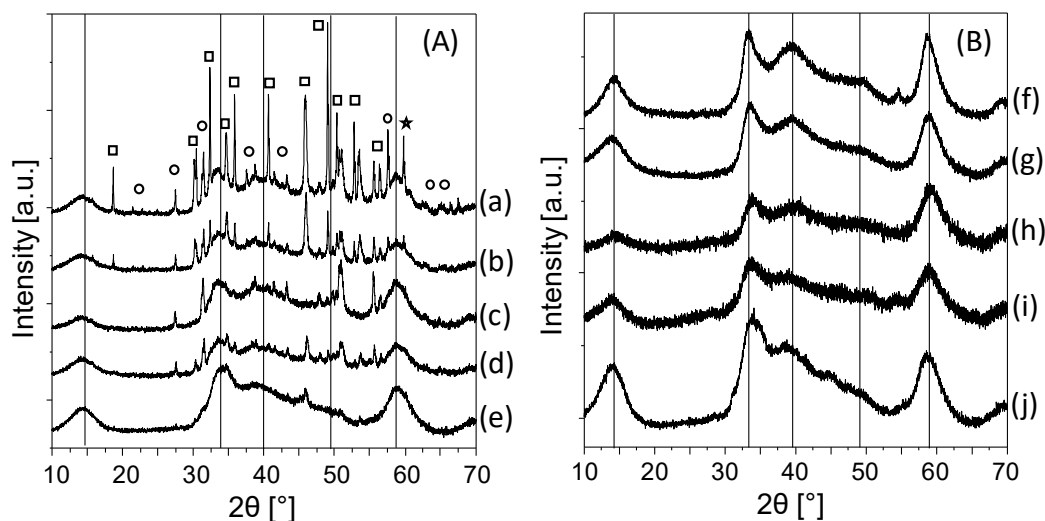


Figure 28. X-ray diffractograms of the parent sulfides (A) and the HCl-treated sulfides (B). The reflections of MoS₂ and WS₂ are indicated by vertical lines.¹³⁹ Squares (□) mark reflections assigned to Ni₃S₂ and circles (○) the one assigned to Ni₉S₈. The reflection (★) at 62° is assigned to silicon carbide (SiC, used as the diluent for sulfidation of the oxidic precursor).

In all X-ray diffractograms of the parent sulfides (Figure 28, (A)), the reflections of MoS₂, WS₂, and/or the mixed Mo(W)S₂ are present. The broad XRD reflections indicate that the Mo(W)S₂ phase is composed of small, coherently scattering domains that might also contain lattice strain and/or defects. This is also evident in the TEM images (Figure 32 and 33) in which overlapping and bending of the Mo(W)S₂ slabs are clearly visible.

For the untreated samples, sharp peaks are additionally present in all X-ray diffractograms. These reflections are assigned to crystalline nickel sulfide phases, predominantly Ni₃S₂ (ICSD # 27521) and Ni₉S₈ (ICSD # 63080). Going from a high molybdenum content to a high tungsten content, the number and the relative intensity of reflections from the nickel sulfide phases decreased. Hardly any crystalline nickel sulfide phase was detectable with NiWS. Regardless of the phase composition of parent sulfides, the HCl treatment removed all reflections assigned to these crystalline nickel sulfide phases, without affecting the reflections assigned to MoS₂ and WS₂ (Figure 28, (B)).¹³⁹

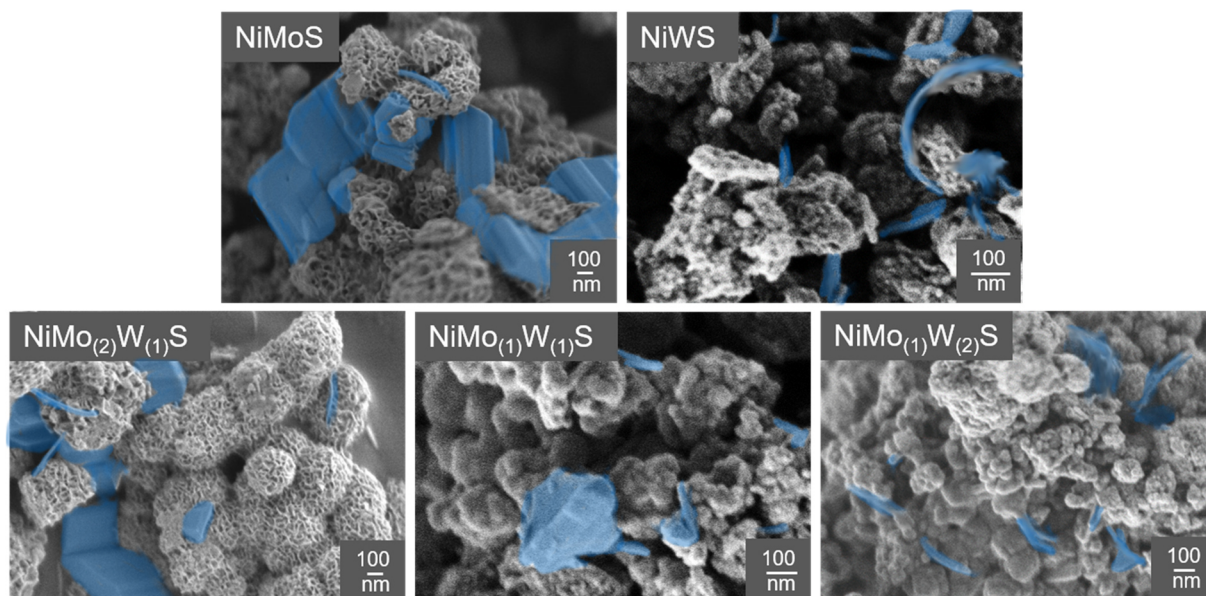


Figure 29. SEM images of the parent sulfide materials NiMoS, NiMo₂W₁S, NiMo₁W₁S, NiMo₁W₂S, and NiWS. Ni sulfide crystals are artificially colored.

The SEM images of the parent sulfides (Figure 29) confirm the presence of two very different phases in each image, i.e., rough agglomerates are observable besides smooth crystals. The agglomerates represent the Ni-containing Mo(W)S₂ phase and have an open sponge-like structure in the cases of NiMoS and NiMo₂W₁S. Increasing tungsten content leads to a more compact structure of these agglomerates. The composition of the Ni-containing Mo(W)S₂ phase additionally seems to influence the crystallization of nickel sulfides as higher contents of molybdenum also led to the formation of large nickel sulfide crystallites. In contrast, nickel sulfides formed on materials with a high content of tungsten crystallize in a thin shape. The lower amount of crystalline nickel sulfide removed by HCl from NiWS (Table 15), together with its SEM image and X-ray diffractogram, implies that a WS₂ phase retards nickel sulfide crystal growth on the Ni-containing WS₂ surface, i.e., minor presence of chunk morphologies compared to the Mo-rich samples.

The SEM images of the HCl-treated sulfides (Figure 30) confirm the removal of crystalline nickel sulfides from the Ni-containing Mo(W)S₂ surface, as neither needles nor chunks of nickel sulfides are observable. Note that the appearance of Ni-containing Mo(W)S₂ phase does not change upon the HCl treatment. The remaining nickel, on the one hand, is incorporated at the Mo(W)S₂ edges acting as promoter and on the other hand is present as crystalline nickel sulfides surrounded by Ni-containing Mo(W)S₂. Crystalline nickel sulfides completely covered by the active Mo(W)S₂ are likely to occur in these materials.⁸⁸

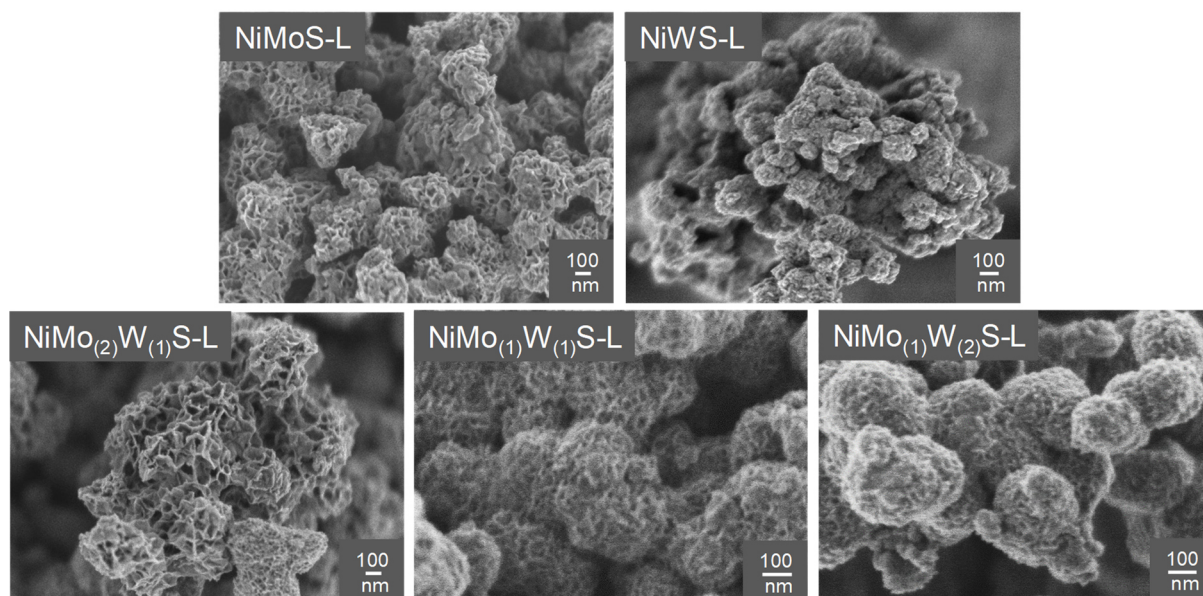


Figure 30. SEM images of the HCl-treated sulfide materials NiMoS-L, NiMo₍₂₎W₍₁₎S-L, NiMo₍₁₎W₍₁₎S-L, NiMo₍₁₎W₍₂₎S-L, and NiWS-L.

The N₂ sorption isotherms of parent and HCl-treated materials (Figure 31) are attributed to a type IV isotherm with a H3 hysteresis, characteristic of mesoporous materials.¹⁸³ The surface area and porosity of the material increased with the content of molybdenum in the sulfide (Table 16).

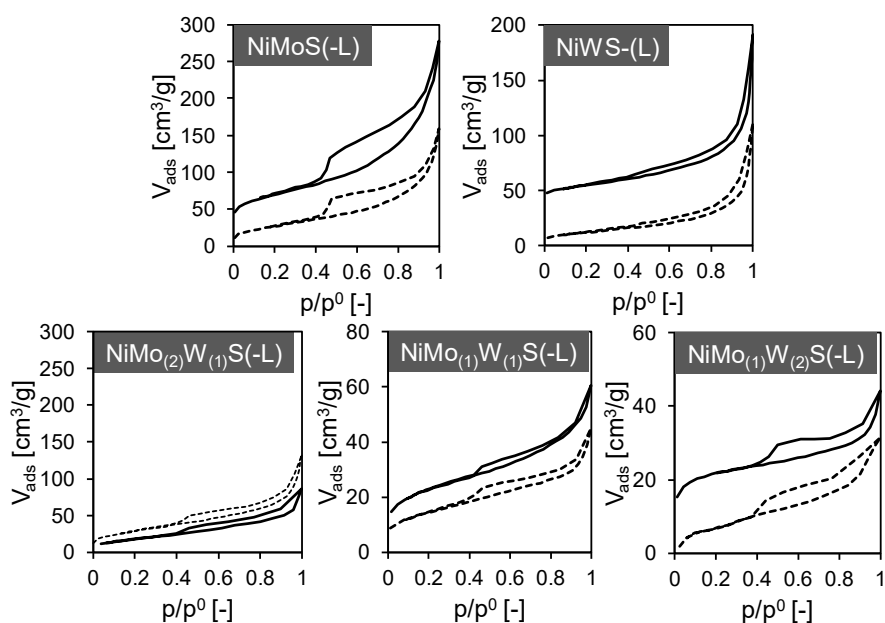


Figure 31. BET isotherms of the parent (dashed lines) and leached (solid lines) sulfide materials NiMoS(-L), NiMo₍₂₎W₍₁₎S(-L), NiMo₍₁₎W₍₁₎S(-L), NiMo₍₁₎W₍₂₎S(-L), and NiWS(-L).

While the trend of specific surface area and pore volume did not change after the HCl treatment, the both increased for each sample. Hence, crystalline nickel sulfides removed from

the parent materials are concluded to have a lower specific surface area and to block pores of the Ni-containing Mo(W)S₂ particles. Note that compared to the high specific surface and the large pores of the MoS₂, WS₂ forms denser agglomerates with significantly lower specific surface areas and smaller pore volumes (Figures 29 and 30, Table 16).

Table 16. Specific BET surface area [m²/g] and pore volume [cm³/g] of the parent sulfide materials NiMoS, NiMo₍₂₎W₍₁₎S, NiMo₍₁₎W₍₁₎S, NiMo₍₁₎W₍₂₎S, and NiWS and the corresponding sulfide materials after the HCl treatment, i.e., NiMoS-L, NiMo₍₂₎W₍₁₎S-L, NiMo₍₁₎W₍₁₎S-L, NiMo₍₁₎W₍₂₎S-L, and NiWS-L.

Catalyst	Specific surface area [m ² /g]		Pore volume [cm ³ /g]	
	Parent	HCl treated	Parent	HCl treated
NiMoS(-L)	101	149	0.16	0.35
NiMo ₍₂₎ W ₍₁₎ S(-L)	106	188	0.13	0.33
NiMo ₍₁₎ W ₍₁₎ S(-L)	52	81	0.04	0.07
NiMo ₍₁₎ W ₍₂₎ S(-L)	48	79	0.07	0.03
NiWS(-L)	44	57	0.07	0.11

Analysis of TEM pictures (Figure 32 and 33) reveals that the phase composition of the Ni-containing Mo(W)S₂ does not seem to systematically influence the length of the Mo(W)S₂ slabs and their stacking height. Slab diameter and stacking degree were not significantly affected by the HCl treatment considering the large deviations (Table 17). The exact distribution of the sulfide slab lengths for each material is shown in the Appendix (Figures A92 and A93).

Table 17. Length and stacking degree of the Mo(W)S₂ slabs of the parent sulfide materials NiMoS, NiMo₍₂₎W₍₁₎S, NiMo₍₁₎W₍₁₎S, NiMo₍₁₎W₍₂₎S, and NiWS and the corresponding HCl-treated sulfide materials, NiMoS-L, NiMo₍₂₎W₍₁₎S-L, NiMo₍₁₎W₍₁₎S-L, NiMo₍₁₎W₍₂₎S-L, and NiWS-L. The standard deviations are shown in brackets.

Catalyst	Slab length [nm]		Stacking degree [-]	
	Parent	HCl treated	Parent	HCl treated
NiMoS(-L)	5.2 (± 2.4)	6.1 (± 2.5)	4.3 (± 1.8)	4.2 (± 1.4)
NiMo ₍₂₎ W ₍₁₎ S(-L)	4.7 (± 2.7)	5.6 (± 2.1)	4.1 (± 2.3)	4.2 (± 1.5)
NiMo ₍₁₎ W ₍₁₎ S(-L)	4.8 (± 1.9)	4.8 (± 1.9)	3.8 (± 1.3)	3.8 (± 1.2)
NiMo ₍₁₎ W ₍₂₎ S(-L)	5.2 (± 2.7)	5.4 (± 1.8)	3.7 (± 1.5)	3.9 (± 1.5)
NiWS(-L)	4.0 (± 2.6)	5.4 (± 2.6)	4.4 (± 1.8)	4.3 (± 1.8)

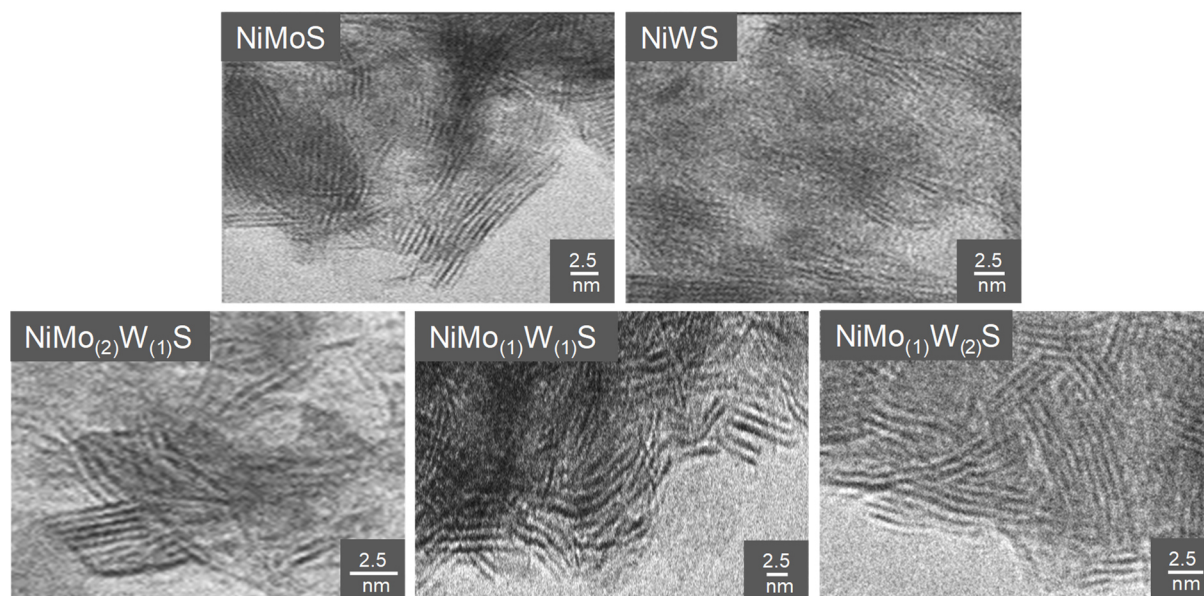


Figure 32. Representative TEM images of the parent sulfides: NiMoS, NiMo₍₂₎W₍₁₎S, NiMo₍₁₎W₍₁₎S, NiMo₍₁₎W₍₂₎S, and NiWS. The scale bar is 2.5 nm in all cases.

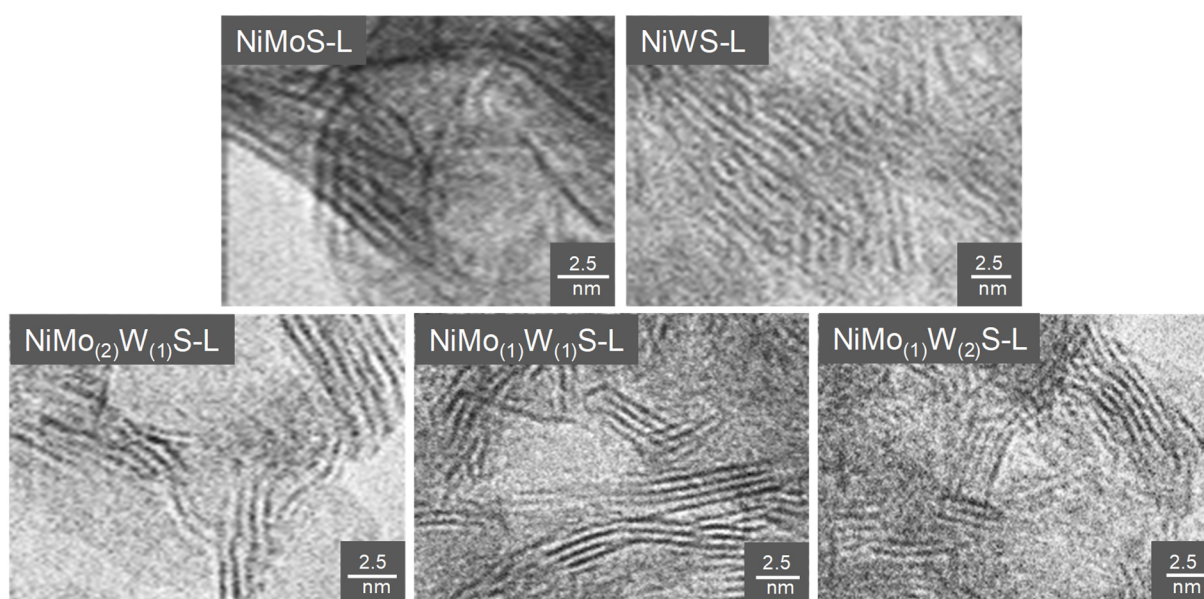


Figure 33. Representative TEM images of the leached sulfides: NiMoS-L, NiMo₍₂₎W₍₁₎S-L, NiMo₍₁₎W₍₁₎S-L, NiMo₍₁₎W₍₂₎S-L, and NiWS-L. The scale bar is 2.5 nm in all cases.

3.2. Reaction network of the hydrodenitrogenation of quinoline

A general scheme of the reaction network of the hydrodenitrogenation of quinoline is depicted in Figure 34.

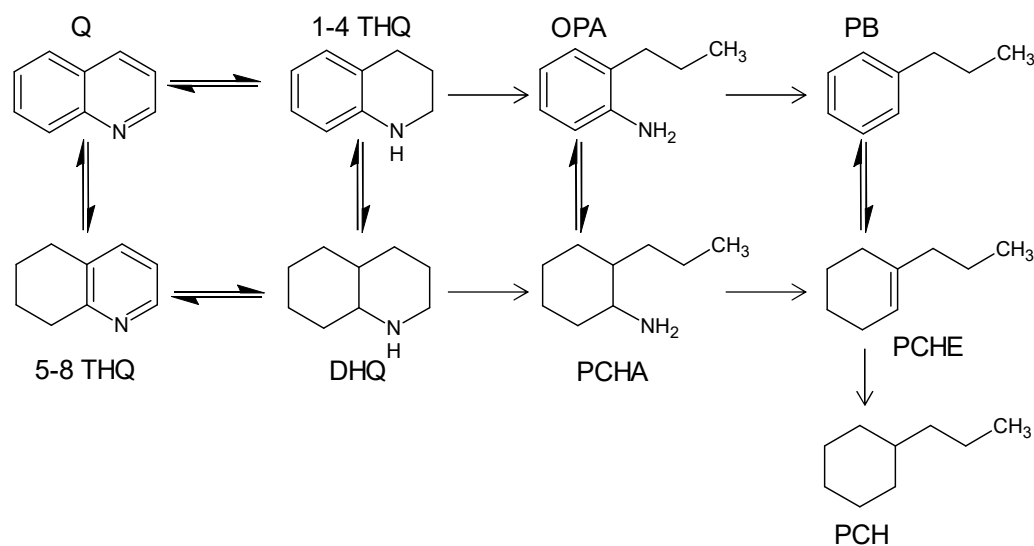


Figure 34. Scheme of the reaction network of the hydrodenitrogenation of quinoline. Equilibria among the bicyclic compounds quinoline (Q), 1,2,3,4-tetrahydroquinoline (1-4 THQ), 5,6,7,8-tetrahydroquinoline (5-8 THQ), and *cis, trans*-decahydroquinoline (DHQ) are possible. Further intermediates and products are *o*-propylaniline (OPA), *o*-propylcyclohexylamine (PCHA), propylcyclohexene (PCHE), propylcyclohexane (PCH), and propylbenzene (PB). Hydrogenation-dehydrogenation equilibria between *o*-propylaniline and *o*-propylcyclohexylamine as well as propylbenzene and propylcyclohexene can also occur.

The bicyclic N-containing compounds, i.e., quinoline, 1,2,3,4-tetrahydroquinoline, 5,6,7,8-tetrahydroquinoline, and *cis, trans*-decahydroquinoline, can possibly interconvert into each other; calculated data concerning their thermodynamic equilibria have been reported.^{34,}

159, 184

Under all applied reaction conditions, the equilibrium between quinoline and 1,2,3,4-tetrahydroquinoline was rapidly established (within the whole range of contact time), far to the side of 1,2,3,4-tetrahydroquinoline.¹⁵⁹ Quinoline and 1,2,3,4-tetrahydroquinoline are, therefore, lumped together for kinetic evaluations. Other possible equilibria among the bicyclic intermediates were not reached even at the longest contact time tested. The selectivity to 5,6,7,8-tetrahydroquinoline was 2 % at maximum due to its slower formation and faster consumption¹⁸⁵ and thus, not taken into further account in the detailed kinetic analysis presented below.

1,2,3,4-tetrahydroquinoline can be converted either via ring opening of its heterocycle to *o*-propylaniline or via full hydrogenation of its benzene ring to form *cis, trans*-decahydroquinoline. Both intermediates, *cis, trans*-decahydroquinoline and *o*-propylaniline, can in

principle react to form *o*-propylcyclohexylamine via ring opening of the heterocycle or hydrogenation of the benzene ring, respectively. The nitrogen atom can be removed from *o*-propylcyclohexylamine through Hofmann-type elimination, and isomers of propylcyclohexene, i.e., 1-propylcyclohexene, 3-propylcyclohexene, and propylidene cyclohexane, are formed. Subsequent hydrogenation of the double bond led to propylcyclohexane.³⁹ Propylbenzene forms via dehydrogenation of propylcyclohexene or propylcyclohexane,^{30, 40-41} or direct denitrogenation of *o*-propylaniline.⁴²⁻⁴³

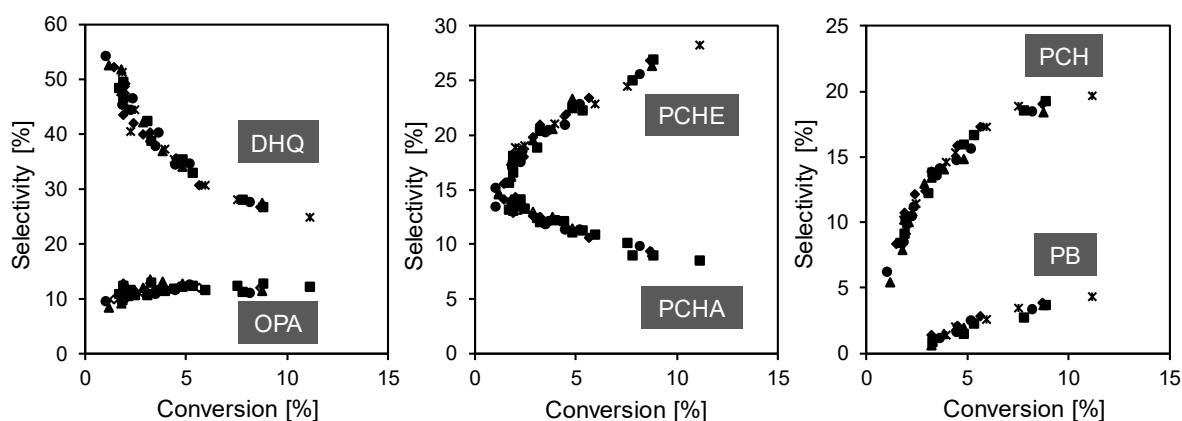


Figure 35. Plots of the selectivities to *cis*, *trans*-decahydroquinoline (DHQ), *o*-propylaniline (OPA), *o*-propylcycloamine (PCHA), propylcyclohexene (PCHE, including three regioisomers with different C=C positions), propylcyclohexane (PCH), and propylbenzene (PB) as a function of quinoline conversion on the parent sulfides NiMoS (\blacktriangle), NiMo₂W₍₁₎S (\blacksquare), NiMo₍₁₎W₍₁₎S (\blacklozenge), NiMo₍₁₎W₍₂₎S (\ast), and NiWS (\bullet). Reaction conditions: 330 °C, 50 bar total pressure (N₂ balance), quinoline (1000 ppm N in *n*-hexadecane), molar ratio of hydrocarbon to H₂ = 1:300.

Plots of product selectivities as a function of quinoline and 1,2,3,4-tetrahydroquinoline conversion showed the same trends on parent and leached sulfides (Figure 35 and 36). The main conversion pathway was clearly through *cis*, *trans*-decahydroquinoline. It was suggested by Shih et al. that the formation of *o*-propylaniline from 1,2,3,4-tetrahydroquinoline is limited, due to the conjugation of the lone pair of nitrogen with the benzene ring of 1,2,3,4-tetrahydroquinoline.¹⁸⁶ Competitive hydrodenitrogenation studies of aniline and *cis*, *trans*-decahydroquinoline have shown that *cis*, *trans*-decahydroquinoline adsorbs 20 times more strongly than aniline.²⁶

Thus, 1,2,3,4-tetrahydroquinoline to *cis*, *trans*-decahydroquinoline is kinetically favored.^{34, 186} The substantial selectivity decrease of *cis*, *trans*-decahydroquinoline with increasing residence time reflects its facile conversion to *o*-propylcyclohexylamine.³⁴ The Hofmann-type elimination of *o*-propylcyclohexylamine to propylcyclohexene also occurred rather rapidly.¹⁸⁷

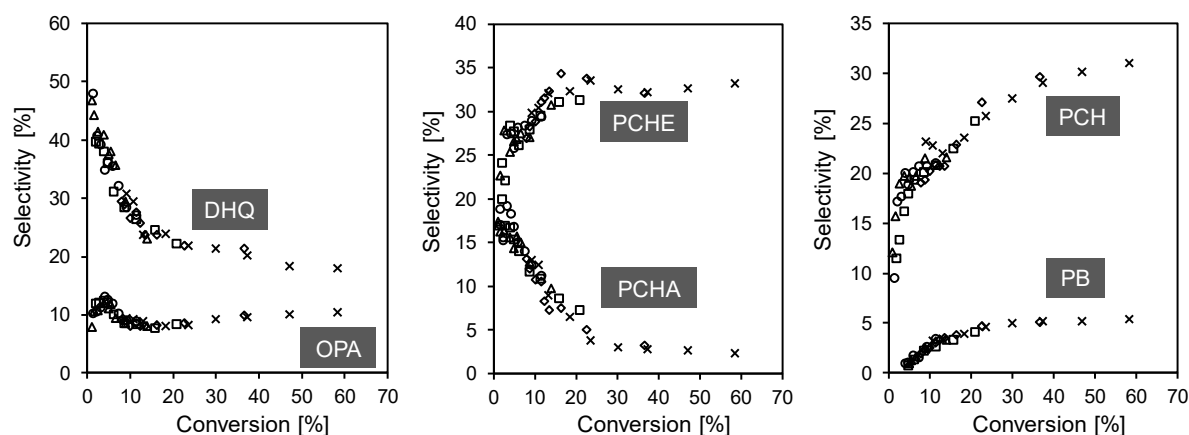


Figure 36. Plots of the selectivities to *cis*, *trans*-decahydroquinoline (DHQ), *o*-propylaniline (OPA), *o*-propylcycloamine (PCHA), propylcyclohexene (PCHE), propylcyclohexane (PCH) and propylbenzene (PB) as a function of conversion on the leached sulfides NiMoS-L (Δ), NiMo₂W₁S-L (\square), NiMo₁W₁S-L (\diamond), NiMo₁W₂S-L (\times), and NiWS-L (\circ). Reaction conditions: 330 °C, 50 bar total pressure (N₂ balance), quinoline (1000 ppm N in *n*-hexadecane), molar ratio of hydrocarbon to H₂ = 1:300.

The selectivity of *o*-propylaniline hardly changed over the studied conversion range, which, at first sight, seems to be related to the much smaller adsorption constant of *o*-propylaniline compared to those of the bicyclic N-containing compounds, i.e., quinoline, 1,2,3,4-tetrahydroquinoline, 5,6,7,8-tetrahydroquinoline, and *cis*, *trans*-decahydroquinoline, making *o*-propylaniline conversion strongly inhibited in their presence.^{26, 31, 34, 188} Moreover, the strong C(sp²)-N bond in *o*-propylaniline limits the formation of propylbenzene via direct C-N cleavage.^{6, 161}

Thus, we conclude that on the unsupported sulfide catalysts studied, propylbenzene is formed through dehydrogenation of propylcyclohexene, and that *o*-propylaniline is not converted further under the applied reaction conditions. The hydrogenation of propylbenzene to propylcyclohexane does not proceed in the presence of N-containing compounds.¹⁸⁸

Summarizing these results, the simplified reaction network is depicted in Figure 37 for the hydrodenitrogenation of quinoline, which can occur via two pathways, i.e., ring opening and hydrogenation. The classification refers to the nature of the first step along each pathway starting with 1,2,3,4-tetrahydroquinoline.

The fact that neither 1,2,3,4-tetrahydroquinoline nor *o*-propylaniline was detected in the hydrodenitrogenation of *cis*, *trans*-decahydroquinoline (Figure 38) suggests that the two pathways are not interlinked under the applied reaction conditions.

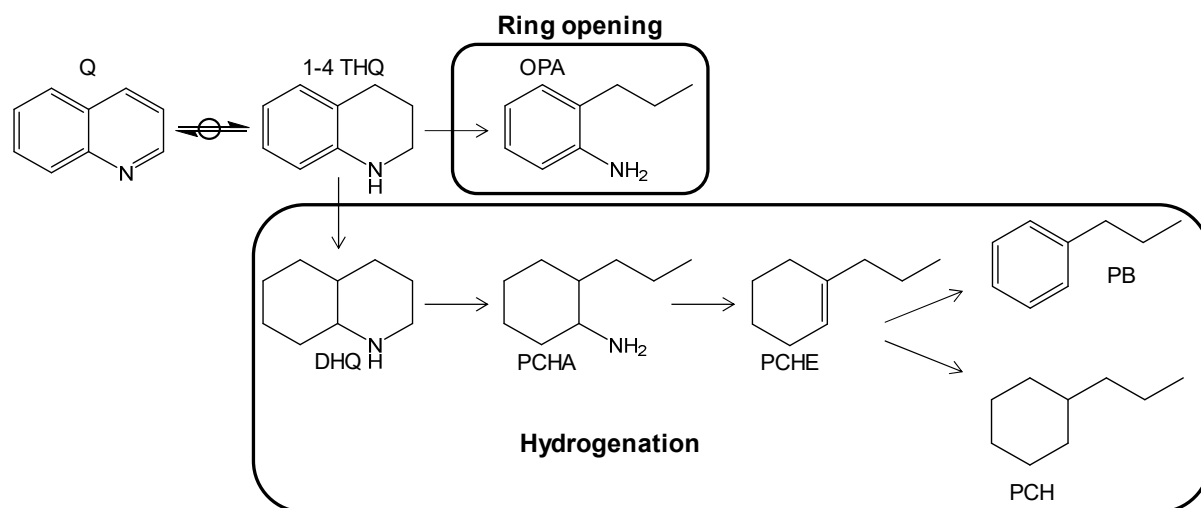


Figure 37. Scheme of the reaction network of the hydrodenitrogenation of quinoline including the detected intermediates and products. The abbreviations of the compounds are the same as those in Figure 34 (see caption).

3.3. Hydrodenitrogenation of *cis, trans*-decahydroquinoline

The hydrodenitrogenation of *cis, trans*-decahydroquinoline was performed on all HCl-treated sulfides at 330 °C and a total pressure of 50 bar H₂. The products detected were *o*-propylcyclohexylamine, the 3 isomers of propylcyclohexene, i.e., 1- and 3-propylcyclohexenes, and propylidene cyclohexane, and propylcyclohexane (Figure 38). Based on the selectivity plots the reaction network for the hydrodenitrogenation of *cis, trans*-decahydroquinoline, shown in Figure 39, is proposed. Herein, the heterocycle of *cis, trans*-decahydroquinoline undergoes ring opening to form *o*-propylcyclohexylamine. Subsequent N removal via a Hofmann-type elimination leads to propylcyclohexene with is then hydrogenated to propylcyclohexane.

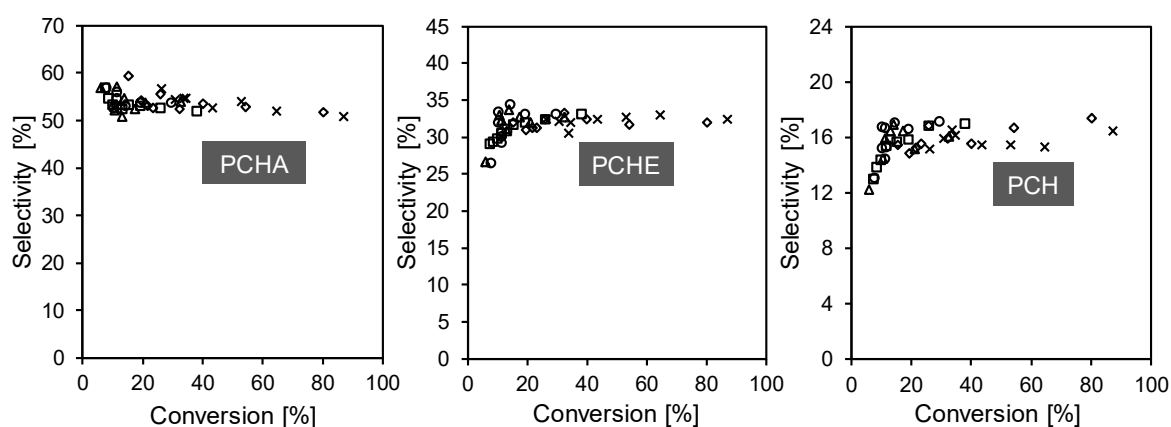


Figure 38. Plots of the selectivities to *o*-propylcycloamine (PCHA), propylcyclohexene (PCHE), and propylcyclohexane (PCH) as a function of *cis, trans*-decahydroquinoline conversion on the HCl-treated sulfides NiMoS-L (Δ), NiMo₂W₁S-L (\square), NiMo₁W₁S-L (\diamond), NiMo₁W₂S-L (\times), and NiWS-L (\circ).

Neither dehydrogenation of *cis, trans*-decahydroquinoline to 1,2,3,4-tetrahydroquinoline or 5,6,7,8-tetrahydroquinoline nor dehydrogenation of propylcyclohexene or propylcyclohexane to propylbenzene was observed. The lack of the latter reaction, which occurred in the hydrodenitrogenation of quinoline, is attributed to the different hydrogen demand of the two hydrogenation reactions being higher for the conversion of quinoline. The higher consumption of hydrogen enables dehydrogenation by shifting the hydrogenation/dehydrogenation equilibrium.

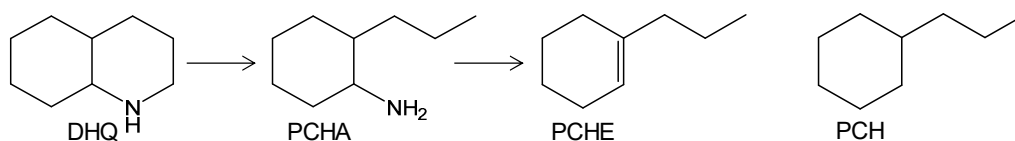


Figure 39. Scheme of the reaction network of the hydrodenitrogenation of *cis, trans*-decahydroquinoline (DHQ) with the products *o*-propylcyclohexylamine (PCHA), propylcyclohexene (PCHE), and propylcyclohexane (PCH).

Comparing the hydrodenitrogenation rates of quinoline with the ones for hydrodenitrogenation of *cis, trans*-decahydroquinoline reveals that the hydrodenitrogenation of *cis, trans*-decahydroquinoline is faster on all tested sulfides (Figure 40). This implies that the rate determining step in the hydrodenitrogenation of quinoline is within the hydrogenation of 1,2,3,4-tetrahydroquinoline to *cis, trans*-decahydroquinoline. However, the trend among the sulfide catalysts is the same for both hydrodenitrogenation reactions, i.e.,

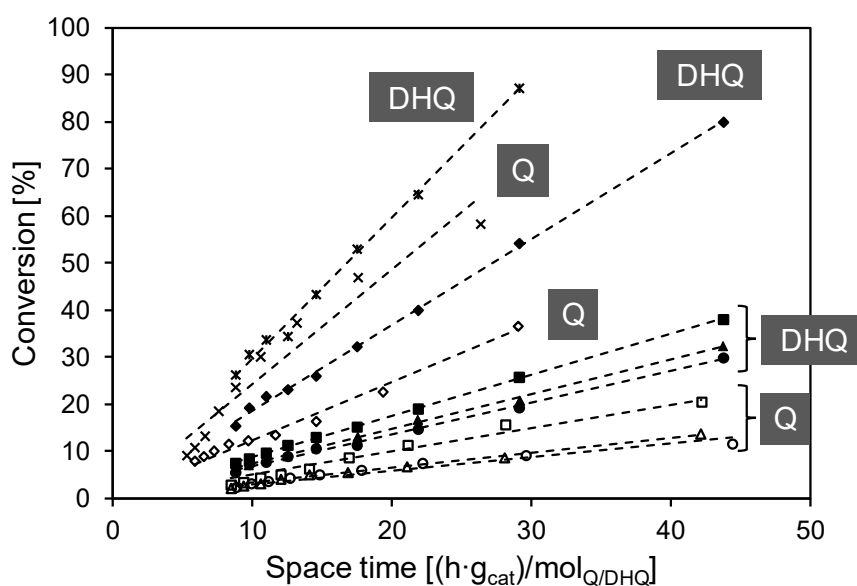
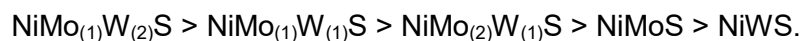


Figure 40. Conversion of quinoline (Q, empty symbols) and *cis, trans*-decahydroquinoline (DHQ, filled symbols) as a function of space time [(h·g_{cat})/mol] on NiMoS-L (△, ▲), NiMo₍₂₎W₍₁₎S-L (□, ■), NiMo₍₁₎W₍₁₎S-L (◇, ♦), NiMo₍₁₎W₍₂₎S-L (x, *), and NiWS-L (○, ●).

3.4. Comparison of the catalytic activity of parent and HCl-treated sulfides

On the parent sulfides, the mass-specific activities for quinoline conversion were generally higher on trimetallic formulations than on bimetallic ones, following the order



Among the trimetallic sulfides, a higher tungsten content in the trimetallic phase (metal molar fraction of tungsten increasing from 0.10 to 0.21, Table 15) was found to be associated with a higher hydrodenitrogenation activity.

Table 18. Hydrodenitrogenation (HDN) rates of the parent sulfides NiMoS, NiMo₍₂₎W₍₁₎S, NiMo₍₁₎W₍₁₎S, NiMo₍₁₎W₍₂₎S, and NiWS, and the corresponding HCl-treated sulfides NiMoS-L, NiMo₍₂₎W₍₁₎S-L, NiMo₍₁₎W₍₁₎S-L, NiMo₍₁₎W₍₂₎S-L, and NiWS-L. Reaction conditions: 330 °C, 50 bar total pressure, quinoline (1000 ppm N in *n*-hexadecane), molar ratio of hydrocarbon to H₂ = 1:300.

Catalyst	HDN rates [mmol _Q /(h·g _{cat})]	
	Parent	HCl-treated
NiMoS(-L)	0.3	0.4
NiMo ₍₂₎ W ₍₁₎ S(-L)	0.4	0.7
NiMo ₍₁₎ W ₍₁₎ S(-L)	0.8	1.6
NiMo ₍₁₎ W ₍₂₎ S(-L)	1.5	2.8
NiWS(-L)	0.2	0.3

The HCl treatment significantly increased their mass-specific hydrodenitrogenation rates by up to a factor of 2 but did not change the activity ranking (Table 18 and Figure 40). On all sulfides, the rates for the hydrogenation pathway (1-4 THQ → DHQ → PCHA → PCHE → PCH) were at least 4 times faster than for the ring opening pathway (1-4 THQ → OPA) (Figure 41 for the parent sulfides and Figures 42 and 43 for the HCl-treated sulfides, respectively).

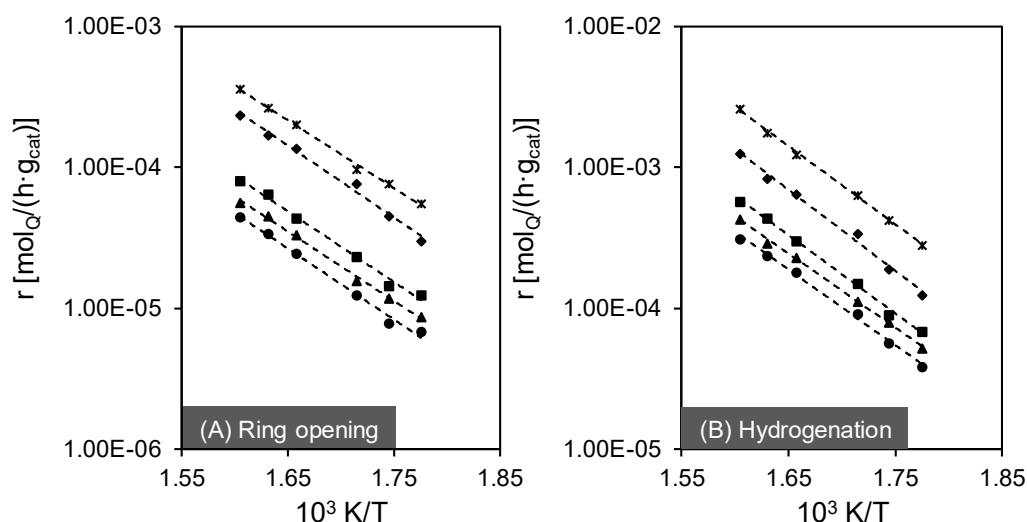


Figure 41. Rates [$\text{mol}_Q/(\text{h}\cdot\text{g}_{\text{cat}})$] (A) for the ring opening pathway ($14\text{-THQ} \rightarrow \text{OPA} \rightarrow \text{PB}$) and (B) for the hydrogenation pathway ($14\text{-THQ} \rightarrow \text{DHQ} \rightarrow \text{PCHA} \rightarrow \text{PCHE} \rightarrow \text{PCH}$) in the hydrodenitrogenation of quinoline (Q) in the temperature range from 290-350 °C on the parent sulfides NiMoS (\blacktriangle), NiMo₍₂₎W₍₁₎S (\blacksquare), NiMo₍₁₎W₍₁₎S (\blacklozenge), NiMo₍₁₎W₍₂₎S ($*$), and NiWS (\bullet).

The apparent activation energies of the overall hydrodenitrogenation and of the two individual pathways also hardly changed after the HCl treatment (Table 20). This probably indicates that the catalytically active Ni-containing Mo(W)S₂ phase was not affected by the HCl treatment, i.e., HCl treatment only removes physical blockage by NiS_x from active sites.

Table 19. Ratio of the hydrogenation (HYD) route to the ring opening route (RO) route on the parent sulfides NiMoS, NiMo₍₂₎W₍₁₎S, NiMo₍₁₎W₍₁₎S, NiMo₍₁₎W₍₂₎S, and NiWS and the corresponding HCl-treated sulfide materials NiMoS-L, NiMo₍₂₎W₍₁₎S-L, NiMo₍₁₎W₍₁₎S-L, NiMo₍₁₎W₍₂₎S-L, and NiWS-L.

Catalyst	HYD/RO [-]	
	Parent	HCl-treated
NiMoS(-L)	6.6	5.2
NiMo ₍₂₎ W ₍₁₎ S(-L)	6.5	5.5
NiMo ₍₁₎ W ₍₁₎ S(-L)	4.4	5.9
NiMo ₍₁₎ W ₍₂₎ S(-L)	5.6	5.6
NiWS(-L)	7.2	5.7

The variation of selectivities to the six main products (DHQ, OPA, PCHE, PCHA, PCH, and PB) as a function of pool (Q + 1-4 THQ) conversion appeared quantitatively identical (Figures 35 and 36) and the ratios of rates along the hydrogenation and ring opening pathways were very similar for all sulfide catalysts (Table 20), indicating that phase composition of the Ni-containing Mo(W)S₂ phase has little impact on the product distribution.

The relative kinetics and the measured activation energies of the different reaction steps in the reaction network of the hydrodenitrogenation of quinoline (Figure 37) are not affected by the composition of the catalytically active sulfide phase, but the materials showed different mass-specific activities (Table 18).

These observations suggest that active sites of the same nature govern the hydrodenitrogenation activity of unsupported bimetallic and trimetallic sulfides, which were synthesized in the same manner, via ring opening and hydrogenation pathways.

Table 20. Apparent activation energies [E_{app} , kJ/mol] of the overall quinoline hydrodenitrogenation (HDN) as well as of both pathways, ring opening and hydrogenation, determined on the parent sulfide materials NiMoS, NiMo₍₂₎W₍₁₎S, NiMo₍₁₎W₍₁₎S, NiMo₍₁₎W₍₂₎S, and NiWS and the corresponding HCl-treated sulfide materials NiMoS-L, NiMo₍₂₎W₍₁₎S-L, NiMo₍₁₎W₍₁₎S-L, NiMo₍₁₎W₍₂₎S-L, and NiWS-L. Error analysis using linear regression revealed an error < 1 kJ/mol for a confidence level of 95 %. Reaction conditions: 290-350 °C, 50 bar total pressure, quinoline (1000 ppm N in *n*-hexadecane), molar ratio of hydrocarbon to H₂ = 1:300.

Catalyst	E_{app} , HDN [kJ/mol]		E_{app} , Hydrogenation [kJ/mol]		E_{app} , Ring opening [kJ/mol]	
	Parent	HCl treated	Parent	HCl treated	Parent	HCl treated
NiMoS(-L)	100	106	101	106	94	95
NiMo ₍₂₎ W ₍₁₎ S(-L)	106	106	106	106	96	93
NiMo ₍₁₎ W ₍₁₎ S(-L)	108	102	110	104	98	95
NiMo ₍₁₎ W ₍₂₎ S(-L)	105	107	106	107	92	87
NiWS(-L)	103	103	103	103	96	93

3.5. Detailed evaluation of ring opening and hydrogenation pathway

The HCl-treated sulfides with minimal presence of the site-blocking nickel sulfide entities were further employed to assess in greater detail the impact of the sulfide phase on the two individual hydrodenitrogenation pathways.

3.5.1. Ring opening pathway

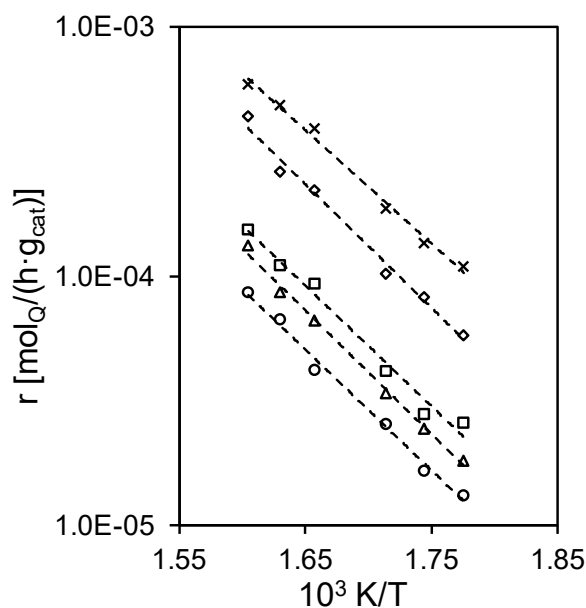


Figure 42. Rates [$\text{mol}_Q/(\text{h}\cdot\text{g}_{\text{cat}})$] of the ring opening pathway (Q and 1-4 THQ \rightarrow OPA \rightarrow PB) as a function of temperature on NiMoS-L (Δ), NiMo₂W₁S-L (\square), NiMo₁W₁S-L (\diamond), NiMo₁W₂S-L (\times), and NiWS-L (\circ). Reaction conditions: 290-350 °C, 50 bar total pressure, quinoline (1000 ppm N in *n*-hexadecane), molar ratio of hydrocarbon to H₂ = 1:300.

The ring opening pathway involves the C(sp³)-N cleavage of 1,2,3,4-tetrahydroquinoline to form *o*-propylaniline. The selectivity to *o*-propylaniline did not change with conversion at least up to 20 % (Figure 36). Thus, *o*-propylaniline appeared to be an end product in the present work. The rate of the ring opening route, i.e., the formation of *o*-propylaniline on the different sulfides decreased in the following order (Figure 42)



A reaction order of one in quinoline and of zero in hydrogen for all sulfides (Table 22) together with the nearly identical apparent activation energies (Table 21), suggest the same mechanism of the ring opening pathway independent of the phase composition of these sulfide catalysts.

Table 21. Reaction order in quinoline and hydrogen determined on NiMoS-L, NiMo₍₂₎W₍₁₎S-L, NiMo₍₁₎W₍₁₎S-L, NiMo₍₁₎W₍₂₎S-L, and NiWS-L for the ring opening pathway. Reaction conditions: 330 °C, total pressure of 50 bar, inlet pressures or concentrations of quinoline and H₂ being $\omega_Q = 0.4\text{--}1.2$ wt. %, $p_{H_2} = 34\text{--}42$ bar. The regressed errors in reaction orders are < 0.01 (95% confidence level) for all cases.

Catalyst	Reaction order at 330 °C	
	Quinoline	Hydrogen
NiMoS-L	1.0	0.0
NiMo ₍₂₎ W ₍₁₎ S-L	0.9	0.1
NiMo ₍₁₎ W ₍₁₎ S-L	0.9	0.0
NiMo ₍₁₎ W ₍₂₎ S-L	1.0	0.0
NiWS-L	1.0	0.0

The reaction orders show that the rates of ring opening depend on the surface coverage of quinoline and surface intermediates equilibrated with quinoline in the fluid phase but not on that of adsorbed hydrogen.

The first order in quinoline speaks for a low surface coverage of quinoline-derived reactive intermediates along this reaction route. Note that σ -adsorption (end-on) via the nitrogen atom on a Lewis acid site, which is commonly called as coordinatively unsaturated site (CUS), is hypothesized to precede the ring opening reaction.^{32, 161, 189}

Quinoline and 1,2,3,4-tetrahydroquinoline are much less basic molecules than *cis*, *trans*-decahydroquinoline, *o*-propylcyclohexylamine, and ammonia (NH₃) in terms of pK_a (lower by 5-6 pK_a units), a property that was found to qualitatively track the regressed adsorption constants for these compounds from liquid phase hydrodenitrogenation of quinoline on a sulfided NiMo(P)/Al₂O₃ catalyst.¹⁸⁵

If protonation of quinoline or 1,2,3,4-tetrahydroquinoline is required prior to the C(sp³)-N bond cleavage, the extent of protonation should be negligibly small because of its lower basicity than pyridine and the weak Brønsted acidity of -SH. Note in this context that adsorption of pyridine on sulfide surfaces does not form detectable concentration of pyridinium ions at high temperatures.¹⁹⁰⁻¹⁹² Consequently, we expect that the neutral and protonated surface intermediates derived from σ -adsorption of quinoline and 1,2,3,4-tetrahydroquinoline, respectively, would be a minority surface species. In this case, the surface coverage of such reactive intermediates for ring opening would be proportional to the combined partial pressures/fugacities of quinoline and 1,2,3,4-tetrahydroquinoline, in line with the measured first order kinetics with respect to the inlet pressure of quinoline (Table 21).

Next, the measured zero-order kinetics with respect to the hydrogen pressure is explained. Intuitively, hydrogen cannot be so strongly adsorbed that the surface becomes saturated by

hydrogen-derived species under these conditions.³² This minor possibility of surface sites being saturated with adsorbed hydrogen can be discarded also on the basis of positive reaction orders in hydrogen along the hydrogenation pathway (section 3.5.2.). Thus, it is more likely that the rate-determining step in the formation of *o*-propylaniline does not involve species derived from hydrogen.

Although it is still debatable as to whether dissociation of hydrogen and quinoline adsorption takes place on the same surface site or on different sites, the competitive adsorption scenario for hydrogen, solvent, and N-containing compounds is chosen below for the sake of argument.³² The conclusions would still hold in the case of non-competitive adsorption for quinoline and hydrogen.^{34-35, 193-194}

A generalized Langmuir–Hinshelwood formalism is used to express the fractional coverage of an organic molecule *i* (θ_i) on the catalytic sites (Equation 5).

Equation 5. Fractional coverage of an organic molecule *i* (θ_i) with the intrinsic adsorption constants *K* and the concentrations *c* of the organic molecule *i*, the solvent *s*, hydrogen *H*, and other present compounds including ammonia (NH₃) and dihydrogen sulfide (H₂S).

$$\theta_i = \frac{K_i c_i}{1 + K_s c_s + (K_H c_H)^{0.5} + \sum K_j c_j}$$

The partial pressure of H₂S was kept constant under the applied reaction conditions. The concentration of ammonia, in contrast, varied with conversion. But the linear increase of conversion rate as a function of space time (Figure 40) shows that ammonia does not appreciably inhibit quinoline conversion. Thus, the adsorption constant of ammonia must be much smaller compared to the N-containing organics.¹⁹⁵⁻¹⁹⁶

There are a number of mechanisms proposed for C(sp³)-N bond cleavage.^{32, 197}

For 1,2,3,4-tetrahydroquinoline, where the α -C(sp³) is unsubstituted corresponding to a highly unstable primary carbenium ion for E1 and S_N1 pathways, the removal of nitrogen is expected to occur either via a S_N2 nucleophilic substitution of one bond in the -NH- bridge by an -SH group, being a pretty strong nucleophile, followed by further C(sp³)-S bond cleavage or directly via Hofmann-type E2 elimination.^{32, 198}

The latter mechanism requires a coordinatively unsaturated metal site on which 1,2,3,4-tetrahydroquinoline can adsorb perpendicular to the metal atom via its nitrogen lone-pair electrons.¹⁹⁹ Further, a basic sulfur atom on the catalyst surface is needed to abstract the β -H from the organic molecule.⁶

Unsupported sulfides, which do not carry additional acid sites from other sources, e.g., oxide support, would only produce the active hydrogen in the form of an -SH, generated upon equilibrated H₂/H₂S dissociation at a sulfur vacancy or (S-S)²⁻ dimer.²⁰⁰⁻²⁰¹ If ring opening

occurs via an elimination mechanism, the reactant adsorbed at the coordinatively unsaturated site, in principle, either undergoes protonation by an adjacent SH group or not prior to the rate determining step.

Although the protonated species must be present at a much lower concentration than the neutral species (*vide supra*), protonation preceding C-N cleavage is a possibility. However, the zero order in hydrogen not only indicates that the ring opening reaction takes place without the requirement of protonating the reactant prior to the rate determining step or protonation even as the rate determining step itself for an elimination mechanism, but also dismisses nucleophilic substitution as the prevalent mechanism where SH is involved as a nucleophile whose surface concentration exhibits a dependence on hydrogen pressure.

Literature data also suggest that a Hofmann-type E2 elimination should be mainly responsible for the C(sp³)-N bond cleavage involved in the ring opening pathway of 1,2,3,4-tetrahydroquinoline to *o*-propylaniline. Cattenot et al. and Nelson et al. found that in the case of 1,2,3,4-tetrahydroquinoline, ring opening takes place via elimination rather than nucleophilic substitution on MoS₂.^{197, 202} Similarly, Prins and co-workers found Hofmann-type elimination to be mainly responsible for hydrodenitrogenation of *o*-methylaniline.^{32, 203} In addition, the high reaction temperature applied generally favors elimination over nucleophilic substitution.¹⁹⁷

Altogether, we conclude that the rate determining step for the ring opening reaction of 1,2,3,4-tetrahydroquinoline cannot involve any chemical identity, e.g., protonated reactant or SH groups, whose surface coverage exhibits a hydrogen pressure dependence and thus, most likely occurs via an E2-type elimination with a non-protonated species derived from quinoline and/or 1,2,3,4-tetrahydroquinoline.

Accordingly, Equation 6 shows the corresponding rate expression.

Equation 6. Rate expression of the ring opening r_{RO} where $[L_1]$ is the concentration of active sites for ring opening, $k_{RDS,RO}$ $K_{THQ,1}$ is the equilibrium constant for σ -adsorption of 1,2,3,4-tetrahydroquinoline or the adsorption mode that mediates the ring opening route, and c_{THQ} is the concentration of 1,2,3,4-tetrahydroquinoline.

$$\frac{r_{RO}}{[L_1]} = \frac{k_{RDS,RO} K_{THQ,1} c_{THQ}}{(1 + K_s c_s + (K_H c_H)^{0.5} + \sum K_j c_j)^2}$$

Equation 6 is consistent with the measured reaction orders in quinoline and in hydrogen along the ring opening pathway. In this case, the observed reaction order of zero in hydrogen (Table 21) would also be consistent with the perception that the adsorbed hydrogen species are present at low coverages ($(K_H c_H)^{0.5} \ll (1 + K_s c_s + \sum_{j=1}^n K_j c_j)$ in Equation 5).

3.5.2. Hydrogenation pathway

The hydrogenation pathway proceeds via saturation of the benzenic ring to form *cis*, *trans*-decahydroquinoline, followed by C(sp³)-N bond cleavage to form *o*-propylcyclohexylamine and finally by C(sp³)-N bond breaking of the latter to form propylcyclohexene, propylcyclohexane, and via dehydrogenation propylbenzene (Figure 37).

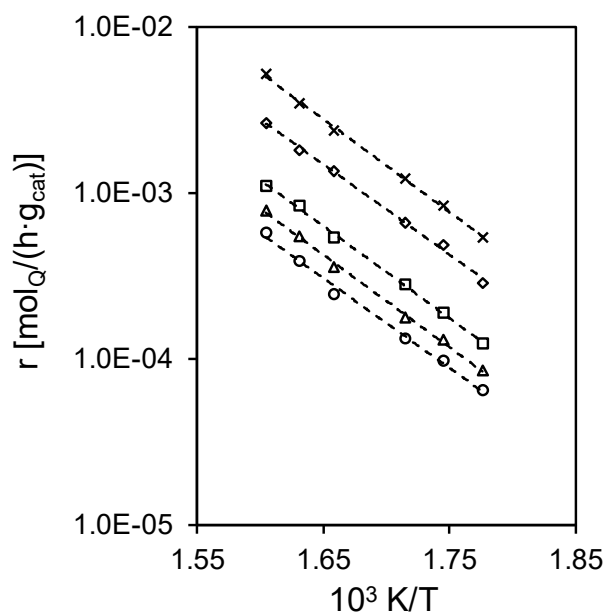


Figure 43. Rates [mol_Q/(h·g_{cat})] of the hydrogenation pathway (Q and 1-4 THQ → DHQ → PCHA → PCHE → PCH) as a function of temperature on NiMoS-L (Δ), NiMo₍₂₎W₍₁₎S-L (□), NiMo₍₁₎W₍₁₎S-L (◇), NiMo₍₁₎W₍₂₎S-L (x), and NiWS-L (○). Reaction conditions: 290-350 °C, 50 bar total pressure, quinoline (1000 ppm N in *n*-hexadecane), molar ratio of hydrocarbon to H₂ = 1:300.

The rates along the hydrogenation pathway also followed the order (Figure 43)



The apparent activation energies were similar at ~100 kJ/mol, independent of the sulfide phase composition (Table 20). Interestingly, this value appears to be coincidentally identical to that measured for the ring opening pathway.

In contrast to the first order in quinoline for ring opening kinetics, the hydrogenation rate was insensitive to the variation of quinoline concentration in the fluid phase (Table 22). In the literature, zero as well as first order reactions are proposed for hydrodenitrogenation reactions depending on the catalyst used and the reaction network assumed.³⁶ Satterfield et al. found, in agreement with our reaction network, the hydrodenitrogenation rate to be zero order with hydrogenation being the dominant conversion route in quinoline on a NiMo/Al₂O₃ catalyst. This was rationalized by the relatively strong adsorption of the reactants.^{30, 35}

We tentatively attribute the different reaction orders in quinoline along the two routes to different adsorption modes. Specifically, σ -adsorption (end-on) via the nitrogen atom on a coordinatively unsaturated site is hypothesized to precede ring opening, whereas π -adsorption (side-on or flatwise) is required for hydrogenation reactions.^{6, 32}

Table 22. Reaction orders in quinoline and hydrogen on NiMoS-L, NiMo₍₂₎W₍₁₎S-L, NiMo₍₁₎W₍₁₎S-L, NiMo₍₁₎W₍₂₎S-L, and NiWS-L. The regressed errors in reaction orders are < 0.01 for all cases. Reaction conditions: 330 °C, total pressure 50 bar (N₂ as balance), inlet pressures or concentrations of quinoline and hydrogen being $\omega_Q = 0.4\text{--}1.2$ wt. %, $p_{H_2} = 34\text{--}42$ bar.

Catalyst	Reaction order at 330 °C	
	Quinoline	Hydrogen
NiMoS-L	0.0	0.5
NiMo ₍₂₎ W ₍₁₎ S-L	0.0	1.3
NiMo ₍₁₎ W ₍₁₎ S-L	0.1	1.4
NiMo ₍₁₎ W ₍₂₎ S-L	0.0	2.1
NiWS-L	0.0	0.7

As π -adsorption does not require a coordinatively unsaturated sites, it is plausible that two different types of active sites are involved in ring opening and hydrogenation reactions.^{6, 32, 161, 204} Further, in view of the observed first and zero reaction orders in quinoline for ring opening and hydrogenation, respectively, we infer that the fractional coverage with respect to the active sites for each individual route should be much higher for the π -adsorption intermediate than for the σ -adsorption intermediate.

The inference that π -adsorption is stronger than σ -adsorption is perhaps somewhat counterintuitive. Indeed, basic N-containing molecules are usually expected to bind to acid sites more strongly through the nitrogen atom in a perpendicular upright manner than adsorption via dispersive interactions.

However, at least two factors can change this trend.²⁰⁵ First, non-basic nitrogen compounds are generally found, mainly by DFT calculations, to interact with the NiMoS edge surface through the π -electrons of the carbon atoms (side-on), rather than the end-on mode through the nitrogen atom; thus, it seems reasonable to infer that the less basic N-heterocycles as 1,2,3,4-tetrahydroquinoline also show an increased tendency to interact via the parallel or side-on adsorption compared to the more basic counterparts.²⁰⁰

Second, the dispersive interactions get stronger with an increasing number of carbon atoms. Some DFT calculations also indicated that π -adsorption is much more favorable than σ -adsorption for quinoline on MoS₂ and WS₂.²⁰⁶ Thus, we suggest that the parallel or side-on

adsorption, not the end-on adsorption, is the prevalent mode of adsorption for quinoline and 1,2,3,4-tetrahydroquinoline. This would be in line with the observed reaction orders in quinoline for the ring opening and hydrogenation routes (1 and 0, respectively; Tables 21 and 22). Because both adsorbed species exist at surface concentrations in equilibrium with the fluid phase, the different orders must be rationalized ultimately by invoking two types of active sites for ring opening and hydrogenation routes (section 3.5.1.).

In contrast to the ring opening pathway, the catalytic rate along the hydrogenation pathway depended on the partial pressure of hydrogen. The reaction order in hydrogen along the hydrogenation pathway was dramatically influenced by the sulfide phase composition varying from 0.5 on NiMoS-L to 2.1 on NiMo₍₁₎W₍₂₎S-L (Table 22). Some authors also found the rate of the hydrogenation of 1,2,3,4-tetrahydroquinoline to depend on the pressure of hydrogen on NiMo/Al₂O₃ catalysts.^{6, 34, 194} To our knowledge, however, the effect of sulfide phase composition on reaction order in hydrogen was never reported.

Performing the hydrodenitrogenation of *cis*, *trans*-decahydroquinoline under the same reaction conditions showed that the conversion of *cis*, *trans*-decahydroquinoline was faster than that of quinoline on all sulfides (Figure 43). This indicates that hydrogenation of the benzene ring of 1,2,3,4-tetrahydroquinoline dominant in the reactant pool to form *cis*, *trans*-decahydroquinoline is slower than the ring opening of *cis*, *trans*-decahydroquinoline to *o*-propylcyclohexylamine and its consecutive reactions.³⁸ Thus, the rate determining step along the hydrogenation route is hypothesized to occur prior to the ring opening of *cis*, *trans*-decahydroquinoline (Figure 37).

Moreover, (re)formation of SH groups on sulfides is expected to occur at a much higher rate than those of the rate determining step within the quinoline reaction network under the applied conditions. Consequently, a hydrogen addition step from a SH group on the sulfide surface to the benzene ring 1,2,3,4-tetrahydroquinoline must be the rate determining step. In the mechanistic framework of stepwise addition hydrogen atoms for the hydrogenation pathway,²⁰⁷ a straightforward explanation for the variations in the order of hydrogen can be a shift in rate determining step within the hydrogen addition sequence with a later hydrogen addition step being associated with a higher reaction order.

3.5.3. Site requirement for ring opening and hydrogenation on the unsupported sulfide catalysts

Site requirements and mechanistic pathways for ring opening and hydrogenation of quinoline over transition metal sulfides have not been sufficiently elucidated in the literature. In this work, the different reaction orders measured for quinoline and hydrogen along ring opening and hydrogenation routes speak for different adsorbed species that mediate the two reaction routes and perhaps even different active sites, where ring opening and hydrogenation reactions take place.

If ring opening and hydrogenation occur on the same type of sites and all species adsorb on the same type sites, then we introduce the adsorption constant $K_{THQ,1}$ for σ -adsorption of 1,2,3,4-tetrahydroquinoline, and the adsorption constant $K_{THQ,2}$ for π -adsorption of 1,2,3,4-tetrahydroquinoline. and by applying the site balance (Equation 7).

Equation 7. Site balance of the available active sites on the catalyst surface.

$$[L]_0 = [L] + (K_s c_s) \cdot [L] + (K_H c_H)^{0.5} \cdot [L] + (K_{1-4 THQ,1} c_{1-4 THQ,1}) \cdot [L] + (K_{1-4 THQ,2} c_{1-4 THQ,2}) \cdot [L] + (\sum K_j c_j) \cdot [L]$$

↑
Empty

↑
Solvent*

↑
 H^*

↑
 σ -adsorption

↑
 π -adsorption

↑
Other species

By applying the site balance (Equation 7), the following equations for the surface coverages of the two types of adsorbed 1,2,3,4-tetrahydroquinoline ($\theta_{THQ,\sigma}$ and $\theta_{THQ,\pi}$, respectively) species and adsorbed hydrogen (θ_{H^*}) can be derived (Equations 8-10).

Equation 8. Surface coverage of 1,2,3,4-tetrahydroquinoline adsorbed in the σ -mode ($\theta_{THQ,\sigma}$) where K is the adsorption constant and c the concentration of 1,2,3,4-tetrahydroquinoline adsorbed in the σ -mode ($THQ,1$), the solvent (s), hydrogen (H), and other organic molecules present (j), respectively.

$$\theta_{THQ,\sigma} = \frac{K_{THQ,1} c_{THQ}}{1 + K_s c_s + (K_H c_H)^{0.5} + (K_{THQ,1} + K_{THQ,2}) c_{THQ} + \sum K_j c_j}$$

Equation 9. Surface coverage of 1,2,3,4-tetrahydroquinoline adsorbed in the π -mode ($\theta_{THQ,\pi}$) where K is the adsorption constant and c the concentration of 1,2,3,4-tetrahydroquinoline adsorbed in the π -mode ($THQ,2$), the solvent (s), hydrogen (H), and other organic molecules present (j), respectively.

$$\theta_{THQ,\pi} = \frac{K_{THQ,2} c_{THQ}}{1 + K_s c_s + (K_H c_H)^{0.5} + (K_{THQ,1} + K_{THQ,2}) c_{THQ} + \sum K_j c_j}$$

Equation 10. Surface coverage of adsorbed hydrogen (θ_{H^*}) where K is the adsorption constant and c the concentration of 1,2,3,4-tetrahydroquinoline adsorbed in the π -mode ($THQ,1$ and $THQ,2$), the solvent (s), hydrogen (H), and other organic molecules present (j), respectively.

$$\theta_{H^*} = \frac{(K_H c_H)^{0.5}}{1 + K_s c_s + (K_H c_H)^{0.5} + (K_{THQ,1} + K_{THQ,2}) c_{THQ} + \sum K_j c_j}$$

At low conversions, $\sum K_j c_j$ should be small compared to the other terms in the denominator. In the main text, we have provided a tandem of arguments that the coverage hydrogen (H^*) must be low under our conditions. Thus, the dominant term in the denominator has to be $(1+K_s c_s)$ (constant) in order to account for the reaction order in quinoline. In this case, σ -adsorption of 1,2,3,4-tetrahydroquinoline is required and thus, the reactive intermediate (*vide supra*).

However, the second equation for π -adsorption must also be first order in quinoline. Because the rate expression for the hydrogenation route must include the coverage of the π -adsorbed species as well as the adsorbed hydrogen species (in the form of SH groups) whose coverage expression has the same denominator as the species derived from 1,2,3,4-tetrahydroquinoline and a numerator term that does not have a 1,2,3,4-tetrahydroquinoline dependence. Conceivably, the rate expression for hydrogenation would contradict the measured reaction order of zero in the organic reactant along this route. Together, we conclude that ring opening and hydrogenation must occur on two types of surface sites.

3.5.4. Towards the understanding of hydrodenitrogenation activity across different elemental compositions of bulk sulfide catalysts

As the hydrogen pressure dependence of the dominant reaction pathway, hydrogenation, tremendously changes with the sulfide phase composition (Table 22), the concentration of H-providing SH groups on the sulfide surface must be key to hydrogenation reactions. However, the number of techniques is scant that can provide quantitative information about the active sites or precursors to the active sites, e.g., SH groups or sulfur vacancies associated with edge-substituted nickel, on unsupported sulfides.

An indirect measurement of SH group concentration is the H₂-D₂ scrambling experiment (Experimental), since it was previously established that the rates of HD formation correlate linearly with the concentration of SH groups created by adsorption and dissociation of H₂S/H₂ on coordinatively unsaturated metal cations and neighboring S²⁻.¹²⁷

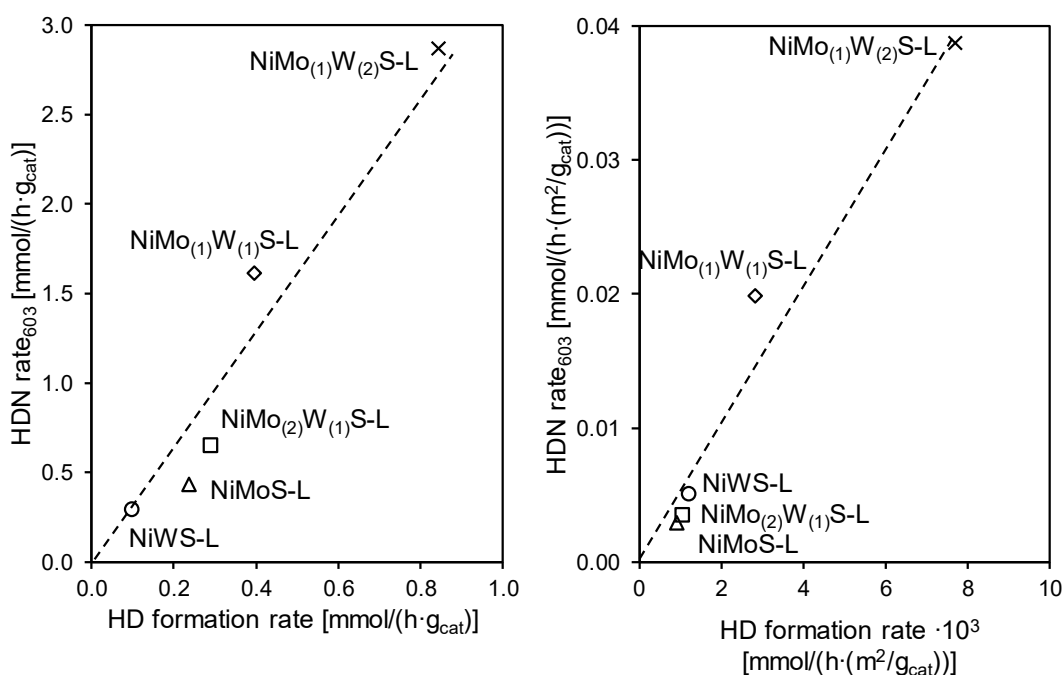


Figure 44. Correlation of the mass-specific (A) and areal-specific (B) HD formation rates (at 100 °C, 1 bar total) with the mass-specific and areal hydrodenitrogenation (HDN) rates (at 330 °C, 50 bar total) on NiMoS-L (△), NiMo₍₂₎W₍₁₎S-L (□), NiMo₍₁₎W₍₁₎S-L (◇), NiMo₍₁₎W₍₂₎S-L (x), and NiWS-L (○).

The HD formation rates determined this way (at 100 °C) were found to correlate with the hydrodenitrogenation activities in a linear fashion (Figure 44, (A)). The amount of HD formed as a function of residence time on each leached sulfide is shown in Figure 45.

Specifically, the most active catalyst NiMo₍₁₎W₍₂₎S-L in hydrodenitrogenation of quinoline also showed the highest HD formation rate, while the bimetallic sulfides, NiMoS-L and NiWS-L, showed the lowest HD formation rates and the lowest hydrodenitrogenation rate activities. These

results suggest that the sulfide phase composition influences the concentration of nickel substituted at the edges of the Mo(W)S₂ phase as well as the ability to stabilize sulfur vacancies in close proximity.

Due to the relatively low specific surface area, the areal concentration of SH groups was higher on the surface of NiWS-L than on NiMoS-L and NiMo₍₂₎W₍₁₎S-L, the two Mo-rich materials ($f_{\text{Mo}} = 0.77$ and 0.55), hence a somewhat different ranking when the HD formation rates and hydrodenitrogenation rates were normalized to mass specific surface areas (Figure 44, (B)). Nevertheless, by either of the standards (mass- or surface area-based), NiMo₍₁₎W₍₂₎S-L was the most active hydrodenitrogenation catalyst among the studied, as a result of the highest surface concentration of SH groups.

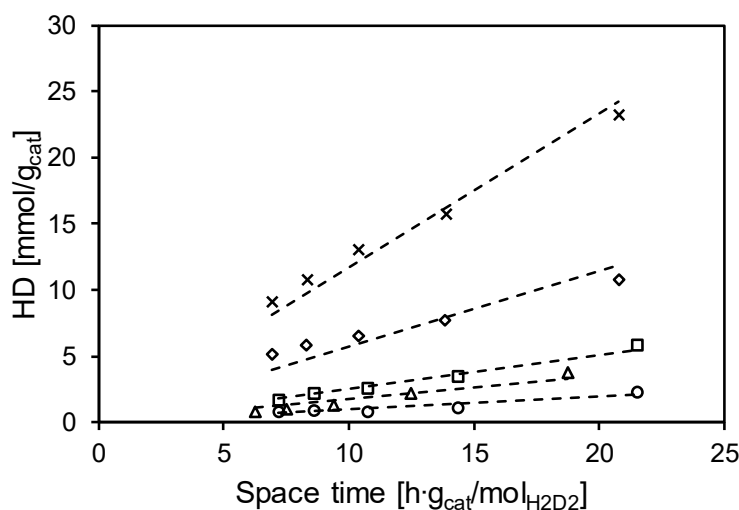


Figure 45. HD formation [mmol/g_{cat}] along with space time [h·g_{cat}/mol_{H₂D₂]} on NiMoS-L (Δ), NiMo₍₂₎W₍₁₎S-L (□), NiMo₍₁₎W₍₁₎S-L (◇), NiMo₍₁₎W₍₂₎S-L (x), and NiWS-L (○).

In general, a trimetallic sulfide phase is able to incorporate a higher concentration of nickel at the slab edge compared to the bimetallic sulfides, as also shown by Hein et al.⁴³ The trimetallic sulfide catalysts feature higher surface concentrations of edge-substituted nickel and thus more SH groups than bimetallic NiMo and NiW sulfides, perhaps due to a lower surface energy of the ternary sulfide phase compared to Ni-W and Ni-Mo facilitating the incorporation of nickel(II) cations at the slab edge.¹²⁶

Electronic properties also change by mixing molybdenum and tungsten cations within one sulfide slab leading to a more metallic character of the sulfide, an effect that increases with the fraction of tungsten cations in the Mo-W mixed sulfide phase since tungsten can provide more electrons than molybdenum and an increased availability of electrons above the Fermi level intensifies the metallic character.^{64, 126, 132} It is plausible that modulating the electronic properties of the sulfide slab affects primarily the dissociative adsorption of H₂/H₂S generating SH groups, but not so much the subsequent addition of hydrogen or C–N bond cleavage

events. Nevertheless, the catalytic consequences of these electronic effects are generally more difficult to predict.

Finally, the variation of reaction order in hydrogen along the hydrogenation pathway (Table 22) appears, to a large extent, also connected to the concentration of SH groups (reflected from H₂-D₂ scrambling rate; Figure 44) on these materials, showing that the higher the concentration of SH groups is, the larger the reaction order in hydrogen becomes. We surmise that the availability of SH groups in the vicinity of the adsorbed reactive intermediates could limit, at least in parts, the hydrogen addition rates, probably even suggesting that the rate of hydrogen supply is not high enough to keep up with the hydrogen addition rate under these conditions.

4. Conclusion

Post-synthetic treatment with boiling HCl of the unsupported NiMo, NiW, and NiMoW sulfides with different compositions removes the majority of undesirable complications, e.g., physical blockage of active sites, induced by the presence of nickel sulfide crystals. Compared to bimetallic NiMo and NiW sulfides, a Ni-Mo-W ternary sulfide phase leads to a higher overall hydrogenation activity for the two separate pathways, i.e., ring opening (minor, < 20%) and hydrogenation (major). Ring opening requires less strongly adsorbed species (presumably σ -adsorption) of quinoline, whereas hydrogenation reactions are mediated by strongly adsorbed species (π -adsorption of quinoline). While the rate of ring opening does not change with hydrogen partial pressure over the whole range of catalyst compositions studied, the sulfide phase composition causes systematic variations in the reaction order in hydrogen along the hydrogenation pathway. These considerations are consistent with the very different dependences of rates on the partial pressures of quinoline and hydrogen along ring opening and hydrogenation pathways.

In this work, differences in mass-specific activity are caused primarily by different concentrations of active sites, as the relative ratio of rate constants and measured activation energies for both, ring opening and hydrogenation, are essentially independent of the catalyst composition. Drawing on the correlation between the hydrodenitrogenation activity proceeding primarily via hydrogenation and the concentration of SH groups (indirectly probed by H₂-D₂ exchange rates) on the unsupported sulfide catalysts across a relatively wide range of compositions, this study demonstrates that the decisive factor in hydrogenation reactions is the concentration of SH groups.

This key parameter is controlled by the sulfide phase composition, as a high content of tungsten in a trimetallic sulfide phase leads to a high concentration of sulfur vacancies, which generate a correspondingly high concentration of SH groups via dissociative adsorption of H₂ and H₂S. A balanced molybdenum to tungsten ratio in the ternary phase leads to an optimal catalytic performance through empirically known effects of tungsten in dispersing nickel and promoting the formation of sulfur vacancies and that of molybdenum in enhancing the accessibility of reactive surfaces by improving textural characteristics.

Chapter 4

HYDROTREATING CATALYST –

Liquid-phase Sulfidation

1. Introduction

Unsupported trimetallic Ni-MoWS₂ catalysts show superior activity in the removal of heteroatoms, i.e., sulfur, nitrogen, and oxygen from heavy crude oil feedstocks compared to the conventionally used supported Ni-MoS₂ catalysts. This has increased interest and research activities on these trimetallic sulfide materials over the last decades.^{10-11, 21, 52, 64, 111}

In trimetallic sulfides, molybdenum and tungsten cations are statistically mixed within one sulfide slab.⁴³ The active phase of the trimetallic sulfide catalysts is the so-called Ni-MoW-S phase which is similar to the bimetallic Ni-MoS₂ and Ni-WS₂ phase, respectively.^{1, 6} In the model of active Ni-MoW-S phase nickel(II) cations are substituted into the edges of the Mo(W)S₂ slabs.^{1, 6, 114} The higher hydrotreating activity of trimetallic sulfides is rationalized by the higher concentration of nickel(II) cations substituted into the mixed Mo(W)S₂ slabs since the concentration of substituted nickel(II) cations is directly related to a higher concentration of catalytically active sites resulting in an increased hydrotreating activity.^{43, 65, 207} Hence, a key point in the preparation of the sulfide catalyst is to ensure a high substitution degree of nickel(II) cations into the Mo(W)S₂ slab and to avoid, in turn, any loss of nickel due to the formation of catalytically hardly active nickel sulfide entities.^{10, 88}

Because of their high hydrotreating activity a variety of new preparation methods of unsupported sulfide catalysts have been developed in the last decades. Most of these preparation methods require *in-situ* or *ex-situ* sulfidation.^{11, 52-53, 60, 145, 172, 208-209} A close interaction among all the metal cations is already present in the oxide precursor. In case of a trimetallic oxide precursor one layer is formed by [MoO₄]-tetrahedra and [WO₆]-octahedra which are edge or corner connected. The other layer consists of [NiO₆]-octahedra. The interactions of the various metal polyhedra results in a distortion of the them in the metallate structure. However, the structure of the oxide precursor is not homogeneous as a significant amount of the metal cations is still present in their corresponding oxide form, i. e., nickel oxide, molybdenum oxide, and tungsten oxide phases.⁶⁵

As a consequence of this heterogeneity, the conditions of the transformation of the oxide form into the active sulfide form have to be chosen carefully. The existing interactions among the metal cations in the oxide precursor ease substitution of nickel(II) cations in the Mo(W)S₂ slab.⁶⁵ But nickel(II) cations present in pure nickel oxide phases must also be substituted into the Mo(W)S₂ slab to enhance the concentration of active sites. This is challenging as the sulfidation process itself proceeds via a complex mechanism and differs for the three metal cations. The sulfidation process of each metal cation includes various O-S exchanges and redox reaction steps.^{15, 71, 80, 82, 210-211}

In case of molybdenum and nickel, the terminal oxygen(-II) anions (O^{2-}) groups at the oxide surface are first replaced by sulfur as they are relatively unstable. Driving force for the O-S exchange is the formation of water.^{15, 82} With increasing temperature, the formed oxysulfides undergo further O-S exchange, various reductions steps, and structural rearrangements until sulfidation is completed. Indeed, the various steps occur at different temperatures in the environment of nickel and molybdenum cations.^{15, 210} Sulfidation of nickel oxide phases is rather easy as it starts already at room temperature and is completed below 150 °C.^{15, 210, 212} But significantly higher temperatures are needed for the sulfidation of molybdenum oxide phases.^{15, 71, 210} Catteneo et al., for instance, showed using Quick-XANES that a temperature above 310 °C is needed for complete sulfidation of the molybdenum oxide phase in case of a NiMo/SiO₂ material. This study also showed that after the complete O-S exchange molybdenum trisulfide (MoS₃) is formed as intermediate and subsequently reduced to MoS₂.²¹⁰ Sulfidation of tungsten oxide phases require even harsher conditions than sulfidation of molybdenum due to the stronger tungsten-oxygen (W-O) bonds.^{15, 68, 213} In contrast to molybdenum and nickel, a reduction of tungsten is prerequisite prior to the first replacement of terminal oxygen anions groups by sulfur. The subsequent intramolecular redox reactions then lead to the formation of tungsten oxysulfide phases and result in the formation of tungsten trisulfide (WS₃). The final reduction to tungsten disulfide (WS₂), however, requires temperatures above 350 °C.^{68, 80-82, 214}

Thus, transformation of the oxide phase into the sulfide phase depends on temperature and takes place in the order nickel < molybdenum < tungsten. This trend remains also in mixed metal phases, although, the presence of nickel lowers the sulfidation temperature and increases the sulfidation rate of molybdenum and even more pronounced of tungsten.^{15, 68, 79, 215-216} The presence of molybdenum and tungsten in turn also influence the sulfidation of nickel as the sulfidation of nickel oxide species proceeds faster and at lower temperature in a trimetallic oxide compared to a bimetallic oxide.⁶⁵ Amongst others Hensen et al. observed via Mössbauer spectroscopy that during the formation of WS₂ from partly sulfided tungsten species already formed nickel sulfide species re-disperse resulting in the active Ni-W-S phase.⁶⁸

Nickel(II) cations can in principle end up in two Ni-containing species, i.e., substituted into the Mo(W)S₂ edge leading to the active Ni-Mo(W)-S phase or forming various nickel sulfide crystals. These nickel sulfide crystals, however, are hardly active in hydrotreating reactions and lower the amount of nickel available for edge substitution.^{88, 166} Consequently, formation of nickel sulfide crystals during sulfidation is detrimental for highly active catalyst and should, therefore, be minimized.

The sulfidation of a trimetallic oxide precursor is very challenging as the requirements of the transformation of three metals cations need to be addressed. Further, all transformations should occur within a narrow temperature range to ensure a maximum substitution degree of nickel into the Mo(W)S₂ edge. The key point is to retard the sulfidation of nickel in the trimetallic oxide precursor and simultaneously lower the sulfidation temperature of molybdenum and especially of tungsten to achieve a high nickel substitution degree. Moreover, phase agglomeration should be limited to enhance the accessibility of the active sites which are located at the sulfide slab perimeter.¹¹⁸

This work aims to study the liquid-phase sulfidation of a trimetallic oxide precursor in detail and to elucidate the impact of different sulfidation parameters on the texture and morphology finally leading to a more active hydrotreating catalyst. The hypothesis is to delay nickel sulfidation and limit phase agglomeration by a low chemical potential of sulfur and/or hydrogen during sulfidation. But this can also change the catalytic performance of the sulfide as the properties of the catalyst surface, such as surface Brønsted and Lewis acidity, might change. A different sulfiding agent could further influence sulfidation and sulfide properties by a higher decomposition temperature, different sulfiding agents, and/or a complexation effect of the alkyl entities.^{69, 78, 217} Indeed, this additionally might affect the morphology of the sulfide catalyst and the final catalytic performance.

The impact of these sulfidation parameters on the hydrotreating performance of the trimetallic sulfide catalyst was evaluated by performing hydrodenitrogenation of *o*-propylaniline simultaneously with hydrodesulfurization of dibenzothiophene and 4,6-dimethyldibenzothiophene. Conducting simultaneous hydrodenitrogenation and hydrodesulfurization reactions also elucidated the different requirements of the reactants on the catalyst surface and the mutual influence among the reactions. With this a sulfidation procedure can be designed which leads to a deep removal of heteroatoms as required to reach the legislative restrictions.

2. Experimental

2.1. Synthesis of the Trimetallic Oxide Precursor

A co-precipitation method was used to synthesize the trimetallic oxide precursor, designated as NiWMo-ox in the following.^{51, 53} First, ammonium molybdate ($(\text{NH}_4)_6\text{Mo}_7\text{O}_{24}\cdot 4\text{H}_2\text{O}$, Sigma Aldrich, $\geq 99.0\%$) and ammonium metatungstate ($(\text{NH}_4)_6\text{H}_2\text{W}_{12}\text{O}_{40}\cdot \text{H}_2\text{O}$, Sigma Aldrich, 99.0%) in a Mo:W ratio of 1:7 were dissolved in 360 mL bidistilled water. The solution was heated to $90\text{ }^\circ\text{C}$ under stirring and after reaching the temperature, the pH was adjusted to 9.5 using an aqueous ammonia solution (NH_4OH , Sigma Aldrich, $28.0\text{-}30.0\%$).

Subsequently, 1 mL pre-heated ($70\text{ }^\circ\text{C}$) aqueous nickel(II) nitrate hexahydrate ($\text{Ni}(\text{NO}_3)_2$, Sigma-Aldrich, $\geq 98.5\%$) solution was added, and the pH was again adjusted to 9.5. This procedure was repeated twice, i.e., adding 1 mL of nickel(II) nitrate solution and adjusting the pH each time. Thereafter, the remaining nickel(II) nitrate solution (18 mol/L) was added dropwise while the oxide precursor precipitated. After another 30 minutes at $90\text{ }^\circ\text{C}$, stirring was stopped and the mixture was hot filtrated. The precipitated solid after filtration was suspended in an aqueous solution of maleic acid (0.05 M , Fluka, $\geq 98.0\%$) and kept at $70\text{ }^\circ\text{C}$ for 30 minutes while stirring. After filtration and drying in vacuum overnight, the powdered precursor was dried in synthetic air (100 mL/min) at $120\text{ }^\circ\text{C}$ for 12 hours.

2.2. Liquid-phase Sulfidation

The oxide precursor NiWMo-ox was used in all sulfidation experiments. The sulfidation experiments were conducted in a glass-coated trickle bed downflow-reactor. The liquid feed was introduced via a HPLC pump (Shimadzu LC-20AD) whereas high-pressure mass flow controllers (MFCs, Bronkhorst) were used to control the flow rates of gases. The pressure was regulated by a mechanical back-pressure valve (with a gauge) and the temperature was controlled via an Eurotherm controller. NiWMo-ox (300 mg) was diluted with silicon carbide (SiC, ESK-SiC GmbH, $500\text{-}1000\text{ }\mu\text{m}$) and fixed inside the flow-reactor with glass wool.

The temperature program applied in all sulfidation procedures is depicted in Figure 46. First, the oxide precursor (NiWMo-ox) was dried at $120\text{ }^\circ\text{C}$ in nitrogen (N_2) atmosphere (40 mL/min) for 20 hours. Thereafter, the operating pressure was set and the S-containing liquid feed (0.2 mL/min) and hydrogen flow were introduced. The temperature was increased from 120 to $250\text{ }^\circ\text{C}$ ($1\text{ }^\circ\text{C/min}$). After 2 hours at $250\text{ }^\circ\text{C}$, the content of sulfur in the liquid feed was increased and the temperature was maintained for another 2 hours at $250\text{ }^\circ\text{C}$. After increasing the temperature to $350\text{ }^\circ\text{C}$ ($1\text{ }^\circ\text{C/min}$) the content of sulfur in the liquid feed was further increased. After a dwell of 2 hours at $350\text{ }^\circ\text{C}$, heating was stopped. Liquid and gas flows were maintained

at the same flow rates during cooling. They were turned off and the pressure was released when room temperature was reached. In all experiments, *cis, trans*-decahydronaphthalene (decalin, C₁₀H₁₈, Merck Millipore, ≥99.0 %) was used as the solvent. The H₂ flow was adjusted in each sulfidation step to the particular molar H₂/S ratio of the experiment. Nitrogen was accordingly supplemented to keep a constant total volumetric flow (160 mL/min).

Table 23 summarizes the sulfidation parameters varied in the respective sulfidation protocols.

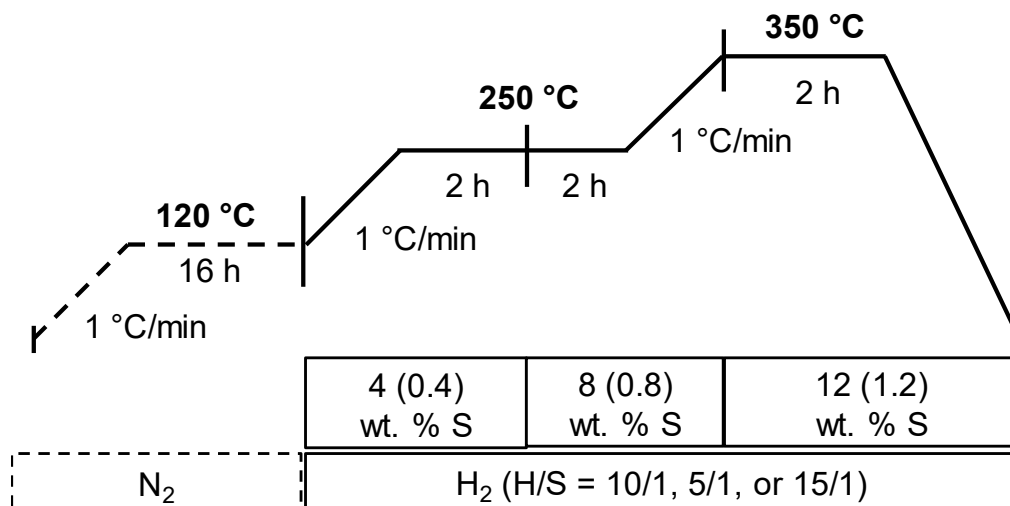


Figure 46. Scheme of the temperature program used in the different sulfidation procedures including the changes of the liquid feed. The numbers in brackets show the content of sulfur (S) in the procedures “S-min” and “BT-min”. The H/S ratio was varied to 5 and to 15 in the procedures “S-H/S-” and “S-H/S+”, respectively.

In the standard sulfidation procedure (“S-ref”) the total pressure was set at 20 bar and the H₂/S ratio was 5 in each sulfidation step. The S content was increased from 4 wt. % S in the first step to 8 wt. % S (Step 2), and finally in step 3 to 12 wt. % S. Dimethyl disulfide (C₂H₆S₂, Sigma Aldrich, ≥99.0 %) was chosen as sulfiding agent.

The impact of an increased total pressure (“S-p+”) was investigated by setting the total pressure to 40 bar instead of 20 bar in the “S-ref” procedure. The other sulfidation parameters of the “S-ref” protocol remained.

n-butanethiol (BT, C₄H₉SH, Sigma Aldrich, 99.9 %) was used as alternative sulfiding agent (“S-BT”). The amounts of *n*-butanethiol in the liquid sulfidation mixture were calculated to 4 wt. % S (Step 1), 8 wt. % S (Step 2), and 12 wt. % S (Step 3) to the “S-ref” protocol.

The impact of a lower S content using different sulfiding agents was studied in the sulfidation procedures “S-min” and “S-BT-min”. Therefore, the S content was lowered by a factor of 10 in each sulfidation step, i.e., 0.4 wt. % S (Step 1), 0.8 wt. % S (Step 2), and 1.2 wt. % S (Step 3). In the “S-min” protocol dimethyl disulfide was used as sulfiding agent while *n*-butanethiol was

used as sulfiding agent in the “S-BT-min” procedure. In both procedures, the H₂/S ratio was set to 5 in each sulfidation step.

In the sulfidation protocols of “S-H/S+” and “S-H/S-” the H₂/S ratio was changed from the standard H₂/S ratio of 5 (“S-ref”) to 7.5 and 2.5, respectively. The other parameters were the same as in the “S-ref” procedure, i.e., dimethyl disulfide was used as sulfiding agent and the total pressure was set at 20 bar.

Table 23. Sulfur (S) content [wt. %], sulfiding agent, H₂/S ratio, and total pressure [bar] used in the different sulfidation protocols.

Sulfidation procedure	S content [wt. %]	Sulfiding agent	H ₂ /S ratio	Total pressure [bar]
S-ref	4, 8, 12	Dimethyl disulfide	5	20
S-p+	4, 8, 12	Dimethyl disulfide	5	40
S-min	0.4, 0.8, 1.2	Dimethyl disulfide	5	20
S-H/S+	4, 8, 12	Dimethyl disulfide	7.5	20
S-H/S-	4, 8, 12	Dimethyl disulfide	2.5	20
S-BT	4, 8, 12	<i>n</i> -Butanethiol	5	20
S-BT-min	0.4, 0.8, 1.2	<i>n</i> -Butanethiol	5	20

2.3. Kinetic measurements

The catalytic performance of the resulting sulfides was evaluated in a simultaneous hydrodenitrogenation of *o*-propylaniline and hydrodesulfurization of dibenzothiophene and 4,6-dimethyldibenzothiophene.

The activity tests were conducted in the same glass-coated trickle bed downflow-reactor as liquid-phase sulfidation. The reactor was loaded with 15-25 mg of the sulfide catalyst diluted 1:4 with silicon carbide (SiC, ESK-SiC GmbH, 63-90 μm).

Prior to kinetic measurements, the catalysts were re-sulfided in liquid-phase with a liquid feed containing 4 wt. % S as dimethyl disulfide or *n*-butanethiol, according to the sulfiding agent used during sulfidation. The H_2/S ratio and the total pressure during re-sulfidation were set in accordance to the previous sulfidation conditions. In any case, the temperature was set to 250 °C (2 °C/min, 2 hours dwell) and the pressure at 20 bar during re-sulfidation expect for the “S-p+” sulfide where a pressure of 40 bar was also applied during re-sulfidation.

For the kinetic measurements, the liquid feed contained 100 ppm N as *o*-propylaniline ($\text{C}_9\text{H}_{13}\text{N}$, Sigma-Aldrich, 97 %) and 500 ppm S as dibenzothiophene ($\text{C}_{12}\text{H}_8\text{S}$, Sigma-Aldrich, ≥ 99 %) and 4,6-dimethyldibenzothiophene ($\text{C}_{14}\text{H}_{12}\text{S}$, Sigma-Aldrich, 97 %) each. Moreover, ethylcyclohexane (1 wt. %, C_8H_{16} , Sigma-Aldrich, ≥ 99 %) was added as internal standard for GC analysis of the liquid product stream. Dimethyl disulfide (0.15 wt. %, $\text{C}_2\text{H}_6\text{S}_2$, Sigma-Aldrich, ≥ 99 %) or *n*-butanethiol (0.29 wt. %, $\text{C}_4\text{H}_9\text{SH}$, Sigma Aldrich, 99.9 %), according to the sulfiding agent used in the sulfidation procedure, were added to the liquid feed to prevent catalyst deactivation. *Cis*, *trans*-decahydronaphthalene (decalin, $\text{C}_{10}\text{H}_{18}$, Merck Millipore, ≥ 99.0 %) was used as solvent.

The hydrocarbon to H_2 ratio was 1:300 Ndm^3/dm^3 . The total pressure during the kinetic measurements was 50 bar while the temperature ranged from 310-350 °C.

The impact of the individual reactants was investigated on the catalyst sulfided with the procedure “S-ref”. In a series of experiments the content of *o*-propylaniline in the feed was varied from 50 ppm N over 100 ppm N to 200 ppm. The content of dibenzothiophene and 4,6-dimethyldibenzothiophene was maintained at 500 ppm S.

For another set of experiments, only two reactants were tested simultaneously, i.e., the liquid feeds contained 200 ppm N as *o*-propylaniline and 500 ppm S in form of dibenzothiophene or 4,6-dimethyldibenzothiophene or the liquid feed contained 500 ppm of each S-containing compound.

As in the other experiments, the solvent was decalin and ethylcyclohexane and dimethyl disulfide were also added to the liquid feed (vide infra). Moreover, the hydrocarbon to H_2 ratio

was again 1:300 Ndm³/dm³. The total pressure was equally set to 50 bar and the temperature ranged also from 310-370 °C.

Prior to data acquisition the catalyst was first stabilized for 12 hours on stream at 350 °C to obtain results representative of stable catalysts. Thereafter, each temperature was kept constant for at least 6 hours to ensure steady state prior to sampling. Samples of the product stream were taken using a 16-port valve every hour and analyzed via an off-line gas chromatograph (HP 6890). This GC was equipped with a flame ionization detector (FID) and an Agilent DB-17 capillary column.

In data evaluation, isomers of products were lumped together and treated as one species, e.g., 1-propylcyclohexene, 3-propylcyclohexene, and propylidene cyclohexane are summarized to propylcyclohexene. Catalyst deactivation during the experiment was below 5 % on all tested sulfides. The carbon mass balance was for all kinetic experiments in the range of ±3 %.

2.4. Characterization

Elemental analysis of the oxide precursor NiWMo-ox and the sulfide catalysts were carried out at the microanalytic laboratory of the Technische Universität München. The concentrations of nickel, molybdenum, and tungsten were determined photometrically whereas the contents of hydrogen, carbon, nitrogen, and sulfur were analyzed by an automated element analyzer instrument (Vario EL CHN Analyser, ELEMENTAR).

Specific surface area and pore volume of the oxide precursor NiWMo-ox and all synthesized sulfides were determined using BET and BJH analysis. Isotherms of adsorption and desorption of nitrogen at -196 °C were measured with an automated nitrogen adsorption analyzer Sorptomatic 1990 Series (Thermo Finnigan). Before the measurements, all samples were evacuated at 120 °C for 4 hours.

Crystalline phases present in the oxide precursor NiWMo-ox and the sulfides were identified using powder X-ray diffraction (XRD). All XRD measurements were performed in a PANalytical system equipped with a copper X-ray tube (Cu-K α radiation, 0.154 nm), a nickel K β -filter, and solid-state detector (X'Celerator) operated at 45 kV and 40 mA with step size of 0.017° and scan time of 115 seconds per step. The different reflections were identified by means of reference diffractograms of commercially available compounds (MoS₂ (Sigma-Aldrich, 99 %) and WS₂ (Sigma-Aldrich, 99 %), and the inorganic crystal structure database (ICSD).¹⁸²

Transmission electron microscopy (TEM) was carried out in a TEM instrument (JEOL JEM 2010) equipped with a LaB₆-cathode with an accelerating voltage of 120 kV. The specimens of the oxide precursor NiWMo-ox and the sulfides were prepared by grinding a small amount of material and dispersing it ultrasonically in absolute ethanol (Merck Millipore). Subsequently, drops of this suspension were applied on a copper grid (200 mesh) with a lacey carbon film (Quantifoil Micro Tools) and the ethanol was evaporated at room temperature.

Temperature-programmed sulfidation (TPS) of the trimetallic oxide precursor NiWMo-ox (100 mg, 250-355 μ m) was performed in a quartz-tube flow-reactor placed in a ceramic oven. A thermocouple was twisted around the quartz tube at the height of the precursor and the temperature was controlled by Eurotherm controllers. The gas flow (H₂, N₂, He, and 10 vol. % H₂S in H₂) was regulated by mass flow controllers (Bronkhorst). The outlet of the reactor was connected to a quadrupole mass spectrometer (Pfeiffer Vacuum Blazers QME 200) which detected the evolved gas stream. The mass spectrometer recorded the signals of the masses (m/e) 2 (H₂) and 34 (H₂S). Thus, evolution and consumption of H₂ and H₂S were monitored along with temperature. Prior to the TPS, the oxide precursor was dried at 120 °C (5 °C/min) in N₂ atmosphere (10 mL/min) for 2 hours. After cooling to 40 °C, a mixture of 10 vol. % H₂S in H₂ (10 mL/min) was introduced and the temperature was increased to 900 °C at a ramp rate

of 2 °C/min. At 900 °C the conditions were kept constant for 2 hours before cooling down to room temperature.

Electronic and structural changes of the metals in the trimetallic oxide precursor during liquid phase sulfidation was followed along with temperature by *in-situ* X-ray absorption spectroscopy (XAS) at the BM 26A—DUBBLE, (Dutch-Belgian) beamline at the ESRF, Grenoble, France. Spectra were recorded in the fluorescence mode at the Ni K-edge (8333 eV), the Mo K-edge (20000 eV), and the W L_{III}-edge (10207 eV). The samples were on weight-bases diluted in a ratio of 1:3 with boron nitride (BN, ≥ 98 %, Sigma-Aldrich). After pressing and sieving (250-355 μm) the sample was placed in a quartz-capillary reactor (1 mm outer diameter, 0.02 mm wall thickness (WJM-Glas)). The gas flow (H₂ and He) was controlled by mass flow controllers (Bronkhorst) while the liquid flow was regulated by a HPLC pump (Shimadzu LC-20AD). A hot air gas blower (FMB Oxford) equipped with a controller heated the capillary reactor with an accuracy of 1 °C. The pressure was set to 4 bar using a back-pressure regulator (Swagelok). The H₂/S ratio (S as dimethyl disulfide) was 5 during liquid-phase sulfidation and the solvent was *cis, trans*-decahydronaphthalene (decalin, C₁₀H₁₈, Merck Millipore, ≥99.0 %). The temperature was increased stepwise and several EXAFS scans were taken at 30, 120, and at an interval of every 25 °C from 200 °C until 350 °C. The measured reference compounds were also mixed with BN. All spectra were analyzed with the Demeter-package (ATHENA and ARTEMIS, version 0.9.26). After background correction to the average post-edge height of one, the EXAFS scans of the same temperature step were merged.

Linear combination fitting (LCF) was applied to follow the temperature-dependent change of the metal cation from an oxide to a sulfide coordination sphere. LCF of the spectra of the sulfide catalysts were performed using the recorded EXAFS spectra of the references nickel(II) oxide (NiO, Sigma-Aldrich, 99.99 %), nickel(II) hydroxide (Ni(OH)₂, Sigma-Aldrich), molybdenum(IV) oxide (MoO₂, Sigma-Aldrich, 99 %), molybdenum(VI) trioxide (MoO₃, Sigma-Aldrich, 99.97 %), nickel(II) molybdenum oxide (NiMoO₄, Alfa Aesar, ≥ 98 %), tungsten(VI) trioxide (WO₃, Sigma-Aldrich, 99.9 %) nickel(II) tungstate (NiWO₄, Alfa Aesar, ≥ 99.9 %), nickel subsulfide (Ni₃S₂, Sigma-Aldrich, 99.7 %), molybdenum(IV) disulfide (MoS₂, Sigma-Aldrich, 99 %), and tungsten(IV) disulfide (WS₂, Sigma-Aldrich, 99 %).

3. In-situ XAS Investigation of the Liquid-phase Sulfidation

The merged EXAFS scans recorded at all three metal edges are shown in Figure 47. The decrease of the white line on the nickel K-edge indicates a decreasing ionic character of the absorber atom with increasing temperature.^{65, 218-219} This phenomenon appears between the EXAFS spectra taken at 225 and 250 °C and suggests the transformation of nickel oxide species into nickel sulfide species (Figure 47, (A)). The pre-edge feature (~8327 eV) arises from the electric dipole transition from an *s* orbital to the *p* component of a *d-p* hybrid orbital and is typical for nickel cations in a distorted octahedral coordination sphere. The presence of the pre-edge feature in all EXAFS spectra (see Appendix Figures A94-A96), irrespective of the sulfidation temperature, indicates that one nickel(II) cation (Ni^{2+}) is surrounded by six oxygen atoms forming a distorted octahedra.^{65, 218, 220}

In the same temperature range observed for the transformation of nickel sulfidation of molybdenum also occurs. This can be clearly seen from the disappearance of the intense pre-edge feature at ~20003 eV typical for molybdenum in the oxidation state VI. Thus, molybdenum is present as molybdenum(VI) cation (Mo^{6+}) in the oxide precursor. In the resulting sulfide, in contrast, molybdenum cations are coordinated trigonal prismatic and are present in the oxidation state IV. Consequently, the pre-edge peak disappeared between a sulfidation temperature of 225 and 250 °C (Figure 47, (B)).^{65, 220-221}

Like molybdenum, tungsten is present in the oxidation state VI (W^{6+}) in the oxide precursor and is reduced to IV (W^{4+}) during the sulfidation process as comparison with reference spectra of NiWO_4 and WS_2 revealed. However, the transformation of tungsten requires higher sulfidation temperature compared to nickel and molybdenum as it was sulfided between 275 °C and 300 °C (Figure 47, (C)). This is related to the stronger W-O bond compared to the Mo-O and Ni-O bonds.^{15, 68, 81, 85, 215}

A linear combination fit (LCF) was performed to follow the transformation of each metal cation from its oxide environment to its sulfide environment as a function of temperature. As references recorded spectra of NiO , $\text{Ni}(\text{OH})_2$, Ni_3S_2 , MoO_2 , MoO_3 , NiMoO_4 , MoS_2 , WO_3 , NiWO_4 , and WS_2 were used to determine the fractions of the oxide and sulfide phases of the corresponding metal cation. Intermediate phases such as oxysulfides were not taken into account in the LCF analysis.

A good fit of the oxide precursor at 30 °C for the nickel K-edge spectra of the trimetallic sample was achieved using solely the references NiO and NiMoO_4 . The NiWO_4 component was not needed due to the similar octahedral coordination sphere of nickel(II) cations in NiMoO_4 and NiWO_4 (Table 24).²²²⁻²²⁵

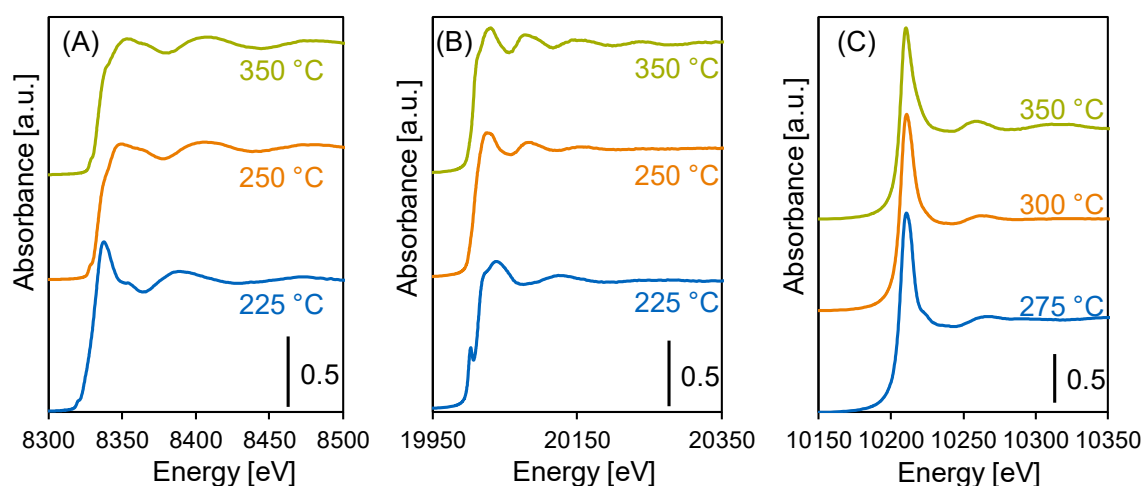


Figure 47. Merged and normalized EXAFS spectra of the trimetallic NiWMo-ox oxide precursor recorded during liquid phase sulfidation at (A) the Ni K-edge, (B) the Mo K-edge, and (C) the W L_{III}-edge at 225, 250, 275, and 350 °C at 4 bar.

The environment of nickel(II) cations in the oxide precursor can be satisfactorily fitted by almost equal proportions of NiO (57 %) and NiMoO₄ (43 %) in the oxide precursor.

The LCF analysis shows that sulfidation of nickel occurred as soon as the sulfidation was started (from 120 °C). Already at 200 °C half of nickel was sulfided. Note that the fraction of nickel which was sulfided seems to arise solely from nickel atoms present in a NiMoO₄ environment as the proportion of NiMoO₄, needed for a sufficient fit, decreased dramatically as soon as sulfidation started.

This suggests that the covalent Ni-O bonds in the [NiO₆]-octahedra of the wolframite-type NiMo(W)O₄ structure are very labile. In contrast, transformation of the NiO environment into a nickel sulfide is more challenging as a higher temperature was needed (Table 24).

This is surprising as NiO crystallized in a NaCl-type structure. Therefore, the Ni-O bond is ionic, which should be weaker than covalent Ni-O bonds.²²⁶⁻²²⁷ The corner connection of [NiO₆]-octahedra with both [MoO₆]- and [WO₆]-octahedra seems therefore to considerably weaken the covalent Ni-O bond and facilitate the nickel O-S exchange.^{222, 224} This is in line with the observation of Hein et al. who found using an *in-situ* quick-XANES study that nickel starts to sulfide at lower temperature in a trimetallic oxide precursor compared to the bimetallic oxide precursors.⁶⁵ However, the nickel cation was completely sulfided at 300 °C and higher. Thus, sulfidation of nickel proceeded over a wide temperature range (Figure 48, (A)). We surmise that this is related to the close interaction of nickel with molybdenum and tungsten directly influencing the transformation of Ni-O to Ni-S. A re-dispersion of nickel(II) cations and subsequent substitution into the Mo(W)S₂ edge, as suggested in literature, is a possible explanation for this.^{68, 82, 85, 214, 228}

Table 24. Fractions of nickel(II) oxide (NiO), nickel(II) hydroxide (Ni(OH)₂), nickel(II) ammonium molybdenum oxide (NiMoO₄), nickel(II) tungstate (NiWO₄), and nickel sulfide (Ni₃S₂) estimated from the linear combination fit (LCF) analysis of the XAS spectra at the Ni K-edge at the indicated temperature [°C]. The goodness of the LCF is indicated by the R-factor.

Temperature [°C]	Weight of used EXAFS [%]					R-factor
	NiO	Ni(OH) ₂	NiMoO ₄	NiWO ₄	Ni ₃ S ₂	
30	56.9	-	43.1	-	-	0.0349
120	57.1	-	42.9	-	-	0.0348
200	52.8	-	-	-	47.21	0.0966
225	47.7	-	-	-	52.3	0.1718
250	4.2	-	8.0	-	87.8	0.0012
275	7.3	-	-	-	92.7	0.0127
300	-	-	0.2	-	99.8	0.0173
325	-	-	-	-	100.0	0.0029
350	-	-	-	-	100.0	0.0627

The LCF analysis of the Mo K-edge spectra reveals that the molybdenum cations are mostly in a coordination environment as in NiMoO₄ (80 %). However, a fraction of 20 % as MoO₂ was needed to obtain a satisfactory fit. The sulfidation of molybdenum cations started between 200-225 °C (Table 25), with the MoS₂ component increasing to approximately 13% mainly at the expense of MoO₂ component. This suggests that the Mo-O bond in a MoO₂ environment is more prone to O-S exchange than the Mo-O bond in a NiMoO₄ environment. The largest fraction of molybdenum was transformed into a sulfide at temperatures between 225-250 °C and sulfidation was nearly complete around ca. 300 °C. Thus, sulfidation of Mo occurs in a narrower temperature window (within 100 °C) than sulfidation of nickel (Figure 48, (B)) though, the sulfidation ranges of both cations overlapped and ended at 300 °C.

The LCF analysis of the W L_{III}-edge spectra reveals that tungsten (W) cations are surrounded by a coordination sphere comparable to wolframite-type structure of NiWO₄ (Table 26).²²² Sulfidation of tungsten started at 300 °C but was complete already at 325 °C (Figure 48, (C)).

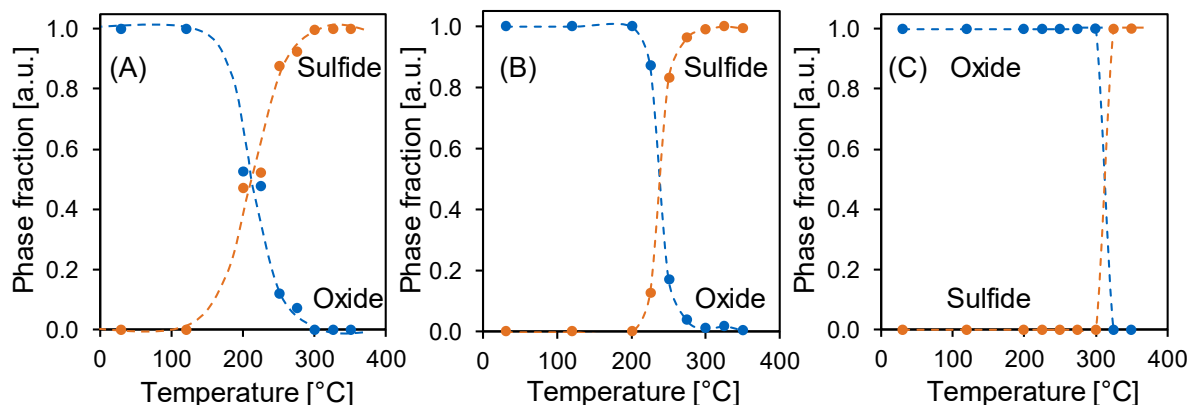


Figure 48. Fractions of (A) the nickel oxide (blue) and the nickel sulfide phase (orange), (B) the molybdenum oxide (blue) and the molybdenum sulfide phase (orange), and (C) the tungsten oxide (blue) and the tungsten sulfide phase (orange) phase as a function of temperature, obtained via linear combination fit (LCF) analysis of the recorded EXAFS spectra at 4 bar.

Table 25. Fractions of molybdenum(IV) dioxide (MoO_2), molybdenum(VI) trioxide (MoO_3), nickel(II) molybdenum oxide (NiMoO_4), and molybdenum disulfide (MoS_2) estimated from the linear combination fit (LCF) analysis of the XAS spectra at the Mo K-edge at the indicated temperatures [°C]. The goodness of the LCF is indicated by the R-factor.

Temperature [°C]	Weight of used EXAFS [%]				R-factor
	MoO_2	MoO_3	NiMoO_4	MoS_2	
30	19.6	-	80.4	-	0.0085
120	19.1	-	80.9	-	0.0090
200	18.5	-	81.5	-	0.0068
225	10.1	-	77.1	12.7	0.0058
250	9.9	-	7.1	83.0	0.0142
275	0.7	-	3.0	96.2	0.0135
300	-	-	1.0	99.0	0.0151
325	-	-	1.8	100	0.0076
350	-	-	0.5	99.5	0.0050

The delayed sulfidation of nickel and molybdenum cations might be caused by the sulfidation of tungsten. In line with this, Kishan et al. and Hensen et al. proposed that the re-dispersion of nickel is initiated by the sulfidation of tungsten.^{68, 85} This re-dispersion favors the incorporation of nickel(II) cations into the Mo(W)S_2 edge finally leading to a higher concentration of active sites. Anyhow, complete sulfidation of nickel and molybdenum occur around 300 °C parallel to the complete sulfidation of tungsten.

The *in-situ* XAS investigation of the liquid phase sulfidation shows that the applied standard sulfidation conditions applied in this work (the highest temperature being 350 °C) lead to a complete sulfidation of all three metals. Consequently, the chosen parameters suggest a close interaction of molybdenum and tungsten cations with the nickel(II) cation resulting in a higher fraction of nickel(II) cations substituted at the Mo(W)S₂ edge and thus a more active sulfide catalyst.

Table 26. Fractions of tungsten(VI) trioxide (WO₃), nickel(II) tungstate (NiWO₄), and tungsten disulfide (WS₂) estimated from the linear combination fit (LCF) analysis of the XAS spectra at the W L_{III}-edge at the indicated temperatures [°C]. The goodness of the LCF is indicated by the R-factor.

Temperature [°C]	Weight of used EXAFS [%]			R-factor
	WO ₃	NiWO ₄	WS ₂	
30	-	100.0	-	1.0732
120	-	100.0	-	1.2999
200	-	100.0	-	1.3406
225	-	100.0	-	0.9198
250	-	100.0	-	1.2292
275	-	100.0	-	1.2424
300	-	100.0	-	1.4680
325	-	-	100.0	1.7512
350	-	-	100.0	1.8866

4. Temperature-programmed Sulfidation

Temperature-programmed sulfidation (TPS) of the trimetallic oxide precursor NiWMo-ox was performed in gas phase (10 vol. % H₂S in H₂) at atmospheric pressure. The recorded TPS profile (Figure 49) shows that the consumption of H₂S already started at 100 °C. This is attributed to the O-S exchange which is claimed to be the first step in the sulfidation process of nickel and molybdenum.^{15, 65-66, 84}

Herein, the H₂S consumption below 200 °C is mainly attributed to the O-S exchange in the environment of nickel(II) cations (Ni²⁺) due the weaker Ni-O bond strength compared to Mo-O bond strength.^{15, 39, 71} Most H₂S was consumed between 200 and 400 °C. The consumption of H₂ in the same temperature range indicates reduction of the metal cations which is another part reaction in the complex sulfidation mechanism.^{15, 71, 82, 229} In the case of tungsten, van der Vlies et al. showed that the reduction of tungsten is prerequisite prior to the O-S exchange because of the strong W-O bond.⁸⁰⁻⁸¹ Therefore, we surmise that the H₂S consumption peak at 450°C can be assigned to the sulfidation of tungsten.

A differentiation between the sulfidation temperatures of the three different metal cations, however, cannot be made because of the broad consumption ranges. The lack of distinct H₂ consumption peaks is in line with the result from the *in-situ* XAS analysis of the liquid-phase sulfidation which also showed that the different sulfidation steps of the metal cations overlapped. Note that the sulfidation temperatures of molybdenum and tungsten in the trimetallic catalyst precursor are lower than in the references MoO₃, NiMoO₄, WO₃, and NiWO₄ (Appendix Figures A97-A101).^{84, 230-231}

The lower sulfidation temperatures of molybdenum and tungsten cations in the trimetallic oxide precursor compared to the respective pure oxide references suggests that the interaction in the precursor weakens the metal-O bond strength and in turn, facilitates the O-S exchange. Moreover, the reduction of the metal cations may be favored. A close interaction among the metal cations already present in the oxide precursor, as proposed by Hein et al., facilitates the transformation of the oxide form into the sulfide form, especially of molybdenum and tungsten leading to a more active sulfide catalyst.⁶⁵ However, the differences in sulfidation temperatures obtained in the TPS and the *in-situ* XAS can be attributed to the pressure difference and the different sulfiding agents between the gas-phase and liquid-phase sulfidation procedures.

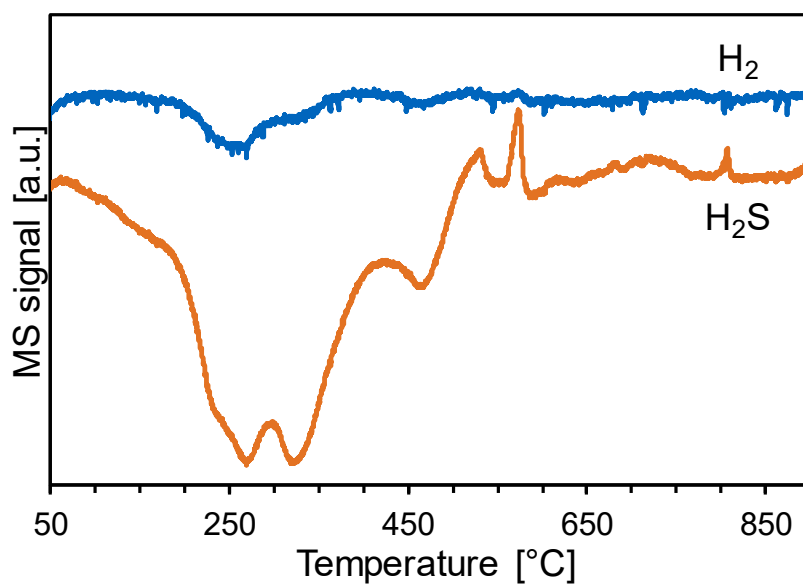


Figure 49. Profile of the temperature-programmed sulfidation of the trimetallic oxide precursor NiWMo-ox using a flow of 10 vol. % H₂S in H₂ (10 mL/min) at atmospheric pressure. The H₂S consumption is depicted by the orange line whereas the blue line indicates the consumption of H₂ as temperature increases.

5. Reaction Networks for the Conversion of the Reactants

Hydrodenitrogenation and hydrodesulfurization reactions can proceed generally via two parallel pathways. One conversion route is the direct removal of the heteroatom from the reactant. In the other pathway, (partial) hydrogenation of the reactant occurs before the heteroatom is removed.^{6, 17} This pathway requires π -adsorption of the reactant on the catalyst surface whereas the reactant adsorbs in a σ -mode in the case of the direct removal of heteroatoms. Thus, both conversion routes occur on different active sites.^{1, 32} Since the adsorption mode is influenced by the electronic and constitutional structure of the reactant, the pathway selectivity depends also on the nature of the reactant and thereby especially the environment of the heteroatom.^{6, 32, 193}

In the following section the reaction network of the hydrodenitrogenation of *o*-propylaniline, the hydrodesulfurization of dibenzothiophene and of 4,6-dimethyldibenzothiophene are analyzed for a reaction mixture containing all these three reactants. The pathway selectivity of these simultaneously occurring reactions was influenced by the sulfidation procedure and the temperature (section 7) but the products detected were the same for all performed experiments. The kinetic data shown in this section was obtained on a catalyst sulfided via the "S-ref" procedure (Table 23).

5.1. Hydrodenitrogenation of *o*-propylaniline

In the reaction network for the hydrodenitrogenation of *o*-propylaniline, *o*-propylcyclohexylamine, the isomers of propylcyclohexene, i.e., 1-propylcyclohexene, 3-propylcyclohexene, and propylidene cyclohexane, as well as propylcyclohexane, and propylbenzene are possible products.^{32, 38, 188, 232} All experiments were conducted in the presence of dibenzothiophene and 4,6-dimethyldibenzothiophene.

Propylcyclohexene and propylcyclohexane were the main product detected while *o*-propylcyclohexylamine was not detected (Figure 50).

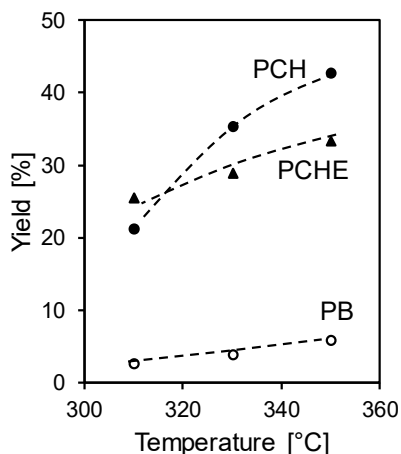


Figure 50. Yields of the products of hydrodenitrogenation of *o*-propylaniline as function of temperature. Propylcyclohexene (\blacktriangle , PCHE) and propylcyclohexane (\bullet , PCH) are assigned to the hydrogenation pathway whereas propylbenzene (\circ , PB) is possibly the product of the direct denitrogenation pathway. The catalyst was the one produced from sulfidation protocol "S-ref" (Table 23). The reaction mixture also contained DBT and DMDBT (see Experimental).

In agreement with literature and the products detected, it is assumed that the hydrodenitrogenation of *o*-propylaniline proceeds via the following reaction network on all catalysts tested (Figure 51).

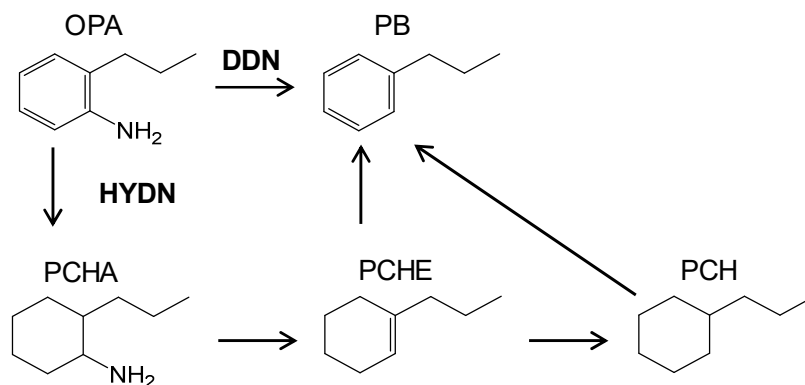


Figure 51. The hydrodenitrogenation of *o*-propylaniline (OPA) can proceed via two possible pathways the direct denitrogenation (DDN) to propylbenzene (PB) and the hydrogenation pathway (HYDN) to form *o*-propylcyclohexylamine (PCHA). The isomers of propylcyclohexene (PCHE) are formed after the removal of nitrogen. PCHE can be hydrogenated to PCH and both, PCHE and PCH, can be dehydrogenated to PB. The reverse direction of each step is not indicated.

Along the hydrogenation pathway, the aromatic ring of *o*-propylaniline is first hydrogenated to *o*-propylcyclohexylamine. Subsequently, nitrogen is removed by splitting the C(sp³)-N bond to form propylcyclohexene. The C=C bond of propylcyclohexene is further hydrogenated to propylcyclohexane.

As *o*-propylcyclohexylamine was not detected, its conversion to propylcyclohexene must be faster than its formation. Thus, the rate determining step of this pathway, if any, is assumed to

be one of the hydrogenation steps along the route of the conversion of *o*-propylaniline to *o*-propylcyclohexylamine.

The other possible conversion pathway of *o*-propylaniline, the so-called direct denitrogenation pathway, starts with the direct removal of nitrogen via C(sp²)-N bond cleavage to form propylbenzene. However, propylbenzene was only detected in rather low amounts even at the highest temperature studied (Figure 50).

Propylbenzene can also be formed via dehydrogenation of propylcyclohexene or propylcyclohexane. *o*-Propylaniline was mainly converted via the hydrogenation pathway, as the hydrogenation rate was 25 times faster than the direct denitrogenation rate for the studied range of reaction temperature (Figure 52). The preference of hydrogenation compared to direct denitrogenation is attributed to the stronger bond strength of the C(sp²)-N bond compared to the C(sp³)-N bond.^{39, 161, 184, 188}

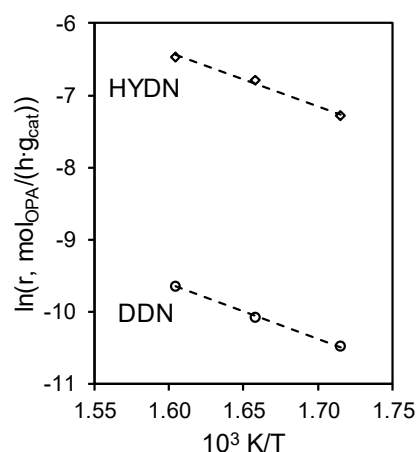


Figure 52. Reaction rates of the direct denitrogenation of *o*-propylaniline (○, DDN) and the hydrogenation route of *o*-propylaniline (◇, HYDN) as a function of temperature. The catalyst was the one produced from sulfidation protocol “S-ref” (Table 23). The reaction mixture also contained DBT and DMDBT (Experimental).

5.2. Hydrodesulfurization of dibenzothiophene

The reaction network for the conversion of dibenzothiophene is shown in Figure 53, consistent with the literature precedents.^{6, 20, 158, 233} Similar to hydrodenitrogenation reactions, hydrodesulfurization of dibenzothiophene can also proceed via two parallel conversion routes, namely direct desulfurization and hydrogenation. Along the direct desulfurization route for dibenzothiophene conversion, the sulfur atom is directly removed by splitting the two C(sp²)-S bonds to form biphenyl.

Biphenyl was the main product detected in all experiments (Figure 54). Further hydrogenation of biphenyl to phenylcyclohexane is possible but is rather slow due to the strong adsorption of biphenyl on the active direct desulfurization sites.²³³⁻²³⁵

Along the hydrogenation pathway one of the aromatic rings of dibenzothiophene is hydrogenated first to form tetrahydrodibenzothiophene prior to the removal of sulfur. After the removal of sulfur, phenylcyclohexane is formed which is subsequently hydrogenated to bicyclohexane. All these products and intermediates were detected in this work.

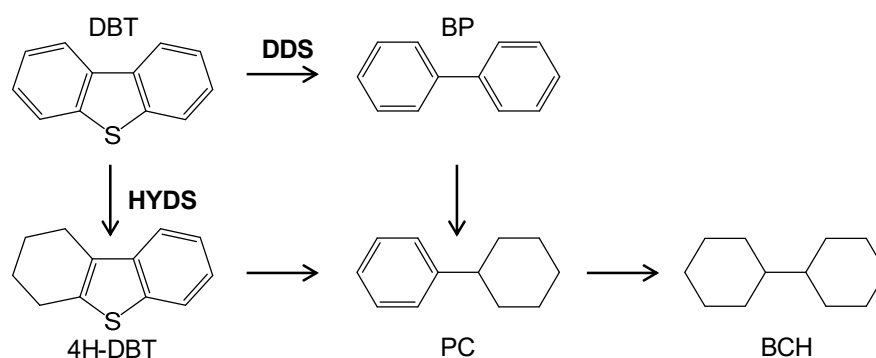


Figure 53. The hydrodesulfurization of dibenzothiophene (DBT) can proceed via two possible pathways the direct desulfurization (DDS) to biphenyl (BP) and the hydrogenation pathway (HYDS) to form first tetrahydro-dibenzothiophene (4H-DBT) and after the C-S bond cleavages phenylcyclohexane (PC). Saturation of one aromatic ring of biphenyl also leads to phenylcyclohexane. Bicyclohexane (BCH) is formed through complete saturation of PC. The reverse direction of each step is not indicated.

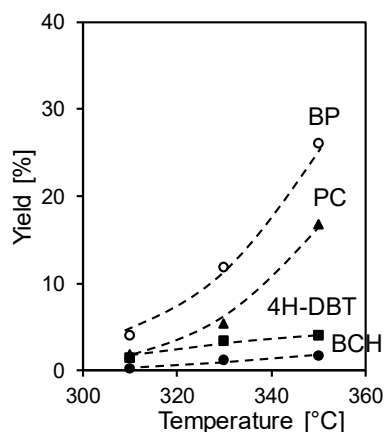


Figure 54. Yields of the products in the hydrodesulfurization of dibenzothiophene as function of temperature. Tetrahydro-dibenzothiophene (■, 4H-DBT), phenylcyclohexane (▲, PC), and bicyclohexane (●, PCH) are assigned to the hydrogenation pathway whereas biphenyl (○, BP) is the product of the direct desulfurization pathway. The catalyst was the one produced from sulfidation protocol "S-ref" (Table 23). The reaction mixture also contained OPA and DMDBT (Experimental).

The much lower amount of tetrahydrodibenzothiophene (~4 wt. % at 350 °C) compared to phenylcyclohexane (~17 wt. % at 350 °C) points to a faster conversion of the former to latter (Figure 54). This in turn means that hydrogenation of the aromatic ring in dibenzothiophene

was slower than the further steps. Complete hydrogenation of the aromatic system of phenylcyclohexane to bicyclohexane, in contrast, seemed to be rather slow because bicyclohexane was only present at low amounts (< 2 wt. % at 350 °C). This might be caused by a smaller adsorption constant of phenylcyclohexane, a non-heteroatom containing molecule, on the active hydrogenation sites compared to multiple S- and N-containing compounds present during reaction.^{20, 158, 236}

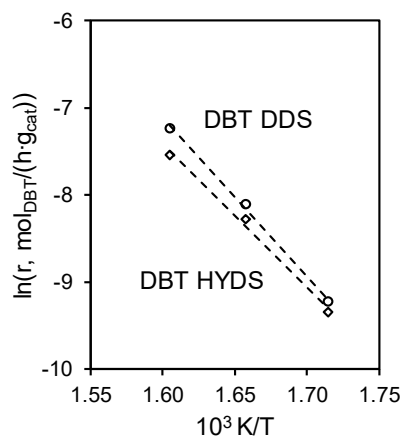


Figure 55. Reaction rates of the direct desulfurization of dibenzothiophene (\circ , DBT DDS) and the hydrogenation route of dibenzothiophene (\diamond , DBT HYDS) as a function of temperature. The catalyst was the one produced from sulfidation protocol “S-ref” (Table 23). The reaction mixture also contained OPA and DMDBT (Experimental).

The conversion of dibenzothiophene on the current NiMoW catalyst proceeded mainly via the direct desulfurization route although the difference in reaction rates was small, especially at lower temperatures. (Figure 55).

5.3. Hydrodesulfurization of 4,6-dimethyldibenzothiophene

A possible reaction network for the conversion of 4,6-dimethyldibenzothiophene is depicted in Figure 56.^{24, 237-238} As with dibenzothiophene, the conversion of 4,6-dimethyldibenzothiophene can also proceed via direct removal of sulfur to form 3,3'-dimethylbiphenyl or via a hydrogenation pathway forming tetrahydro-4,6-dimethyldibenzothiophene as a primary product. Both tetrahydro-4,6-dimethyldibenzothiophene and 3,3'-dimethylbiphenyl can be further hydrogenated to 3,3'-dimethylphenylcyclohexane and finally 3,3'-dimethylbicyclohexane.

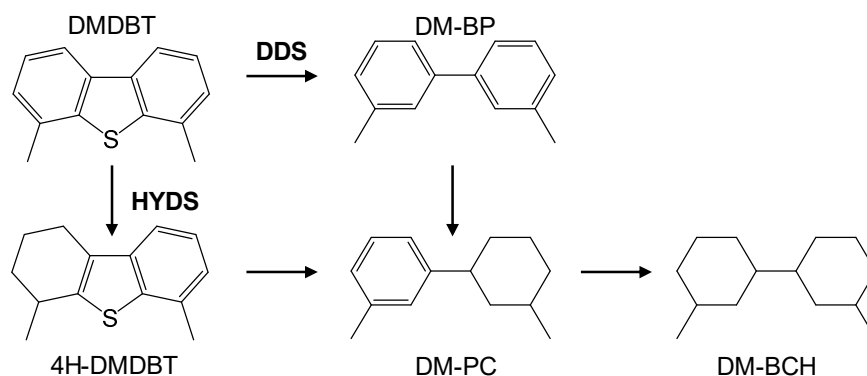


Figure 56. The hydrodesulfurization of 4,6-dimethyldibenzothiophene (DMDBT) can proceed via two possible pathways the direct desulfurization (DDS) to 3,3'-dimethylbiphenyl (DM-BP) and the hydrogenation pathway (HYDS) to form first tetrahydro-4,6-dimethyldibenzothiophene (4H-DMDBT) and after the C-S bond cleavages 3,3'-dimethylphenylcyclohexane (DM-PC). Saturation of one aromatic ring of DM-BP also leads to DM-PC. 3,3'-Dimethylbicyclohexane (DM-BCH) is formed by complete saturation of DM-PC.

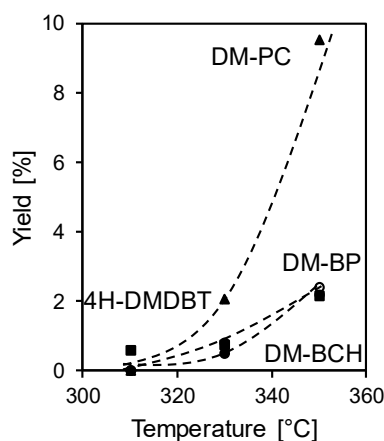


Figure 57. Yields of the products of the hydrodesulfurization of 4,6-dimethyldibenzothiophene (DMDBT) as a function of temperature. Tetrahydro-4,6-dimethyldibenzothiophene (■, 4H-DMDBT), 3,3'-dimethylphenylcyclohexane (▲, DM-PC), and 3,3'-dimethylbicyclohexane (●, PCH) are assigned to the hydrogenation pathway (HYDS) of DMDBT. 3,3'-dimethylbiphenyl (○, DM-BP) is the product of the direct desulfurization route (DDS) of DMDBT. The catalyst was the one produced from sulfidation protocol "S-ref" (Table 23). The reaction mixture also contained OPA and DBT (Experimental).

The product yields as a function of temperature for the hydrodesulfurization of 4,6-dimethyldibenzothiophene (in the presence of dibenzothiophene and *o*-propylaniline and their simultaneous reactions) are shown in Figure 57. The reactivity of 4,6-dimethyldibenzothiophene was apparently lower than dibenzothiophene at the same concentration in the liquid feed, as seen from the lower yields of products at any given temperature. 3,3'-dimethylbiphenyl, i.e., the primary product from direct desulfurization, was not detectable at the lowest temperature of 310 °C, where tetrahydro-4,6-dimethyl-dibenzothiophene was the only product observed. At higher temperatures, 3,3'-dimethyl-biphenyl was observed at comparable concentrations as tetrahydro-4,6-dimethyldibenzothiophene.

The hydrogenation pathway for 4,6-dimethyldibenzothiophene was up to 6 times faster than the direct desulfurization pathway (Figure 58). This is attributed to the steric effects of methyl groups adjacent to the sulfur atom hindering σ -adsorption of the molecule required for the direct removal of sulfur. Thus, the main conversion pathway of 4,6-dimethyldibenzothiophene was the hydrogenation pathway, which proceeds via π -adsorption, an adsorption mode not significantly hindered by the presence of methyl groups.^{21, 24, 239}

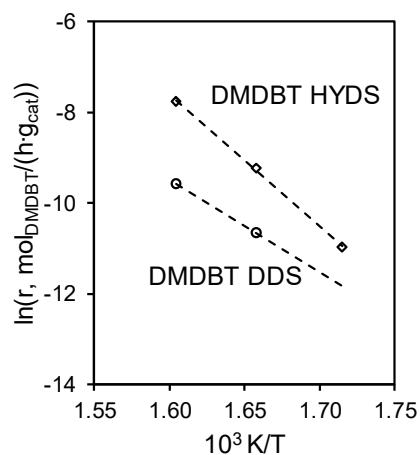


Figure 58. Reaction rates of the direct desulfurization of 4,6-dimethyldibenzothiophene (\circ , DMDBT DDS) and the hydrogenation route of 4,6-dimethyldibenzothiophene (\diamond , DMDBT HYDS) as function of temperature. The catalyst was the one produced from sulfidation protocol "S-ref" (Table 23). The reaction mixture also contained OPA and DBT (Experimental).

6. Mutual Impact of the Hydrotreating Reactions

The inhibition effect of a N-containing compound on hydrodesulfurization reactions was evaluated by increasing the concentration of *o*-propylaniline in the liquid feed from 50 to 100 and to 200 ppm. The conversion of both, dibenzothiophene and 4,6-dimethyldibenzothiophene, decreased with increasing concentration of *o*-propylaniline (Figure 59). On the other hand, neither dibenzothiophene nor 4,6-dimethyldibenzothiophene affected the conversion rates of the *o*-propylaniline.

The impact of *o*-propylaniline on the hydrodesulfurization of dibenzothiophene was modest when the *o*-propylaniline content was increased from 50 to 100 ppm. The highest concentration of *o*-propylaniline (200 ppm), however, inhibited the conversion rates of dibenzothiophene by a factor of 2. This was accompanied with an increase in the selectivity for the direct desulfurization pathway of dibenzothiophene compared to the hydrogenation pathway, with the ratio of DDS/HYD increasing from ~2 in the presence of 50 and 100 ppm N to ~3.75 in the presence of 200 ppm N (at 350 °C). Thus, *o*-propylaniline preferentially suppressed the hydrogenation route of dibenzothiophene. In comparison, direct desulfurization of dibenzothiophene was less affected by *o*-propylaniline (Figure 59).

The presence of *o*-propylaniline decreased the hydrodesulfurization rate of 4,6-dimethyldibenzothiophene by more than 8 times, especially when the concentration of *o*-propylaniline was increased to 200 ppm (Figure 59). Similar to the observed trend for hydrodesulfurization of dibenzothiophene, the hydrogenation pathway was much more affected than the direct desulfurization pathway by an increasing concentration of *o*-propylaniline as seen from the decrease in the pathway selectivity of HYDS/DDS from ~13.5 to 5.5 at 350 °C (Figure 59).

These kinetic observations appear to support the proposal that two different catalytic sites are responsible for the direct removal of the heteroatom and the hydrogenation of aromatic rings.¹⁶¹ Since the N-containing compound, which adsorbs more strongly than S-containing compounds, is preferentially converted via the hydrogenation route, affects the hydrogenation route of S-containing compounds to a greater extent.^{25, 151, 240} For similar reasons, the poisoning effect of *o*-propylaniline on the hydrodesulfurization of 4,6-dimethyldibenzothiophene was much more pronounced than on the hydrodesulfurization of dibenzothiophene because the hydrodesulfurization of 4,6-dimethyldibenzothiophene relies more heavily on the hydrogenation route due to steric hinderance.^{6, 8, 161, 241-243}

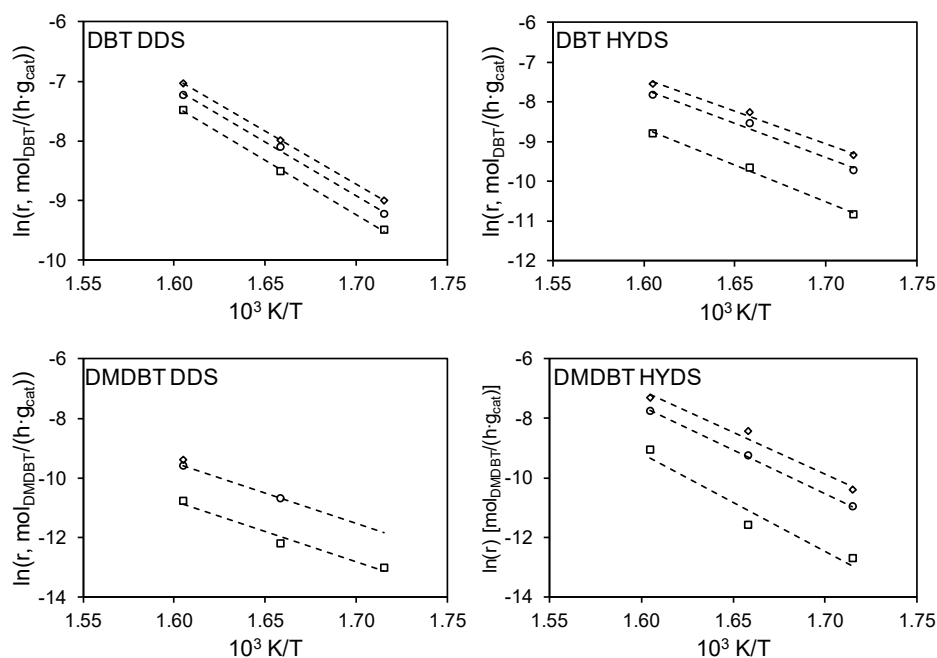


Figure 59. Reaction rates as a function of temperatures for the direct desulfurization (DBT DDS) and hydrogenation pathway (DBT HYDS) of dibenzothiophene as well as for the direct desulfurization (DMDBT DDS) and hydrogenation pathway (DMDBT HYDS) of 4,6-dimethyldibenzothiophene. The content of *o*-propylaniline in the liquid feed increases from 50 ppm N (\diamond) over 100 ppm N (\circ) to 200 ppm N (\square). The catalyst was the one produced from sulfidation protocol “S-ref” (Table 23).

Control experiments containing only two reactants of the three in the liquid feed confirm that the poisoning effect on the hydrodesulfurization of dibenzothiophene and 4,6-dimethyldibenzothiophene was mainly attributed to *o*-propylaniline. Therefore, the highest conversion rates of dibenzothiophene and 4,6-dimethyldibenzothiophene were obtained if the liquid feed contained only dibenzothiophene and 4,6-dimethyldibenzothiophene and no *o*-propylaniline (Figure 60).

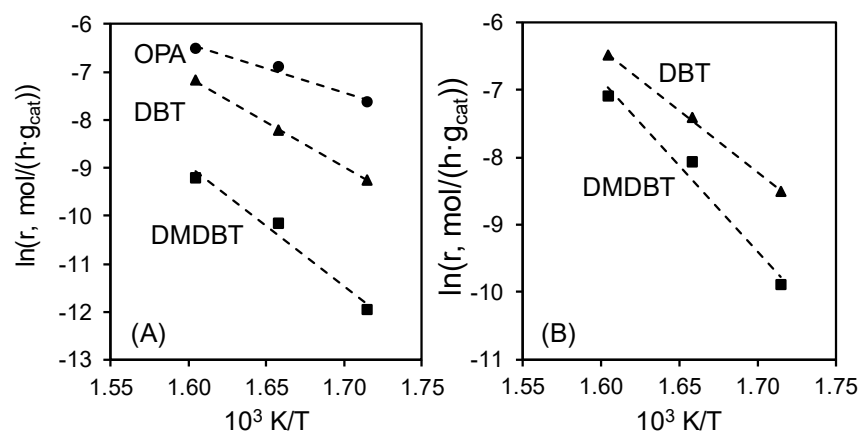


Figure 60. (A) Conversion rates of *o*-propylaniline (OPA, 50 ppm N), dibenzothiophene (DBT, 500 ppm), and 4,6-dimethyldibenzothiophene (DMDBT, 500 ppm) as a function of temperature in a simultaneous reaction of all three model compounds. (B) Conversion rates of dibenzothiophene (DBT, 500 ppm) and 4,6-dimethyldibenzothiophene (DMDBT, 500 ppm) without *o*-propylaniline being present. The catalyst was the one produced from sulfidation protocol “S-ref” (Table 23).

7. Impact of Sulfidation Parameters on the Catalytic Performance

7.1. Influence of an increased sulfidation pressure

It was found that the hydrodesulfurization activity of supported CoMo-type catalysts increased when a higher pressure was applied during sulfidation.²⁴⁴⁻²⁴⁶ This was related to a higher concentration of Co-substituted MoS₂ edges²⁴⁴ and structural change of the sulfide leading to a larger fraction of exposed metal edges.²⁴⁵⁻²⁴⁶ Therefore, a possible positive impact of an increased total pressure (“S-p+”, 40 bar) on the catalytic performance of a bulk ternary sulfide was tested and compared to the standard sulfidation protocol “S-ref”. All other sulfidation parameters were kept constant (Table 23).

All physicochemical properties of the “S-ref” and “S-p+” sulfides, shown in Table 27, are similar within the experimental error and considering the standard deviations in the TEM analysis of stacking degree and length of the Mo(W)S₂ slabs. Only the specific surface area and the pore volume of the sulfide seemed to be affected by the total pressure as a higher pressure led to an almost doubled pore volume and an increased surface area of the resulting sulfide.

Table 27. Metal molar fraction of nickel (Ni), tungsten (W), and molybdenum (Mo), stacking degree, slab length [nm], specific surface area [m²/g], and pore volume [cm³/g] of the sulfide catalysts obtained after sulfidation according to the procedure “S-ref” and “S-p+”. The number in brackets behind stacking degree and slab length represent the standard deviation in the TEM analysis.

Catalyst	Metal molar fraction			Stacking degree	Slab length [nm]	Specific surface area [m ² /g]	Pore volume [cm ³ /g]
	Ni	W	Mo				
S-ref	0.48	0.41	0.11	6.1 (±2.1)	3.5 (±1.6)	39.8	0.068
S-p+	0.42	0.46	0.12	5.6 (±2.3)	4.0 (±1.6)	48.2	0.116

Moreover, the X-ray diffraction patterns of the “S-ref” and the “S-p+” sulfides also look similar (Figure 61). Both contain reflections of the Mo(W)S₂ phases (ICSD # 644245, 202366) and reflections assigned to the Ni₃S₂ (ICSD # 27521) phase, which was the only nickel sulfide species identified. The reflections of the Mo(W)S₂ phase are typically broad due to their anisotropy whereas the nickel sulfide phase exhibits a higher crystallinity as indicated by the sharper reflections.^{43, 70}

Catalytic evaluation in the “three-way” hydrotreating reaction (OPA-DBT-DMDBT) also showed very similar activities of the two sulfides for the conversion of all three compounds (Figure 62). A slightly higher hydrodenitrogenation activity of *o*-propylaniline was registered on the “S-p+” sulfide (Figure 62, left), which was mainly attributed to a faster hydrogenation (Figure 63, left).

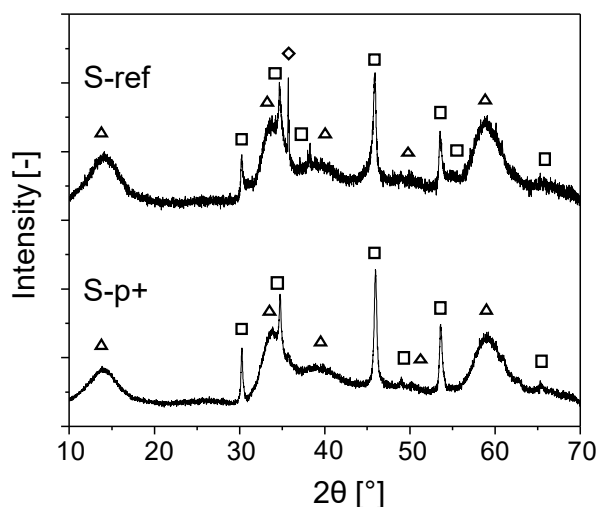


Figure 61. X-ray diffractograms of the sulfides obtained after the sulfidation procedure “S-ref” and “S-p+”. Reflections of the Mo(W)S_2 (ICSD # 644245, 202366) phases are marked with Δ . The nickel sulfide phase identified was Ni_3S_2 (\square , ICSD # 27521). Reflections assigned to the diluting material SiC are marked with a \diamond .

Similarly, the conversion through the hydrogenation pathway of dibenzothiophene was also faster on the “S-p+” than on the “S-ref” sulfide (Figure 64, right), although the direct desulfurization of dibenzothiophene was faster on the “S-ref” sulfide (Figure 64, left). The hydrodesulfurization activity of 4,6-dimethyldibenzothiophene was slightly higher on the “S-ref” sulfide along both pathways (Figure 63, right).

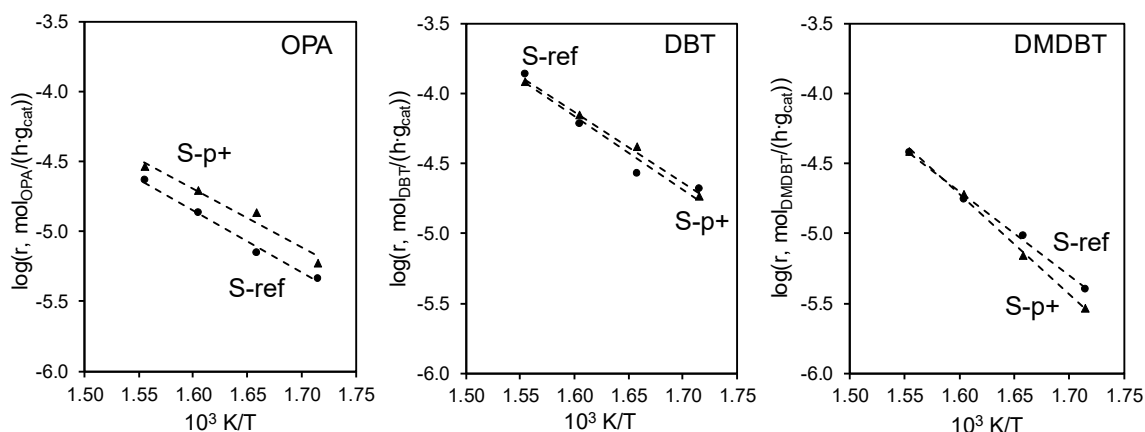


Figure 62. Reaction rates for the hydrodenitrogenation of *o*-propylaniline (OPA) (left) and the hydrodesulfurization of dibenzothiophene (DBT) (middle) and of 4,6-dimethyldibenzothiophene (DMDBT) (right) as a function of temperature obtained on the sulfide catalysts after the sulfidation procedure “S-ref” (\bullet) and “S-p+” (\blacktriangle). Temperatures: 310–370 °C, total pressure: 50 bar.

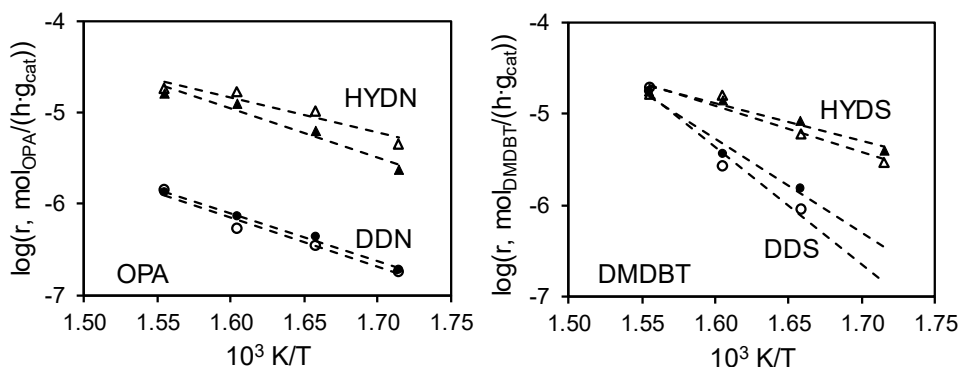


Figure 63. Left: Reaction rates as a function of temperature for the direct denitrogenation pathway (DDN) (●, ○) and the hydrogenation pathway (HYDN) (▲, △) of *o*-propylaniline (OPA) obtained on the “S-ref” (filled symbols) and the “S-p+” sulfide (empty symbols). Right: Reaction rates as function of temperature for the direct desulfurization pathway (DDS) (○, ●) and the hydrogenation pathway (HYDS) (▲, △) of 4,6-dimethyldibenzothiophene (DMDBT) obtained on the “S-ref” (filled symbols) and the “S-p+” sulfide (empty symbols). Temperature: 310-370 °C, total pressure 50 bar.

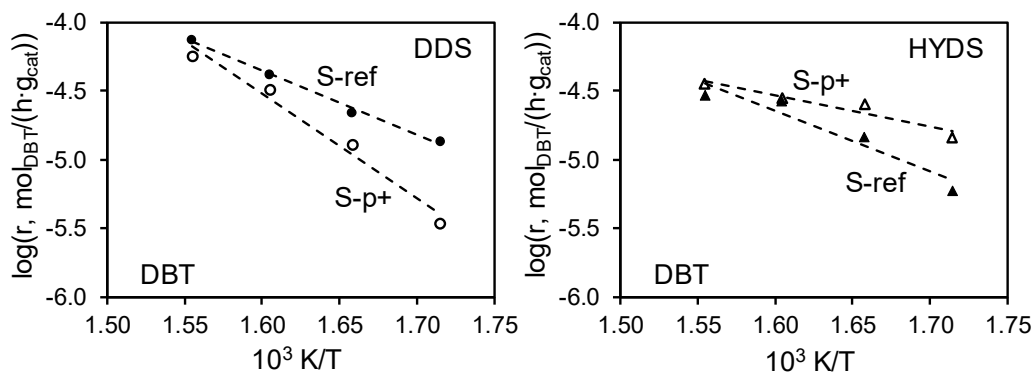


Figure 64. Reaction rates as a function of temperature for the direct desulfurization pathway (DDS) (left) and the hydrogenation pathway (HYDS) (right) of dibenzothiophene (DBT) obtained on the “S-ref” (filled symbols) and the “S-p+” sulfide (empty symbols). Temperature: 310-370 °C, total pressure 50 bar.

Summarizing, a higher total pressure during sulfidation had no remarkable impact on either sulfide structure or on catalytic performance, despite a notably higher specific surface area and a larger pore volume of the “S-p+” sulfide. A closer look showed that a higher sulfidation pressure caused a modest increase in the activity along the hydrogenation route for both hydrodenitrogenation of *o*-propylaniline and hydrodesulfurization of dibenzothiophene selectively the catalytic sites involved in hydrogenation reactions which was in expense of sites active for the direct removal of heteroatoms.¹⁶¹

7.2. Effect of the sulfur content

The chemical potential of sulfur during sulfidation was lowered by a tenth (“S-min” protocol, Table 23) in each sulfidation step compared to the reference procedure (“S-ref”). The H_2 partial pressure was lowered accordingly to keep the H_2/S ratio of 5 in every sulfidation step. The other reaction conditions were also kept constant. It is surmised that lower concentration of sulfur decreases the sulfidation rates of each metal and especially the sulfidation of nickel at lower temperatures. The formation of crystalline nickel sulfides might thereby be retarded resulting in a higher fraction of nickel incorporated at the $Mo(W)S_2$ edges and thus, an increased catalytic activity. Moreover, softer sulfidation conditions could enlarge the fraction of exposed active edge sites by prevention of catalyst sintering.

Table 28 compares the physicochemical properties of the sulfides obtained after the procedure “S-ref” and “S-min”. The elemental composition of the sulfide as well as the stacking height of the $Mo(W)S_2$ slabs were not affected by using a lower sulfur content in the liquid sulfidation mixture. But the $Mo(W)S_2$ slabs are on average shorter in the “S-min” sulfide. Another difference is the doubled pore volume for the “S-min” sulfide compared to the “S-ref” sulfide, although the specific surface areas of the two catalysts are similar.

Table 28. Metal molar fraction of nickel (Ni), tungsten (W), and molybdenum (Mo), stacking degree, slab length [nm], specific surface area [m^2/g], and pore volume [cm^3/g] of the sulfide catalysts obtained after sulfidation according to the procedure “S-ref” and “S-min”. The number in brackets behind stacking degree and slab length represent the standard deviation in the TEM analysis.

Catalyst	Metal molar fraction			Stacking degree	Slab length [nm]	Specific surface area [m^2/g]	Pore volume [cm^3/g]
	Ni	W	Mo				
S-ref	0.48	0.41	0.11	3.5 (± 1.6)	6.1 (± 2.1)	39.8	0.068
S-min	0.46	0.43	0.12	3.5 (± 1.4)	4.8 (± 1.8)	40.2	0.116

The typical broad reflections assigned to the $Mo(W)S_2$ (ICSD # 644245, 202366) phase were present in the X-ray diffractograms of the sample sulfided with the “S-min” protocol (Figure 65). However, sulfidation with lower sulfur contents (0.4-1.2 wt. % S) caused the formation of Ni_9S_8 (ICSD # 63080) and Ni_3S_2 (ICSD # 27521) phases whereas only reflections of the thermodynamically most stable Ni_3S_2 phases had been identified in the “S-ref” sulfide. Moreover, the relative intensity of the nickel sulfide reflections indicate that larger nickel sulfide particles were formed during the “S-ref” procedure while the “S-min” procedure led to smaller nickel sulfide domains.

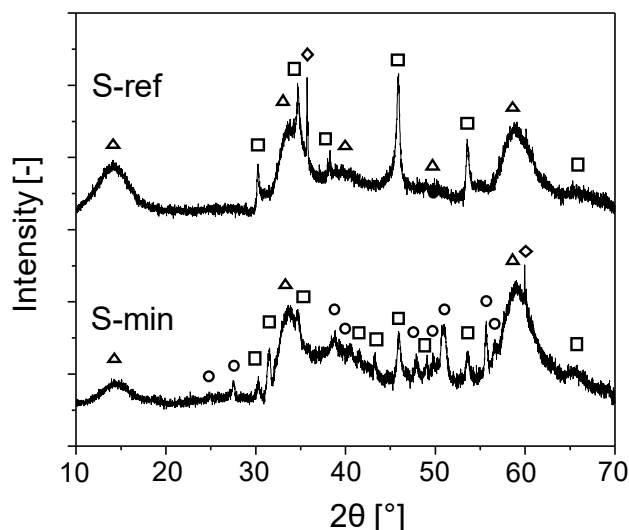


Figure 65. X-ray diffractograms of the sulfides obtained after the sulfidation procedure “S-ref” and “S-min”. Reflections of the Mo(W)S₂ (ICSD # 644245, 202366) phase are marked with Δ . The nickel sulfide phases identified are Ni₃S₂ (\square , ICSD # 27521) and Ni₉S₈ (\circ , ICSD # 63080). Reflections assigned to the diluting material SiC are marked with a \diamond .

The activities at 310 °C in the three reactions on the catalyst sulfided with the procedure “S-ref” follows the order

DBT HDS > DMDBT HDS > OPA HDN (Figure 66).

On the “S-min” sulfide the catalytic activity in hydrodesulfurization of dibenzothiophene increased at least by a factor of 1.5 (310 °C) compared to the “S-ref” sulfide. The difference in the overall hydrodesulfurization of dibenzothiophene between the two sulfides became more pronounced with increasing temperature (up to a factor of ~3 at 370°C), while the activities for the hydrodenitrogenation of *o*-propylaniline and hydrodesulfurization of 4,6-dimethyldibenzothiophene were very close at high temperatures.

At low temperatures, the hydrodenitrogenation rate was higher by a factor of ~1.5 on the “S-min” sulfide compared to the “S-ref” sulfide. A closer look reveals that the higher activity at low temperature resulted from faster hydrogenation pathway on the “S-min” sulfide, while the direct denitrogenation rates were lower compared to the “S-ref” sulfide (Figure 67).

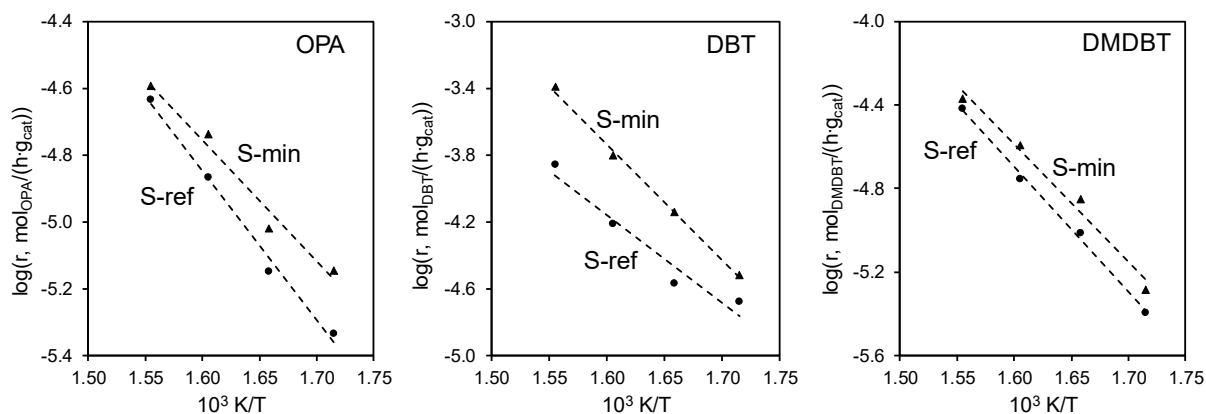


Figure 66. Reaction rates for the hydrodenitrogenation of *o*-propylaniline (OPA) (left), the hydrodesulfurization of dibenzothiophene (DBT) (middle), and of 4,6-dimethyldibenzothiophene (DMDBT) (right) as a function of temperature obtained on the sulfide catalysts after the sulfidation procedure "S-ref" (●) and "S-min" (▲). Temperatures: 310–370 °C, total pressure: 50 bar.

The hydrodesulfurization rate of dibenzothiophene increased significantly on the "S-min" sulfide compared to the reference catalyst and was caused by rate enhancement in both conversion routes, i.e., direct desulfurization and hydrogenation, to approximately the same extent at all reaction temperatures (Figure 68). This might be related to a degraded inhibition effect of *o*-propylaniline on the hydrodesulfurization of dibenzothiophene in the case of the "S-min" sulfide increasing the conversion of dibenzothiophene.

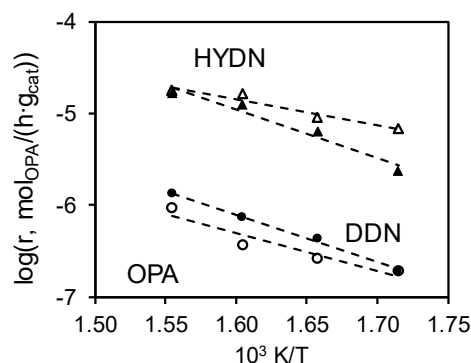


Figure 67. Rate constants as a function of temperature for the direct denitrogenation pathway (DDN) (●, ○) and the hydrogenation pathway (HYDN) (▲, △) of *o*-propylaniline (OPA) obtained on the "S-ref" (filled symbols) and the "S-min" sulfide (empty symbols), respectively. Temperature: 310–370 °C, total pressure 50 bar.

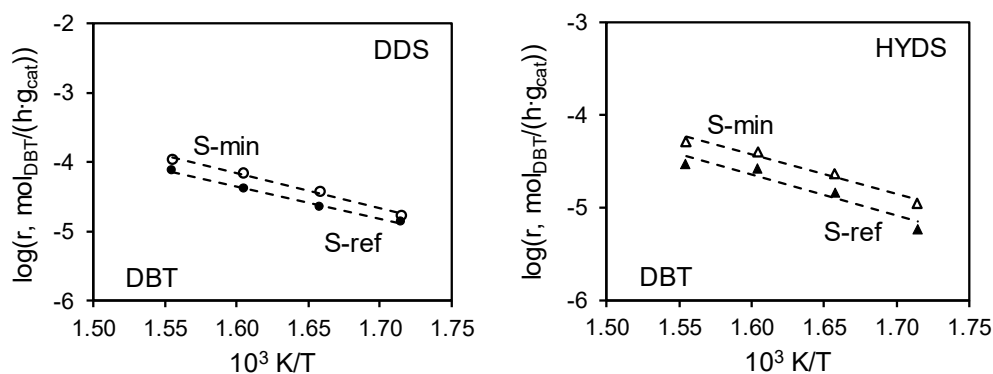


Figure 68. Reaction rates as a function of temperature for the direct desulfurization pathway (DDS) (left) and the hydrogenation pathway (HYDS) (right) of dibenzothiophene (DBT) obtained on the “S-ref” (filled symbols) and the “S-min” sulfide (empty symbols). Temperature: 310-370 °C, total pressure 50 bar.

The conversion of 4,6-dimethyldibenzothiophene was hardly affected by the sulfidation procedure. Indeed, only a slight increase of the hydrogenation activity (by a factor ~ 1.3) was observed over the whole tested temperature range on the “S-min” sulfide compared to the reference material (Figure 69).

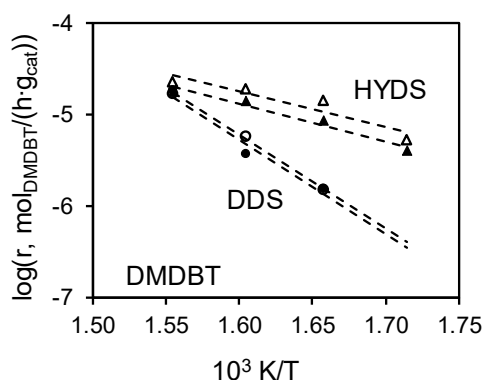


Figure 69. Reaction rates as a function of temperature for the direct desulfurization pathway (DDS) (○, ●) and the hydrogenation pathway (HYDS) (▲, △) of 4,6-dimethyldibenzothiophene (DMDBT) obtained on the “S-ref” (filled symbols) and the “S-min” sulfide (empty symbols). Temperature: 310-370 °C, total pressure 50 bar.

In summary, a lower sulfur concentration (as DMDS) used for liquid-phase sulfidation retarded the growth of $\text{Mo(W)}\text{S}_2$ slabs leading to a larger perimeter exposed to the reactants. Further, the growth of nickel sulfide crystals and the formation of the thermodynamically stable Ni_3S_2 phase were limited.²⁴⁷⁻²⁴⁸ All these hint towards a closer interaction between the phases resulting in a higher amount of nickel(II) cations substituted into the $\text{Mo(W)}\text{S}_2$ edge leading to a higher concentration of active sites and in turn a higher hydrotreating activity.

The higher activity for the hydrodesulfurization of dibenzothiophene compared to the hydrodenitrogenation of *o*-propylaniline suggests that a lower sulfur content in the liquid-phase led to a S-deficient sulfide phase especially at the surface. This implies that the surface of the sulfide was more Lewis acidic. A higher concentration of Lewis acid sites, in turn, resulted in a

higher concentration of adsorption sites for reactants in the σ - and π -adsorption mode.^{1, 6, 32} Further, Lewis acid sites were known to play a fundamental role in hydrogen splitting creating SH groups which were the H providing groups in hydrogenation reactions.^{127, 249} The activity increase, especially in the hydrodesulfurization of dibenzothiophene, was caused by the sulfur deficient catalyst surface leading to a strong interaction between Lewis acid sites and dibenzothiophene.

This also explains the enhancement of both reaction pathways, i.e., direct desulfurization and hydrogenation, in the conversion of dibenzothiophene. The rates of the hydrogenation pathways of *o*-propylaniline and 4,6-dimethyldibenzothiophene were also increased due to the overall higher activity of the “S-min” sulfide as explained before.

In both cases, the direct removal of the heteroatoms was hardly affected or even decrease with a lower S concentration in the sulfidation mixture. The decrease in the direct denitrogenation of *o*-propylaniline and direct desulfurization of 4,6-dimethyldibenzothiophene can be related to the high affinity of the S-deficient sulfide surface of the “S-min” catalyst to the sulfur atom of dibenzothiophene leading to an inhibition of the adsorption of *o*-propylaniline and 4,6-dimethyldibenzothiophene on the adsorption sites for the direct removal of nitrogen and sulfur. The two methyl-groups in 4,6-dimethyldibenzothiophene sterically limit surface interaction of the sulfur atom of this molecule and thus, adsorption via the sulfur atom.⁸

7.3. Influence of the hydrogen to sulfur ratio

Transformation from the oxide to the sulfide phase of the metals comprises various O-S exchanges and reduction steps. The timing of the different steps of each metal is decisive to maximize the fraction of the active Ni-substituted Mo(W)S₂ phase.^{15, 68, 229} Because of this the impact of the hydrogen to sulfur (H₂/S) ratio on the catalytic performance was investigated. Besides the H₂/S ratio of 5 used in the reference sulfidation procedure (“S-ref”), the H₂/S ratio was therefore increased to 7.5 in the procedure “S-H/S+” and decreased to 2.5 in the “S-H/S-“ sulfidation procedure (Table 23).

The metal molar fraction in the sulfided catalysts did not change with the H₂/S ratio applied in the sulfidation (Table 29). The length of the Mo(W)S₂ slabs, in contrast, decreased compared to the “S-ref” sulfide no matter if the hydrogen to sulfur ratio was increased (“S-H/S+”) or decreased (“S-H/S-“). The higher the H₂/S ratio was, the higher the specific surface area of the sulfide without affecting the pore volume of the sulfides became. Both stacking degree of the Mo(W)S₂ slabs and the pore volume of the sulfides were comparable among the three samples listed in Table 29.

Table 29. Metal molar fraction of nickel (Ni), tungsten (W), and molybdenum (Mo), stacking degree, slab length [nm], specific surface area [m²/g], and pore volume [cm³/g] of the sulfide catalysts obtained after sulfidation according to the procedure “S-ref”, “S-H/S+”, and “S-H/S-“. The number in brackets behind stacking degree and slab length represent the standard deviation in the TEM analysis.

Catalyst	Metal molar fraction			Stacking degree	Slab length [nm]	Specific surface area [m ² /g]	Pore volume [cm ³ /g]
	Ni	W	Mo				
S-ref	0.48	0.41	0.11	3.5 (±1.6)	6.1 (±2.1)	39.8	0.068
S-H/S+	0.45	0.45	0.10	3.5 (±1.5)	4.8 (±1.8)	48.8	0.084
S-H/S-	0.45	0.45	0.10	3.0 (±1.1)	4.7 (±1.6)	30.0	0.075

In the XRD pattern of all three sulfide catalysts the typical reflections assigned to Mo(W)S₂ (ICSD # 644245, 202366) are present. Ni₃S₂ (ICSD # 27521) phases have been additionally identified on the sulfides “S-ref” and “S-H/S-“. The diffractogram of the “S-H/S+” sulfide, in contrast, contains reflections attributable to Ni₉S₈ (ICSD # 63080) phases. Comparison of the relative intensities of the reflections assigned to nickel sulfide phases indicate that an increased H₂/S ratio seems to retard the growth of nickel sulfide crystals (Figure 70).

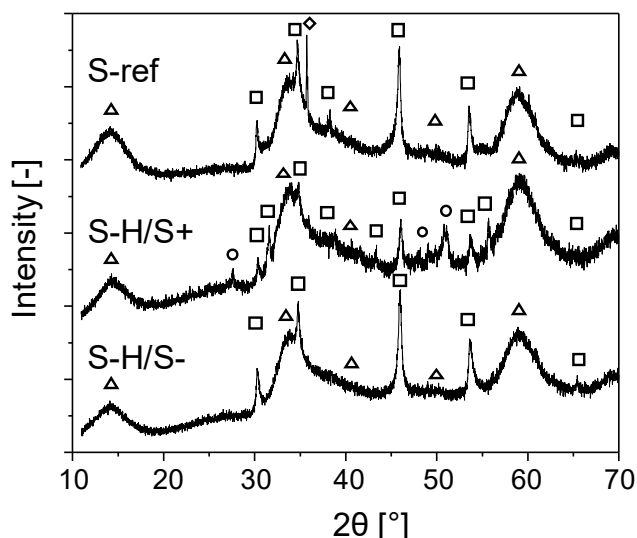


Figure 70. X-ray diffractograms of the sulfides obtained after the sulfidation procedure “S-ref”, “S-H/S+”, and “S-H/S-”. Reflections of the Mo(W)S_2 (ICSD # 644245, 202366) phase are marked with Δ . The nickel sulfide phases identified are Ni_3S_2 (\square , ICSD # 27521) and Ni_9S_8 (\circ , ICSD # 63080). Reflections assigned to the diluting material SiC are marked with a \diamond .

Increasing the H_2/S ratio during sulfidation led to a sulfide catalyst which exhibited similar activity in the hydrodenitrogenation of *o*-propylaniline and the hydrodesulfurization of 4,6-dimethyldibenzothiophene as obtained on the “S-ref” sulfide (Figure 71).

Separation into different conversion pathways for both reactants, *o*-propylaniline and 4,6-dimethyldibenzothiophene, confirmed that these two sulfides, i.e., “S-ref” and “S-H/S+”, hardly differed in their catalytic activities (Figure 72).

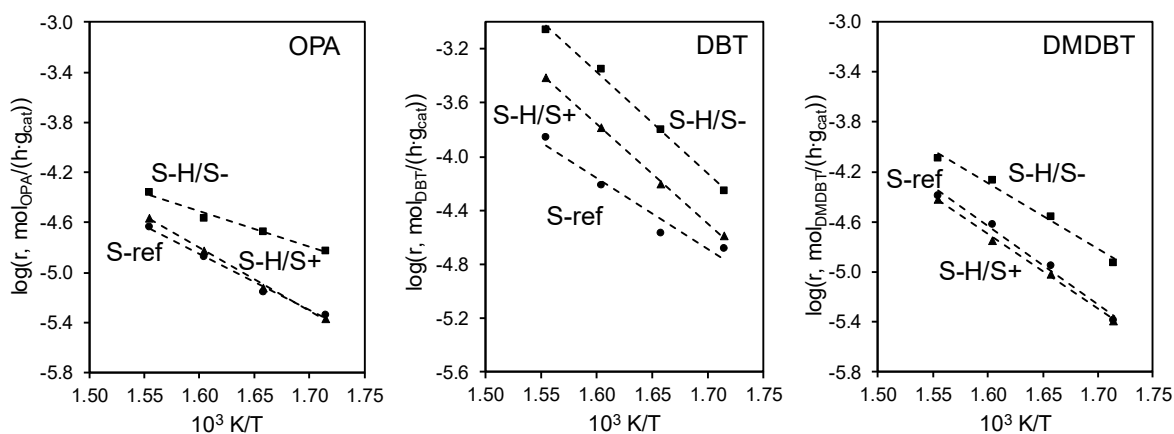


Figure 71. Reaction rates for the hydrodenitrogenation of *o*-propylaniline (OPA) (left), the hydrodesulfurization of dibenzothiophene (DBT) (middle), and of 4,6-dimethyldibenzothiophene (DMDBT) (right) as a function of temperature obtained on the sulfide catalysts after the sulfidation procedure “S-ref” (\bullet), “S-H/S+” (\blacktriangle), and “S-H/S-” (\blacksquare). Temperatures: 310–370 °C, total pressure: 50 bar.

The activity of the hydrodesulfurization of dibenzothiophene on the “S-H/S+” sulfide, in contrast, increased by a factor of ~ 3 at 370 °C and by a factor of ~ 1.5 at 310 °C compared to the “S-ref” sulfide. (Figures 71 and 73).

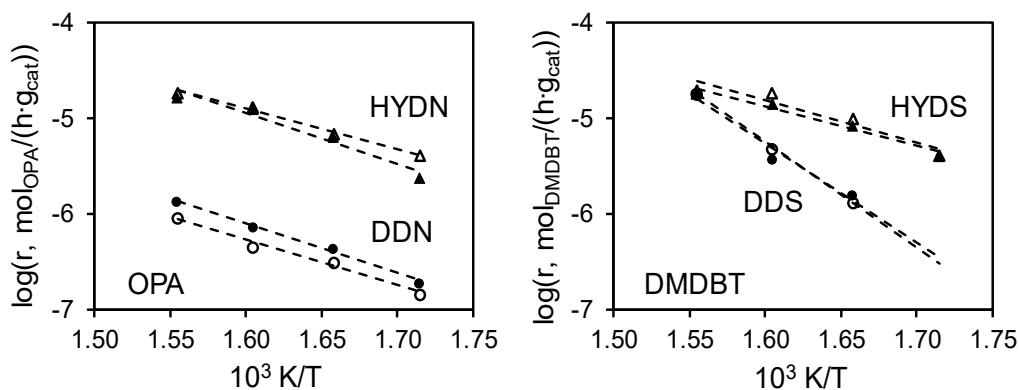


Figure 72. Left: Reaction rates as a function of temperature for the direct denitrogenation pathway (DDN) (●, ○) and the hydrogenation pathway (HYDN) (▲, △) of o-propylaniline (OPA) obtained on the “S-ref” (filled symbols) and the “S-H/S+” sulfide (empty symbols). Right: Reaction rates as a function of temperature for the direct desulfurization pathway (DDS) (○, ●) and the hydrogenation pathway (HYDS) (▲, △) of 4,6-dimethyldibenzothiophene (DMDBT) obtained on the “S-ref” (filled symbols) and the “S-H/S+” sulfide (empty symbols). Temperature: 310-370 °C, total pressure 50 bar.

The difference in the activity for the direct desulfurization pathway of dibenzothiophene became more pronounced with increasing temperature and resulted in a ~ 1.5 times higher activity of the “S-H/S+” sulfide compared to the “S-ref” sulfide at 370 °C (Figure 73). In the hydrogenation pathway of the hydrodesulfurization of dibenzothiophene the “S-H/S+” sulfide was approximately doubled over the whole temperature range (Figure 73).

The enhanced activity of the “S-H/S+” sulfide compared to the “S-ref” sulfide can be related to the shorter Mo(W)S₂ slab leading to the exposure of a larger fraction of the active perimeter. This fraction must be especially active in the hydrodesulfurization of dibenzothiophene as the differences in the catalytic performance among the two sulfides was most pronounced in this reaction.

Halving the H₂/S ratio (“S-H/S-”) compared to the reference sulfidation procedure (“S-ref”) resulted in a significantly more active catalyst for all reactants (Figure 73). The mass specific activity on the “S-H/S-” sulfide was 2-6 times as active as on the “S-ref” sulfide.

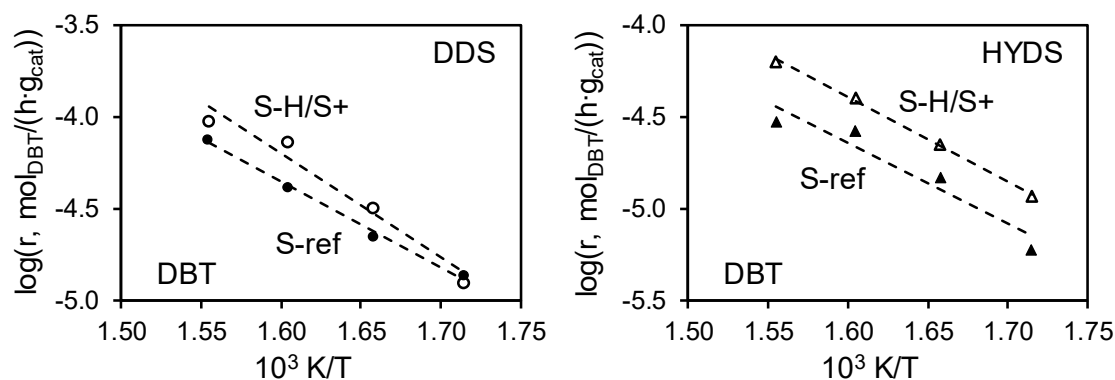


Figure 73. Reaction rates as a function of temperature for the direct desulfurization pathway (DDS) (left) and the hydrogenation pathway (HYDS) (right) of dibenzothiophene (DBT) obtained on the “S-ref” (filled symbols) and the “S-H/S+” sulfide (empty symbols). Temperature: 310-370 °C, total pressure 50 bar.

For the hydrodenitrogenation of *o*-propylaniline, the direct denitrogenation was only slightly affected by the H_2/S ratio while the rate of the hydrogenation was enhanced, especially at lower temperatures (Figure 74, left).

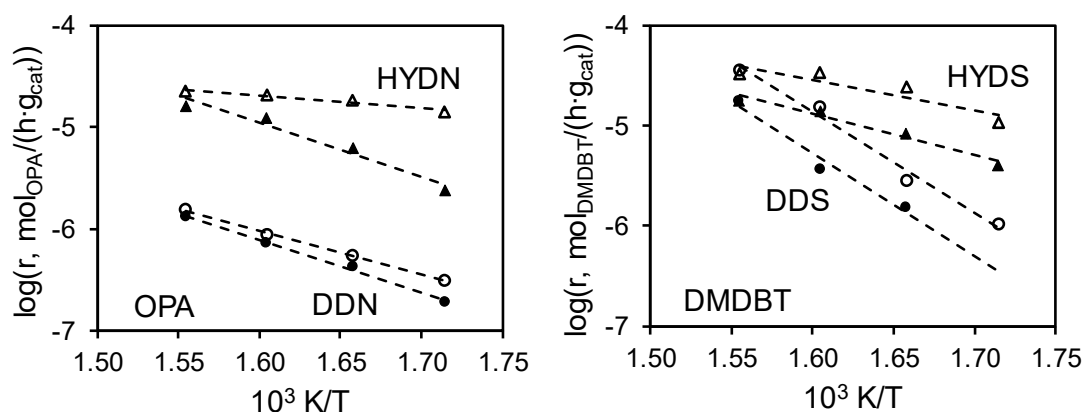


Figure 74. Left: Reaction rates as a function of temperature for the direct denitrogenation pathway (DDN) (●, ○) and the hydrogenation pathway (HYDN) (▲, △) of *o*-propylaniline (OPA) obtained on the “S-ref” (filled symbols) and the “S-H/S-” sulfide (empty symbols). Right: Reaction rates as a function of temperature for the direct desulfurization pathway (DDS) (○, ●) and the hydrogenation pathway (HYDS) (▲, △) of 4,6-dimethyldibenzothiophene (DMDBT) obtained on the “S-ref” (filled symbols) and the “S-H/S-” sulfide (empty symbols). Temperature: 310-370 °C, total pressure 50 bar.

The activity in both hydrodesulfurization reactions (DBT and DMDBT) significantly increased when a lower H_2/S ratio (Figure 74, right and Figure 75) was used during sulfidation. The apparent activation energies for individual rates along both pathways hardly changed, in view of the very similar extents of rate enhancements over the whole temperature range.

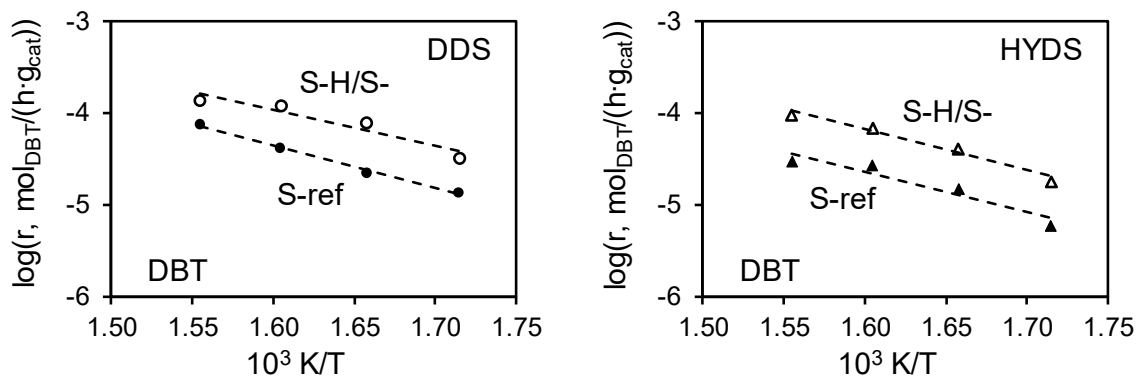


Figure 75. Reaction rates as a function of temperature for the direct desulfurization pathway (DDS) (left) and the hydrogenation pathway (HYDS) (right) of dibenzothiophene (DBT) obtained on the “S-ref” (filled symbols) and the “S-H/S-“ sulfide (empty symbols). Temperature: 310-370 °C, total pressure 50 bar.

Indeed, the shorter Mo(W)S_2 slabs in the “S-H/S-“ sulfide would lead to a larger perimeter exposed to the reactants compared to “S-ref”. However, the slab length in “S-H/S-“ was similar to “S-H/S+” (Table 29) whereas the hydrotreating activity of the “S-H/S-“ sulfide was by far superior to the activity of the “S-H/S+” sulfide. Assuming the same active sites present on all sulfide catalyst, the concentration of active sites on the “S-H/S-“ sulfide must be enhanced to a greater extent compared to the other sulfides. The determination of the active site concentrations remains a topic of future investigations.

Payen et al. and Silvy et al. suggested that the reduction of the metal in a too early stage in the sulfidation procedure hinders the O-S exchange and thus, affects the sulfidation degree of the metals.^{13, 82} A lower H_2/S ratio might delay the reduction of the metals or lead to incomplete induced only partial reduction. Consequently, the transformation of nickel oxide phases, molybdenum oxide phases, and tungsten oxide phases into their respective and mixed sulfide phases might occur in a narrower temperature range resulting in higher fraction of nickel(II) cations being substituted into the Mo(W)S_2 edge and in turn, a higher concentration of active sites.

7.4. Effect of the sulfiding agent

Instead of dimethyl disulfide (DMDS) as sulfiding agent in the standard sulfidation procedure “S-ref”, *n*-butanethiol (BT) was also used as a sulfiding agent and generated the “S-BT” sulfide when standard conditions were applied (Table 23). Silvy et al. achieved the most active supported CoMo sulfide for the hydrodesulfurization of thiophene using *n*-butanethiol as sulfiding agent at 300 °C. The positive effect of *n*-butanethiol was attributed to a better coupling of the reduction and O-S exchange reactions of the different metals.¹³ Moreover, *n*-butanethiol and dimethyl disulfide have a similar decomposition temperature (~200 °C for DMDS and ~225 °C for BT).^{13, 250} Decomposition of both molecules results in the formation of H₂S.^{1, 250-252} On the other hand, the resulting hydrocarbon residues after decomposition of the thiol and the disulfide are different, butenes and *n*-butane, can be formed out of butanethiol, whereas methane results from dimethyl disulfide.^{1, 250} Thus, different molecules with different vapor pressures and solubilities in the solvent are present during sulfidation and possibly interact with the surface of the catalyst precursor. These factors all could influence the transformation of the oxide precursor.¹³ In the procedures, “S-ref” and “S-BT”, the liquid feed contained an equal amount of sulfur. All other sulfidation parameters were kept constant.

The metal molar fraction was hardly affected by the sulfiding agent. Moreover, the residual carbon contents of both sulfides were similar (1.9 and 2.2 mmol/g for “S-ref” and “S-BT”, respectively) and were most likely associated with the solvent (decalin) because the sulfiding agents had been decomposed.

Thus, a possible effect of carbon on the catalytic performance^{217, 253} can be excluded. The morphology of the sulfide, in contrast, changed when butanethiol was used as the sulfiding agent. Specifically, longer and higher stacked Mo(W)S₂ slabs, with a broader distribution in both stacking degree and slab length, were formed upon BT-based sulfidation in comparison to DMDS-based sulfidation. Moreover, the specific surface area and pore volume increased after the “S-BT” procedure (Table 30).

Table 30. Metal molar fraction of nickel (Ni), tungsten (W), and molybdenum (Mo), stacking degree, slab length [nm], specific surface area [m²/g], and pore volume [cm³/g] of the sulfide catalysts obtained after sulfidation according to the procedure “S-ref” and “S-BT”. The number in brackets behind stacking degree and slab length represent the standard deviation in the TEM analysis.

Catalyst	Metal molar fraction			Stacking degree	Slab length [nm]	Specific surface area [m ² /g]	Pore volume [cm ³ /g]
	Ni	W	Mo				
S-ref	0.48	0.41	0.11	3.5 (±1.6)	6.1 (±2.1)	39.8	0.068
S-BT	0.44	0.46	0.10	7.2 (±3.5)	9.1 (±4.1)	44.6	0.097

Besides the reflection pattern of Mo(W)S_2 (ICSD # 644245, 202366) and Ni_3S_2 phases (ICSD # 27521), reflections assigned to Ni_9S_8 (ICSD # 63080) phases were identified additionally in the “S-BT” sulfide (Figure 76). The relative intensity of the nickel sulfide phase in the “S-BT” sulfide, however, was rather low suggesting small crystallite sizes of such nickel sulfides.

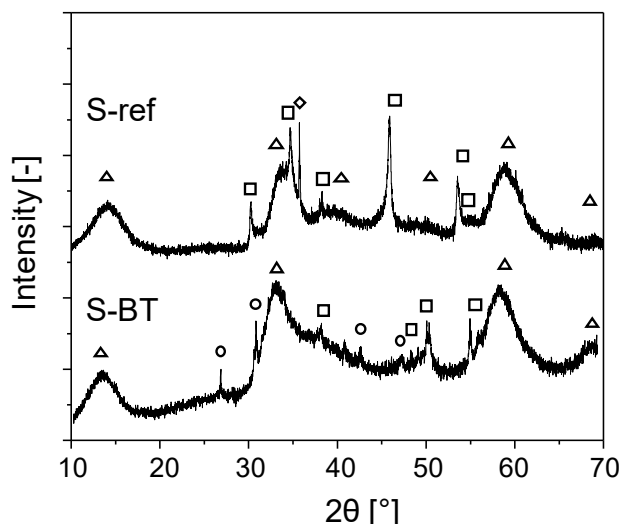


Figure 76. X-ray diffractograms of the sulfides obtained after the sulfidation procedure “S-ref” and “S-BT”. Reflections of the Mo(W)S_2 phase are marked with Δ (ICSD # 644245, 202366). The nickel sulfide phases identified are Ni_3S_2 (\square , ICSD # 27521) and Ni_9S_8 (\circ , ICSD # 63080). Reflections assigned to the diluting material SiC are marked with a \diamond .

The use of *n*-butanethiol as sulfiding agent led to marginally higher hydrodenitrogenation activity compared to the DMDS-derived sulfide (Figures 77 and 78, left panels).

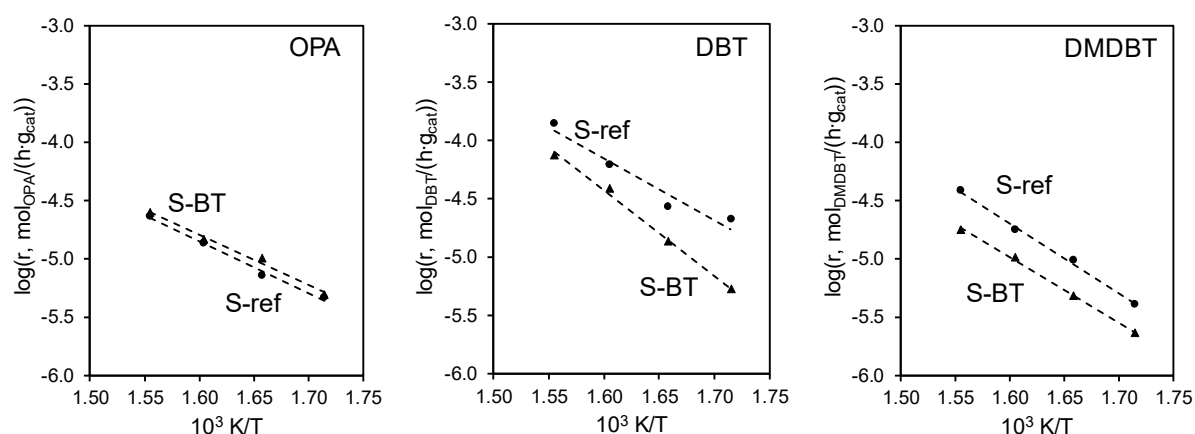


Figure 77. Reaction rates for the hydrodenitrogenation of *o*-propylaniline (OPA) (left), the hydrodesulfurization of dibenzothiophene (DBT) (middle), and of 4,6-dimethyldibenzothiophene (DMDBT) (right) as a function of temperature obtained on the sulfide catalysts after the sulfidation procedure “S-ref” (\bullet), and “S-BT” (\blacktriangle). Temperatures: 310–370 °C, total pressure: 50 bar.

Contrary to hydrodenitrogenation reactions, both hydrodesulfurization reactions exhibited higher rates on the catalyst sulfided with dimethyl disulfide (“S-ref”) (Figure 77, middle and right). In the conversion of 4,6-dimethyldibenzothiophene, the rates along both pathways were higher on the “S-ref” sulfide than on the “S-BT” sulfide with the direct desulfurization route being especially favored on the “S-ref” sulfide (Figure 78, right).

Similarly, the “S-ref” sulfide also showed higher rates for both conversion pathways of dibenzothiophene (Figure 79). As in the case of 4,6-dimethyldibenzothiophene, the difference in the hydrodesulfurization activity between the BT- and DMDS-derived sulfide catalysts was more pronounced along the direct desulfurization route than along the hydrogenation route. Interestingly, the apparent activation energy for the direct desulfurization rates was much higher on the “S-BT” sulfide than on the “S-ref” sulfide, as seen from the greater difference between the two catalysts at lower reaction temperatures (Figure 79, left).

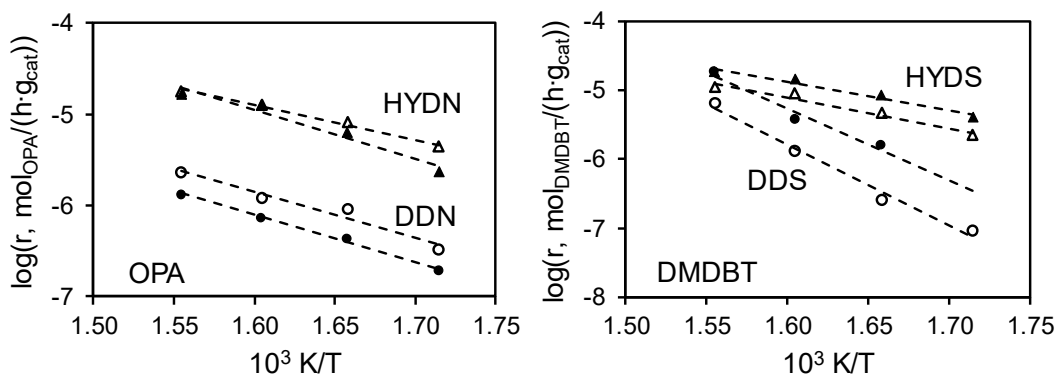


Figure 78. Left: Reaction rates as a function of temperature for the direct denitrogenation pathway (DDN) (●, ○) and the hydrogenation pathway (HYDN) (▲, △) of *o*-propylaniline (OPA) obtained on the “S-ref” (filled symbols) and the “S-BT” sulfide (empty symbols). Right: Reaction rates as a function of temperature for the direct desulfurization pathway (DDS) (○, ●) and the hydrogenation pathway (HYDS) (▲, △) of 4,6-dimethyldibenzothiophene (DMDBT) obtained on the “S-ref” (filled symbols) and the “S-BT” sulfide (empty symbols). Temperature: 310–370 °C, total pressure 50 bar.

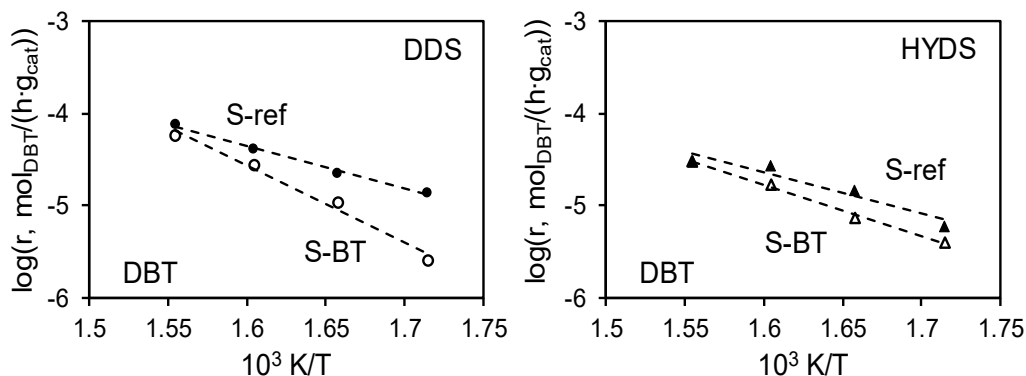


Figure 79. Reaction rates as a function of temperature for the direct desulfurization pathway (DDS) (left) and the hydrogenation pathway (HYDS) (right) of dibenzothiophene (DBT) obtained on the “S-ref” (filled symbols) and the “S-BT” sulfide (empty symbols). Temperature: 310–370 °C, total pressure 50 bar.

Thus, *n*-butanethiol as sulfiding agent had a positive effect on the hydrodenitrogenation rate of *o*-propylaniline while negatively affecting the rates of both hydrodesulfurization reactions. Particularly, the rate for the direct sulfur removal was diminished.

A possible explanation is that the highly stacked and long Mo(W)S₂ slab causes a decrease in the concentration of active sites needed for the direct removal of heteroatoms. In addition, the larger alkyl chain of *n*-butanethiol, which was present in the reaction mixture (Experimental), could influence adsorption of the reactants. As a consequence, π -adsorption required for hydrogenation reaction would be favored whereas σ -adsorption, which is prerequisite for the direct removal of heteroatoms, is retarded.^{1, 189, 254}

7.5. Combined effects of nature and concentration of the sulfiding agent

As a low concentration of dimethyl disulfide during sulfidation was observed to result in a more active catalyst (Section 6.7.2), the sulfur content in the case of BT-based sulfidation was lowered also by a tenth (“S-BT-min”) as in the case of the DMDS-based “S-min” protocol with reduced sulfur concentrations (Table 23). The H₂/S ratio was adjusted to 5 and the other parameters were again kept constant.

Table 31. Metal molar fraction of nickel (Ni), tungsten (W), and molybdenum (Mo), stacking degree, slab length [nm], specific surface area [m²/g], and pore volume [cm³/g] of the sulfide catalysts obtained after sulfidation according to the procedure “S-min” and “S-BT-min”. The number in brackets behind stacking degree and slab length represent the standard deviation in the TEM analysis.

Catalyst	Metal molar fraction			Stacking degree	Slab length [nm]	Specific surface area [m ² /g]	Pore volume [cm ³ /g]
	Ni	W	Mo				
S-min	0.46	0.43	0.12	3.5 (±1.4)	4.8 (±1.8)	40.2	0.116
S-BT-min	0.45	0.44	0.11	4.0 (±1.4)	4.2 (±1.5)	19.8	0.062

The metal molar fractions, stacking degree, and length of the Mo(W)S₂ slabs were hardly affected by the sulfiding agent (Table 31). Moreover, the carbon content of the sulfides (2.1 and 2.0 mmol/g for “S-min” and “S-BT-min”, respectively) was hardly affected. Thus, a lower content of *n*-butanethiol in the liquid sulfidation mixture produced Mo(W)S₂ with dimensions in the z- and y-directions similar to sulfide obtained via the “S-min” protocol (DMDS-based), but much smaller than those of the “S-BT” sulfided material (Table 30). However, the specific surface area and pore volume of the “S-BT-min” sulfide decreased by half, compared to the “S-min” sulfide (Table 31).

A comparison of the X-ray diffractograms of the “S-min” and “S-BT-min” samples revealed that Mo(W)S₂ (ICSD # 644245, 202366), Ni₃S₂ (ICSD # 27521), and Ni₉S₈ (ICSD # 63080) phases are present independent of the sulfiding agent. As mentioned above, the low sulfur content in liquid phase retarded crystal growth of the nickel sulfide crystals indicated by the low relative intensity of the corresponding reflections (Figure 80).

Comparing the hydrotreating activities of the “S-min” and “S-BT-min” catalysts showed that butanethiol (BT) as sulfiding agent led to the more active catalyst in the conversion of all three reactants, most pronounced with S-compounds (Figure 81).

In the conversion of *o*-propylaniline, the direct denitrogenation pathway was slightly favored on the “S-BT-min” sulfide compared to the “S-min” sulfide, becoming more pronounced at higher temperatures. The rates of hydrogenative denitrogenation, in contrast, were hardly affected by the sulfiding agent used (Figure 82, left).

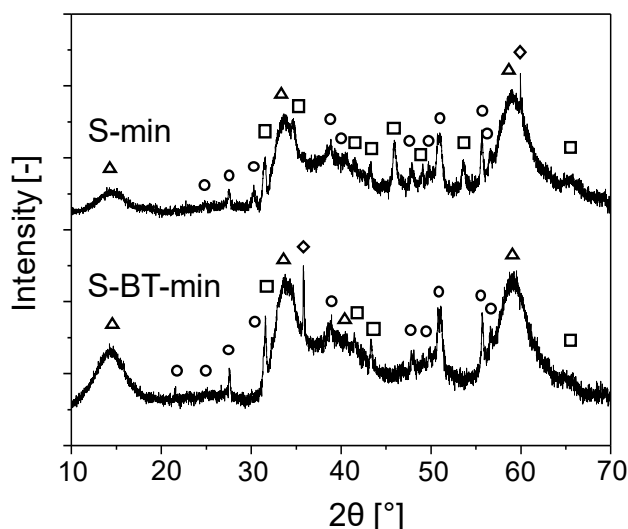


Figure 80. X-ray diffractograms of the sulfides obtained after the sulfidation procedure “S-min” and “S-BT-min”. Reflections of the Mo(W)S₂ phase are marked with Δ (ICSD # 644245, 202366). The nickel sulfide phases identified are Ni₃S₂ (\square , ICSD # 27521) and Ni₉S₈ (\circ , ICSD # 63080). Reflections assigned to the diluting material SiC are marked with \diamond .

In contrast to the lower mass-specific hydrodesulfurization activities of the “S-BT” catalyst compared to the “S-ref” counterpart, both of which had been sulfided using higher concentrations (4-12 wt % of S) of sulfiding agent, the “S-BT-min” catalyst showed higher rates for the hydrodesulfurization reactions compared to the “S-min” sulfide (Figure 81). In the conversion of dibenzothiophene and 4,6-dimethyldibenzothiophene the rates of both pathways almost doubled on the “S-BT-min” catalyst (Figure 82 and 83).

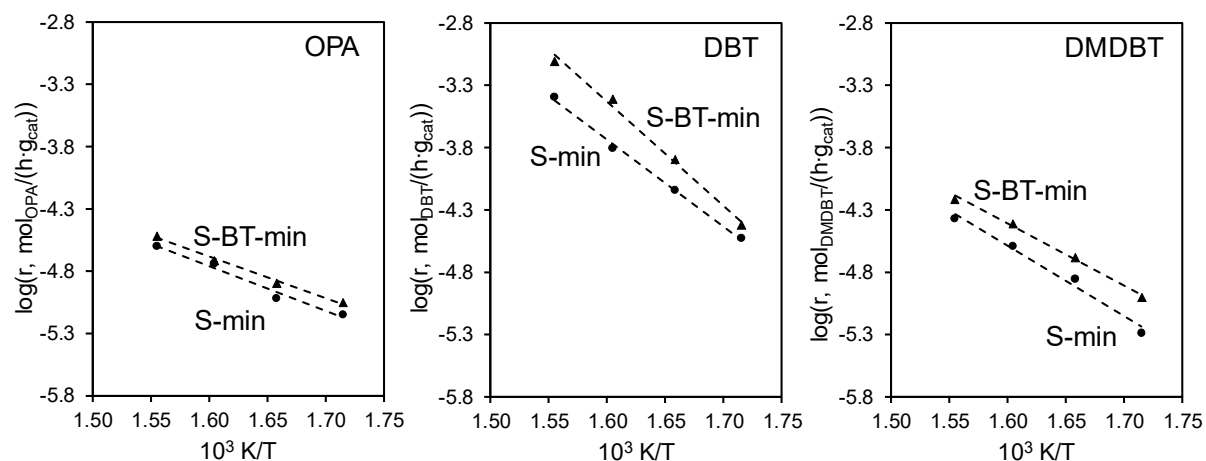


Figure 81. Reaction rates for the hydrodenitrogenation of *o*-propylaniline (OPA) (left), the hydrodesulfurization of dibenzothiophene (DBT) (middle), and of 4,6-dimethyldibenzothiophene (DMDBT) (right) as a function of temperature obtained on the sulfide catalysts after the sulfidation procedure “S-min” (\bullet), and “S-BT-min” (\blacktriangle). Temperatures: 310–370 °C, total pressure: 50 bar.

In contrast to the lower mass-specific hydrodesulfurization activities of the “S-BT” catalyst compared to the “S-ref” counterpart, both of which had been sulfided using higher concentrations (4-12 wt % S) of sulfiding agent, the “S-BT-min” catalyst showed higher rates for the hydrodesulfurization reactions compared to the “S-min” sulfide (Figure 81). In the conversion of dibenzothiophene and 4,6-dimethyldibenzothiophene the rates of both pathways almost doubled on the “S-BT-min” catalyst (Figure 82 and 83).

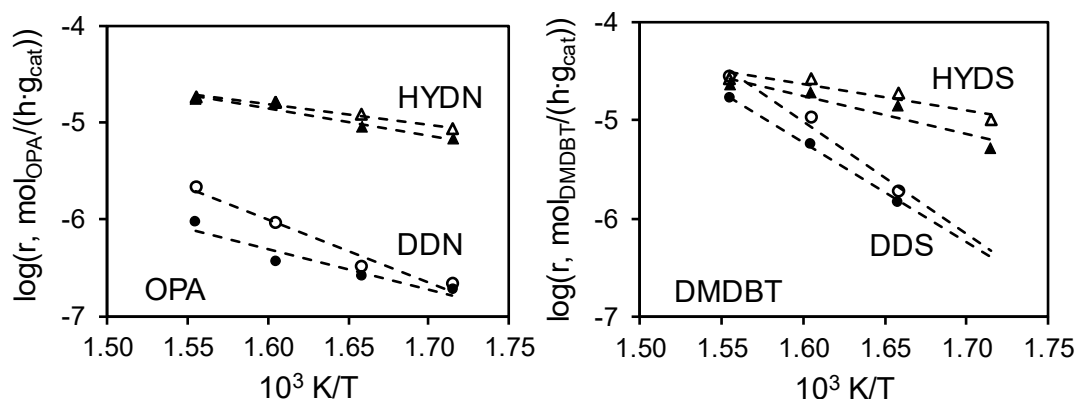


Figure 82. Left: Reaction rates as a function of temperature for the direct denitrogenation pathway (DDN) (●, ○) and the hydrogenation pathway (HYDN) (▲, △) of *o*-propylaniline (OPA) obtained on the “S-min” (filled symbols) and the “S-BT-min” sulfide (empty symbols). Right: Reaction rates as a function of temperature for the direct desulfurization pathway (DDS) (○, ●) and the hydrogenation pathway (HYDS) (▲, △) of 4,6-dimethyldibenzothiophene (DMDBT) obtained on the “S-min” (filled symbols) and the “S-BT-min” sulfide (empty symbols). Temperature: 310-370 °C, total pressure 50 bar.

Thus, using a lower content of butanethiol (BT) in the liquid sulfidation mixture resulted in a more active sulfide catalyst compared to the DMDS-based sulfidation with the same low S concentration. The retarded crystal growth of Mo(W)S₂ in the sulfidation procedure “S-BT-min” compared to “S-BT” resulted in exposure of a larger area of the active sulfide perimeter. This impact might have stemmed from a higher decomposition temperature (225 °C for butanethiol and 200 °C for dimethyl disulfide) resulting in a better coupling of the reduction and sulfidation steps of the different metal cations which in turn leads to a higher concentration of substituted nickel(II) cations in the Mo(W)S₂ edge.^{13, 69} The different hydrocarbon residues after decomposition may also play a role. Decomposition of dimethyl disulfide produces methane whereas butane is produced via the decomposition of butanethiol. The solubility effects may thereby positively affect the conversion of the reactants.

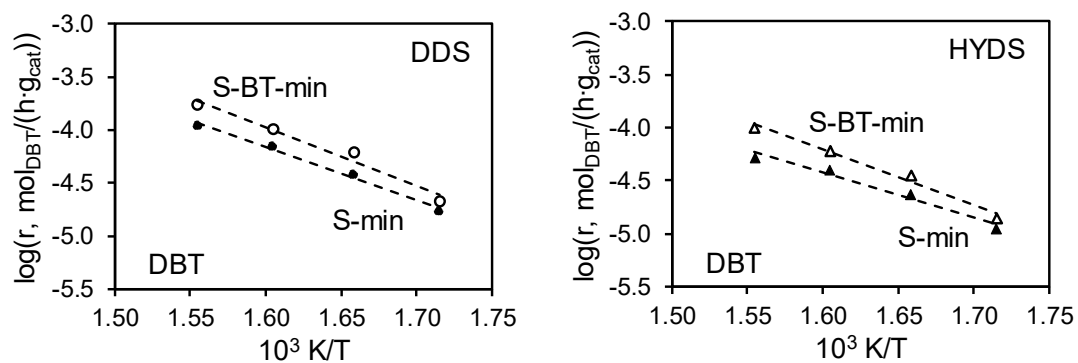


Figure 83. Reaction rates as a function of temperature for the direct desulfurization pathway (DDS) (left) and the hydrogenation pathway (HYDS) (right) of dibenzothiophene (DBT) obtained on the "S-min" (filled symbols) and the "S-BT-min" sulfide (empty symbols). Temperature: 310-370 °C, total pressure 50 bar.

8. Conclusion

The *in-situ* XAS study in liquid-phase shows that sulfidation of the three metal cations takes place in similar temperature ranges. Indeed, sulfidation of tungsten occurs at slightly higher temperatures than sulfidation of molybdenum and nickel. However, transformation of these two cations is only completed after the sulfidation of tungsten. Thus, the transformation of each metal cation directly affects the transformation of the two others. This points to a close interaction among the three metal cations already present in the oxide precursor.⁶⁵ This is also evident by the reduced sulfidation temperatures of the trimetallic precursor compared to the sulfidation temperatures of the corresponding reference oxides obtained by temperature-programmed sulfidation. Moreover, the broad temperature range of the nickel sulfidation suggests that the transformation of molybdenum and tungsten retard complete sulfidation of nickel. In other words, complex structural rearrangements and electronic effects of the direct neighborhood of molybdenum and tungsten delay the transformation of nickel oxide species but in turn, facilitate the transformation of molybdenum and tungsten oxide species.

The liquid-phase sulfidation procedure can be further optimized to increase the hydrotreating activity of the resulting sulfide in general and to tune the catalyst according to the requirements of the feedstock. The most active sulfide was obtained after the sulfidation with a H₂/S ratio of 2.5 ("S-H/S-"). The low H₂ partial pressure delays or provides an incomplete reduction of the metal cations. This especially retards sulfidation of nickel(II) cations finally resulting in a better interaction of this nickel(II) cations with Mo(W)S₂ and thus, a higher concentration of active sites. An enhanced hydrotreating activity was also observed using butanethiol as sulfiding agent at low chemical potential of sulfur. A kind of complexation of nickel(II) cations by the alkyl chain also leads to a retarded nickel sulfidation and thus, a better interaction with the molybdenum and tungsten phase similar to the effect of the low partial pressure of hydrogen. Both sulfidation procedures lead to a sulfide catalyst being more active in the conversion of dibenzothiophene than in the conversion of *o*-propylaniline. This suggests that both procedures increase the Lewis acidity of the material. Lewis acid sites act as adsorption sites for S-containing species and therefore, increase the direct desulfurization of dibenzothiophene. The increase of the activity of the hydrogenation pathway of dibenzothiophene to approximately the same extent together with the increase of the activity for the hydrogenation pathway on the *o*-propylaniline conversion suggests that Lewis acid sites are also involved in the formation of SH groups which are the hydrogen providing groups.¹²⁷ Despite remarkable differences in the hydrotreating activity significant changes in morphology and texture have not observed using any sulfidation procedure. Indeed, shorter Mo(W)S₂ slabs expose a larger fraction of the active perimeter. Consequently, sulfides with short slabs show a higher activity,

for instance "S-BT-min" is superior to "S-BT" as well as "S-min", "S-H/S+", and "S-H/S-" are superior to "S-ref". However, other features of the sulfides, e.g., specific surface area and formation of crystalline nickel sulfides, can also influence the catalytic performance so that short sulfide slab do not guarantee high hydrotreating activity.

Chapter 5

SUMMARY & CONCLUSION –

Kurzzusammenfassung

Summary

The need of processing low-quality feedstocks and simultaneously stricter environmental regulations yearn for more efficient hydrotreating catalysts. Unsupported ternary Ni-Mo-W sulfides are promising materials for the conversion of heavy feedstocks and to fulfill the legal specifications. This work has identified the differences between bimetallic and trimetallic sulfide phases. Further, requirements of various hydrodefunctionalization reactions on the morphology and texture of the active sulfide phase and the achievement of them via synthesis have been tackled.

A post-synthetic treatment was performed to uncover the active Ni-containing Mo(W)S₂ sulfide phase and thereby enable correlations between activity and properties of the sulfide material. The acid treatment selectively removed excess nickel sulfides from the active Ni-Mo(W)S₂ surface. Analysis of the reaction route of the hydrodenitrogenation of quinoline revealed a common nature of active sites on bimetallic and trimetallic Ni-Mo-W sulfides independent from the atomic composition of the catalyst. Thus, the active site comprises edge-substituted nickel, the common feature of all these sulfides.

The atomic Mo(W)S₂ composition, indeed, governs the concentration of nickel incorporated into the Mo(W)S₂ edges, in turn leading to different concentration of active sites. In general, a ternary sulfide phase results in a higher concentration of edge-substituted nickel compared to bimetallic phases. The highest concentration of active sites was detected on a W-enriched ternary phase leading to the most active catalyst.

An increased concentration of active sites also appears to shift the rate-determining in the hydrogenation of 1,2,3,4-tetrahydroquinoline (dominant conversion route in the hydrodenitrogenation of quinoline) to a later hydrogen addition step. This is reflected in an increased reaction order in hydrogen. The rate of the hydrogenation route did not depend on the quinoline concentration, but the other pathway, the so-called ring opening pathway (minor route), depended on the surface concentration of quinoline. This difference is related to different adsorption modes of the reactant along the two pathways, i.e., σ -adsorption for ring opening and π -adsorption for hydrogenation. Thus, hydrogenation and ring opening reactions require two different types of active sites.

The fact that the rate of the ring opening route was independent of the surface concentration of hydrogen, suggests that hydrogen is not involved in the rate-determining step of the C-N bond cleavage in 1,2,3,4-tetrahydroquinoline.

Investigation of different trimetallic sulfides in the hydrodenitrogenation of *o*-propylaniline or quinoline combined with a parallel hydrodesulfurization of dibenzothiophene revealed a

complex dependence on the concentration and accessibility of active sites and the primary structure of the sulfide phase. Properties in general leading to high hydrotreating activity are high specific surface area, short Mo(W)S₂ slabs, high tungsten content, and low nickel content at the surface. If the concentration of active sites is high enough, the accessibility of active sites governs the activity of the sulfide in the conversion of *o*-propylaniline and dibenzothiophene in presence of *o*-propylaniline. As soon as quinoline is present shorter Mo(W)S₂ slabs are beneficial due to the molecular size of quinoline. Moreover, a W-enriched phase increases the hydrogenation functionality which is more demanded in the hydrodenitrogenation of quinoline than in the hydrodenitrogenation of *o*-propylaniline.

Besides morphology and texture of the sulfide, the most decisive factor is a high concentration of nickel substituted into the Mo(W)S₂ edge as this leads to the active site. The incorporation of nickel can be tremendously influence by the sulfidation procedure of the catalyst precursor. In liquid-phase sulfidation of a ternary sulfide complete transformation of the nickel and molybdenum oxide phase, which already starts below 200 °C in the case of nickel, is retarded until sulfidation of tungsten occurs. The transformation of tungsten, in contrast, proceeds rapid as soon as a temperature of 300 °C is reached. Thus, the transformation of one metal directly affects the transformation of the others. Despite complete nickel sulfidation is retarded, the largest fraction of nickel is already sulfided and forms undesired nickel sulfides. A low sulfur content in the liquid sulfidation mixture as well as a low H₂/S ratio cause an increased hydrotreating activity. At low sulfur concentration, the use of *n*-butanethiol as sulfiding agent further increases the activity of the resulting sulfide. These changes of the sulfidation parameters hardly affected surface area, slab length, and stacking degree of the resulting sulfide. Thus, the higher activity is supposed to be caused by a better interaction among the metal cations during liquid-phase sulfidation leading to a higher concentration of edge-substituted nickel.

Summarizing, the active sites for all hydrotreating reactions comprises edge-substituted nickel. The concentration of these sites, however, depends on the atomic composition of Mo(W)S₂. Indeed, synthesis parameters can further facilitate the incorporation of nickel. Moreover, the different molecular structures of the reactants accompanied with the different pathway selectivities in their conversion require tuning of the morphology and texture of the sulfide catalyst during synthesis.

Zusammenfassung

Die geringer werdende Qualität des Erdöls in Kombination mit den steigenden Anforderungen bezüglich des Schadstoffgehaltes in Kraftstoffen machen es notwendig effizientere Katalysatoren für Hydrotreating-Prozesse zu entwickeln. Ungeträgerte Ni-Mo-W Sulfide sind dafür vielversprechende Katalysatoren. Im Rahmen dieser Arbeit wurden die Unterschiede zwischen bimetallischen und trimetallischen Sulfiden identifiziert. Des Weiteren konnte festgestellt werden, welche morphologischen und strukturellen Eigenschaften die katalytisch aktive Phase aufweisen sollte, um eine hohe katalytische Aktivität zu gewährleisten und wie dies durch die Katalysatorsynthese erreicht werden kann.

Mit Hilfe einer Nachbehandlung in Säure konnte überschüssiges Nickelsulfid selektiv von der Oberfläche der Ni-Mo(W)S₂ Phase entfernt werden. Dies ermöglichte eine Korrelation der Aktivität mit Eigenschaften des Sulfids. Die detaillierte Analyse der Reaktionswege innerhalb der Hydrodenitrogenierung von Chinolin zeigte, dass sich die aktiven Zentren bimetallischer Sulfide nicht von denen trimetallischer Sulfide unterscheiden. Da das gemeinsame Merkmal dieser Katalysatoren die Substitution von Molybdän- bzw. Wolfram- Kationen an den Ecken der Sulfidschichten mit Nickelkationen ist, muss das aktive Zentrum genau diese substituierten Nickelkationen beinhalten.

Das aktive Zentrum ist also unabhängig von der atomaren Zusammensetzung der Mo(W)S₂ Phase. Allerdings beeinflusst die atomare Zusammensetzung die Konzentration an substituierten Nickelkationen und somit die Konzentration an aktiven Zentren. Die höchste Konzentration an aktiven Zentren wurde bei einem mit Wolfram angereicherten, trimetallischen Sulfid gefunden. Dementsprechend war dies auch der aktivste Katalysator.

Eine höhere Konzentration an aktiven Zentren hat auch zur Folge, dass der geschwindigkeitsbestimmende Schritt innerhalb des bevorzugten Reaktionsweges in der Umsetzung von Chinolin (Hydrierung von 1,2,3,4-Tetrahydrochinoline) zu einer späteren Wasserstoffaddition verschoben wird, was sich in einer steigenden Reaktionsordnung in Wasserstoff widerspiegelt. Im Gegensatz dazu hat die Oberflächenkonzentration an Chinolin keinen Einfluss auf die Reaktionsrate.

Die Reaktionsrate des anderen Reaktionsweges, bei dem zuerst eine Ringöffnung des Heterozykluses von 1,2,3,4-Tetrahydrochinolin stattfindet, ist jedoch von der Oberflächenkonzentration an Chinolin abhängig. Dieser Unterschied in den Reaktionsordnungen ist auf unterschiedliche Adsorptionsmodi des Reaktanden zurückzuführen, da eine σ -Adsorption für die Ringöffnung nötig ist, wohingegen die Hydrierung eine π -Adsorption des Moleküls verlangt. Folglich benötigen beide Reaktionswege unterschiedliche aktive Zentren.

Im Gegensatz zur Hydrierung ist die Reaktionsrate der Ringöffnung unabhängig von der Oberflächenkonzentration an Wasserstoff. Dies lässt den Rückschluss zu, dass keine Wasserstoffspezies in den geschwindigkeitsbestimmenden Schritt der Spaltung der C-N Bindung von 1,2,3,4-Tetrahydrochinoline involviert ist.

Eine komplexe Abhängigkeit der katalytischen Aktivität von der Konzentration und Zugänglichkeit der aktiven Zentren, sowie von der Primärstruktur des Sulfides wurde durch den Einsatz verschiedener trimetallischer Ni-Mo-W Sulfide in parallel ablaufenden Hydrodesulfurierungs- und Hydrodenitrogenierungsreaktionen festgestellt. Eine hohe spezifische Oberfläche, kurze Mo(W)S₂-Schichten, ein hoher Wolframgehalt sowie ein niedriger Nickelgehalt auf der Oberfläche führen allgemein zu hoher katalytischer Aktivität. Die Zugänglichkeit der aktiven Zentren ist der entscheidende Faktor für die Umsetzung von *o*-Propylanilin und die Umsetzung von Dibenzothiophen in Gegenwart von *o*-Propylanilin, falls eine ausreichend hohe Konzentration an aktiven Zentren vorhanden ist. Mit der Anwesenheit von Chinolin steigt die Bedeutung eines hohen Wolframgehaltes in der Sulfidphase und kurzer Mo(W)S₂-Schichten deutlich an. Dies ist auf die Molekülgröße und auf den höheren Wasserstoffbedarf während der Umsetzung von Chinolin im Gegensatz zu *o*-Propylanilin zurückzuführen.

Neben Morphologie und Struktur des Sulfids ist die Konzentration an aktiven Zentren, die mit der Substitution von Nickelkation in die Ecken der Mo(W)S₂-Schicht einhergeht, der entscheidende Faktor für eine hohe katalytische Aktivität. Diese Substitution kann maßgeblich durch die Reaktionsbedingungen während Sulfidierung der Katalysatorvorstufe beeinflusst werden. Die Umwandlung der Nickeloxidphase in die Sulfidphase beginnt bereits unter 200 °C, die der Molybdänoxidphase kurze Zeit später. Allerdings ist eine vollständige Sulfidierung beider Metalle erst erreicht, nachdem auch die Transformation der Wolframoxidphase begonnen hat, wofür jedoch eine Temperatur von mindestens 300 °C nötig ist. Die Sulfidierung eines Metalls wird daher maßgeblich von den zwei anderen Metallen beeinträchtigt. Obwohl die vollständige Sulfidierung der Nickeloxidphase bereits verzögert stattfindet, bilden sich kristalline Nickelsulfidphasen. Dies kann durch die Verwendung von niedrigen Schwefelkonzentrationen in der flüssigen Sulfidierungsmischung, ein niedriges H₂/S Verhältnis und der Verwendung von *n*-Butanthiol als Sulfidierungsreagenz deutlich vermindert werden und so die Aktivität gesteigert werden. Diese Änderungen der Sulfidierungsbedingungen haben kaum Auswirkungen auf die spezifische Oberfläche des Sulfides, die Schichthöhe, und die Länge der Sulfidschichten. Folglich ist die höhere Aktivität auf eine höhere Konzentration an substituierten Nickelkationen und somit an aktiven Zentren zurückzuführen.

Zusammenfassend kann festgehalten werden, dass die atomare Zusammensetzung der Mo(W)S₂ Phase keinerlei Auswirkungen auf die Art des aktiven Zentrums hat, wohl aber auf dessen Konzentration. Die Konzentration an aktiven Zentren kann außerdem maßgeblich

durch die Wahl der Sulfidierungsbedingungen beeinflusst werden. Unterschiedliche Strukturen der Reaktanden erfordern zudem ein Anpassen der Morphologie und Struktur des Katalysators mittels unterschiedlicher Synthesemethoden.

References

1. Toulhoat, H. R., P., *Catalysis by Transition Metal Sulfides*. Energies Nouvelles Publications: Paris, 2013.
2. Ancheyta, J.; Rana, M. S., Future technology in heavy oil processing. *Encyclopedia of Life Support Systems (EOLSS)* **2004**.
3. Miller, J. D.; Façanha, C., International Council on Clean Transportation (ICCT). *Washington DC (USA)* **2014**.
4. Council, E. P. a. o. t., Directive 2012/33/EU of the European Parliament and of the Council. *Official Journal of the European Union* **2012**, 327.
5. Rana, M. S.; Sámano, V.; Ancheyta, J.; Diaz, J. A. I., A review of recent advances on process technologies for upgrading of heavy oils and residua. *Fuel* **2007**, *86* (9), 1216-1231.
6. Topsøe, H.; Clausen, B. S.; Massoth, F. E., Hydrotreating catalysis. In *Catalysis*, Springer: 1996; pp 1-269.
7. Kressmann, S.; Boyer, C.; Colyar, J. J.; Schweitzer, J. M.; Viguie, J. C., Improvements of Ebullated-Bed Technology for Upgrading Heavy Oils. *Oil & Gas Science and Technology - Rev. IFP* **2000**, *55* (4), 397-406.
8. Bataille, F.; Lemberon, J.-L.; Michaud, P.; Pérot, G.; Vrinat, M.; Lemaire, M.; Schulz, E.; Breyse, M.; Kasztelan, S., Alkyldibenzothiophenes Hydrodesulfurization-Promoter Effect, Reactivity, and Reaction Mechanism. *Journal of Catalysis* **2000**, *191* (2), 409-422.
9. Ho, T. C., A theory of ultradeep hydrodesulfurization of diesel in stacked-bed reactors. *AIChE Journal* **2018**, *64* (2), 595-605.
10. Eijsbouts, S.; Mayo, S. W.; Fujita, K., Unsupported transition metal sulfide catalysts: From fundamentals to industrial application. *Applied Catalysis A: General* **2007**, *322* (0), 58-66.
11. Plantenga, F. L.; Cerfontain, R.; Eijsbouts, S.; van Houtert, F.; Anderson, G. H.; Miseo, S.; Soled, S.; Riley, K.; Fujita, K.; Inoue, Y., 89 "Nebula": A hydroprocessing catalyst with breakthrough activity. In *Studies in Surface Science and Catalysis*, Anpo, M.; Onaka, M.; Yamashita, H., Eds. Elsevier: 2003; Vol. 145, pp 407-410.
12. Soled, S. L.; Miseo, S.; Krycak, R.; Vroman, H.; Ho, T. C.; Riley, K. L., Nickel molybdotungstate hydrotreating catalysts.; US Patent 6156695A, 2000.
13. Silvy, R. P.; Grange, P.; Delannay, F.; Delmon, B., Influence of the nature of the activating molecules on the catalytic activity of cobalt—molybdenum/alumina catalysts. *Applied catalysis* **1989**, *46* (1), 113-129.
14. Maesen, T. L. M.; Kuperman, A. E., Hydroconversion processes employing multi-metallic catalysts and method for making thereof.; US Patent 8206575B2, 2012.
15. Bensch, W.; Reedijk, J.; Poepelmeier, K., Hydrotreating: Removal of Sulfur from Crude Oil Fractions with Sulfide Catalysts. *Comprehensive Inorganic Chemistry II* **2013**, *2*, 287-321.
16. Frizi, N.; Blanchard, P.; Payen, E.; Baranek, P.; Rebeilleau, M.; Dupuy, C.; Dath, J., Genesis of new HDS catalysts through a careful control of the sulfidation of both Co and Mo atoms: Study of their activation under gas phase. *Catalysis Today* **2008**, *130* (2-4), 272-282.
17. Prins, R., Hydrotreating. In *Handbook of Heterogeneous Catalysis*, Wiley-VCH Verlag GmbH & Co. KGaA: 2008.
18. Whitehurst, D. D.; Farag, H.; Nagamatsu, T.; Sakanishi, K.; Mochida, I., Assessment of limitations and potentials for improvement in deep desulfurization through detailed kinetic analysis of mechanistic pathways. *Catalysis Today* **1998**, *45* (1-4), 299-305.
19. Egorova, M.; Prins, R., Hydrodesulfurization of dibenzothiophene and 4,6-dimethyldibenzothiophene over sulfided NiMo/ γ -Al₂O₃, CoMo/ γ -Al₂O₃, and Mo/ γ -Al₂O₃ catalysts. *Journal of Catalysis* **2004**, *225* (2), 417-427.
20. Houalla, M.; Nag, N. K.; Sapre, A. V.; Broderick, D. H.; Gates, B. C., Hydrodesulfurization of dibenzothiophene catalyzed by sulfided CoO-MoO₃/ γ -Al₂O₃: The reaction network. *AIChE Journal* **1978**, *24* (6), 1015-1021.
21. Stanislaus, A.; Marafi, A.; Rana, M. S., Recent advances in the science and technology of ultra low sulfur diesel (ULSD) production. *Catalysis Today* **2010**, *153* (1), 1-68.

22. Topsøe, H.; Egeberg, R. G.; Knudsen, K. G., Future challenges of hydrotreating catalyst technology. *Prepr. Pap.-Am. Chem. Soc., Div. Fuel Chem* **2004**, *49* (2), 568.
23. Ho, T. C., A Theory of Ultra-Deep Hydrodesulfurization of Diesel in Stacked-Bed Reactors. *AIChE Journal* **2017**.
24. Kim, J. H.; Ma, X.; Song, C.; Lee, Y.-K.; Oyama, S. T., Kinetics of Two Pathways for 4,6-Dimethyldibenzothiophene Hydrodesulfurization over NiMo, CoMo Sulfide, and Nickel Phosphide Catalysts. *Energy & Fuels* **2005**, *19* (2), 353-364.
25. Beltramone, A. R.; Crossley, S.; Resasco, D. E.; Alvarez, W. E.; Choudhary, T. V., Inhibition of the Hydrogenation and Hydrodesulfurization Reactions by Nitrogen Compounds over NiMo/Al₂O₃. *Catal Lett* **2008**, *123* (3), 181-185.
26. La Vopa, V.; Satterfield, C. N., Poisoning of thiophene hydrodesulfurization by nitrogen compounds. *Journal of Catalysis* **1988**, *110* (2), 375-387.
27. Nagai, M.; Sato, T.; Aiba, A., Poisoning effect of nitrogen compounds on dibenzothiophene hydrodesulfurization on sulfided NiMo/Al₂O₃ catalysts and relation to gas-phase basicity. *Journal of Catalysis* **1986**, *97* (1), 52-58.
28. Laine, R. M., Comments on the Mechanisms of Heterogeneous Catalysis of the Hydrodenitrogenation Reaction. *Catalysis Reviews* **1983**, *25* (3), 459-474.
29. Prado, G. H. C.; Rao, Y.; de Klerk, A., Nitrogen Removal from Oil: A Review. *Energy & Fuels* **2016**.
30. Ho, T. C., Hydrodenitrogenation Catalysis. *Catalysis Reviews* **1988**, *30* (1), 117-160.
31. Pérot, G., The reactions involved in hydrodenitrogenation. *Catalysis Today* **1991**, *10* (4), 447-472.
32. Prins, R., Catalytic hydrodenitrogenation. In *Advances in Catalysis*, Academic Press: 2001; Vol. 46, pp 399-464.
33. Cocchetto, J. F.; Satterfield, C. N., Chemical equilibria among quinoline and its reaction products in hydrodenitrogenation. *Industrial & Engineering Chemistry Process Design and Development* **1981**, *20* (1), 49-53.
34. Satterfield, C. N.; Cocchetto, J. F., Reaction network and kinetics of the vapor-phase catalytic hydrodenitrogenation of quinoline. *Industrial & Engineering Chemistry Process Design and Development* **1981**, *20* (1), 53-62.
35. Satterfield, C. N.; Yang, S. H., Catalytic hydrodenitrogenation of quinoline in a trickle-bed reactor. Comparison with vapor phase reaction. *Industrial & Engineering Chemistry Process Design and Development* **1984**, *23* (1), 11-19.
36. Girgis, M. J.; Gates, B. C., Reactivities, reaction networks, and kinetics in high-pressure catalytic hydroprocessing. *Industrial & Engineering Chemistry Research* **1991**, *30* (9), 2021-2058.
37. Wei, H.; Hong, N.; Yun, L. x.; Feng, L. M.; He, Y. Q.; Dong, L. D., Study on the origin of the active sites of HDN catalysts using alumina-supported MoS₃ nanoparticles as a precursor. *Catalysis Science & Technology* **2015**.
38. Prins, R.; Jian, M.; Flechsenhar, M., Mechanism and kinetics of hydrodenitrogenation. *Polyhedron* **1997**, *16* (18), 3235-3246.
39. Hrabar, A.; Hein, J.; Gutiérrez, O. Y.; Lercher, J. A., Selective poisoning of the direct denitrogenation route in *o*-propylaniline HDN by DBT on Mo and NiMo/γ-Al₂O₃ sulfide catalysts. *Journal of Catalysis* **2011**, *281* (2), 325-338.
40. Satterfield, C. N.; Gultekin, S., Effect of hydrogen sulfide on the catalytic hydrodenitrogenation of quinoline. *Industrial & Engineering Chemistry Process Design and Development* **1981**, *20* (1), 62-68.
41. Eijsbouts, S.; de Beer, V. H. J.; Prins, R., Hydrodenitrogenation of quinoline over carbon-supported transition metal sulfides. *Journal of Catalysis* **1991**, *127* (2), 619-630.
42. Jian, M.; Prins, R., Mechanism of the Hydrodenitrogenation of Quinoline over NiMo(P)/Al₂O₃ Catalysts. *Journal of Catalysis* **1998**, *179* (1), 18-27.
43. Hein, J.; Gutiérrez, O. Y.; Schachtl, E.; Xu, P.; Browning, N. D.; Jentys, A.; Lercher, J. A., Distribution of Metal Cations in Ni-Mo-W Sulfide Catalysts. *ChemCatChem* **2015**, *7* (22), 3692-3704.

44. Huber, G. W.; O'Connor, P.; Corma, A., Processing biomass in conventional oil refineries: Production of high quality diesel by hydrotreating vegetable oils in heavy vacuum oil mixtures. *Applied Catalysis A: General* **2007**, *329*, 120-129.
45. Elliott, D. C., Historical developments in hydroprocessing bio-oils. *Energy & Fuels* **2007**, *21* (3), 1792-1815.
46. Ruddy, D. A.; Schaidle, J. A.; Ferrell Iij, J. R.; Wang, J.; Moens, L.; Hensley, J. E., Recent advances in heterogeneous catalysts for bio-oil upgrading via "ex situ catalytic fast pyrolysis": catalyst development through the study of model compounds. *Green Chemistry* **2014**, *16* (2), 454-490.
47. Zacher, A. H.; Olarte, M. V.; Santosa, D. M.; Elliott, D. C.; Jones, S. B., A review and perspective of recent bio-oil hydrotreating research. *Green Chemistry* **2014**, *16* (2), 491-515.
48. Nag, N. K., On the mechanism of the hydrogenation reactions occurring under hydroprocessing conditions. *Applied Catalysis* **1984**, *10* (1), 53-62.
49. Zdražil, M., Recent advances in catalysis over sulphides. *Catalysis Today* **1988**, *3* (4), 269-365.
50. Baerns, M.; Behr, A.; Brehm, A.; Gmehling, J.; Hofmann, H.; Onken, U., *Technische Chemie*. John Wiley & Sons: 2013.
51. Maesen, T. L. M.; Kuperman, A. E., Hydroconversion multi-metallic catalyst and method for making thereof.; US Patent 8702970B2, 2014.
52. Soled, S. L.; Miseo, S.; Hou, Z., Bulk Ni-Mo-W catalysts made from precursors containing an organic agent.; US Patent 7544632B2, 2009.
53. Maesen, T.; Kuperman, A. E.; Dykstra, D., Hydroconversion multi-metallic catalyst and method for making thereof.; US Patent 8383543, 2013.
54. Kuperman, A. E.; Maesen, T.; Dykstra, D.; Wang, P.; Uckung, S., Hydroconversion multi-metallic catalyst and method for making thereof.; US Patent 8703641B2, 2014.
55. Soled, S. L.; Miseo, S.; Eijsbouts, S.; Plantenga, F. L., Hydroprocessing using hydrothermally-prepared bulk multimetallic catalysts.; US Patent 7686943B2, 2010.
56. Yin, C.; Zhao, L.; Bai, Z.; Liu, H.; Liu, Y.; Liu, C., A novel porous ammonium nickel molybdate as the catalyst precursor towards deep hydrodesulfurization of gas oil. *Fuel* **2013**, *107* (0), 873-878.
57. Yoosuk, B.; Kim, J. H.; Song, C.; Ngamcharussrivichai, C.; Prasassarakich, P., Highly active MoS₂, CoMoS₂ and NiMoS₂ unsupported catalysts prepared by hydrothermal synthesis for hydrodesulfurization of 4,6-dimethyldibenzothiophene. *Catalysis Today* **2008**, *130* (1), 14-23.
58. Yin, C.; Wang, Y.; Xue, S.; Liu, H.; Li, H.; Liu, C., Influence of sulfidation conditions on morphology and hydrotreating performance of unsupported Ni-Mo-W catalysts. *Fuel* **2016**, *175*, 13-19.
59. Alonso, G.; Espino, J.; Berhault, G.; Alvarez, L.; Rico, J., Activation of tetraalkylammonium thiotungstates for the preparation of Ni-promoted WS₂ catalysts. *Applied Catalysis A: General* **2004**, *266* (1), 29-40.
60. Huirache-Acuña, R.; Albiter, M. A.; Ornelas, C.; Paraguay-Delgado, F.; Martínez-Sánchez, R.; Alonso-Nuñez, G., Ni(Co)-Mo-W sulphide unsupported HDS catalysts by ex situ decomposition of alkylthiomolybdotungstates. *Applied Catalysis A: General* **2006**, *308*, 134-142.
61. Yoosuk, B.; Kim, J. H.; Song, C.; Ngamcharussrivichai, C.; Prasassarakich, P., Highly active MoS₂, CoMoS₂ and NiMoS₂ unsupported catalysts prepared by hydrothermal synthesis for hydrodesulfurization of 4, 6-dimethyldibenzothiophene. *Catalysis Today* **2008**, *130* (1), 14-23.
62. Alonso, G.; Berhault, G.; Aguilar, A.; Collins, V.; Ornelas, C.; Fuentes, S.; Chianelli, R. R., Characterization and HDS Activity of Mesoporous MoS₂ Catalysts Prepared by in Situ Activation of Tetraalkylammonium Thiomolybdates. *Journal of Catalysis* **2002**, *208* (2), 359-369.
63. Nava, H.; Ornelas, C.; Aguilar, A.; Berhault, G.; Fuentes, S.; Alonso, G., Cobalt-Molybdenum Sulfide Catalysts Prepared by In Situ Activation of Bimetallic (Co-Mo) Alkylthiomolybdates. *Catal Lett* **86** (4), 257-265.

64. Olivas, A.; Galván, D. H.; Alonso, G.; Fuentes, S., Trimetallic NiMoW unsupported catalysts for HDS. *Applied Catalysis A: General* **2009**, *352* (1–2), 10-16.
65. Hein, J.; Gutiérrez Tinoco, O. Y.; Albersberger, S.; Han, J.; Jentys, A.; Lercher, J. A., Towards understanding structure-activity relationships of Ni-Mo-W sulfide hydrotreating catalysts. *ChemCatChem* **2016**, *9* (4), 629-641.
66. Breyse, M.; Cattenot, M.; Decamp, T.; Frety, R.; Gachet, C.; Lacroix, M.; Leclercq, C.; de Mourgues, L.; Portefaix, J. L.; Vrinat, M.; Houari, M.; Grimblot, J.; Kasztelan, S.; Bonnelle, J. P.; Housni, S.; Bachelier, J.; Duchet, J. C., Influence of sulphidation conditions on the properties of NiW/Al₂O₃ hydrotreating catalysts. *Catalysis Today* **1988**, *4* (1), 39-55.
67. Hardcastle, F. D.; Wachs, I. E., Determination of the molecular structures of tungstates by Raman spectroscopy. *Journal of Raman Spectroscopy* **1995**, *26* (6), 397-405.
68. Hensen, E. J. M.; van der Meer, Y.; van Veen, J. A. R.; Niemantsverdriet, J. W., Insight into the formation of the active phases in supported NiW hydrotreating catalysts. *Applied Catalysis A: General* **2007**, *322*, 16-32.
69. Labruyère, F.; Dufresne, P.; Lacroix, M.; Breyse, M., Ex situ sulfidation by alkylpolysulfides: A route for the preparation of highly dispersed supported sulfides. *Catalysis Today* **1998**, *43* (1), 111-116.
70. Gochi, Y.; Ornelas, C.; Paraguay, F.; Fuentes, S.; Alvarez, L.; Rico, J. L.; Alonso-Núñez, G., Effect of sulfidation on Mo-W-Ni trimetallic catalysts in the HDS of DBT. *Catalysis Today* **2005**, *107–108* (0), 531-536.
71. Texier, S.; Berhault, G.; Pérot, G.; Diehl, F., Activation of alumina-supported hydrotreating catalysts by organosulfides or H₂S: Effect of the H₂S partial pressure used during the activation process. *Applied Catalysis A: General* **2005**, *293*, 105-119.
72. Vandeputte, A. r. G.; Reyniers, M.-F.; Marin, G. B., Theoretical study of the thermal decomposition of dimethyl disulfide. *The Journal of Physical Chemistry A* **2010**, *114* (39), 10531-10549.
73. Texier, S.; Berhault, G.; Pérot, G.; Harlé, V.; Diehl, F., Activation of alumina-supported hydrotreating catalysts by organosulfides: comparison with H₂S and effect of different solvents. *Journal of Catalysis* **2004**, *223* (2), 404-418.
74. Vandeputte, A. G.; Reyniers, M.-F.; Marin, G. B., Theoretical Study of the Thermal Decomposition of Dimethyl Disulfide. *The Journal of Physical Chemistry A* **2010**, *114* (39), 10531-10549.
75. Guludec, E.; Oliviero, L.; Gilson, J. P.; Maugé, F.; Rebeilleau, M.; Grandi, V.; Donk, S., From Gas to Liquid Phase Sulfidation: An IR Spectroscopy Study. *Catal Lett* **2012**, *142* (6), 736-743.
76. Okamoto, Y.; Kawano, M.; Kubota, T., Fraction of the CoMoS phases accessible to NO in Co-Mo hydrodesulfurization catalysts. *Chemical Communications* **2003**, (9), 1086-1087.
77. Scheffer, B.; Dekker, N. J. J.; Mangnus, P. J.; Moulijn, J. A., A temperature-programmed reduction study of sulfided Co-Mo/Al₂O₃ hydrodesulfurization catalysts. *Journal of Catalysis* **1990**, *121* (1), 31-46.
78. De la Rosa, M. P.; Texier, S.; Berhault, G.; Camacho, A.; Yácaman, M. J.; Mehta, A.; Fuentes, S.; Montoya, J. A.; Murrieta, F.; Chianelli, R. R., Structural studies of catalytically stabilized model and industrial-supported hydrodesulfurization catalysts. *Journal of Catalysis* **2004**, *225* (2), 288-299.
79. van Gestel, J.; Leglise, J.; Duchet, J. C., Catalytic Properties of a CoMo/Al₂O₃ Catalyst Presulfided with Alkyl Polysulfides: Comparison with Conventional Sulfiding. *Journal of Catalysis* **1994**, *145* (2), 429-436.
80. van der Vlies, A. J.; Kishan, G.; Niemantsverdriet, J. W.; Prins, R.; Weber, T., Basic Reaction Steps in the Sulfidation of Crystalline Tungsten Oxides. *The Journal of Physical Chemistry B* **2002**, *106* (13), 3449-3457.
81. van der Vlies, A. J.; Prins, R.; Weber, T., Chemical Principles of the Sulfidation of Tungsten Oxides. *The Journal of Physical Chemistry B* **2002**, *106* (36), 9277-9285.
82. Payen, E.; Kasztelan, S.; Grimblot, J.; Bonnelle, J. P., Study of the sulphurization of WO₃/γ-Al₂O₃ catalysts by in situ laser raman spectroscopy. *Catalysis Today* **1988**, *4* (1), 57-70.

83. Muijsers, J. C.; Weber, T.; Vanhardeveld, R. M.; Zandbergen, H. W.; Niemantsverdriet, J. W., Sulfidation Study of Molybdenum Oxide Using $\text{MoO}_3/\text{SiO}_2/\text{Si}(100)$ Model Catalysts and Mo-IV-Sulfur Cluster Compounds. *Journal of Catalysis* **1995**, *157* (2), 698-705.
84. Arnoldy, P.; van den Heijkant, J. A. M.; de Bok, G. D.; Moulijn, J. A., Temperature-programmed sulfiding of $\text{MoO}_3/\text{Al}_2\text{O}_3$ catalysts. *Journal of Catalysis* **1985**, *92* (1), 35-55.
85. Kishan, G.; Coulier, L.; de Beer, V. H. J.; van Veen, J. A. R.; Niemantsverdriet, J. W., Sulfidation and Thiophene Hydrodesulfurization Activity of Nickel Tungsten Sulfide Model Catalysts, Prepared without and with Chelating Agents. *Journal of Catalysis* **2000**, *196* (1), 180-189.
86. Sun, M.; Bürgi, T.; Cattaneo, R.; van Langeveld, D.; Prins, R., TPS, XPS, QEXAFS, and XANES Investigation of the Sulfidation of $\text{NiW}/\text{Al}_2\text{O}_3\text{-F}$ Catalysts. *Journal of Catalysis* **2001**, *201* (2), 258-269.
87. Coulier, L.; de Beer, V. H. J.; van Veen, J. A. R.; Niemantsverdriet, J. W., Correlation between Hydrodesulfurization Activity and Order of Ni and Mo Sulfidation in Planar Silica-Supported NiMo Catalysts: The Influence of Chelating Agents. *Journal of Catalysis* **2001**, *197* (1), 26-33.
88. Eijsbouts, S.; Li, X.; Bergwerff, J.; Louwen, J.; Woning, L.; Loos, J., Nickel sulfide crystals in Ni-Mo and Ni-W catalysts: Eye-catching inactive feature or an active phase in its own right? *Catalysis Today* **2017**, *292*, 38-50.
89. Zuo, D.; Li, D.; Nie, H.; Shi, Y.; Lacroix, M.; Vrinat, M., Acid-base properties of $\text{NiW}/\text{Al}_2\text{O}_3$ sulfided catalysts: relationship with hydrogenation, isomerization and hydrodesulfurization reactions. *Journal of Molecular Catalysis A: Chemical* **2004**, *211* (1), 179-189.
90. Carlsson, A.; Brorson, M.; Topsøe, H., Morphology of WS_2 nanoclusters in WS_2/C hydrodesulfurization catalysts revealed by high-angle annular dark-field scanning transmission electron microscopy (HAADF-STEM) imaging. *Journal of Catalysis* **2004**, *227* (2), 530-536.
91. Brunier, T. M.; Drew, M. G. B.; Mitchell, P. C. H., Molecular mechanics study of the interaction of thiophene with a molybdenum disulfide catalyst. *Journal of the Chemical Society, Faraday Transactions* **1992**, *88* (21), 3225-3232.
92. Verble, J. L.; Wieting, T. J., Lattice Mode Degeneracy in MoS_2 and Other Layer Compounds. *Physical Review Letters* **1970**, *25* (6), 362-365.
93. Orita, H.; Uchida, K.; Itoh, N., A volcano-type relationship between the adsorption energy of thiophene on promoted MoS_2 cluster-model catalysts and the experimental HDS activity: ab initio density functional study. *Applied Catalysis A: General* **2004**, *258* (1), 115-120.
94. Parsapour, F.; Kelley, D. F.; Craft, S.; Wilcoxon, J. P., Electron transfer dynamics in MoS_2 nanoclusters: Normal and inverted behavior. *The Journal of Chemical Physics* **1996**, *104* (13), 4978-4987.
95. Bollinger, M. V.; Lauritsen, J. V.; Jacobsen, K. W.; Nørskov, J. K.; Helveg, S.; Besenbacher, F., One-Dimensional Metallic Edge States in MoS_2 . *Physical Review Letters* **2001**, *87* (19), 196803.
96. Hilton, M. R.; Fleischauer, P. D., TEM lattice imaging of the nanostructure of early-growth sputter-deposited MoS_2 solid lubricant films. *Journal of Materials Research* **2011**, *5* (2), 406-421.
97. Helveg, S.; Lauritsen, J. V.; Lægsgaard, E.; Stensgaard, I.; Nørskov, J. K.; Clausen, B. S.; Topsøe, H.; Besenbacher, F., Atomic-Scale Structure of Single-Layer MoS_2 Nanoclusters. *Physical Review Letters* **2000**, *84* (5), 951-954.
98. Lauritsen, J. V.; Bollinger, M. V.; Lægsgaard, E.; Jacobsen, K. W.; Nørskov, J. K.; Clausen, B. S.; Topsøe, H.; Besenbacher, F., Atomic-scale insight into structure and morphology changes of MoS_2 nanoclusters in hydrotreating catalysts. *Journal of Catalysis* **2004**, *221* (2), 510-522.
99. Byskov, L. S.; Hammer, B.; Nørskov, J. K.; Clausen, B. S.; Topsøe, H., Sulfur bonding in MoS_2 and Co-Mo-S structures. *Catal Lett* **1997**, *47* (3), 177-182.
100. Merki, D.; Hu, X., Recent developments of molybdenum and tungsten sulfides as hydrogen evolution catalysts. *Energy & Environmental Science* **2011**, *4* (10), 3878-3888.
101. Agarwal, M.; Reddy, K. N.; Patel, H., Growth of tungstenite single crystals by direct vapour transport method. *Journal of Crystal Growth* **1979**, *46* (1), 139-142.

102. Furimsky, E., Role of MoS₂ and WS₂ in Hydrodesulfurization. *Catalysis Reviews* **1980**, 22 (3), 371-400.
103. Robinson, W. R. A. M.; Van Veen, J. A. R.; De Beer, V. H. J.; Van Santen, R. A., Development of deep hydrodesulfurization catalysts: II. NiW, Pt and Pd catalysts tested with (substituted) dibenzothiophene. *Fuel processing technology* **1999**, 61 (1), 103-116.
104. Yasuda, H.; Higo, M.; Yoshitomi, S.; Sato, T.; Imamura, M.; Matsubayashi, H.; Shimada, H.; Nishijima, A.; Yoshimura, Y., Hydrogenation of tetralin over sulfided nickel-tungstate/alumina and nickel-molybdate/alumina catalysts. *Catalysis Today* **1997**, 39 (1-2), 77-87.
105. Chianelli, R. R., Fundamental Studies of Transition Metal Sulfide Hydrodesulfurization Catalysts. *Catalysis Reviews* **1984**, 26 (3-4), 361-393.
106. Chianelli, R., Periodic trends transition metal sulfide catalysis: intuition and theory. *Oil & Gas Science and Technology-Revue de l'IFP* **2006**, 61 (4), 503-513.
107. Voorhoeve, R. J. H.; Stuiver, J. C. M., Kinetics of hydrogenation on supported and bulk nickel-tungsten sulfide catalysts. *Journal of Catalysis* **1971**, 23 (2), 228-235.
108. Farragher, A., P. Cossee in Proc. 5th Int. Congress Catalysis. Palm Beach. 1972. North-Holland: 1973.
109. Chianelli, R. R.; Berhault, G.; Raybaud, P.; Kasztelan, S.; Hafner, J.; Toulhoat, H., Periodic trends in hydrodesulfurization: in support of the Sabatier principle. *Applied Catalysis A: General* **2002**, 227 (1-2), 83-96.
110. Delmon, B., Advances in Hydropurification Catalysts and Catalysis. In *Studies in Surface Science and Catalysis*, Trimm, D. L.; Akashah, S.; Absi-Halabi, M.; Bishara, A., Eds. Elsevier: 1989; Vol. 53, pp 1-40.
111. Grange, P.; Vanhaeren, X., Hydrotreating catalysts, an old story with new challenges. *Catalysis Today* **1997**, 36 (4), 375-391.
112. Prins, R.; de Beer, V. H. J.; Somorjai, G. A., Structure and Function of the Catalyst and the Promoter in Co—Mo Hydrodesulfurization Catalysts. *Catalysis Reviews* **1989**, 31 (1-2), 1-41.
113. Topsøe, H.; Clausen, B. S., Importance of Co-Mo-S Type Structures in Hydrodesulfurization. *Catalysis Reviews* **1984**, 26 (3-4), 395-420.
114. Topsøe, H.; Clausen, B. S.; Candia, R.; Wivel, C.; Mørup, S., In situ Mössbauer emission spectroscopy studies of unsupported and supported sulfided Co-Mo hydrodesulfurization catalysts: Evidence for and nature of a Co-Mo-S phase. *Journal of Catalysis* **1981**, 68 (2), 433-452.
115. Eijsbouts, S., On the flexibility of the active phase in hydrotreating catalysts. *Applied Catalysis A: General* **1997**, 158 (1-2), 53-92.
116. Besenbacher, F.; Brorson, M.; Clausen, B. S.; Helveg, S.; Hinnemann, B.; Kibsgaard, J.; Lauritsen, J. V.; Moses, P. G.; Nørskov, J. K.; Topsøe, H., Recent STM, DFT and HAADF-STEM studies of sulfide-based hydrotreating catalysts: Insight into mechanistic, structural and particle size effects. *Catalysis Today* **2008**, 130 (1), 86-96.
117. Carlsson, A.; Brorson, M.; TOPSØE, H., Supported metal sulphide nanoclusters studied by HAADF-STEM. *Journal of Microscopy* **2006**, 223 (3), 179-181.
118. Lauritsen, J. V.; Kibsgaard, J.; Olesen, G. H.; Moses, P. G.; Hinnemann, B.; Helveg, S.; Nørskov, J. K.; Clausen, B. S.; Topsøe, H.; Lægsgaard, E.; Besenbacher, F., Location and coordination of promoter atoms in Co- and Ni-promoted MoS₂-based hydrotreating catalysts. *Journal of Catalysis* **2007**, 249 (2), 220-233.
119. Raybaud, P.; Hafner, J.; Kresse, G.; Kasztelan, S.; Toulhoat, H., Structure, Energetics, and Electronic Properties of the Surface of a Promoted MoS₂ Catalyst: An ab Initio Local Density Functional Study. *Journal of Catalysis* **2000**, 190 (1), 128-143.
120. Grimblot, J., Genesis, architecture and nature of sites of Co(Ni)—MoS₂ supported hydroprocessing catalysts. *Catalysis Today* **1998**, 41 (1-3), 111-128.
121. Krebs, E.; Silvi, B.; Raybaud, P., Mixed sites and promoter segregation: A DFT study of the manifestation of Le Chatelier's principle for the Co(Ni)MoS active phase in reaction conditions. *Catalysis Today* **2008**, 130, 160-169.
122. Schweiger, H.; Raybaud, P.; Toulhoat, H., Promoter Sensitive Shapes of Co(Ni)MoS Nanocatalysts in Sulfo-Reductive Conditions. *Journal of Catalysis* **2002**, 212 (1), 33-38.

123. Harris, S.; Chianelli, R. R., Catalysis by transition metal sulfides: A theoretical and experimental study of the relation between the synergic systems and the binary transition metal sulfides. *Journal of Catalysis* **1986**, *98* (1), 17-31.
124. Pecoraro, T. A.; Chianelli, R. R., Hydrodesulfurization catalysis by transition metal sulfides. *Journal of Catalysis* **1981**, *67* (2), 430-445.
125. Byskov, L. S.; Nørskov, J. K.; Clausen, B. S.; Topsøe, H., DFT Calculations of Unpromoted and Promoted MoS₂-Based Hydrodesulfurization Catalysts. *Journal of Catalysis* **1999**, *187* (1), 109-122.
126. Cervantes-Gaxiola, M. E.; Arroyo-Albiter, M.; Pérez-Larios, A.; Balbuena, P. B.; Espino-Valencia, J., Experimental and theoretical study of NiMoW, NiMo, and NiW sulfide catalysts supported on an AlTiMg mixed oxide during the hydrodesulfurization of dibenzothiophene. *Fuel* **2013**, *113*, 733-743.
127. Schachtl, E.; Kondratieva, E.; Gutiérrez Tinoco, O. Y.; Lercher, J. A., Pathways for H₂ Activation on (Ni)-MoS₂ Catalysts. *The Journal of Physical Chemistry Letters* **2015**, *6*, 2929-2932.
128. Luo, W.; Shi, H.; Willnecker, E.; Gutiérrez, O. Y.; Lercher, J., Active sites on Ni-promoted transition metal sulfides that catalyze aromatics hydrogenation. *Angewandte Chemie International Edition* **2018**, *57* (44), 14555-14559.
129. Dumcenco, D. O.; Kobayashi, H.; Liu, Z.; Huang, Y.-S.; Suenaga, K., Visualization and quantification of transition metal atomic mixing in Mo_{1-x}W_xS₂ single layers. *Nat Commun* **2013**, *4*, 1351.
130. Shan, S.; Liu, H.; Yue, Y.; Shi, G.; Bao, X., Trimetallic WMoNi diesel ultra-deep hydrodesulfurization catalysts with enhanced synergism prepared from inorganic-organic hybrid nanocrystals. *Journal of Catalysis* **2016**, *344*, 325-333.
131. van Haandel, L.; Bremmer, M.; Kooyman, P. J.; van Veen, J. A. R.; Weber, T.; Hensen, E. J. M., Structure-Activity Correlations in Hydrodesulfurization Reactions over Ni-Promoted Mo_xW_(1-x)S₂/Al₂O₃ Catalysts. *ACS Catalysis* **2015**, *5* (12), 7276-7287.
132. Olivas, A.; Antúnez-García, J.; Fuentes, S.; Galván, D. H., Electronic properties of unsupported trimetallic catalysts. *Catalysis Today* **2014**, *220-222* (0), 106-112.
133. Weber, T.; Rob van Veen, J. A., A density functional theory study of the hydrodesulfurization reaction of dibenzothiophene to biphenyl on a single-layer NiMoS cluster. *Catalysis Today* **2008**, *130* (1), 170-177.
134. Anderson, A. B.; Al-Saigh, Z. Y.; Hall, W. K., Hydrogen on molybdenum disulfide: theory of its heterolytic and homolytic chemisorption. *The Journal of Physical Chemistry* **1988**, *92* (3), 803-809.
135. Travert, A.; Nakamura, H.; van Santen, R. A.; Cristol, S.; Paul, J.-F.; Payen, E., Hydrogen Activation on Mo-Based Sulfide Catalysts, a Periodic DFT Study. *Journal of the American Chemical Society* **2002**, *124* (24), 7084-7095.
136. Prodhomme, P.-Y.; Raybaud, P.; Toulhoat, H., Free-energy profiles along reduction pathways of MoS₂ M-edge and S-edge by dihydrogen: A first-principles study. *Journal of Catalysis* **2011**, *280* (2), 178-195.
137. Chianelli, R. R.; Berhault, G.; Torres, B., Unsupported transition metal sulfide catalysts: 100 years of science and application. *Catalysis Today* **2009**, *147* (3-4), 275-286.
138. Poisot, M.; Bensch, W.; Fuentes, S.; Alonso, G., Decomposition of tetraalkylammonium thiomolybdates characterised by thermoanalysis and mass spectrometry. *Thermochimica acta* **2006**, *444* (1), 35-45.
139. Ramos, M.; Berhault, G.; Ferrer, D. A.; Torres, B.; Chianelli, R. R., HRTEM and molecular modeling of the MoS₂-Co₉S₈ interface: understanding the promotion effect in bulk HDS catalysts. *Catalysis Science & Technology* **2012**, *2* (1), 164-178.
140. Bocarando, J.; Huirache-Acuña, R.; Bensch, W.; Huang, Z. D.; Petranovskii, V.; Fuentes, S.; Alonso-Núñez, G., Unsupported Ni-Mo-W sulphide HDS catalysts with the varying nickel concentration. *Applied Catalysis A: General* **2009**, *363* (1), 45-51.
141. Thomazeau, C.; Geantet, C.; Lacroix, M.; Harlé, V.; Benazeth, S.; Marhic, C.; Danot, M., Two cation disulfide layers in the W_xMo_(1-x)S₂ lamellar solid solution. *Journal of Solid State Chemistry* **2001**, *160* (1), 147-155.

142. Maesen, T.; Kuperman, A. E., Hydroconversion Processes Employing Multi-Metallic Catalysts and Method for Making Thereof.; US Patent 20090107883A1, 2009.
143. Han, J.; Kuperman, A. E., Hydroconversion Multi-Metallic Catalyst and Method For Making Thereof; US Patents 9327274, 2016.
144. Yi, Y.; Jin, X.; Wang, L.; Zhang, Q.; Xiong, G.; Liang, C., Preparation of unsupported Ni–Mo–S catalysts for hydrodesulfurization of dibenzothiophene by thermal decomposition of tetramethylammonium thiomolybdates. *Catalysis Today* **2011**, *175* (1), 460-466.
145. Yi, Y.; Zhang, B.; Jin, X.; Wang, L.; Williams, C. T.; Xiong, G.; Su, D.; Liang, C., Unsupported NiMoW sulfide catalysts for hydrodesulfurization of dibenzothiophene by thermal decomposition of thiosalts. *Journal of Molecular Catalysis A: Chemical* **2011**, *351*, 120-127.
146. Maesen, T.; Kuperman, A. E., Hydroconversion Processes Employing Multi-Metallic Catalysts and Method for Making Thereof.; US Patent 7807599B2, 2009.
147. Soled, S. L.; Miseo, S.; Eijsbouts, S.; Plantenga, F. L., Bulk bimetallic catalysts, method of making bulk bimetallic catalysts and hydroprocessing using bulk bimetallic catalysts; US Patent 7648941, 2010.
148. Nava, H.; Pedraza, F.; Alonso, G., Nickel-molybdenum-tungsten sulfide catalysts prepared by in situ activation of tri-metallic (Ni-Mo-W) alkylthiomolybdotungstates. *Catal Lett* **2005**, *99* (1-2), 65-71.
149. Yu, Y.; Fonf , B.; Jentys, A.; Haller, G. L.; Rob van Veen, J. A.; Guti rrez, O. Y.; Lercher, J. A., Bimetallic Pt–Pd/silica–alumina hydrotreating catalysts. Part II: Structure–activity correlations in the hydrogenation of tetralin in the presence of dibenzothiophene and quinoline. *Journal of Catalysis* **2012**, *292*, 13-25.
150. Ross-Medgaarden, E. I.; Wachs, I. E., Structural Determination of Bulk and Surface Tungsten Oxides with UV–vis Diffuse Reflectance Spectroscopy and Raman Spectroscopy. *The Journal of Physical Chemistry C* **2007**, *111* (41), 15089-15099.
151. Saleem, S. S., Infrared and Raman spectroscopic studies of the polymorphic forms of nickel, cobalt and ferric molybdates. *Infrared Physics* **1987**, *27* (5), 309-315.
152. Mestl, G.; Srinivasan, T. K. K., Raman Spectroscopy of Monolayer-Type Catalysts: Supported Molybdenum Oxides. *Catalysis Reviews* **1998**, *40* (4), 451-570.
153. Schrader, G. L.; Cheng, C. P., In situ laser raman spectroscopy of the sulfiding of Mo/ γ -Al₂O₃ catalysts. *Journal of Catalysis* **1983**, *80* (2), 369-385.
154. Tops e, N.-Y.; Tuxen, A.; Hinnemann, B.; Lauritsen, J. V.; Knudsen, K. G.; Besenbacher, F.; Tops e, H., Spectroscopy, microscopy and theoretical study of NO adsorption on MoS₂ and Co–Mo–S hydrotreating catalysts. *Journal of Catalysis* **2011**, *279* (2), 337-351.
155. Thomazeau, C.; Geantet, C.; Lacroix, M.; Danot, M.; Harle, V., EXAFS characterization of new active phases for catalytic hydrotreatment: Two cations disulfide layers in the Mo_xW_(1-x)S₂ lamellar solid solution. *Oil & Gas Science and Technology* **2005**, *60* (5), 781-790.
156. Wang, L.; Zhang, Y.; Zhang, Y.; Jiang, Z.; Li, C., Ultra-Deep Hydrodesulfurization of Diesel Fuels on Trimetallic NiMoW Sulfide Catalysts. *Chemistry – A European Journal* **2009**, *15* (46), 12571-12575.
157. Dumcenco, D. O.; Su, Y. C.; Wang, Y. P.; Chen, K. Y.; Huang, Y. S.; Ho, C. H.; Tiong, K. K. In Piezoreflectance and Raman characterization of Mo_{1-x}W_xS₂ layered mixed crystals. *Solid State Phenomena*, Trans Tech Publ: **2011**; pp 55-59.
158. Hein, J.; Hrabar, A.; Jentys, A.; Guti rrez, O. Y.; Lercher, J. A., γ -Al₂O₃-Supported and Unsupported (Ni)MoS₂ for the Hydrodenitrogenation of Quinoline in the Presence of Dibenzothiophene. *ChemCatChem* **2014**, *6* (2), 485-499.
159. Guti rrez, O. Y.; Hrabar, A.; Hein, J.; Yu, Y.; Han, J.; Lercher, J. A., Ring opening of 1,2,3,4-tetrahydroquinoline and decahydroquinoline on MoS₂/ γ -Al₂O₃ and Ni–MoS₂/ γ -Al₂O₃. *Journal of Catalysis* **2012**, *295* (0), 155-168.
160. Guti rrez, O. Y.; Singh, S.; Schachtl, E.; Kim, J.; Kondratieva, E.; Hein, J.; Lercher, J. A., Effects of the Support on the Performance and Promotion of (Ni)MoS₂ Catalysts for Simultaneous Hydrodenitrogenation and Hydrodesulfurization. *ACS Catalysis* **2014**, *4* (5), 1487-1499.

161. Prins, R.; Egorova, M.; Röthlisberger, A.; Zhao, Y.; Sivasankar, N.; Kukula, P., Mechanisms of hydrodesulfurization and hydrodenitrogenation. *Catalysis Today* **2006**, *111* (1–2), 84–93.
162. Ho, T. C.; Qiao, L., Competitive adsorption of nitrogen species in HDS: Kinetic characterization of hydrogenation and hydrogenolysis sites. *Journal of Catalysis* **2010**, *269* (2), 291–301.
163. Topsoe, N. Y.; Topsoe, H., FTIR Studies of Mo/Al₂O₃-Based Catalysts: II. Evidence for the Presence of SH Groups and Their Role in Acidity and Activity. *Journal of Catalysis* **1993**, *139* (2), 641–651.
164. Gao, Q.; Ofosu, T. N. K.; Ma, S. G.; Komvokis, V. G.; Williams, C. T.; Segawa, K., Catalyst development for ultra-deep hydrodesulfurization (HDS) of dibenzothiophenes. I: Effects of Ni promotion in molybdenum-based catalysts. *Catalysis Today*, **2011**, *164*, 538–543.
165. Tétényi, P.; Schnörch, P.; Tellingner, O., Promoter effect of nickel in thiophene hydrodesulfurization as monitored by sulfur uptake and cyclohexane conversion. *Reaction Kinetics and Catalysis Letters* **2009**, *97* (1), 141–150.
166. Schachtl, E.; Zhong, L.; Kondratieva, E.; Hein, J.; Gutiérrez, O. Y.; Jentys, A.; Lercher, J. A., Understanding Ni Promotion of MoS₂/γ-Al₂O₃ and its Implications for the Hydrogenation of Phenanthrene. *ChemCatChem* **2015**, *7* (24), 4118–4130.
167. Van Veen, J. A. R., Zeolites for cleaner technology. **2002**, *3*, 131–152.
168. Kabe, T.; Aoyama, Y.; Wang, D.; Ishihara, A.; Qian, W.; Hosoya, M.; Zhang, Q., Effects of H₂S on hydrodesulfurization of dibenzothiophene and 4,6-dimethyldibenzothiophene on alumina-supported NiMo and NiW catalysts. *Applied Catalysis A: General* **2001**, *209* (1), 237–247.
169. Abrahams, S.; Reddy, J., Crystal Structure of the Transition-Metal Molybdates. I. Paramagnetic Alpha-MnMoO₄. *The Journal of Chemical Physics* **1965**, *43* (7), 2533–2543.
170. Hensen, E. J. M.; Kooyman, P. J.; van der Meer, Y.; van der Kraan, A. M.; de Beer, V. H. J.; van Veen, J. A. R.; van Santen, R. A., The Relation between Morphology and Hydrotreating Activity for Supported MoS₂ Particles. *Journal of Catalysis* **2001**, *199* (2), 224–235.
171. Licea, Y. E.; Grau-Crespo, R.; Palacio, L. A.; Faro Jr, A. C., Unsupported trimetallic Ni (Co)-Mo-W sulphide catalysts prepared from mixed oxides: Characterisation and catalytic tests for simultaneous tetralin HDA and dibenzothiophene HDS reactions. *Catalysis Today* **2017**, *292*, 84–96.
172. Albersberger, S.; Hein, J.; Schreiber, M. W.; Guerra, S.; Han, J.; Gutiérrez, O. Y.; Lercher, J. A., Simultaneous hydrodenitrogenation and hydrodesulfurization on unsupported Ni-Mo-W sulfides. *Catalysis Today* **2017**, *297* (Supplement C), 344–355.
173. Lauritsen, J. V.; Helveg, S.; Lægsgaard, E.; Stensgaard, I.; Clausen, B. S.; Topsøe, H.; Besenbacher, F., Atomic-Scale Structure of Co–Mo–S Nanoclusters in Hydrotreating Catalysts. *Journal of Catalysis* **2001**, *197* (1), 1–5.
174. Berhault, G.; Lacroix, M.; Breyse, M.; Maugé, F.; Lavalley, J.-C.; Nie, H.; Qu, L., Characterization of Acidic Sites of Silica-Supported Transition Metal Sulfides by Pyridine and 2,6-Dimethylpyridine Adsorption: Relation to Activity in CH₃SH Condensation. *Journal of Catalysis* **1998**, *178* (2), 555–565.
175. Topsøe, H., The role of Co–Mo–S type structures in hydrotreating catalysts. *Applied Catalysis A: General* **2007**, *322*, 3–8.
176. Thomas, C.; Vivier, L.; Lambertson, J. L.; Kasztelan, S.; Pérot, G., Deuterium Tracer Studies on Hydrotreating Catalysts—Isotopic Exchange between Hydrogen and Hydrogen Sulfide on Sulfided NiMo/Al₂O₃. *Journal of Catalysis* **1997**, *167* (1), 1–11.
177. Yang, S. H.; Satterfield, C. N., Some effects of sulfiding of a NiMoAl₂O₃ catalyst on its activity for hydrodenitrogenation of quinoline. *Journal of Catalysis* **1983**, *81* (1), 168–178.
178. Luo, W.; Shi, H.; Schachtl, E.; Gutiérrez, O. Y.; Lercher, J. A., Active Sites on Nickel-Promoted Transition-Metal Sulfides That Catalyze Hydrogenation of Aromatic Compounds. *Angewandte Chemie* **2018**, *57* (44), 14555–14559.
179. Katzer, J. R.; Sivasubramanian, R., Process and Catalyst Needs for Hydrodenitrogenation. *Catalysis Reviews* **1979**, *20* (2), 155–208.

180. Landau, M.; Agievskii, D.; Slinkin, A.; Kipnis, M.; Alekseenko, L.; Fedorovskaya, E.; Pavlova, L.; Kucherovat, T., Active structures of the product of sulfiding of nickel molybdate. Hydrogenation of aromatic hydrocarbons. *Kinet. Catal. (Engl. Transl.); (United States)* **1983**, *23* (2).
181. Jander G., B. E., Strähle J., Schweda E., *Lehrbuch der analytischen und präparativen anorganischen Chemie*. 16 ed.; Stuttgart, 2006.
182. Belsky, A.; Hellenbrandt, M.; Karen, V. L.; Luksch, P., New developments in the Inorganic Crystal Structure Database (ICSD): accessibility in support of materials research and design. *Acta Crystallographica Section B: Structural Science* **2002**, *58* (3), 364-369.
183. Alothman, Z., *A Review: Fundamental Aspects of Silicate Mesoporous Materials* **2012**, *5*, 2874-2902.
184. Cocchetto, J. F.; Satterfield, C. N., Thermodynamic Equilibria of Selected Heterocyclic Nitrogen Compounds with Their Hydrogenated Derivatives. *Industrial & Engineering Chemistry Process Design and Development* **1976**, *15* (2), 272-277.
185. Nguyen, M.-T.; Tayakout-Fayolle, M.; Pirngruber, G. D.; Chainet, F.; Geantet, C., Kinetic Modeling of Quinoline Hydrodenitrogenation over a NiMo(P)/Al₂O₃ Catalyst in a Batch Reactor. *Industrial & Engineering Chemistry Research* **2015**, *54* (38), 9278-9288.
186. Shih, S. S.; Katzer, J. R.; Kwart, H.; Stiles, A. B., Quinoline hydrodenitrogenation: reaction network and kinetics. *Prepr., Div. Pet. Chem., in United States Am. Chem. Soc.* **1977**, *22*.
187. Jian, M.; Prins, R., Kinetics of the Hydrodenitrogenation of Decahydroquinoline over NiMo(P)/Al₂O₃ Catalysts. *Industrial & Engineering Chemistry Research* **1998**, *37* (3), 834-840.
188. Jian, M.; Kapteijn, F.; Prins, R., Kinetics of the Hydrodenitrogenation of ortho-Propylaniline over NiMo(P)/Al₂O₃ Catalysts. *Journal of Catalysis* **1997**, *168* (2), 491-500.
189. Valencia, D.; Peña, L.; García-Cruz, I., Reaction mechanism of hydrogenation and direct desulfurization routes of dibenzothiophene-like compounds: A density functional theory study. *International Journal of Quantum Chemistry* **2012**, *112* (22), 3599-3605.
190. Ratnasamy, P.; Knözinger, H., Infrared and optical spectroscopic study of Co-Mo-Al₂O₃ catalysts. *Journal of Catalysis* **1978**, *54* (2), 155-165.
191. Riseman, S. M.; Bandyopadhyay, S.; Massoth, F.; Eyring, E. M., Photoacoustic spectroscopy of pyridine chemisorbed on calcined and sulfided molybdenum catalysts. *Applied catalysis* **1985**, *16* (1), 29-37.
192. Breyse, M.; Berhault, G.; Kasztelan, S.; Lacroix, M.; Maugé, F.; Pérot, G., New aspects of catalytic functions on sulfide catalysts. *Catalysis Today* **2001**, *66* (1), 15-22.
193. Broderick, D. H.; Gates, B. C., Hydrogenolysis and hydrogenation of dibenzothiophene catalyzed by sulfided CoO-MoO₃/γ-Al₂O₃: The reaction kinetics. *AIChE Journal* **1981**, *27* (4), 663-673.
194. Gioia, F.; Lee, V., Effect of hydrogen pressure on catalytic hydrodenitrogenation of quinoline. *Industrial & Engineering Chemistry Process Design and Development* **1986**, *25* (4), 918-925.
195. Sonnemans, J.; van den Berg, G. H.; Mars, P., The mechanism of pyridine hydrogenolysis on molybdenum-containing catalysts: II. Hydrogenation of pyridine to piperidine. *Journal of Catalysis* **1973**, *31* (2), 220-230.
196. Miller, J. T.; Hineman, M. F., Non-first-order hydrodenitrogenation kinetics of quinoline. *Journal of Catalysis* **1984**, *85* (1), 117-126.
197. Cattenot, M.; Portefaix, J.-L.; Afonso, J.; Breyse, M.; Lacroix, M.; Pérot, G., Mechanism of Carbon-Nitrogen Bond Scission on Unsupported Transition Metal Sulfides. *Journal of Catalysis* **1998**, *173* (2), 366-373.
198. Vivier, L.; Dominguez, V.; Perot, G.; Kasztelan, S., Mechanism of C-N bond scission. Hydrodenitrogenation of 1,2,3,4-tetrahydroquinoline and of 1,2,3,4-tetrahydroisoquinoline. *Journal of Molecular Catalysis* **1991**, *67* (2), 267-275.
199. Sánchez-Delgado, R. A., *Organometallic modeling of the hydrodesulfurization and hydrodenitrogenation reactions*. Springer Science & Business Media: 2002; Vol. 24.
200. Sun, M.; Nelson, A. E.; Adjaye, J., Adsorption and dissociation of H₂ and H₂S on MoS₂ and NiMoS catalysts. *Catalysis Today* **2005**, *105* (1), 36-43.

201. Sun, M.; Nelson, A. E.; Adjaye, J., Ab initio DFT study of hydrogen dissociation on MoS₂, NiMoS, and CoMoS: mechanism, kinetics, and vibrational frequencies. *Journal of Catalysis* **2005**, *233* (2), 411-421.
202. Nelson, N.; Levy, R. B., The organic chemistry of hydrodenitrogenation. *Journal of Catalysis* **1979**, *58* (3), 485-488.
203. Qu, L.; Flechsenhar, M.; Prins, R., Kinetics of the hydrodenitrogenation of o-toluidine over fluorinated NiMoS/Al₂O₃ and NiMoS/ASA catalysts. *Journal of catalysis* **2003**, *217* (2), 284-291.
204. Stanislaus, A.; Cooper, B. H., Aromatic Hydrogenation Catalysis: A Review. *Catalysis Reviews* **1994**, *36* (1), 75-123.
205. Rangarajan, S.; Mavrikakis, M., Adsorption of nitrogen-and sulfur-containing compounds on NiMoS for hydrotreating reactions: A DFT and vdW-corrected study. *AIChE Journal* **2015**, *61* (12), 4036-4050.
206. Valencia, D.; Olivares-Amaya, R.; Aburto, J.; García-Cruz, I., Topological and Electronic Structure of Heterocyclic Compounds Adsorbed on Hydrotreating Catalysts. *Catal Lett* **2013**, *143* (12), 1354-1361.
207. Schachtl, E.; Yoo, J. S.; Gutiérrez, O. Y.; Studt, F.; Lercher, J. A., Impact of Ni promotion on the hydrogenation pathways of phenanthrene on MoS₂/γ-Al₂O₃. *Journal of Catalysis* **2017**, *352*, 171-181.
208. Chen, Y.; Wang, L.; Zhang, Y.; Liu, T.; Liu, X.; Jiang, Z.; Li, C., A new multi-metallic bulk catalyst with high hydrodesulfurization activity of 4,6-DMDBT prepared using layered hydroxide salts as structural templates. *Applied Catalysis A: General* **2014**, *474*, 69-77.
209. Contreras, L. A.; Elguezabal, A. A.; Martínez, A. I., Obtention of low loading catalysts for deep hydrocarbon hydrodesulfurization based of CoMoS, with NiMoS hydrodenitrogenant additive supported on three-dimensional nanostructured mesoporous materials. Google Patents: 2015.
210. Cattaneo, R.; Weber, T.; Shido, T.; Prins, R., A Quick EXAFS Study of the Sulfidation of NiMo/SiO₂ Hydrotreating Catalysts Prepared with Chelating Ligands. *Journal of Catalysis* **2000**, *191* (1), 225-236.
211. Schrader, G. L.; Cheng, C. P., Sulfiding of cobalt molybdate catalysts: Characterization by Raman spectroscopy. *Journal of Catalysis* **1984**, *85* (2), 488-498.
212. Reinhoudt, H. R.; van der Meer, Y.; van der Kraan, A. M.; van Langeveld, A. D.; Moulijn, J. A., The sulfidation mechanism of NiW/γ-Al₂O₃ as a function of the calcination temperature studied with ⁵⁷Fe-MAS and temperature programmed sulfidation. *Fuel Processing Technology* **1999**, *61* (1-2), 43-54.
213. Gleeson, B.; Douglass, D. L.; Gesmundo, F., A comprehensive investigation of the sulfidation behavior of binary Co-Mo alloys. *Oxid Met* **1990**, *33* (5-6), 425-455.
214. van der Meer, Y.; Hensen, E. J. M.; van Veen, J. A. R.; van der Kraan, A. M., Characterization and thiophene hydrodesulfurization activity of amorphous-silica-alumina-supported NiW catalysts. *Journal of Catalysis* **2004**, *228* (2), 433-446.
215. Vissenberg, M. J.; van der Meer, Y.; Hensen, E. J. M.; de Beer, V. H. J.; van der Kraan, A. M.; van Santen, R. A.; van Veen, J. A. R., The Effect of Support Interaction on the Sulfidability of Al₂O₃- and TiO₂-Supported CoW and NiW Hydrodesulfurization Catalysts. *Journal of Catalysis* **2001**, *198* (2), 151-163.
216. Yin, C.; Wang, Y., Effect of sulfidation process on catalytic performance over unsupported Ni-Mo-W hydrotreating catalysts. *Korean Journal of Chemical Engineering* **2017**, 1-9.
217. Berhault, G.; Mehta, A.; Pavel, A. C.; Yang, J.; Rendon, L.; Yácaman, M. J.; Araiza, L. C.; Moller, A. D.; Chianelli, R. R., The Role of Structural Carbon in Transition Metal Sulfides Hydrotreating Catalysts. *Journal of Catalysis* **2001**, *198* (1), 9-19.
218. Glatzel, P.; Bergmann, U., High resolution 1s core hole X-ray spectroscopy in 3d transition metal complexes—electronic and structural information. *Coordination chemistry reviews* **2005**, *249* (1), 65-95.
219. Ward, M. J.; Rupar, P. A.; Murphy, M. W.; Yiu, Y.-M.; Baines, K. M.; Sham, T., Ionic nature of Ge (II)-centered dications: a germanium K-edge X-ray absorption near edge structures study. *Chemical Communications* **2010**, *46* (37), 7016-7018.

220. Yamamoto, T., Assignment of pre-edge peaks in K-edge x-ray absorption spectra of 3d transition metal compounds: electric dipole or quadrupole? *X-Ray Spectrometry* **2008**, *37* (6), 572-584.
221. Aritani, H.; Tanaka, T.; Funabiki, T.; Yoshida, S.; Kudo, M.; Hasegawa, S., Structure of Mo–Mg Binary Oxides in Oxidized/Reduced States Studied by X-ray Absorption Spectroscopy at the Mo K Edge and Mg K Edge. *The Journal of Physical Chemistry* **1996**, *100* (13), 5440-5446.
222. Keeling, R. O., The structure of NiWO₄. *Acta Crystallographica* **1957**, *10* (3), 209-213.
223. Busca, G., Differentiation of mono-oxo and polyoxo and of monomeric and polymeric vanadate, molybdate and tungstate species in metal oxide catalysts by IR and Raman spectroscopy. *Journal of Raman Spectroscopy* **2002**, *33* (5), 348-358.
224. Matar, S. F.; Largeteau, A.; Demazeau, G., AMoO₄ (A = Mg, Ni) molybdates: Phase stabilities, electronic structures and chemical bonding properties from first principles. *Solid State Sciences* **2010**, *12* (10), 1779-1785.
225. Levin, D.; Soled, S. L.; Ying, J. Y., Crystal Structure of an Ammonium Nickel Molybdate Prepared by Chemical Precipitation. *Inorganic Chemistry* **1996**, *35* (14), 4191-4197.
226. Wells, A. F., *Structural inorganic chemistry*. Oxford university press: 2012.
227. Wiberg, N.; Dehnicke, K., Hollemann-Wiberg, Lehrbuch der Anorganischen Chemie. *Angewandte Chemie-German Edition* **1996**, *108* (21), 2696.
228. Reinhoudt, H. R.; Crezee, E.; van Langeveld, A. D.; Kooyman, P. J.; van Veen, J. A. R.; Moulijn, J. A., Characterization of the Active Phase in NiW/ γ -Al₂O₃ Catalysts in Various Stages of Sulfidation with FTIR(NO) and XPS. *Journal of Catalysis* **2000**, *196* (2), 315-329.
229. van Haandel, L.; Bremmer, G. M.; Hensen, E. J. M.; Weber, T., Influence of sulfiding agent and pressure on structure and performance of CoMo/Al₂O₃ hydrodesulfurization catalysts. *Journal of Catalysis* **2016**, *342*, 27-39.
230. Scheffer, B.; Mangnus, P. J.; Moulijn, J. A., A temperature-programmed sulfiding study of NiO-WO₃/Al₂O₃ catalysts. *Journal of Catalysis* **1990**, *121* (1), 18-30.
231. Okamoto, Y.; Kato, A.; Usman; Rinaldi, N.; Fujikawa, T.; Koshika, H.; Hiromitsu, I.; Kubota, T., Effect of sulfidation temperature on the intrinsic activity of Co–MoS₂ and Co–WS₂ hydrodesulfurization catalysts. *Journal of Catalysis* **2009**, *265* (2), 216-228.
232. Satterfield, C. N.; Modell, M.; Hites, R. A.; Declerck, C. J., Intermediate Reactions in the Catalytic Hydrodenitrogenation of Quinoline. *Industrial & Engineering Chemistry Process Design and Development* **1978**, *17* (2), 141-148.
233. Vanrysselberghe, V.; Froment, G. F., Hydrodesulfurization of Dibenzothiophene on a CoMo/Al₂O₃ Catalyst: Reaction Network and Kinetics. *Industrial & Engineering Chemistry Research* **1996**, *35* (10), 3311-3318.
234. Nikulshin, P. A.; Salnikov, V. A.; Mozhaev, A. V.; Minaev, P. P.; Kogan, V. M.; Pimerzin, A. A., Relationship between active phase morphology and catalytic properties of the carbon–alumina-supported Co(Ni)Mo catalysts in HDS and HYD reactions. *Journal of Catalysis* **2014**, *309*, 386-396.
235. Shafi, R.; Hutchings, G. J., Hydrodesulfurization of hindered dibenzothiophenes: an overview. *Catalysis Today* **2000**, *59* (3), 423-442.
236. Grange, P., Catalytic hydrodesulfurization. *Catalysis Reviews—Science and Engineering* **1980**, *21* (1), 135-181.
237. Meille, V.; Schulz, E.; Lemaire, M.; Vrinat, M., Hydrodesulfurization of Alkyldibenzothiophenes over a NiMo/Al₂O₃ Catalyst: Kinetics and Mechanism. *Journal of Catalysis* **1997**, *170* (1), 29-36.
238. Li, X.; Wang, A.; Egorova, M.; Prins, R., Kinetics of the HDS of 4,6-dimethyldibenzothiophene and its hydrogenated intermediates over sulfided Mo and NiMo on γ -Al₂O₃. *Journal of Catalysis* **2007**, *250* (2), 283-293.
239. Tuxen, A. K.; Füchtbauer, H. G.; Temel, B.; Hinnemann, B.; Topsøe, H.; Knudsen, K. G.; Besenbacher, F.; Lauritsen, J. V., Atomic-scale insight into adsorption of sterically hindered dibenzothiophenes on MoS₂ and Co–Mo–S hydrotreating catalysts. *Journal of Catalysis* **2012**, *295*, 146-154.

240. Egorova, M.; Prins, R., Competitive hydrodesulfurization of 4,6-dimethyldibenzothiophene, hydrodenitrogenation of 2-methylpyridine, and hydrogenation of naphthalene over sulfided NiMo/ γ -Al₂O₃. *Journal of Catalysis* **2004**, *224* (2), 278-287.
241. Ding, S.; Zhou, Y.; Wei, Q.; Jiang, S.; Zhou, W., Substituent effects of 4,6-DMDBT on direct hydrodesulfurization routes catalyzed by Ni-Mo-S active nanocluster— A theoretical study. *Catalysis Today* **2018**, *305*, 28-39.
242. Vrinat, M.; Bacaud, R.; Laurenti, D.; Cattenot, M.; Escalona, N.; Gamez, S., New trends in the concept of catalytic sites over sulfide catalysts. *Catalysis Today* **2005**, *107–108*, 570-577.
243. Laredo S, G. C.; De los Reyes H, J. A.; Luis Cano D, J.; Jesús Castillo M, J., Inhibition effects of nitrogen compounds on the hydrodesulfurization of dibenzothiophene. *Applied Catalysis A: General* **2001**, *207* (1–2), 103-112.
244. Dugulan, A. I.; Hensen, E. J. M.; van Veen, J. A. R., High-pressure sulfidation of a calcined CoMo/Al₂O₃ hydrodesulfurization catalyst. *Catalysis Today* **2008**, *130* (1), 126-134.
245. Oliviero, L.; Marley, L.; Lélias, M. A.; Aiello, S.; van Gestel, J.; Maugé, F., Effect of High Pressure Sulfidation on the Structure of Sulfide Sites of Hydrotreatment Catalysts. *Catal Lett* **2010**, *135* (1), 62-67.
246. Chen, J.; Dominguez Garcia, E.; Oliviero, E.; Oliviero, L.; Maugé, F., Effect of high pressure sulfidation on the morphology and reactivity of MoS₂ slabs on MoS₂/Al₂O₃ catalyst prepared with citric acid. *Journal of Catalysis* **2016**, *339*, 153-162.
247. Stølen, S.; Grønvold, F.; Westrum, E. F.; Kolonin, G. R., Heat capacity and thermodynamic properties of synthetic heazlewoodite, Ni₃S₂, and of the high-temperature phase Ni_{3±x}S₂. *The Journal of Chemical Thermodynamics* **1991**, *23* (1), 77-93.
248. Seim, H.; Fjellvåg, H.; Grønvold, F.; Stølen, S., Metastable Nickel Sulfides with Composition Close to Ni₇S₆— Stability and Structural Properties. *Journal of Solid State Chemistry* **1996**, *121* (2), 400-407.
249. Travert, A.; Dujardin, C.; Maugé, F.; Veilly, E.; Cristol, S.; Paul, J. F.; Payen, E., CO Adsorption on CoMo and NiMo Sulfide Catalysts: A Combined IR and DFT Study. *The Journal of Physical Chemistry B* **2006**, *110* (3), 1261-1270.
250. Yang, B.; Tian, S.; Zhao, S., A study of thermal decomposition of alkanethiols in pressure reactor. *Fuel Processing Technology* **2006**, *87* (8), 673-678.
251. Mashkina, A. V.; Grunvald, V. R.; Nasteka, V. I.; Borodin, B. P.; Yakovleva, V. N.; Khairulina, L. N., Decomposition of alkanethiols to dialkyl sulfides and hydrogen sulfide. *Reaction Kinetics and Catalysis Letters* **1990**, *41* (2), 357-362.
252. Peterson, S. L.; Schulz, K. H., Ethanethiol Decomposition Pathways on MoS₂(0001). *Langmuir* **1996**, *12* (4), 941-945.
253. Ge, H.; Wen, X.-D.; Ramos, M. A.; Chianelli, R. R.; Wang, S.; Wang, J.; Qin, Z.; Lyu, Z.; Li, X., Carbonization of Ethylenediamine Coimpregnated CoMo/Al₂O₃ Catalysts Sulfided by Organic Sulfiding Agent. *ACS Catalysis* **2014**, *4* (8), 2556-2565.
254. Yang, H.; Fairbridge, C.; Chen, J.; Ring, Z., Structure-HDS Reactivity Relationship of Dibenzothiophenes Based on Density Functional Theory. *Catal Lett* **2004**, *97* (3), 217-222.

Appendix

A1. Supporting Information of Chapter 2

Assignment of the RAMAN bands

Table A32. Raman bands observed in the spectra of the precursor WMoNi-aO_x, corresponding assignments, and vibration modes. Legend: s: symmetric, as: asymmetric, v: stretching vibration, δ : bending vibration.¹⁵⁰⁻¹⁵²

Raman shift [cm ⁻¹]	Vibration mode	Component
1000-930	$\nu_s(\text{Mo(W)=O})$	Mo(W)O ₄
878	$\nu_{as}(\text{Mo(W)=O})$	Mo(W)O ₄
690	$\nu_s(\text{Mo(W)=O})$	Mo(W)O ₆
530	$\nu(\text{Mo(W)-O-Mo(W)})$	NiMo(W)O ₄
408	$\delta(\text{Mo(W)=O})$	Mo(W)O ₄
348	$\delta(\text{Mo(W)=O})$	Mo(W)O ₄

Table A33. Raman bands observed in the spectra of the precursor WMoNi-aHTO_x, corresponding assignments, and vibration modes. Legend: s: symmetric, as: asymmetric, v: stretching vibration, δ : bending vibration, Γ : lattice vibration.¹⁵⁰⁻¹⁵²

Raman shift [cm ⁻¹]	Vibration mode	Component
943	$\nu_s(\text{Mo(W)=O})$	Mo(W)O ₄
850	$\nu_{as}(\text{Mo(W)-O-Mo(W)})$	Mo(W)O ₄
674	$\nu_s(\text{Mo(W)=O})$	Mo(W)O ₆
160	$\Gamma(\text{Mo(W)})$	Mo(W)O ₄ , Mo(W)O ₆

Table A34. Raman bands observed in the spectra of the precursor WMoNi-bO_x, corresponding assignments, and vibration modes. Legend: s: symmetric, as: asymmetric, v: stretching vibration, δ : bending vibration, Γ : lattice vibration.¹⁵⁰⁻¹⁵²

Raman shift [cm ⁻¹]	Vibration mode	Component
942	$\nu_s(\text{Mo(W)=O})$	Mo(W)O ₄
900	$\nu_{as}(\text{Mo(W)=O})$	Mo(W)O ₄
860	$\nu_{as}(\text{Mo(W)-O-Mo(W)})$	Mo(W)O ₄
806	$\nu_{as}(\text{Mo(W)=O})$	Mo(W)O ₆
700	$\nu_s(\text{Mo(W)=O})$	Mo(W)O ₆
345	$\delta(\text{Mo(W)=O})$	Mo(W)O ₄
320	$\delta(\text{Mo(W)=O})$	Mo(W)O ₆
261	$\delta(\text{Mo(W)-O-Mo(W)})$	Mo(W)O ₆
185	$\Gamma(\text{Mo(W)})$	Mo(W)O ₄ , Mo(W)O ₆

Table A35. Raman bands observed in the spectra of the precursor WMoNi-bHTO_x, corresponding assignments, and vibration modes. Legend: s: symmetric, as: asymmetric, v: stretching vibration, δ : bending vibration, Γ : lattice vibration.¹⁵⁰⁻¹⁵²

Raman shift [cm ⁻¹]	Vibration mode	Component
880	$\nu_{as}(\text{Mo(W)=O})$	Mo(W)O ₄
845	$\nu_{as}(\text{Mo(W)-O-Mo(W)})$	Mo(W)O ₄
679	$\nu_s(\text{Mo(W)=O})$	Mo(W)O ₆
150	$\Gamma(\text{Mo(W)})$	Mo(W)O ₄ , Mo(W)O ₆

Table A36. Raman bands observed in the spectra of the precursor WMoNi-sO_x, corresponding assignments, and vibration modes. Legend: s: symmetric, as: asymmetric, v: stretching vibration, δ : bending vibration.¹⁵⁰⁻¹⁵²

Raman shift [cm ⁻¹]	Vibration mode	Component
977	$v_s(\text{Mo(W)=O})$	Mo(W)O ₄
947	$v_s(\text{Mo(W)=O})$	Mo(W)O ₄
904	$v_{as}(\text{Mo(W)=O})$	Mo(W)O ₄
822	$v_{as}(\text{Mo(W)=O})$	Mo(W)O ₆
700	$v_s(\text{Mo(W)=O})$	Mo(W)O ₆
350	$\delta(\text{Mo(W)=O})$	Mo(W)O ₄

Table A37. Raman bands observed in the spectra of the precursor WMoNi-sHTO_x, corresponding assignments, and vibration modes. Legend: s: symmetric, as: asymmetric, v: stretching vibration, δ : bending vibration.¹⁵³

Raman shift [cm ⁻¹]	Vibration mode
940	$v(\text{S}_2\text{Mo(W)O}_2^{2-})$
839	$v(\text{SMo(W)O}_3^{2-})$
809	$v(\text{Mo(W)}_2\text{O}_2\text{S}_2^{2-})$
783	$v(\text{Mo(W)}_2\text{O}_2\text{S}_2^{2-})$
690	$v_s(\text{Mo(W)=O})$
242	$\delta(\text{Mo(W)}_2\text{O}_2\text{S}_2^{2-})$

TEM analysis – Distribution of Mo(W)₂ slab length

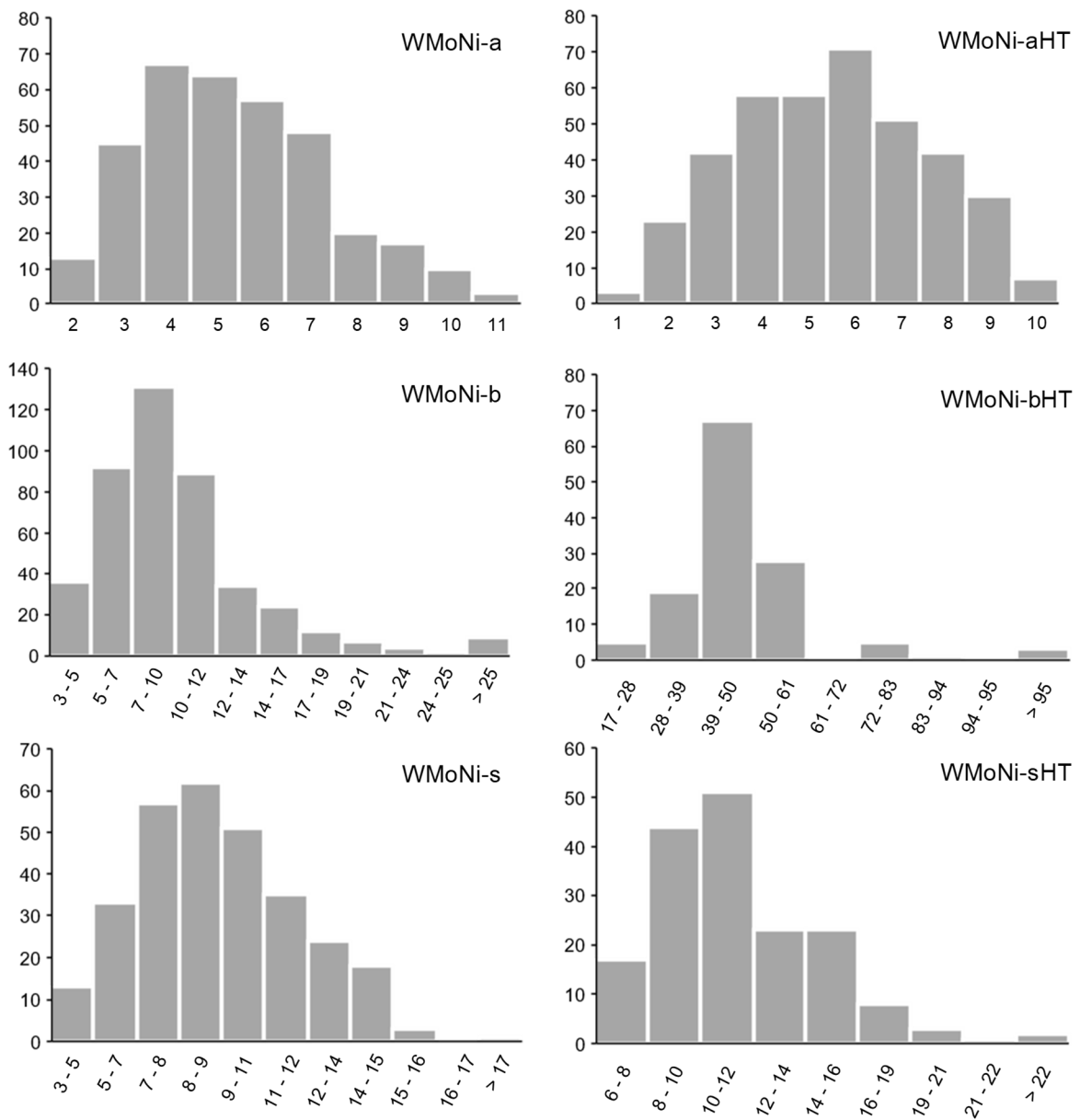


Figure A84. Distribution of the Mo(W)₂S₂ slab length in the sulfide catalysts WMoNi-a, WMoNi-b, WMoNi-s, WMoNi-aHT, WMoNi-bHT, and WMoNi-sHT.

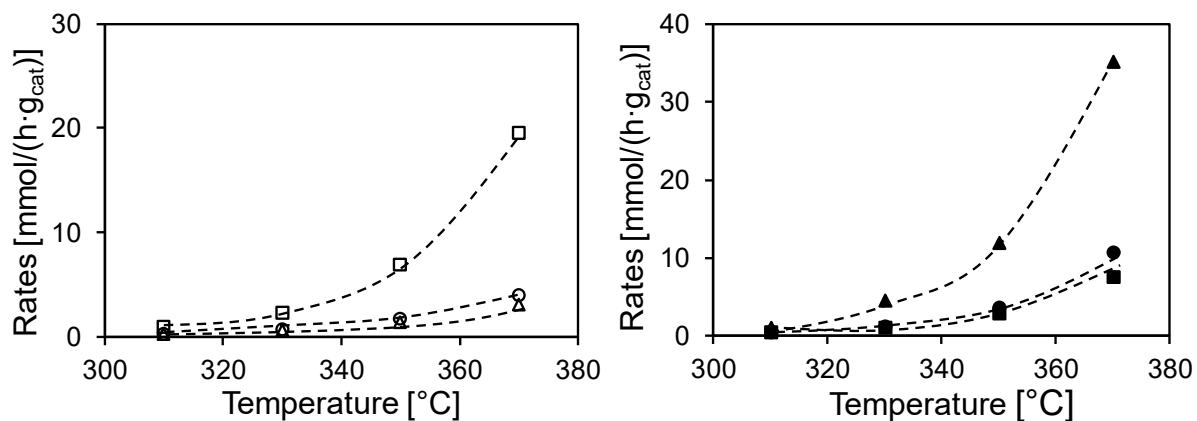
Conversion of the hydrodenitrogenation of *o*-propylaniline with temperature

Figure A85. Reaction rates for the hydrodenitrogenation of *o*-propylaniline at varying temperatures on the sulfided catalysts WMoNi-a (circle, unfilled), WMoNi-b (square, unfilled), WMoNi-s (triangle, unfilled), WMoNi-aHT (circle, filled), WMoNi-bHT (square, filled), and WMoNi-sHT (triangle, filled).

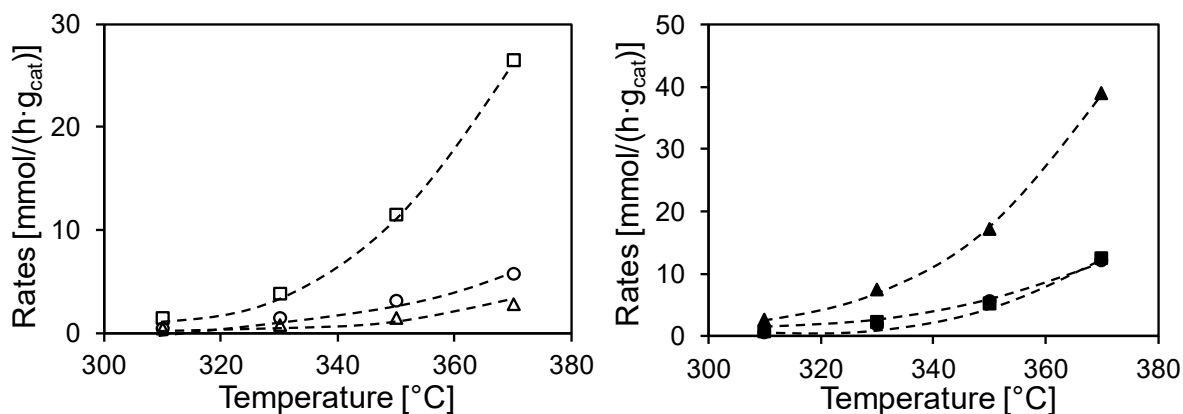


Figure A86. Reaction rates for the hydrodenitrogenation of *o*-propylaniline in the presence of dibenzothiophene at varying temperatures on the sulfided catalysts WMoNi-a (circle, unfilled), WMoNi-b (square, unfilled), WMoNi-s (triangle, unfilled), WMoNi-aHT (circle, filled), WMoNi-bHT (square, filled), and WMoNi-sHT (triangle, filled).

Conversion of the hydrodenitrogenation of quinoline with temperature

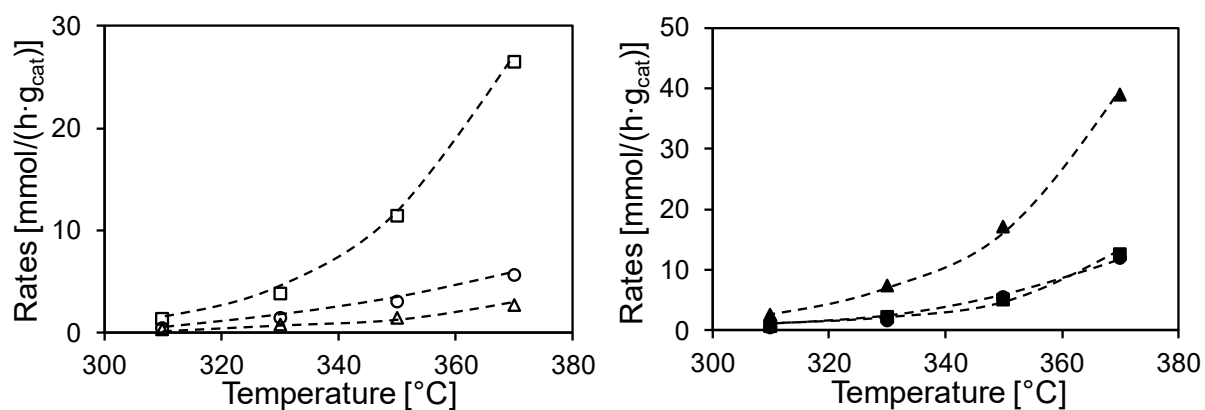


Figure A87. Reaction rates for the hydrodenitrogenation of quinoline (+ 1,2,3,4-tetrahydroquinoline) at varying temperatures on the sulfided catalysts WMoNi-a (circle, unfilled), WMoNi-b (square, unfilled), WMoNi-s (triangle, unfilled), WMoNi-aHT (circle, filled), WMoNi-bHT (square, filled), and WMoNi-sHT (triangle, filled).

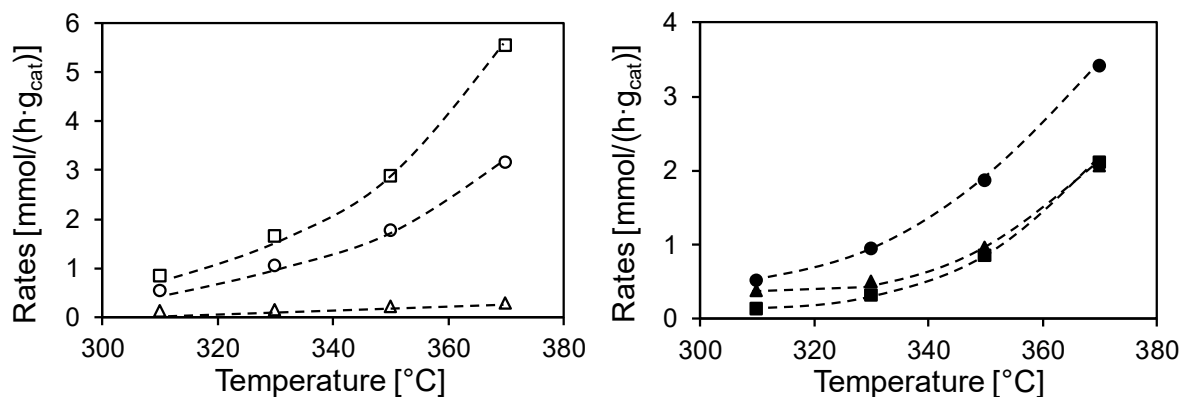


Figure A88. Reaction rates for the hydrodenitrogenation of quinoline (+ 1,2,3,4-tetrahydroquinoline) in the presence of dibenzothiophene at varying temperatures on the sulfided catalysts WMoNi-a (circle, unfilled), WMoNi-b (square, unfilled), WMoNi-s (triangle, unfilled), WMoNi-aHT (circle, filled), WMoNi-bHT (square, filled), and WMoNi-sHT (triangle, filled).

Conversion of the hydrodesulfurization of dibenzothiophene with temperature

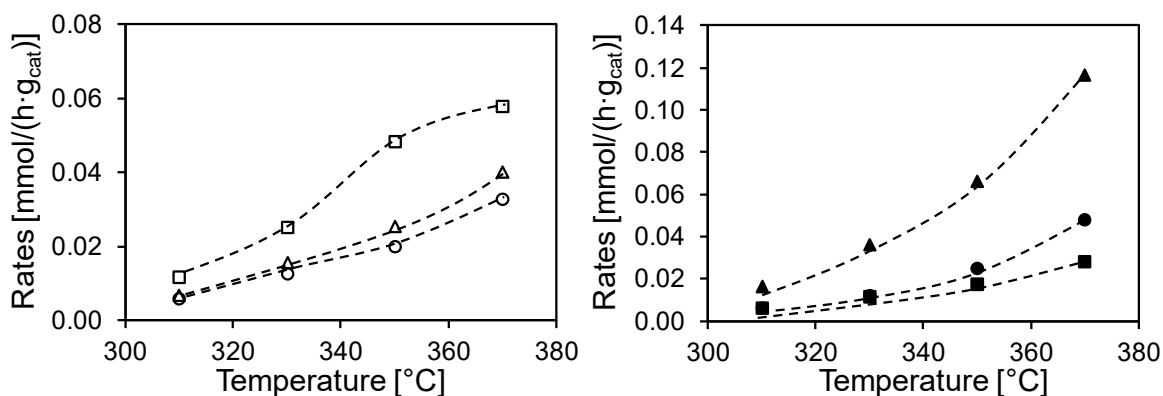


Figure A89. Reaction rates for the hydrodesulfurization of dibenzothiophene at varying temperatures in the presence of *o*-propylaniline on the sulfided catalysts WMoNi-a (circle, unfilled), WMoNi-b (square, unfilled), WMoNi-s (triangle, unfilled), WMoNi-aHT (circle, filled), WMoNi-bHT (square, filled), and WMoNi-sHT (triangle, filled).

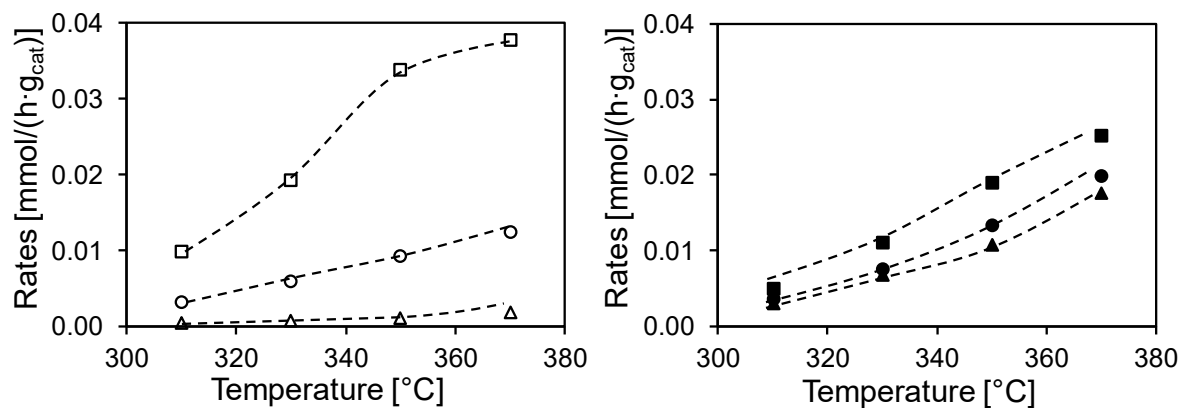


Figure A90. Reaction rates for the hydrodesulfurization of dibenzothiophene at varying temperatures in the presence of quinoline on the sulfided catalysts WMoNi-a (circle, unfilled), WMoNi-b (square, unfilled), WMoNi-s (triangle, unfilled), WMoNi-aHT (circle, filled), WMoNi-bHT (square, filled), and WMoNi-sHT (triangle, filled).

Calculated weighted parameters

Table A38. Weighting factors [mmol/(h·g_{cat})] of relevant physicochemical properties in different reactions at 310 °C: HDN of *o*-propylaniline (OPA) and quinoline (Q) in the absence of dibenzothiophene (DBT) (HDN, OPA, and Q, respectively); HDN of *o*-propylaniline (OPA) and quinoline (Q) in the presence of dibenzothiophene (DBT) (HDN-DBT, OPA, and Q, respectively); and HDS of dibenzothiophene (DBT) in the presence of *o*-propylaniline (OPA) or quinoline (Q) (HDS, DBT-OPA, and DBT-Q, respectively).

Physicochemical property	HDN		HDN-DBT		HDS	
	OPA	Q	OPA	Q	DBT-OPA	DBT-Q
x_W	1.3	0.8	1.8	1.5	1.0	1.5
x_{Mo}	-0.2	0.0	-0.8	-0.1	-0.1	-0.1
$x_{Ni, XPS}$	-1.2	-0.6	-1.7	-0.9	-0.7	-1.3
Adsorbed NO	0.4	0.1	0.9	0.2	0.5	0.2
Slab length	-2.0	-1.4	-3.0	-2.2	-1.4	-1.8
Surface area	2.3	1.2	4.4	1.6	1.8	1.6

Table A39. Weighting factors [mmol/(h·g_{cat})] of relevant physicochemical properties in different reactions at 330 °C: HDN of *o*-propylaniline (OPA) and quinoline (Q) in the absence of dibenzothiophene (DBT) (HDN, OPA, and Q, respectively); HDN of *o*-propylaniline (OPA) and quinoline (Q) in the presence of dibenzothiophene (DBT) (HDN-DBT, OPA, and Q, respectively); and HDS of dibenzothiophene (DBT) in the presence of *o*-propylaniline (OPA) or quinoline (Q) (HDS, DBT-OPA, and DBT-Q, respectively).

Physicochemical property	HDN		HDN-DBT		HDS	
	OPA	Q	OPA	Q	DBT-OPA	DBT-Q
x_W	3.1	1.9	5.3	3.2	2.0	3.2
x_{Mo}	-1.0	-0.1	-2.2	-0.2	-0.4	-0.2
$x_{Ni, XPS}$	-2.9	-1.3	-4.7	-1.9	-1.6	-2.9
Adsorbed NO	1.1	0.1	1.7	0.3	1.4	0.5
Slab length	-5.9	-2.9	-9.4	-4.4	-2.9	-3.8
Surface area	7.7	2.3	13.1	3.0	3.8	3.4

Table A40. Weighting factors [mmol/(h·g_{cat})] of relevant physicochemical properties in different reactions at 350 °C: HDN of *o*-propylaniline (OPA) and quinoline (Q) in the absence of dibenzothiophene (DBT) (HDN, OPA, and Q, respectively); HDN of *o*-propylaniline (OPA) and quinoline (Q) in the presence of dibenzothiophene (DBT) (HDN-DBT, OPA, and Q, respectively); and HDS of dibenzothiophene (DBT) in the presence of *o*-propylaniline (OPA) or quinoline (Q) (HDS, DBT-OPA, and DBT-Q, respectively).

Physicochemical property	HDN		HDN-DBT		HDS	
	OPA	Q	OPA	Q	DBT-OPA	DBT-Q
x_W	9.5	4.0	17.8	5.6	4.2	6.5
x_{Mo}	-2.9	-0.3	-4.5	-0.5	-0.6	-0.5
$x_{Ni, XPS}$	-9.4	-2.8	-14.0	-3.4	-3.7	-6.4
Adsorbed NO	3.5	0.4	2.2	0.9	2.4	1.5
Slab length	-17.5	-5.8	28.5	-7.6	-6.9	-7.7
Surface area	21.7	4.5	34.9	5.5	7.9	6.7

Calculated rate constants

Table A41. Rate constants [mmol/(h·g_{cat})] calculated using the weighting factors for hydrodenitrogenation of *o*-propylaniline (OPA) in the absence (HDN OPA) and presence of dibenzothiophene (DBT) (HDN OPA-DBT).

Catalyst	HDN OPA			HDN OPA-DBT		
	310 °C	330 °C	350 °C	310 °C	330 °C	350 °C
WMoNi-a	0.26	0.73	1.72	0.46	1.45	4.89
WMoNi-aHT	0.49	1.32	3.60	0.59	1.89	5.79
WMoNi-b	0.91	2.32	6.87	1.40	3.85	11.16
WMoNi-bHT	0.45	1.13	2.99	0.91	2.44	6.66
WMoNi-s	0.21	0.55	1.32	0.37	0.78	1.26
WMoNi-sHT	1.15	4.53	11.91	2.68	7.56	16.94

Table A42. Rate constants [mmol/(h·g_{cat})] calculated using the weighting factors for hydrodenitrogenation of quinoline (Q) in the absence (HDN Q) and presence of dibenzothiophene (DBT) (HDN Q-DBT).

Catalyst	HDN Q			HDN Q-DBT		
	310 °C	330 °C	350 °C	310 °C	330 °C	350 °C
WMoNi-a	0.29	0.64	1.00	0.55	1.06	1.78
WMoNi-aHT	0.36	0.58	1.46	0.52	0.96	1.88
WMoNi-b	0.52	1.16	2.16	0.85	1.67	2.89
WMoNi-bHT	0.15	0.15	0.71	0.13	0.33	0.87
WMoNi-s	0.10	0.22	0.14	0.13	0.17	0.22
WMoNi-sHT	0.50	0.76	1.08	0.37	0.49	0.94

Table A43. Rate constants [mmol/(h·g_{cat})] calculated using the weighting factors for hydrodesulfurization of dibenzothiophene (DBT) with simultaneous hydrodenitrogenation of *o*-propylaniline (OPA) (HDS DBT-OPA) and HDN of quinoline (Q) (HDS DBT-Q), respectively.

Catalyst	HDS DBT-OPA			HDS DBT-Q		
	310 °C	330 °C	350 °C	310 °C	330 °C	350 °C
WMoNi-a	0.49	1.04	1.64	0.27	0.49	0.79
WMoNi-aHT	0.51	1.01	2.12	0.32	0.67	1.21
WMoNi-b	0.97	2.10	4.05	0.87	1.82	3.80
WMoNi-bHT	0.52	1.00	1.50	0.43	0.96	1.76
WMoNi-s	0.56	1.30	2.12	0.03	0.04	0.07
WMoNi-sHT	1.35	3.03	5.53	0.27	0.59	0.97

Contributions of the parameters to the hydrotreating activity

Table A44. Contributions (%) of the relevant parameters to the activities (measured at 310 °C): HDN of *o*-propylaniline (OPA) and quinoline (Q) in the absence of dibenzothiophene (DBT) (HDN, OPA, and Q, respectively); HDN of *o*-propylaniline (OPA), and quinoline (Q) in the presence of dibenzothiophene (DBT) (HDN-DBT, OPA, and Q, respectively); and HDS of dibenzothiophene (DBT) in the presence of *o*-propylaniline (OPA) or quinoline (Q) (HDS, DBT-OPA, and DBT-Q, respectively).

Physicochemical property	HDN		HDN-DBT		HDS	
	OPA	Q	OPA	Q	DBT-OPA	DBT-Q
x_W	13.1	16.7	8.7	22.1	13.7	23.2
x_{Mo}	0.3	0.0	1.8	0.1	0.2	0.1
$x_{Ni, XPS}$	11.3	6.9	8.2	7.8	7.6	18.2
Adsorbed NO	1.0	0.1	2.1	0.2	3.7	0.5
Slab length	32.6	42.8	25.1	46.5	28.5	32.7
Surface area	41.7	33.6	54.2	23.4	46.2	25.4

Table A45. Contributions (%) of the relevant parameters to the activities (measured at 330 °C): HDN of *o*-propylaniline (OPA) and quinoline (Q) in the absence of dibenzothiophene (DBT) (HDN, OPA, and Q, respectively); HDN of *o*-propylaniline (OPA), and quinoline (Q) in the presence of dibenzothiophene (DBT) (HDN-DBT, OPA, and Q, respectively); and HDS of dibenzothiophene (DBT) in the presence of *o*-propylaniline (OPA) or quinoline (Q) (HDS, DBT-OPA, and DBT-Q, respectively).

Physicochemical property	HDN		HDN-DBT		HDS	
	OPA	Q	OPA	Q	DBT-OPA	DBT-Q
x_W	8.4	19.3	9.0	23.6	12.5	22.6
x_{Mo}	1.0	0.0	1.5	0.1	0.5	0.1
$x_{Ni, XPS}$	7.2	9.4	6.9	8.8	7.8	19.1
Adsorbed NO	1.0	0.1	0.9	0.3	5.9	0.6
Slab length	30.7	43.6	27.7	45.3	27.2	31.7
Surface area	51.7	27.5	54.1	21.9	46.1	25.9

Table A46. Contributions (%) of the relevant parameters to the activities (measured at 350 °C): HDN of *o*-propylaniline (OPA) and quinoline (Q) in the absence of dibenzothiophene (DBT) (HDN, OPA, and Q, respectively); HDN of *o*-propylaniline (OPA), and quinoline (Q) in the presence of dibenzothiophene (DBT) (HDN-DBT, OPA, and Q, respectively); and HDS of dibenzothiophene (DBT) in the presence of *o*-propylaniline (OPA) or quinoline (Q) (HDS, DBT-OPA, and DBT-Q, respectively).

Physicochemical property	HDN		HDN-DBT		HDS	
	OPA	Q	OPA	Q	DBT-OPA	DBT-Q
x_W	9.3	20.5	12.4	23.5	12.2	22.3
x_{Mo}	0.9	0.12	0.8	0.2	0.2	0.1
$x_{Ni, XPS}$	9.1	10.2	7.6	8.6	9.5	21.5
Adsorbed NO	1.3	0.2	0.2	0.6	4.1	1.1
Slab length	31.4	42.8	32.6	44.2	32.1	31.2
Surface area	48.1	26.3	47.4	23.0	41.9	23.7

Parity plots of the calculated and measured hydrotreating rates

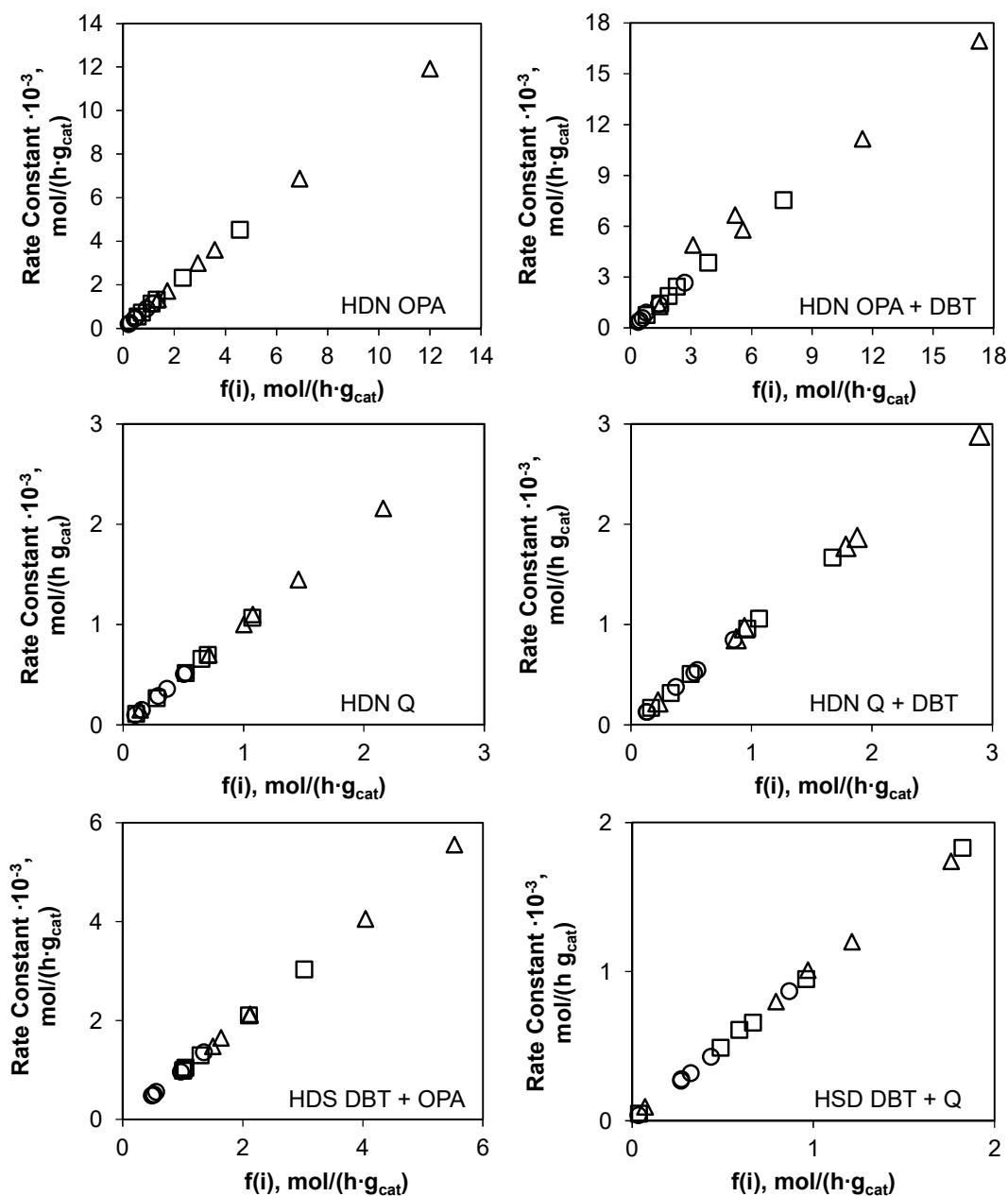


Figure A91. Parity plots of experimental rates along rates predicted by the empirical equation at 310 °C (o), 330 °C (□), and 350 °C (Δ).

A2. Supporting Information of Chapter 3

TEM analysis – Distribution of slab length of parent and leached sulfides

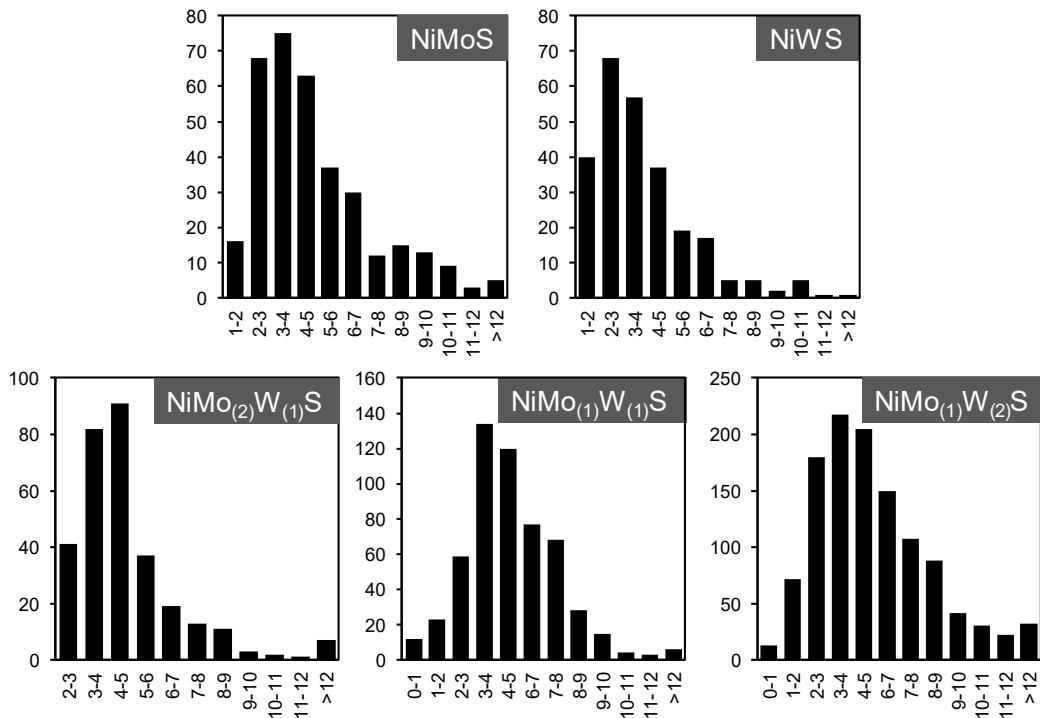


Figure A92. Distribution of the Mo(W)S₂ slab length of the parent sulfides NiMoS, NiMo₂W₍₁₎S, NiMo₍₁₎W₍₁₎S, NiMo₍₁₎W₍₂₎S, and NiWS derived from TEM analysis.

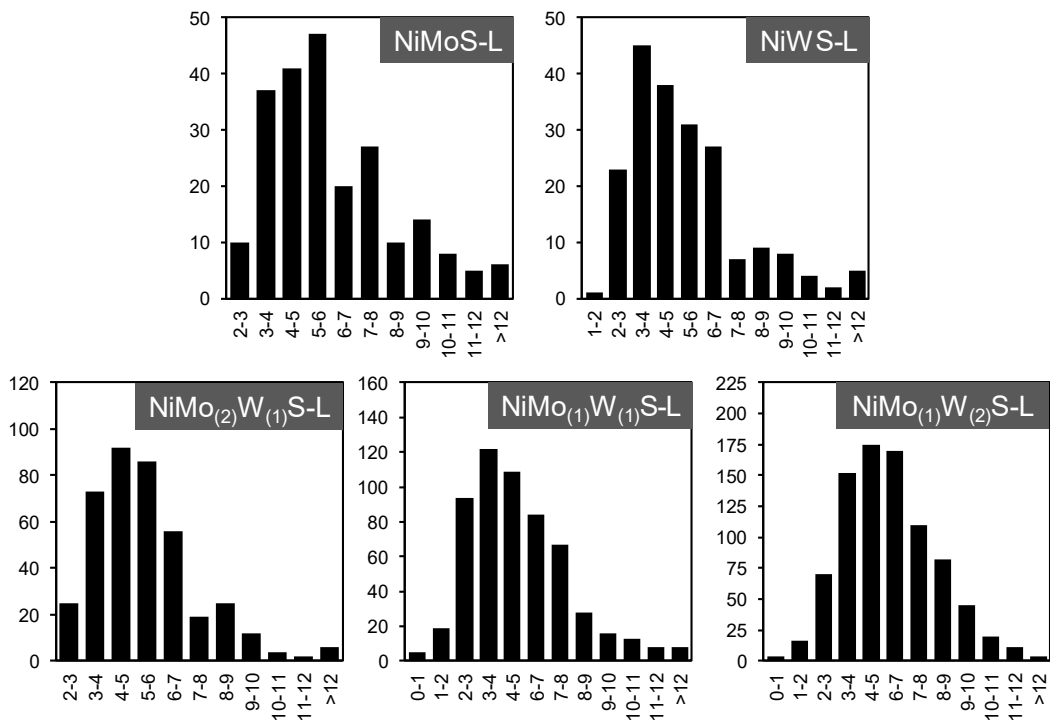


Figure A93. Distribution of the Mo(W)S₂ slab length of the HCl-treated sulfides NiMoS-L, NiMo₂W₍₁₎S-L, NiMo₍₁₎W₍₁₎S-L, NiMo₍₁₎W₍₂₎S-L, and NiWS-L derived from TEM analysis.

A3. Supporting Information of Chapter 4

EXAFS scans on the Ni K-edge

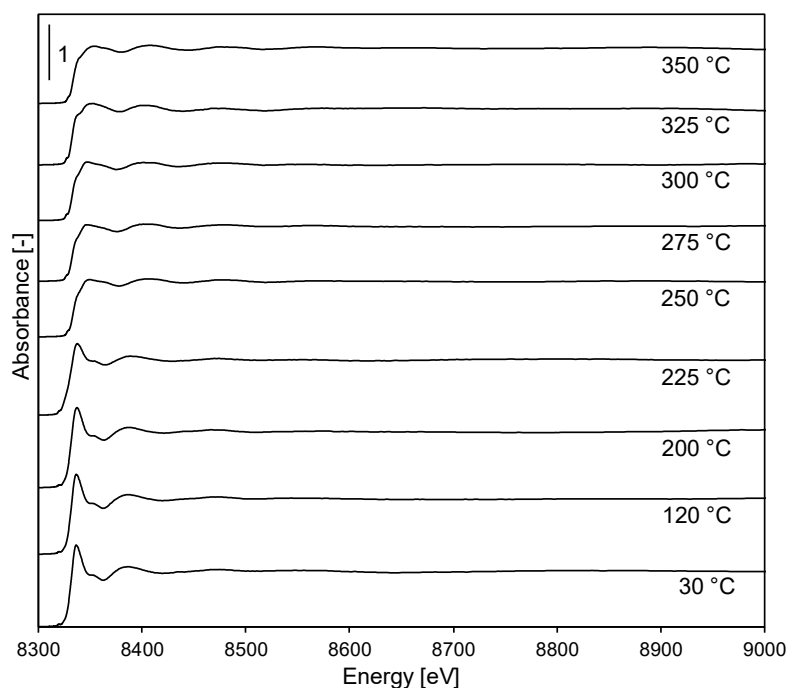


Figure A94. EXAFS scans on the Ni K-edge recorded at different temperatures during liquid-phase sulfidation of a trimetallic oxide precursor at 4 bar total pressure.

EXAFS scans on the Mo K-edge

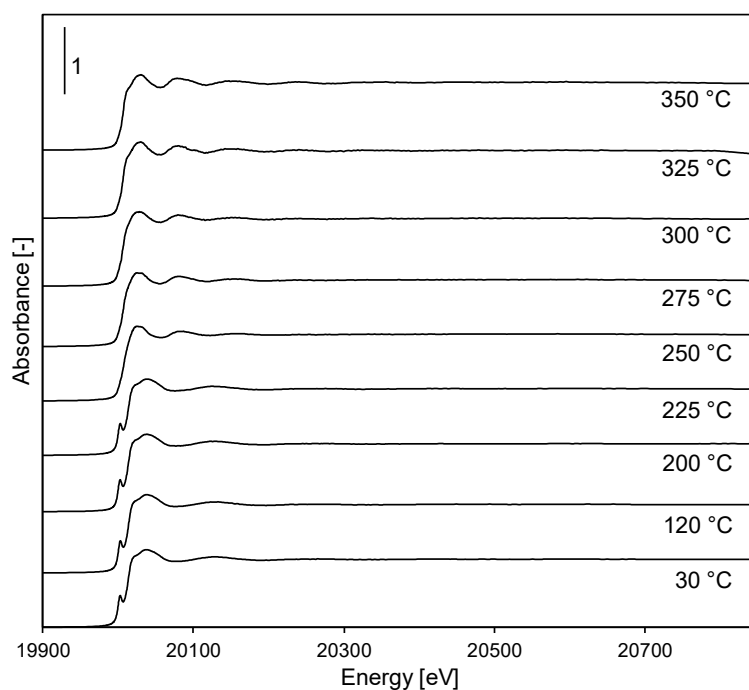


Figure A95. EXAFS scans on the Mo K-edge recorded at different temperatures during liquid-phase sulfidation of a trimetallic oxide precursor at 4 bar total pressure.

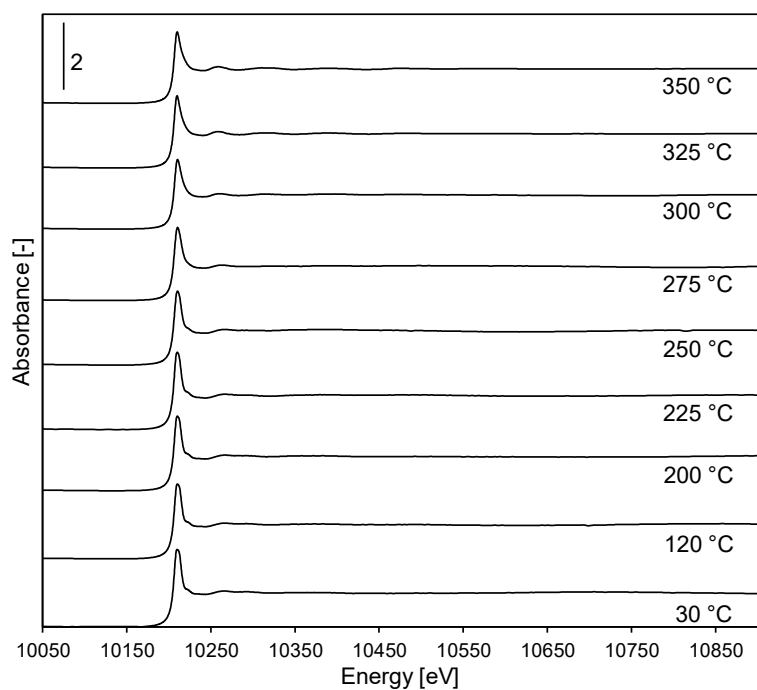
EXAFS scans on the W L_{III}-edge

Figure A96. EXAFS scans on the W L_{III}-edge recorded at different temperatures during liquid-phase sulfidation of a trimetallic oxide precursor at 4 bar total pressure.

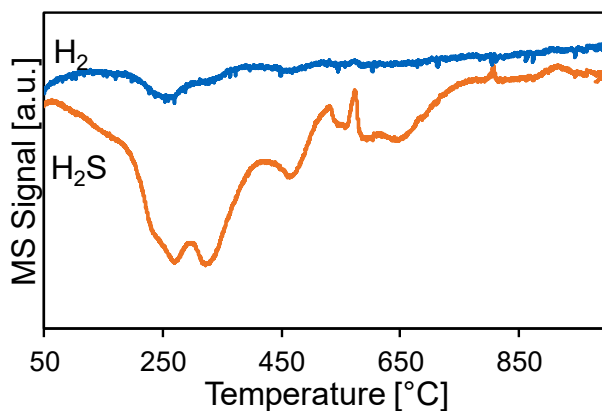
Temperature-programmed sulfidation profiles of reference materials

Figure A97. Temperature-programmed sulfidation of nickel(II) oxide (NiO) using a flow of 10 vol. % H₂S in H₂ (10 mL/min) at atmospheric pressure.

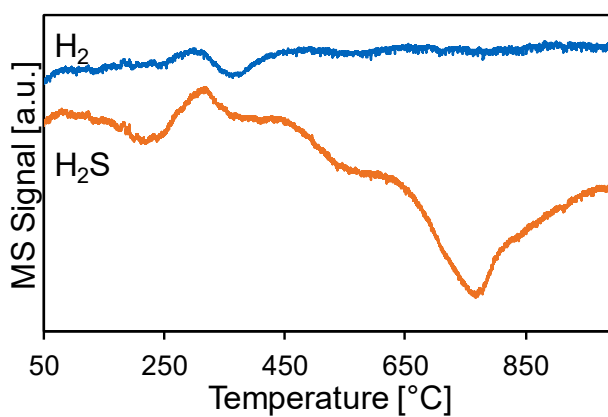


Figure A98. Temperature-programmed sulfidation of molybdenum(VI) trioxide (MoO₃) using a flow of 10 vol. % H₂S in H₂ (10 mL/min) at atmospheric pressure.

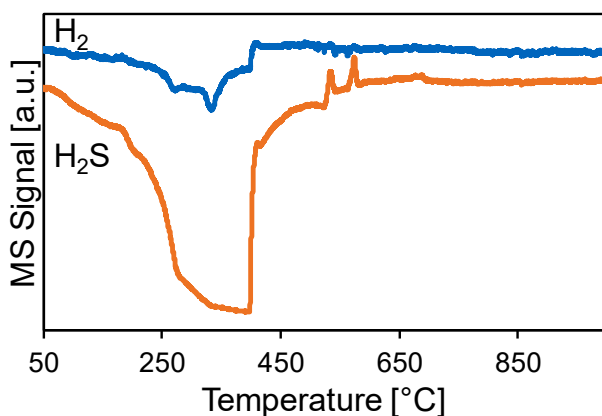


Figure A99. Temperature-programmed sulfidation of nickel(II) molybdate (NiMoO₄) using a flow of 10 vol. % H₂S in H₂ (10 mL/min) at atmospheric pressure.

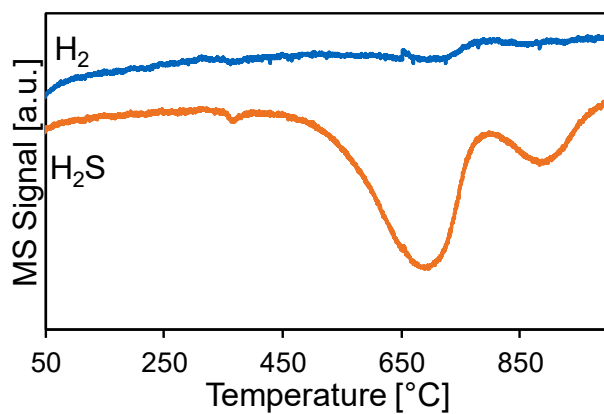


Figure A100. Temperature-programmed sulfidation of tungsten(VI) trioxide (WO₃) using a flow of 10 vol. % H₂S in H₂ (10 mL/min) at atmospheric pressure.

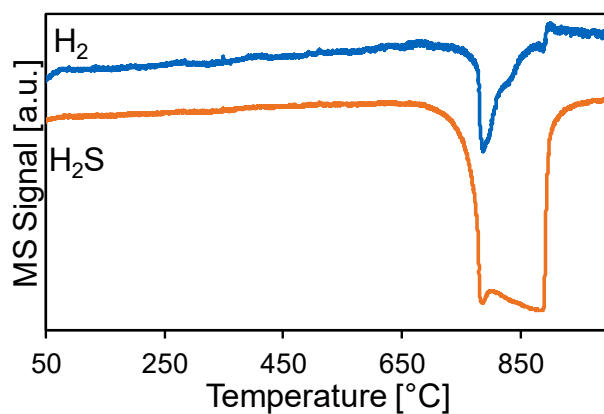


Figure A101. Temperature-programmed sulfidation of nickel(II) tungstate (NiWO₄) using a flow of 10 vol. % H₂S in H₂ (10 mL/min) at atmospheric pressure.

Curriculum Vitae

Name Sylvia Albersberger
Birth 24.08.1986, Eggenfelden

Education

since 09/2014 **PhD candidate**
TU Munich, Technische Chemie II, Catalysis Research Center
Supervisor: Prof. Dr. Johannes A. Lercher

10/2012 - 09/2012 **Master of Science (Chemistry)**
TU Munich
Main subject: Technical Chemistry
Side subject: Catalysis and Reaction Technology
Thesis: "Synthesis and characterization of bimetallic Pd/Au@SiO₂ catalysts" (1.0)
Final Grade: 1.3

10/2009 - 09/2012 **Bachelor of Science (Chemistry)**
Universität Regensburg
Thesis: "Investigation of the concept facilitated hydrotrophy in ternary systems" (1.0)
Final Grade: 1.8

09/2006 - 06/2009 **Vocational training** as a chemical laboratory technician
Wacker Chemie AG

09/1997 – 06/2006 **Abitur**
Tassilo-Gymnasium Simbach/Inn
Main subjects: Chemistry and History
Final Grade: 1.6

Practical experience

08/2013 - 09/2013 Working student in a clean room laboratory
Wacker Chemie AG

04/2013 - 05/2013 Industrial training
Wacker Chemie AG
Development of a gas chromatography method

08/2012 - 09/2012, Working student Wacker Chemie AG
08/2011 - 09/2011 and Wacker Chemie AG
08/2010 - 09/2010 Analysis of polysilicon

07/2009 - 09/2009 Chemical laboratory technician
Wacker Chemie AG
Analysis of polysilicon

Conference Contributions & Publications

Oral presentations

- 51st Jahrestreffen Deutscher Katalytiker in Weimar (Germany) 03/2018
“Revealing structure-activity correlations of hydrodenitrogenation on unsupported Ni-Mo-W sulfide catalysts”
- 13th European Congress on Catalysis (EUROPACAT) in Florence (Italy) 08/2017
“Hydrodenitrogenation of aromatic compounds on Ni-Mo-W sulfides”
- 25th North American Catalysis Society Meeting (NAM) in Denver (Colorado, USA) 06/2017
“Hydrogenation and C-N bond cleavage of aromatic compounds on Ni-Mo-W sulfides”
- 7th International Symposium on Molecular Aspects of Catalysis by Sulfides (MACS-VII) in Doorn (Netherlands) 05/2016
“Morphology and distribution of metal cations in Ni-Mo-W sulfides and its consequences for catalysis”

Posters

- 50th Jahrestreffen Deutscher Katalytiker in Weimar (Germany) 03/2017
“Ni-Mo-W interactions in oxide precursors and sulfide catalysts and their consequences for hydrotreating activity”
- Catalysis - Novel Aspects in Petrochemistry and Refining in Berlin (Germany) 09/2016
“Simultaneous hydrodenitrogenation and hydrodesulfurization of model compounds on unsupported Ni-Mo-W sulfide catalysts” (conference paper included)
- 49th Jahrestreffen Deutscher Katalytiker in Weimar (Germany) 03/2016
“Ni-Mo-W interactions in oxide precursors and sulfide catalysts and their consequences for hydrotreating activity”
- 25th North American Catalysis Society Meeting (NAM) in Pittsburgh (PA, USA) 06/2015
“Revealing structure-activity correlations and surface mechanisms of hydride-nitrogenation on multimetallic sulfide bulk catalysts”
- 48th Jahrestreffen Deutscher Katalytiker in Weimar (Germany) 03/2015
“Elementary steps and structure-activity correlations of hydrodenitrogenation on Ni-Mo-W sulfides”

Publications

- Albersberger, et al., *Catalysis Today* **2017**, 297, 344-355.
“Simultaneous hydrodenitrogenation and hydro-desulfurization on unsupported Ni-Mo-W sulfides”
- Hein, et al., *ChemCatChem* **2016**, 9, 629-641.
“Towards understanding structure-activity relationships of Ni-Mo-W sulfide hydrotreating catalysts”

The right words do not need others to mean something.
(Kimi Räikkönen)